**University of Warsaw**
Faculty of Physics
Institute of Theoretical Physics

Michał Iglicki

# Collider and early-Universe interactions of dark matter in Higgs-portal models

doctoral dissertation
prepared under the supervision of
**prof. dr hab. Bohdan Grządkowski**

Warsaw, June 2023

# Abstract

This dissertation is devoted to interactions of Higgs-portal dark matter in the early Universe and at particle colliders. After recalling the most relevant cosmological concepts, including the Boltzmann equation and the freeze-out mechanism, we provide a short review of dark matter physics: evidence and candidates (chapter 3), and experimental searches (chapter 4).

Chapters 5 and 6 contain original results. The former discusses the issue of $t$-channel singularity: a phenomenon affecting processes with a massive, stable $t$-channel mediator on its mass shell. An occurrence of that issue leads to singularity of the matrix element describing the process, which results in an infinite value of the corresponding cross section. After determining the strict condition for the singularity to occur in a given $2 \to 2$ process, we propose a regularization mechanism, which is based on interactions between the on-shell mediator and the surrounding gas of particles. Those interactions limit the lifetime of the mediator, allowing to introduce an effective decay width, which regularizes the would-be-singular cross section. Chapter 6 presents a study of production of dark particles at the future $e^+e^-$ colliders, operating at energies maximizing the cross section of the Higgs-strahlung process (around 240–250 GeV). We take into account the present limits, constraining the parameter space of the DM models employed, and estimate the maximal possible production cross section. The conclusion is that although the models of DM are severely constrained by the null-results of the present and past experimental searches, the dark particles could be efficiently produced and detected at the future colliders if the values of the parameters are close to the optimal ones. Moreover, in that chapter, we investigate the influence of the spin of the dark particle on production rate: although all three analysed models of dark matter provide a similar maximal production cross section (at the level of 60 fb), the shape of the allowed parameter space differs depending on the spin, which, in principle, could enable to disentangle the cases of dark particles of different spins from each other.

The models of dark matter employed in this dissertation are fully consistent, renormalizable Higgs-portal models. Along with some details of calculations performed throughout the thesis, they are described in the appendices.



# Streszczenie

Niniejsza rozprawa poświęcona jest oddziaływaniom ciemnej materii, opisywanej modelami z portalem Higgsa, we wczesnym Wszechświecie oraz w zderzaczach cząstek. Po przypomnieniu najistotniejszych pojęć z zakresu kosmologii, w tym równania Boltzmanna oraz mechanizmu freeze-outu („wymrożenia"), dokonujemy krótkiego przeglądu fizyki ciemnej materii, obejmującego dowody na jej istnienie oraz dyskusję proponowanych kandydatów na ciemną materię (rozdział 3), jak również doświadczalne poszukiwania ciemnej materii (rozdział 4).

Rozdziały 5 i 6 zawierają oryginalne wyniki. Pierwszy z nich omawia problem osobliwości w kanale $t$: zjawiska mającego wpływ na procesy z masywnym, stabilnym mediatorem w kanale $t$, znajdującym się na powłoce masy. Wystąpienie owego problemu prowadzi do osobliwości elementu macierzowego opisującego proces, co powoduje, że wartość odpowiedniego przekroju czynnego jest nieskończona. Po wyznaczeniu ścisłego warunku na wystąpienie osobliwości w danym procesie typu $2 \to 2$, przedstawiamy mechanizm regularyzacji oparty o uwzględnienie oddziaływań pomiędzy mediatorem na powłoce masy a otaczającym gazem cząstek. Owe oddziaływania ograniczają czas życia mediatora, co pozwala na wprowadzenie efektywnej szerokości rozpadu, regularyzującej potencjalnie osobliwy proces. Rozdział 6 prezentuje analizę produkcji ciemnych cząstek w przyszłych zderzaczach $e^+e^-$, operujących w energiach maksymalizujących przekrój czynny na proces typu Higgs-strahlung (ok. 240–250 GeV). Bierzemy w nim pod uwagę obecne limity ograniczające przestrzeń parametrów wykorzystanych modeli ciemnej materii i szacujemy maksymalny możliwy przekrój czynny na proces produkcji. Dochodzimy do następującego wniosku: mimo że modele ciemnej materii podlegają poważnym ograniczeniom wynikającym z braku rezultatów obecnych i przeszłych doświadczalnych poszukiwań, ciemna cząstka mogłaby być wydajnie produkowana i wykrywana w przyszłych zderzaczach, jeśli wartości parametrów są zbliżone do optymalnych. Ponadto, w wymienionym rozdziale badamy wpływ spinu ciemnej cząstki na tempo produkcji: mimo że wszystkie trzy analizowane modele ciemnej materii dają podobną maksymalną wartość przekroju czynnego na produkcję (na poziomie 60 fb), kształt dozwolonej przestrzeni parametrów różni się w zależności od spinu, co w zasadzie mogłoby umożliwić odróżnienie od siebie przypadków cząstek ciemnej materii o różnych spinach.

Modele ciemnej materii użyte w niniejszej rozprawie są w pełni spójnymi, renormalizowalnymi modelami z portalem Higgsa. Wraz z pewnymi szczegółami obliczeń przeprowadzonych w pracy, są one opisane w dodatkach.

*Potencjał twórczy, zdolność do podźwignięcia problemów zmienia się w człowieku przypływami i odpływami, z których trudno zdać sobie samemu sprawę. Nauczyłem się stosować jako rodzaj testu – lekturę moich własnych prac, tych, które uważam za najlepsze. Jeśli dostrzegam w nich potknięcia, luki, jeśli widzę, że można było rzecz przeprowadzić lepiej, próba wypada pomyślnie. Jeżeli jednak odczytuję własny tekst nie bez podziwu, oznacza to, że jest ze mną niedobrze.*

Stanisław Lem, *Głos Pana*

*Dark matter: Do we need it? What is it? Where is it? How much?*
*What is it? What is it? What is it? What is it?*

David Weinberg, *The Dark Matter Rap: A Cosmological History*
https://www.astronomy.ohio-state.edu/weinberg.21/Rap/

# Acknowledgements

Finally finished, thank God!

First of all, I want to thank prof. Bohdan Grządkowski for all the wise advice, directing my early-stage career, and for his almost unwavering patience. He has been a great doctoral advisor, probably better than I deserved.

I am grateful to my collaborators: Aqueel Ahmed, Duarte Azevedo, Mateusz Duch, Da Huang, Krzysztof Mękała, Stanisław Mrówczyński, Rui Santos, and Aleksander Filip Żarnecki. Without your contribution, my research could not have concerned fields as diverse as thermal interactions and collider studies. Is it time for solid-state physics now?

I wish to thank my faculty friends and colleagues. There are and were so many of them that the full list would surely dominate this section of my dissertation, so here goes an abstract. Special thanks go to Anna Socha, whose support during the last weeks cannot be overestimated, and Adam Kubiela, for each coffee and each chat during the long time spent together at the Faculty of Physics. I also thank Bogumiła Świeżewska, for her support when I searched for a post-doc position, and Bartłomiej Zglinicki, for each "it's gonna be okay".

I want to thank my school teachers: Wanda Turlej and Elżbieta Zawistowska, who introduced me to physics. I am also grateful to all lecturers and assistants who have taught me at the Faculties of Physics and Mathematics.

Dziękuję całej rodzinie, a w sposób szczególny: mamie, która musiała wytrzymać ze mną tyle lat pod jednym dachem, Rafałowi, dzielącemu z nią ten trud, oraz Kai-Teresce – mruczącemu promykowi slońca rozświetlającemu mroki pandemii.

I thank my friends, especially Monia & Piotrek, the whole D&D team, and those who are crossing swords with me from time to time. Life is not only physics!

Last but not least: thank you, Agata. You are simply awesome.

# Contents

# Acronyms and abbreviations

(not including names of experiments and collaborations)

| | |
|---|---|
| **BSM** | beyond the Standard Model (of particle physics) |
| **c.c.** | complex cojugation |
| **CCD** | charge-coupled device |
| **C.L.** | confidence level |
| **CM** | centre-of-momentum (reference frame) |
| **CMB** | cosmic microwave background |
| **DD** | direct detection (of dark matter) |
| **DM** | dark matter |
| **ER** | electronic recoil |
| **ID** | indirect detection (of dark matter) |
| **FDM** | fermion dark matter (model) |
| **FLRW** | Friedmann-Lemaître-Robertson-Walker (metric) |
| **h.c.** | Hermitian conjugation |
| **MACHO** | massive astrophysical compact halo object |
| **MoND** | modified Newtonian dynamics |
| **NR** | nuclear recoil |
| **pGDM** | pseudo-Goldstone dark matter (model) |
| **PMT** | photomultiplier tube |
| **SD** | spin-dependent (scattering of dark matter on nuclei) |
| **SHM** | Standard Halo Model |
| **SI** | spin-independent (scattering of dark matter on nuclei) |
| **SM** | Standard Model (of particle physics) |
| **SSB** | spontaneous symmetry breaking |
| **TeVeS** | tensor-vector-scalar (theory of modified gravity) |
| **VDM** | vector dark matter (model) |
| **VEV** | vacuum expectation value |
| **VFDM** | vector-fermion dark matter (model) |
| **WIMP** | weakly interacting massive particle |

# Units, conventions and some frequently used symbols

- The Greek indices $(\mu, \nu, \ldots)$ take the values $0, 1, 2, 3$, while the Latin indices $(i, j, k, \ldots)$ take the values $1, 2, 3$, unless otherwise explicitly stated.
- Throughout the whole dissertation, the "mostly-minus" Minkowski metric tensor is used:

$$g_{\mu\nu} \equiv \begin{bmatrix} 1 & 0 & 0 & 0 \\ 0 & -1 & 0 & 0 \\ 0 & 0 & -1 & 0 \\ 0 & 0 & 0 & -1 \end{bmatrix} . \tag{0.1}$$

- To express most of the numerical values, we shall use the natural system of units, in which the Boltzmann constant, the speed of light in vacuum, and the Dirac constant are equal to 1:

$$k_B = \hbar = c = 1 . \tag{0.2}$$

  Hence, every quantity has the unit which is the appropriate power of gigaelectronovolts (GeV).

| quantity | symbol | power of GeV |
|---|---|---|
| matrix element | $\lvert\mathcal{M}\rvert^2_{a_1\ldots a_i\to b_1\ldots b_f}$ | $2(4-i-f)$ |
| spinor | $u^s(p),\ v^s(p)$ | $1/2$ |
| distribution function | $f(\mathbf{x},\mathbf{p},t)$ | 0 |
| momentum, energy, mass, decay width | $\mathbf{p},\ E,\ \Gamma,\ m$ | 1 |
| distance, time | $\mathbf{x},\ t$ | $-1$ |
| annihilation/creation operators | $a_p,\ a_p^\dagger$ | $-3/2$ |
| Lagrangian | $\mathcal{L}$ | 4 |
| scalar field | $\phi$ | 1 |
| vector field | $X$ | 1 |
| fermion field | $\psi$ | $3/2$ |
| phase-space element, luminosity | $d\Phi \equiv \frac{d^3p}{(2\pi)^3 2E},\ \mathcal{L}$ | 2 |
| cross section, thermally averaged cross section | $\sigma,\ \langle\sigma v\rangle$ | $-2$ |
| number density, entropy density | $n,\ s$ | 3 |
| energy density, pressure | $\rho,\ p$ | 4 |
| Hubble parameter | $H$ | 1 |

Nevertheless, especially in the introductory part of the dissertation, other units are in use as well. Apart of the SI units, some others are:

- the year (yr),
- the light year (ly), which is the distance covered by light during one year (1 ly $\simeq 9.5\times10^{15}$ m),
- the parsec (pc), defined as the radius of a circle whose second of arc has a length of 1 astronomical unit (equal to the average distance between the Sun and the Earth, i.e., roughly $1.5\times10^{11}$ m, so that 1 pc $\simeq 3.3$ ly $\simeq 3.1\times10^{16}$ m),
- the barn, equal to $10^{-28}$ m$^2$.

and the corresponding derived units (e..g, Mpc $= 10^6$ pc or Gyr $= 10^9$ yr).

- Conventions regarding the Dirac gamma matrices are listed in appendix D.
- The phase-space element, $d\Phi$, is defined as

$$d\Phi \equiv \frac{d^3p}{(2\pi)^3\,2E_p}\ , \tag{0.3}$$

where $E_p \equiv \sqrt{p^2}$ is the corresponding mass-shell energy.

- The Källén triangle function $\lambda$ is defined as

$$\begin{aligned}\lambda(x^2,y^2,z^2) &\equiv \left[x^2-(y+z)^2\right]\left[x^2-(y-z)^2\right]\\ &= \left[y^2-(z+x)^2\right]\left[y^2-(z-x)^2\right]\\ &= \left[z^2-(x+y)^2\right]\left[z^2-(x-y)^2\right]\ .\end{aligned} \tag{0.4}$$

# Preface

## Publications

The results of this dissertation are based on the following publications:

[1] M. Iglicki, *Thermal regularization of t-channel singularities in cosmology and particle physics: the general case*, *JHEP* **06** (2023) 006 [2212.00561].

[2] B. Grzadkowski, M. Iglicki and S. Mrówczyński, *t-channel singularities in cosmology and particle physics*, *Nucl. Phys. B* **984** (2022) 115967 [2108.01757].

[3] B. Grzadkowski, M. Iglicki, K. Mekala and A.F. Zarnecki, *Dark-matter-spin effects at future $e^+e^-$ colliders*, *JHEP* **08** (2020) 052 [2003.06719].

[4] D. Azevedo, M. Duch, B. Grzadkowski, D. Huang, M. Iglicki and R. Santos, *Testing scalar versus vector dark matter*, *Phys. Rev. D* **99** (2019) 015017 [1808.01598].

and conference proceedings:

[5] K. Mekala, A.F. Zarnecki, B. Grzadkowski and M. Iglicki, *Searches for invisible scalar decays at CLIC*, *SciPost Phys. Proc.* **8** (2022) 091 [2107.13903].

[6] CLICdp collaboration, *Sensitivity to invisible scalar decays at CLIC*, *Eur. Phys. J. Plus* **136** (2021) 160 [2002.06034].

[7] B. Grzadkowski, M. Iglicki, K. Mekala and A.F. Zarnecki, *Possibility of Dark Matter Detection at Future $e^+e^-$ Colliders*, *Acta Phys. Polon. B* **50** (2019) 1799.

## Goal of the dissertation

This dissertation tries to answer the following questions:

- Taking into account the current experimental and theoretical constraints, how strong can interactions enabling dark matter production in colliders future $e^+e^-$ be? In particular, can those interactions be efficient enough to enable detection of dark particles and determination of their properties, such as mass or spin?
- Can the interactions between the dark particles and the surrounding gas regularize the so-called $t$-channel singularity, arising in calculation of cross sections for scattering processes involving dark particles in the early Universe?

# Chapter 1

# Introduction: the Higgs portal to the dark sector

## 1.1 Dark matter and the Higgs portal

Dark matter (DM) is a true mystery of the Universe. So far, no proper candidate able to form most of DM has been empirically discovered; on the other hand, basing on the observed gravitational effects (chapter 3), we know that the solution to this mystery must exist. This tension makes the DM-related studies a tempting, vibrant field of research.

Currently, there are numerous known reasons (see chapter 3) to believe that most of DM should consist of weakly interacting massive particles (WIMPs), of beyond-the-Standard-Model (BSM) origin. They have to be massive enough to be cold (no-relativistic) at the moment when their relic density is established, electromagnetically neutral (hence, "dark") and stable or very long lived. Their interactions with the baryonic matter cannot be too strong; otherwise, the dark particles would already have been directly detected.

In principle, it is possible that the dark particles are fully decoupled from the Standard Model of particle physics (SM) and interact with the baryonic matter only gravitationally. However, allowing for DM-SM interactions provides a natural mechanism capable to produce the correct relic density required by observations: the freeze-out mechanism described in section 2.3.4. Moreover, the presence of DM self-interactions can solve several discrepancies (so called small scale problems) between the simulations involving collisionless DM and astronomical observations.

One of the simplest, but theoretically consistent methods to introduce DM-SM interactions is to extend the SM scalar sector by a field coupled to the dark states. If the scalar mass eigenstates mix the new scalar with the SM Higgs field, they couple both to the SM and DM. The coupling between the scalar fields forms a *portal* between the sectors.

## 1.2 Higgs-portal DM as the topic of this dissertation

The DM models adopted in this dissertation are Higgs-portal models. One of them, the vector-fermion DM (VFDM) model described in appendix A, provides two or three (depending on the values of the model parameters) DM candidates; the other three: the pseudo-Goldstone (pGDM), fermion (FDM) and vector (VDM) models of dark matter, described in appendix B, introduce one DM candidate, but are similar to each other, which enables to focus on differences caused by different spins of dark particles. For a comprehensive review and numerous examples of Higgs-portal models, see [8] and the references therein.

As stated in the title of the dissertation, those models have been used to investigate some effects of DM interactions in the early Universe (chapter 5) and at the future $e^+e^-$ colliders (chapter 6).

In the case of multicomponent DM, interactions within the dark sector provide a reach phenomenology, distinct from the SM features, as the DM candidates are simultaneously stable and massive (which is rather uncommon among the SM particles). A phenomenon that occurs in the SM, but naturally arises in theories of dark matter, is the so-called $t$-channel singularity, being a subject of chapter 5.

Interactions between the dark and the SM particles may allow for experimental detection of DM in direct-detection, indirect-detection and collider experiments. Chapter 4 describes those directions of

searches, presenting relevant examples of experiments and summarizing the constraints deduced form their null-results. Chapter 6 focuses on predictions concerning DM production at the future $e^+e^-$ colliders, investigating the influence of DM spin on detection chances.

## 1.3 Composition of the dissertation

The dissertation is composed in the following way. Chapter 2 recalls the most relevant aspects of physical cosmology, including standard theory of dark matter, that are referred to throughout the dissertation. Chapter 3 summarizes the history of the term "dark matter" and presents observational evidence of existence of DM, followed by a short discussion of galactic-scale aspects of DM physics: the structure of the galactic dark halos, and the so-called small-scale problems which justify the assumption that DM is self-interacting. Chapter 4 presents the methods of searches for dark particles and summarizes the constraints corresponding to the null-results of experiments. In chapter 5, the issue of $t$-channel singularity is defined, discussed and resolved. Chapter 6 contains a discussion of DM production at the future $e^+e^-$ colliders. Chapter 7 summarizes results of the dissertation. Appendices A to C describe the models of particle interactions employed in the dissertation: three one-component DM models, the VFDM model and a toy model consisting of three scalar states. Appendices D and E collect some standard identities satisfied by the Dirac matrices and fermionic fields, useful in calculations performed in appendices A to C. In appendix F, the real-time Green's function used in chapter 5 are collected. Appendix G collects the Passarino-Veltman loop functions, while appendix H contains some calculation details of chapter 6.

# Chapter 2

# Relevant aspects of cosmology

## 2.1 Geometry of the Universe

As discussed in [9] (whose conventions are followed in this chapter), the Universe, as a gravitationally bounded system, should satisfy the Einstein equation

$$\mathcal{R}_{\mu\nu} - \frac{1}{2}\, g_{\mu\nu}\, \mathcal{R} = 8\,\pi\, G\, T_{\mu\nu} + \Lambda\, g_{\mu\nu} \,, \tag{2.1}$$

where

- $\mathcal{R}_{\mu\nu}$ and $\mathcal{R}$ denote, respectively, the Ricci tensor and the Ricci scalar,
- $G$ stands for Newton's gravitational constant,
- $\Lambda$ is the cosmological constant,
- $g_{\mu\nu}$ denotes the metric,
- $T_{\mu\nu}$ is the energy-momentum tensor of the Universe.

The metric tensor of a homogeneous, isotropic Universe must have the form of the Friedmann-Lemaître-Robertson-Walker (FLRW) metric [9]. As indicated by measurements of the Planck satellite [10], geometry of the Universe is flat (or almost flat), so the metric is given by

$$ds^2 = dt^2 - R(t)^2 (dx^2 + dy^2 + dz^2) \,, \tag{2.2}$$

where $R(t)$ denotes the scale factor, and $t$ is the cosmic time, i.e., the time measured in the reference frame in which the Universe is isotropic and homogeneous at large scales (of at least 100 Mpc). Existence of such a frame is an assumption called the cosmological principle, tested, e.g., by the observations of the cosmic microwave background (CMB) radiation, which appears to be highly homogeneous [11]. Assuming that the Universe can be treated as a perfect fluid (which is the simplest, but not the only possibility [9]), the energy-momentum tensor is

$$T^{\mu}_{\nu} = \mathrm{diag}(\rho, -p, -p, -p) \,, \tag{2.3}$$

with $\rho$ denoting the energy density and $p$ standing for pressure. Under those assumptions, the $\mu = \nu = 0$ component of the Einstein equation (2.1) is

$$H^2 = \frac{8\,\pi\, G}{3}\, \rho + \frac{\Lambda}{3} \,, \tag{2.4}$$

where $H \equiv \dot{R}/R$ is the Hubble parameter, describing the expansion rate of the Universe. Its present value, $H_0$, has been measured to be

$$H_0 = h^2 \times 100\, \frac{\mathrm{km/s}}{\mathrm{Mpc}} \,, \quad h \simeq 0.7 \,, \tag{2.5}$$

where the precise value of the auxiliary parameter $h$ is subject to some discrepancies [12]. Dividing eq. (2.4) by $H^2$, one obtains

$$1 = \sum_i \Omega_i + \Omega_\Lambda \ , \tag{2.6}$$

where $\Omega_i$, the density parameter of the $i$-th component of the Universe, is defined as

$$\Omega_i \equiv \frac{8\,\pi\,G\,\rho_i}{3\,H^2} \ , \tag{2.7}$$

and the analogous parameter corresponding to the cosmological constant is

$$\Omega_\Lambda \equiv \frac{\Lambda}{3\,H^2} \ . \tag{2.8}$$

Let us remind that eq. (2.6) is valid for a flat Universe only. In a curved geometry, an additional term corresponding to the curvature appears.

As discussed in section 3.1.2, recent observations indicate that the present values of the density parameters corresponding to the baryonic matter ($\Omega_b$), cold dark matter ($\Omega_c$) and the cosmological constant ($\Omega_\Lambda$) are

$$\Omega_b = 0.022\,h^{-2} \ , \quad \Omega_c = 0.120\,h^{-2} \ , \quad \Omega_\Lambda = 0.685 \ , \tag{2.9}$$

while the densities of the relativistic species (photons, neutrinos) are negligible [10].

## 2.2 Thermodynamics of the early Universe

Here, basing on [9], we summarize the relevant concepts of thermodynamics.

At large scales, subject to the cosmological principle, each component of the Universe is treated as a gas described by a phase-space distribution function $f$, representing the density of a given component in the position and momentum space:

$$f = f(k,x) \ . \tag{2.10}$$

Here, $k = (E, \mathbf{k})$ is the four-momentum and $x = (t, \mathbf{x})$ denotes the four-position. The number density $n$, energy density $\rho$ and pressure $p$ are defined as

$$n(x) \equiv \frac{g}{(2\pi)^3} \int f(k,x)\,d^3k \ , \tag{2.11a}$$

$$\rho(x) \equiv \frac{g}{(2\pi)^3} \int E\,f(k,x)\,d^3k \ , \tag{2.11b}$$

$$p(x) \equiv \frac{g}{(2\pi)^3} \int \frac{\mathbf{k}^2}{3\,E}\,f(k,x)\,d^3k \ . \tag{2.11c}$$

The quantity denoted by $g$ is the number if internal degrees of freedom of particles forming the component of interest. The first law of thermodynamics:

$$dU = T\,dS - p\,dV \ , \tag{2.12}$$

with $U$, $S$, $V$ and $T$ denoting the energy, entropy, volume and temperature, respectively, allows to express the entropy density $s \equiv dS/dV$ as

$$\begin{aligned} s &= \frac{\rho + p}{T} \\ &= \frac{g/T}{(2\pi)^3} \int \left( E + \frac{\mathbf{k}^2}{3E} \right) f(k,x)\,d^3k \ . \end{aligned} \tag{2.13}$$

Note that in eq. (2.12), the term containing the chemical potential has been omitted. For components in chemical equilibrium with photons, the chemical potential must be equal to zero [13], while for components outside the equilibrium, is is usually assumed that the chemical potential is negligible in comparison to mass, often (e.g., in [9]) without any comment.

At large scales, at which the cosmological principle applies, the Universe should be homogeneous and isotropic; thus, the distribution functions are assumed to be independent on the spatial coordinates and on the direction of the momentum vector. The remaining relevant parameters are time and energy:

$$f(p,x) = f(E,t)\ . \tag{2.14}$$

For a system in kinetic (thermal) equilibrium, characterized by temperature $T$, the distribution function of a given kind of particles is

$$f(E,t) = (e^{\frac{E-\mu}{T}} \pm 1)^{-1}\ , \tag{2.15}$$

with the plus sign for fermions (Fermi-Dirac distribution) and minus for bosons (Bose-Einstein distribution). Here, we keep the chemical potential $\mu$ as it becomes relevant later. It appears that the time dependence is implicitly encoded in dependence on temperature, so hereafter $T$ is used as an argument of the thermodynamic functions. Using the thermal function (2.15), we express the number density, energy density, pressure and entropy density, given by eqs. (2.11) and (2.13), as

$$n(T) = \frac{g}{2\pi^2}\int_m^\infty \frac{\sqrt{E^2-m^2}}{e^{\frac{E-\mu}{T}}\pm 1}\,E\,dE\ , \tag{2.16a}$$

$$\rho(T) = \frac{g}{2\pi^2}\int_m^\infty \frac{\sqrt{E^2-m^2}}{e^{\frac{E-\mu}{T}}\pm 1}\,E^2\,dE\ , \tag{2.16b}$$

$$p(T) = \frac{g}{6\pi^2}\int_m^\infty \frac{(E^2-m^2)^{3/2}}{e^{\frac{E-\mu}{T}}\pm 1}\,dE\ , \tag{2.16c}$$

$$s(T) = \frac{g}{6\pi^2}\int_m^\infty \frac{\sqrt{E^2-m^2}}{e^{\frac{E-\mu}{T}}\pm 1}\,(4\,E^2-m^2)\,dE\ . \tag{2.16d}$$

Let us calculate those quantities in the regime of non-relativistic ($m \gg T,\mu$) and ultra-relativistic ($m,\mu \ll T$) particles in equilibrium. In the non-relativistic case,

$$\begin{aligned} n(T) &\simeq \frac{g}{2\pi^2}\,e^{\mu/T}\int_m^\infty e^{-E/T}\,\sqrt{E^2-m^2}\,E\,dE \\ &= \frac{g\,T}{2\pi^2}\,m^2\,K_2(m/T)\,e^{\mu/T}\ , \end{aligned} \tag{2.17a}$$

$$\begin{aligned} \rho(T) &\simeq \frac{g}{2\pi^2}\,e^{\mu/T}\int_m^\infty e^{-E/T}\,\sqrt{E^2-m^2}\,E^2\,dE \\ &= \frac{g\,T^2}{2\pi^2}\,m^2\,\left[\frac{m}{T}\,K_1(m/T)+3\,K_2(m/T)\right]\,e^{\mu/T}\ , \end{aligned} \tag{2.17b}$$

$$\begin{aligned} p(T) &\simeq \frac{g}{6\pi^2}\,e^{\mu/T}\int_m^\infty e^{-E/T}\,(E^2-m^2)^{3/2}\,dE \\ &= \frac{g\,T^2}{2\pi^2}\,m^2\,K_2(m/T)\,e^{\mu/T}\ , \end{aligned} \tag{2.17c}$$

$$\begin{aligned} s(T) &\simeq \frac{g}{6\pi^2}\,e^{\mu/T}\int_m^\infty e^{-E/T}\,\sqrt{E^2-m^2}\,\left(4\,E^2-m^2\right)\,dE \\ &= \frac{g\,T}{2\pi^2}\,m^2\,\left[\frac{m}{T}\,K_1(m/T)+4\,K_2(m/T)\right]\,e^{\mu/T}\ , \end{aligned} \tag{2.17d}$$

where $K_i$ ($i=1,2$) denotes the $i$-th modified Bessel function of the second kind. For large arguments, those functions can be approximated by

$$K_i(x) \simeq \sqrt{\frac{\pi}{2\,x}}\,e^{-x}\ ,\quad i=1,2 \tag{2.18}$$

so that

$$n(T) \simeq g \left(\frac{m\,T}{2\pi}\right)^{3/2} e^{-m/T}\, e^{\mu/T}\,, \tag{2.19a}$$

$$\rho(T) \simeq g\,m \left(\frac{m\,T}{2\pi}\right)^{3/2} e^{-m/T}\, e^{\mu/T}\,, \tag{2.19b}$$

$$p(T) \simeq g\,T \left(\frac{m\,T}{2\pi}\right)^{3/2} e^{-m/T}\, e^{\mu/T}\,, \tag{2.19c}$$

$$s(T) \simeq g\,\frac{m}{T} \left(\frac{m\,T}{2\pi}\right)^{3/2} e^{-m/T}\, e^{\mu/T}\,. \tag{2.19d}$$

It can be observed that in the non-relativistic case, all the thermodynamic functions are proportional to the number density $n$:

$$\rho(T) = m\,n(t)\,, \quad p(T) = T\,n(t)\,, \quad s(T) = \frac{m}{T}\,n(t)\,, \tag{2.20}$$

Moreover, all of them are strongly suppressed by the exponential term $e^{-m/T}$. For convenience, let us denote the value of $n$ corresponding to the chemical equilibrium ($\mu = 0$) by $\bar{n}$:

$$\begin{aligned} \bar{n}(T) &\equiv \frac{g\,T}{2\pi^2}\,m^2\,K_2(m/T) \\ &\simeq g\left(\frac{m\,T}{2\pi}\right)^{3/2} e^{-m/T}\,. \end{aligned} \tag{2.21}$$

This function will be useful in section 2.3, concerning the Boltzmann equation describing cold DM.

In the ultra-relativistic case,

$$\begin{aligned} n(T) &\simeq \frac{g}{2\pi^2}\int_0^\infty \frac{E^2}{e^{E/T}\pm 1}\,dE \\ &= \frac{\zeta(3)}{\pi^2}\,g\,T^3 \times \begin{cases} 1 & \text{for bosons} \\ \frac{3}{4} & \text{for fermions} \end{cases}\,, \end{aligned} \tag{2.22a}$$

$$\begin{aligned} \rho(T) &\simeq \frac{g}{2\pi^2}\int_0^\infty \frac{E^3}{e^{E/T}\pm 1}\,dE \\ &= \frac{\pi^2}{30}\,g\,T^4 \times \begin{cases} 1 & \text{for bosons} \\ \frac{7}{8} & \text{for fermions} \end{cases}\,, \end{aligned} \tag{2.22b}$$

$$\begin{aligned} p(T) &\simeq \frac{g}{6\pi^2}\int_0^\infty \frac{E^3}{e^{E/T}\pm 1}\,dE \\ &= \frac{\pi^2}{90}\,g\,T^4 \times \begin{cases} 1 & \text{for bosons} \\ \frac{7}{8} & \text{for fermions} \end{cases}\,, \end{aligned} \tag{2.22c}$$

$$\begin{aligned} s(T) &\simeq \frac{2\,g/T}{3\,\pi^2}\int_0^\infty \frac{E^3}{e^{E/T}\pm 1}\,dE \\ &= \frac{2\pi^2}{45}\,g\,T^3 \times \begin{cases} 1 & \text{for bosons} \\ \frac{7}{8} & \text{for fermions} \end{cases}\,. \end{aligned} \tag{2.22d}$$

Here, $\zeta$ is the Riemann zeta function.

Let us observe that the non-relativistic densities are suppressed in comparison to their ultra-relativistic counterparts, assuming the temperatures are similar. The standard cosmological model states that the inflation period was followed by the radiation-dominated era, in which the energy density of the relativistic species was the main component of the total energy density. This ceased to be true in the next period, called the matter-dominated era, but for temperatures relevant for the evolution of the cold dark species, the Universe was still radiation-dominated [9]. Thus, we shall approximate the total energy density and entropy density of the Universe by the corresponding densities of the relativistic species. Those quantities can be expressed as

$$\rho(T) = \frac{\pi^2}{30}\,T^4\,g_*\,, \quad s(T) = \frac{2\,\pi^2}{45}\,T^3\,g_{*s}\,, \tag{2.23}$$

where the effective numbers of the relativistic degrees of freedom, $g_*$ and $g_{*s}$, are defined as

$$g_*(T) = \sum_b g_b \left(\frac{T_b}{T}\right)^4 + \frac{7}{8} \sum_f g_f \left(\frac{T_f}{T}\right)^4 , \tag{2.24a}$$

$$g_{*s}(T) = \sum_b g_b \left(\frac{T_b}{T}\right)^3 + \frac{7}{8} \sum_f g_f \left(\frac{T_f}{T}\right)^3 , \tag{2.24b}$$

with the indices $b$ and $f$ running through boson and fermion species, respectively. Using $T_b$ and $T_f$ (in contrast to one, common value of temperature) reflects the fact that temperatures of different components may have different values after they kinetically decouple from the thermal bath of photons. By $T$, the temperature of the thermal bath of photons is meant.

## 2.3 Boltzmann equation

The cosmological Boltzmann equation describes the evolution of densities of particle species filling the Universe, taking into account both the expansion of the Universe and particle interactions. Although the Boltzmann equation can be obtained as a semi-classical limit of the so-called Kadanoff-Baym equations [14,15], such a detailed analysis lies beyond the scope of this dissertation. Thus, in this chapter, we shall introduce the Boltzmann equation in the usual, simplified way, presented in [9] and carefully discussed in [16].

Section 2.3.1 contains a standard derivation of the Boltzmann equation. What may be an advantage of this presentation is a special attention that has been paid to express all the collision terms in a consistent way, including all symmetry factors and carefully counting weights of all contributions (which is expressed by the Kronecker deltas). In section 2.3.2, a non-standard discussion of interactions with an energy-dependent matrix element is provided. The results presented there have been used to produce the numerical results of chapter 5. In section 2.3.3, the Boltzmann equation is reformulated using more convenient variables. Section 2.3.4 briefly discusses the freeze-out mechanism, mentioned in chapter 1, and section 2.3.5 describes the so-called WIMP miracle.

### 2.3.1 Derivation

The derivation starts with the following equation:

$$L[f] = C[f] , \tag{2.25}$$

relating the Liouville operator $L$ and the collision operator $C$, acting on a phase-space density function $f$ describing the species of interest. The former of the operators contains the information about the geometry of the spacetime, while the latter describes the relevant particle interactions. In general, the Liouville operator is given by

$$L = p^\mu \, \partial_\mu - \Gamma^\mu_{\alpha\beta} \, p^\alpha \, p^\beta \, \partial_{p^\mu} , \tag{2.26}$$

where $p$ denotes the momentum and $\Gamma^\mu_{\alpha\beta}$ are the Christoffel symbols of the second kind, describing the Levi-Civita connections of the metric. In the FLRW metric, described in section 2.1, this reduces to

$$L = E \, \partial_t - H \, \mathbf{p}^2 \, \partial_E , \tag{2.27}$$

where $E$ is the energy, $t$ is the cosmic time and $H$ denotes the Hubble parameter. This equation is integrated over

$$\frac{g}{(2\pi)^3} \frac{d^3p}{E} , \tag{2.28}$$

with $g$ denoting the number of internal degrees of freedom of the species of interest. Integrating by parts and neglecting the boundary term, we obtain

$$\frac{g}{(2\pi)^3} \int \frac{d^3p}{E} \, L[f] = \dot{n} + 3Hn , \tag{2.29}$$

where $n$ is the number density defined in section 2.2. Then, the Boltzmann equation (2.25) becomes

$$\dot{n} + 3\,H\,n = \frac{g}{(2\pi)^3}\int \frac{d^3p}{E} C[f]\ . \tag{2.30}$$

How does a given process contribute to the right-hand side of the above equation? Let us denote the species of interest by $x$ and investigate the following process:

$$i_1, i_2, \ldots, i_I \to f_1, f_2, \ldots, f_F\ . \tag{2.31}$$

Here, $i_1, \ldots, i_I$ are the initial-state particles ($I$ denotes their number), while $f_1, \ldots, f_F$ are the final-state particles (whose number is $F$). Note that some of the particles denoted by different indices can be identical. The process may contribute to the Boltzmann equation if at least one of the particles $i_1, \ldots, i_I, f_1, \ldots, f_F$ is of type $x$. We shall denote the corresponding contribution, called the collision term, by $C_{i_1,i_2,\ldots,i_I\to f_1,f_2,\ldots,f_F}$, so the Boltzmann equation becomes

$$\dot{n}_x + 3\,H\,n_x = \sum_{\substack{\text{processes}\\ \text{involving } x}} C_{i_1,i_2,\ldots,i_I\to f_1,f_2,\ldots,f_F}\ . \tag{2.32}$$

The collision terms have the following form:

$$\begin{aligned} C_{i_1,i_2,\ldots,i_I\to f_1,f_2,\ldots,f_F} = &-\frac{\delta_{x,i_1}+\delta_{x,i_2}+\ldots+\delta_{x,i_I}-\delta_{x,f_1}-\delta_{x,f_2}-\ldots-\delta_{x,f_F}}{c_I\,c_F}\\ &\times\int d\Phi_{i_1}\,d\Phi_{i_2}\ldots d\Phi_{i_I}\,d\Phi_{f_1}\,d\Phi_{f_2}\ldots d\Phi_{f_F}\\ &\quad\times(2\pi)^4\delta^{(4)}(p_{i_1}+p_{i_2}+\ldots+p_{i_I}-p_{f_1}-p_{f_2}-\ldots-p_{f_F})\\ &\quad\times\Big[f_{i_1}(p_{i_1})f_{i_2}(p_{i_2})\ldots f_{i_I}(p_{i_I})\\ &\qquad\times[1\pm f_{f_1}(p_{f_1})]\,[1\pm f_{f_2}(p_{f_2})]\ldots[1\pm f_{f_F}(p_{f_F})]\\ &\qquad\times\sum_{\text{sp.}}|\mathcal{M}|^2_{i_1,i_2,\ldots,i_I\to f_1,f_2,\ldots,f_F}\\ &\quad-[1\pm f_{i_1}(p_{i_1})]\,[1\pm f_{i_2}(p_{i_2})]\ldots[1\pm f_{i_I}(p_{i_I})]\\ &\qquad\times f_{f_1}(p_{f_1})f_{f_2}(p_{f_2})\ldots f_{f_F}(p_{f_F})\\ &\qquad\times\sum_{\text{sp.}}|\mathcal{M}|^2_{f_1,f_2,\ldots,f_F\to i_1,i_2,\ldots,i_I}\Big]\ , \end{aligned} \tag{2.33}$$

where $c_I$ ($c_F$) denotes combinatoric factor of the initial (final) state, given as 1 multiplied by $k!$ for each set of $k$ identical particles in the initial (final) state. The Kronecker deltas count the number of particles of type $x$ produced and destroyed in the process. The factors $1\pm f$, containing the phase-space density $f$, are taken with the plus for bosons and with the minus for fermions. Assuming that the particle gas is diluted, one approximates those factors by one. Moreover, if the process is $CP$-invariant, both matrix elements squared, integrated over the final state, are equal to each other [16]. Under those assumptions, the collision takes the form

$$\begin{aligned} C_{i_1,i_2,\ldots,i_I\to f_1,f_2,\ldots,f_F} = &-\frac{\delta_{x,i_1}+\delta_{x,i_2}+\ldots+\delta_{x,i_I}-\delta_{x,f_1}-\delta_{x,f_2}-\ldots-\delta_{x,f_F}}{c_I\,c_F}\\ &\times\int d\Phi_{i_1}\,d\Phi_{i_2}\ldots d\Phi_{i_I}\,d\Phi_{f_1}\,d\Phi_{f_2}\ldots d\Phi_{f_F}\\ &\quad\times(2\pi)^4\delta^{(4)}(p_{i_1}+p_{i_2}+\ldots+p_{i_I}-p_{f_1}-p_{f_2}-\ldots-p_{f_F})\\ &\quad\times\Big[f_{i_1}(p_{i_1})f_{i_2}(p_{i_2})\ldots f_{i_I}(p_{i_I})-f_{f_1}(p_{f_1})f_{f_2}(p_{f_2})\ldots f_{f_F}(p_{f_F})\Big]\\ &\quad\times\sum_{\text{sp.}}|\mathcal{M}|^2_{i_1,i_2,\ldots,i_I\to f_1,f_2,\ldots,f_F}\ . \end{aligned} \tag{2.34}$$

Let us denote

$$\bar{f} \equiv \frac{\bar{n}}{n}\,f\ , \tag{2.35}$$

where $\bar{n}$ is the equilibrium number density introduced by eq. (2.21). Neglecting the quantum degeneracies, we approximate the equilibrium distribution functions, $\bar{f}$, by the Maxwell-Boltzmann value

$$\bar{f}(p) \simeq e^{-E/T} \,. \tag{2.36}$$

Assuming all the species to be in the kinetic equilibrium with the thermal bath, we obtain

$$\begin{aligned}
\bar{f}_{i_1}\bar{f}_{i_2}\dots\bar{f}_{i_I} &= \frac{1}{e^{E_{i_1}/T}\pm 1}\frac{1}{e^{E_{i_2}/T}\pm 1}\cdots\frac{1}{e^{E_{i_I}/T}\pm 1} \\
&\simeq e^{-\left[E_{i_1}+E_{i_2}+\ldots+E_{i_I}\right]/T} \\
&= e^{-\left[E_{f_1}+E_{f_2}+\ldots+E_{f_F}\right]/T} \\
&\simeq \frac{1}{e^{E_{f_1}/T}\pm 1}\frac{1}{e^{E_{f_2}/T}\pm 1}\cdots\frac{1}{e^{E_{f_F}/T}\pm 1} \\
&= \bar{f}_{f_1}\bar{f}_{f_2}\dots\bar{f}_{f_F} \,.
\end{aligned} \tag{2.37}$$

The third equality is implied by the energy conservation. Using this relation, one can express the collision term as

$$\begin{aligned}
C_{i_1,i_2,\ldots,i_I\to f_1,f_2,\ldots,f_F} &= -\frac{\delta_{x,i_1}+\delta_{x,i_2}+\ldots+\delta_{x,i_I}-\delta_{x,f_1}-\delta_{x,f_2}-\ldots-\delta_{x,f_F}}{c_I\,c_F} \\
&\quad\times\int d\Phi_{i_1}\,d\Phi_{i_2}\dots d\Phi_{i_I}\,d\Phi_{f_1}\,d\Phi_{f_2}\dots d\Phi_{f_F} \\
&\qquad\times(2\pi)^4\delta^{(4)}(p_{i_1}+p_{i_2}+\ldots+p_{i_I}-p_{f_1}-p_{f_2}-\ldots-p_{f_F}) \\
&\qquad\times\Big[\frac{n_{i_1}}{\bar{n}_{i_1}}\bar{f}_{i_1}(p_{i_1})\frac{n_{i_2}}{\bar{n}_{i_2}}\bar{f}_{i_2}(p_{i_2})\dots\frac{n_{i_I}}{\bar{n}_{i_I}}\bar{f}_{i_I}(p_{i_I}) \\
&\qquad\quad-\frac{n_{f_1}}{\bar{n}_{f_1}}\bar{f}_{f_1}(p_{f_1})\frac{n_{f_2}}{\bar{n}_{f_2}}\bar{f}_{f_2}(p_{f_2})\dots\frac{n_{f_F}}{\bar{n}_{f_F}}\bar{f}_{f_F}(p_{f_F})\Big] \\
&\qquad\times\sum_{\text{sp.}}|\mathcal{M}|^2_{i_1,i_2,\ldots,i_I\to f_1,f_2,\ldots,f_F} \\
&= \frac{\delta_{x,i_1}+\delta_{x,i_2}+\ldots+\delta_{x,i_I}-\delta_{x,f_1}-\delta_{x,f_2}-\ldots-\delta_{x,f_F}}{c_I\,c_F} \\
&\quad\times\Big[\frac{n_{i_1}n_{i_2}\dots n_{i_I}}{\bar{n}_{i_1}\bar{n}_{i_2}\dots\bar{n}_{i_I}}-\frac{n_{f_1}n_{f_2}\dots n_{f_F}}{\bar{n}_{f_1}\bar{n}_{f_2}\dots\bar{n}_{f_F}}\Big] \\
&\quad\times\int d\Phi_{i_1}\,d\Phi_{i_2}\dots d\Phi_{i_I}\,d\Phi_{f_1}\,d\Phi_{f_2}\dots d\Phi_{f_F} \\
&\qquad\times(2\pi)^4\delta^{(4)}(p_{i_1}+p_{i_2}+\ldots+p_{i_I}-p_{f_1}-p_{f_2}-\ldots-p_{f_F}) \\
&\qquad\times\bar{f}_{i_1}(p_{i_1})\bar{f}_{i_2}(p_{i_2})\dots\bar{f}_{i_I}(p_{i_I})\times\sum_{\text{sp.}}|\mathcal{M}|^2_{i_1,i_2,\ldots,i_I\to f_1,f_2,\ldots,f_F} \,.
\end{aligned} \tag{2.38}$$

**Special case: a $2\to F$ scattering process.** Having derived this form of the collision term, let us now discuss two special cases: a $2\to F$ scattering ($I=2$) and a $1\to F$ decay ($I=1$). For the scattering, the collision term becomes

$$\begin{aligned}
C_{i_1,i_2\to f_1,f_2,\ldots,f_F} &= -\frac{\delta_{x,i_1}+\delta_{x,i_2}-\delta_{x,f_1}-\delta_{x,f_2}-\ldots-\delta_{x,f_F}}{c_I\,c_F} \\
&\quad\times\Big[\frac{n_{i_1}n_{i_2}}{\bar{n}_{i_1}\bar{n}_{i_2}}-\frac{n_{f_1}n_{f_2}\dots n_{f_F}}{\bar{n}_{f_1}\bar{n}_{f_2}\dots\bar{n}_{f_F}}\Big] \\
&\quad\times\int d\Phi_{i_1}\,d\Phi_{i_2}\,d\Phi_{f_1}\,d\Phi_{f_2}\dots d\Phi_{f_F} \\
&\qquad\times(2\pi)^4\delta^{(4)}(p_{i_1}+p_{i_2}-p_{f_1}-p_{f_2}-\ldots-p_{f_F}) \\
&\qquad\times\bar{f}_{i_1}(p_{i_1})\bar{f}_{i_2}(p_{i_2})\times\sum_{\text{sp.}}|\mathcal{M}|^2_{i_1,i_2\to f_1,f_2,\ldots,f_F} \\
&= -\frac{\delta_{x,i_1}+\delta_{x,i_2}-\delta_{x,f_1}-\delta_{x,f_2}-\ldots-\delta_{x,f_F}}{c_I} \\
&\quad\times\Big[n_{i_1}n_{i_2}-\bar{n}_{i_1}\bar{n}_{i_2}\dots\bar{n}_{i_I}\frac{n_{f_1}n_{f_2}\dots n_{f_F}}{\bar{n}_{f_1}\bar{n}_{f_2}\dots\bar{n}_{f_F}}\Big] \\
&\quad\times\langle\sigma v\rangle_{i_1,i_2\to f_1,f_2,\ldots,f_F} \,.
\end{aligned} \tag{2.39}$$

Here, $\langle \sigma v \rangle$ denotes the so-called thermally averaged cross section, defined as

$$\begin{aligned}\langle \sigma v \rangle_{i_1,i_2 \to f_1,f_2,\ldots,f_F} \equiv & \frac{1}{c_F} \frac{1}{\bar{n}_{i_1} \bar{n}_{i_2}} \\ & \times \int d\Phi_{i_1}\, d\Phi_{i_2}\, d\Phi_{f_1}\, d\Phi_{f_2} \ldots d\Phi_{f_F} \\ & \quad \times (2\pi)^4 \delta^{(4)}(p_{i_1} + p_{i_2} - p_{f_1} - p_{f_2} - \ldots - p_{f_F}) \\ & \quad \times \bar{f}_{i_1}(p_{i_1}) \bar{f}_{i_2}(p_{i_2}) \times \sum_{\text{sp.}} |\mathcal{M}|^2_{i_1,i_2,\ldots,i_I \to f_1,f_2,\ldots,f_F} \ ,\end{aligned} \tag{2.40}$$

and related to the ..regular" cross section $\sigma$ in the following way:

$$\langle \sigma v \rangle = \frac{g_{i_1} g_{i_2}}{\bar{n}_{i_1} \bar{n}_{i_2}} \int \frac{d^3 p_{i_1}}{(2\pi)^3} \frac{d^3 p_{i_2}}{(2\pi)^3} \, \bar{f}_{i_1}(p_{i_1}) \bar{f}_{i_2}(p_{i_2}) \, v_{i_1,i_2} \, \sigma_{i_1,i_2 \to f_1,f_2,\ldots,f_F} \ . \tag{2.41}$$

In this equation, $v_{i_1,i_2}$ denotes the so-called Møller velocity, given by

$$\begin{aligned} v_{i_1,i_2} &\equiv \sqrt{(\mathbf{v}_{i_1} - \mathbf{v}_{i_2})^2 - (\mathbf{v}_{i_1} \times \mathbf{v}_{i_2})^2} \\ &= \frac{\sqrt{(p_{i_1} p_{i_2})^2 - m_{i_1}^2 m_{i_2}^2}}{E_{i_1} E_{i_2}} \ , \end{aligned} \tag{2.42}$$

with $\mathbf{v}_{i_1} \equiv \frac{\mathbf{p}_{i_1}}{E_{i_1}}$, $\mathbf{v}_{i_2} \equiv \frac{\mathbf{p}_{i_2}}{E_{i_2}}$. Let us recall that $\sigma$ can be calculated as

$$\begin{aligned}\sigma_{i_1,i_2 \to f_1,f_2} \equiv & \frac{1}{c_F} \frac{1}{4\, E_{i_j}\, E_{i_2}\, v_{i_1,i_2}} \int d\Phi_{f_1}\, d\Phi_{f_2} \ldots d\Phi_{f_F} \\ & \quad \times (2\pi)^4 \delta^{(4)}(p_{i_1} + p_{i_2} - p_{f_1} - p_{f_2} - \ldots - p_{f_F}) \\ & \quad \times \frac{1}{g_{i_1} g_{i_2}} \sum_{\text{sp.}} |\mathcal{M}|^2_{i_1,i_2 \to f_1,f_2,\ldots,f_F} \ ,\end{aligned} \tag{2.43}$$

where the summation is performed over spin states.

**Special case: a $1 \to F$ decay process.** For a decay process, the collision term becomes

$$\begin{aligned} C_{i_1 \to f_1,f_2,\ldots,f_F} = & -\frac{\delta_{x,i_1} - \delta_{x,f_1} - \delta_{x,f_2} - \ldots - \delta_{x,f_F}}{c_F} \\ & \times \left[ \frac{n_{i_1}}{\bar{n}_{i_1}} - \frac{n_{f_1} n_{f_2} \ldots n_{f_F}}{\bar{n}_{f_1} \bar{n}_{f_2} \ldots \bar{n}_{f_F}} \right] \\ & \times \int d\Phi_{i_1}\, d\Phi_{f_1}\, d\Phi_{f_2} \ldots d\Phi_{f_F} \\ & \quad \times (2\pi)^4 \delta^{(4)}(p_{i_1} - p_{f_1} - p_{f_2} - \ldots - p_{f_F}) \\ & \quad \times \bar{f}_{i_1}(p_{i_1}) \sum_{\text{sp.}} |\mathcal{M}|^2_{i_1 \to f_1,f_2,\ldots,f_F} \ . \\ = & -(\delta_{x,i_1} - \delta_{x,f_1} - \delta_{x,f_2} - \ldots - \delta_{x,f_F}) \\ & \times \left[ n_{i_1} - \bar{n}_{i_1} \frac{n_{f_1} n_{f_2} \ldots n_{f_F}}{\bar{n}_{f_1} \bar{n}_{f_2} \ldots \bar{n}_{f_F}} \right] \\ & \times \langle \Gamma \rangle_{i_1 \to f_1,f_2,\ldots,f_F} \ . \end{aligned} \tag{2.44}$$

Here, $\langle \Gamma \rangle$ denotes the so-called thermally averaged decay width, defined as

$$\begin{aligned}\langle \Gamma \rangle_{i_1 \to f_1,f_2,\ldots,f_F} \equiv & \frac{1}{c_F} \frac{1}{\bar{n}_{i_1}} \int d\Phi_{i_1}\, d\Phi_{f_1}\, d\Phi_{f_2} \ldots d\Phi_{f_F}\, (2\pi)^4 \delta^{(4)}(p_{i_1} - p_{f_1} - p_{f_2} - \ldots - p_{f_F}) \\ & \times \bar{f}_{i_1}(p_{i_1}) \sum_{\text{sp.}} |\mathcal{M}|^2_{i_1 \to f_1,f_2,\ldots,f_F}\end{aligned} \tag{2.45}$$

or, using the "regular" decay width $\Gamma$,

$$\langle \Gamma \rangle_{i_1 \to f_1,f_2,\ldots,f_F} = \frac{g_{i_1}}{\bar{n}_{i_1}} \int \frac{d^3 p_{i_1}}{(2\pi)^3} \, \bar{f}_{i_1}(p_{i_1}) \, \frac{m_1}{E_1} \, \Gamma_{i_1 \to f_1,f_2,\ldots,f_F} \ . \tag{2.46}$$

For completeness, let us recall the definition of $\Gamma$:

$$\begin{aligned}\Gamma_{i_1\to f_1,f_2,\ldots,f_F} \equiv \frac{1}{c_F}\frac{1}{2m_{i_1}}\int & d\Phi_{f_1} d\Phi_{f_2}\ldots d\Phi_{f_F} \\ & \times (2\pi)^4\delta^{(4)}(p_{f_1}+p_{f_2}\ldots+p_{f_F}) \\ & \times \frac{1}{g_{i_1}}\sum_{\text{sp.}} |\mathcal{M}|^2_{i_1\to f_1,f_2,\ldots,f_F}\ .\end{aligned} \tag{2.47}$$

Note the delta function in the above definition is calculated at different point than the one in eq. (2.45). This comes from the fact that $\frac{m_{i_1}}{E_{i_1}}\Gamma_{i_1\to f_1,f_2,\ldots,f_F}$ is equal to the value of $\Gamma_{i_1\to f_1,f_2,\ldots,f_F}$ boosted to the frame in which particle $i_1$ has energy $E_{i_1}$.

**Boltzmann equation with scattering and decay terms.** Using the thermally averaged cross section (2.40) and decay width (2.45), we can express the Boltzmann equation (2.32) in the following way:

$$\begin{aligned}\dot{n}_x + 3\,H\,n_x = & -\sum_{2\to F}\frac{\delta_{x,i_1}+\delta_{x,i_2}-\delta_{x,f_1}-\delta_{x,f_2}-\ldots-\delta_{x,f_F}}{c_I} \\ & \times\left[n_{i_1}n_{i_2}-\bar{n}_{i_1}\bar{n}_{i_2}\ldots\bar{n}_{i_I}\frac{n_{f_1}n_{f_2}\ldots n_{f_F}}{\bar{n}_{f_1}\bar{n}_{f_2}\ldots\bar{n}_{f_F}}\right] \\ & \times\langle\sigma v\rangle_{i_1,i_2\to f_1,f_2,\ldots,f_F} \\ & -\sum_{1\to F}(\delta_{x,i_1}-\delta_{x,f_1}-\delta_{x,f_2}-\ldots-\delta_{x,f_F}) \\ & \times\left[n_{i_1}-\bar{n}_{i_1}\frac{n_{f_1}n_{f_2}\ldots n_{f_F}}{\bar{n}_{f_1}\bar{n}_{f_2}\ldots\bar{n}_{f_F}}\right] \\ & \times\langle\Gamma\rangle_{i_1\to f_1,f_2,\ldots,f_F}\ ,\end{aligned} \tag{2.48}$$

with the first (second) summation running through the $2\to F$ ($1\to F$) processes involving particles of type $x$.

### 2.3.2 Energy-dependent matrix element of a $t$-channel-singular process

Here, we discuss the case of an energy-dependent matrix element appearing if one performs the regularization of a $t$-channel-singular process using the method described in chapter 5. Although not very illuminating, the results presented here are of practical importance for this dissertation, as they have been used to prepare the $\langle\sigma v\rangle$ plots shown in sections 5.5.3 and 5.5.4. The derivation is provided as potentially useful for the reader who would like to reproduce the numerical results of chapter 5 or perform similar calculations.

We focus on a $2\to 2$ $t$-channel process, with particles denoted as 1 and 2 (in the initial state), 3 and 4 (in the final state). As stated by eq. (2.41), the thermally averaged cross section can be calculated using the "regular" cross section in the following way:

$$\langle\sigma v\rangle_{12\to 34}(T) = \frac{g_1 g_2}{\bar{n}_1\bar{n}_2}\int d\Phi_1\, d\Phi_2\, \bar{f}_1(E_1,T)\,\bar{f}_2(E_2,T)\,4E_1E_2\,v_{12}\,\sigma(E_1,\,E_2,\,\cos\alpha_{12})\ . \tag{2.49}$$

Note that as $\sigma$ contains integration over the final states, it depends only on the values of the initial momenta, $|\mathbf{p}_1|$ and $|\mathbf{p}_2|$ (equivalently: energies $E_1$, $E_2$), and the angle between them, $\alpha_{12}$. Defining new variables, $\rho$ and $\xi$, satisfying

$$|\mathbf{p}_1| = \rho\cos\xi\ ,\quad |\mathbf{p}_2| = \rho\sin\xi\ , \tag{2.50}$$

we rewrite eq. (2.49) as

$$\begin{aligned}\langle\sigma v\rangle_{12\to 34}(T) = & \frac{g_1 g_2}{\bar{n}_1\bar{n}_2}\frac{1}{32\pi^4} \\ & \times\int_0^\infty d\rho\int_0^{\frac{\pi}{2}} d\xi\int_{-1}^{1} d\cos\alpha_{12}\,\frac{\sqrt{\mathbf{p}_1^2+\mathbf{p}_2^2}\,|\mathbf{p}_1|^2\,|\mathbf{p}_2|^2}{E_1E_2}\,\bar{f}_1(E_1,T)\,\bar{f}_2(E_2,T) \\ & \times 4E_1E_2\,v_{12}\,\sigma(E_1,\,E_2,\,\cos\alpha_{12})\ .\end{aligned} \tag{2.51}$$

Using the explicit form of $\bar{n}_{1,2}$, given by eq. (2.21), and approximating $\bar{f}_{1,2}$ by the Maxwell-Boltzmann distribution (2.36), we obtain

$$\begin{aligned}\langle\sigma v\rangle_{12\to34}(T) \simeq \frac{K_2\left(\frac{m_1}{T}\right)^{-1} K_2\left(\frac{m_2}{T}\right)^{-1}}{8\, m_1^2\, m_2^2\, T^2} \\ \times \int_0^\infty d\rho \int_0^{\frac{\pi}{2}} d\xi \int_{-1}^{1} d\cos\alpha_{12}\, \frac{\sqrt{\mathbf{p}_1^2+\mathbf{p}_2^2}\,|\mathbf{p}_1|^2\,|\mathbf{p}_2|^2}{E_1 E_2}\, e^{-\frac{E_1+E_2}{T}} \\ \times 4E_1E_2\, v_{12}\, \sigma(E_1,\, E_2,\, \cos\alpha_{12})\ .\end{aligned} \tag{2.52}$$

As stated in eq. (2.43), the cross section $\sigma$ can be expressed through the matrix element:

$$\sigma \equiv \frac{1}{c_F}\frac{1}{4\,E_1\,E_2\,v_{12}} \int d\Phi_3\, d\Phi_4\, (2\pi)^4 \delta^{(4)}(p_1+p_2-p_3-p_4)\, \frac{1}{g_1 g_2} \sum_{\text{sp.}} |\mathcal{M}|^2_{12\to34}\ . \tag{2.53}$$

It is usually assumed that the matrix element squared is a Lorentz invariant, so one is allowed to calculate the integral in the CM system. This is, however, not the case if the effective thermal width is used to regularize the possible $t$-channel singularity (see chapter 5 for details). To calculate the cross section in that case, let us assume that the spin-averaged matrix element has the following form:

$$\frac{1}{g_1 g_2} \sum_{sp.} |\mathcal{M}|^2_{12\to34} \equiv \frac{A(s,t)}{(t-M^2)^2+\Sigma(E,T)^2}\ , \tag{2.54}$$

where $s$ and $t$ denote the Mandelstam variables

$$s \equiv (p_1+p_2)^2\ , \quad t \equiv (p_1-p_3)^2\ , \tag{2.55}$$

$M$ is the mass of the $t$-channel mediator, and $A$ is Lorentz-invariant, while $\Sigma$ depends on energy $E \equiv E_1 - E_3$ and temperature $T$. Then, we start the calculation with transforming the phase-space elements $d\Phi_{3,4}$ and the delta function to the CM frame. Note that this does not change the result, because the phase-space elements and the delta function are Lorentz-invariant. For clarity, we shall distinguish the integration variables in the CM frame by prime, while the index "cm" will denote the values imposed by the delta functions.

In the CM frame, the cross section is given by

$$\begin{aligned}4E_1E_2\, v_{12}\, \sigma &= \int d\Phi_3'\, d\Phi_4'\, (2\pi)^4 \delta(\sqrt{s}-E_3'-E_4')\, \delta^{(3)}(\mathbf{p}_3'+\mathbf{p}_4')\, |\mathcal{M}|^2_{12\to34} \\ &= \int d\Phi_3'\, d\Phi_4'\, (2\pi)^4 \delta(\sqrt{s}-E_3'-E_4')\, \delta^{(3)}(\mathbf{p}_3'+\mathbf{p}_4')\, \frac{A(s,t)}{(t-M^2)^2+\Sigma(E,T)^2}\ .\end{aligned} \tag{2.56}$$

For convenience, the factor $1/c_F$ has been dropped here. Integrating over $d^3p_4'$, we obtain

$$4E_1E_2\, v_{12}\, \sigma = \frac{1}{16\,\pi^2} \int \frac{d^3p_3'}{E_3'E_4'} \delta(\sqrt{s}-E_3'-E_4')\, \frac{A(s,t)}{(t-M^2)^2+\Sigma(E,T)^2}\ . \tag{2.57}$$

Let us use the spherical coordinates:

$$d^3p_3' = {\mathbf{p}_3'}^2\, d|\mathbf{p}_3'|\, d\Omega_3'\ , \tag{2.58}$$

where $d\Omega_3'$ denotes integration over the solid angle. We can also switch the integration variable from $|\mathbf{p}_3'|$ to $E_3'$, using the relation

$$|\mathbf{p}_3'|\, d|\mathbf{p}_3'| = E_3'\, dE_3'\ . \tag{2.59}$$

Then, the cross section becomes

$$\begin{aligned}4E_1E_2\, v_{12}\, \sigma &= \frac{1}{16\,\pi^2} \int \frac{|\mathbf{p}_3'|\, dE_3'\, d^2\Omega_3'}{\sqrt{s}} \delta(E_3'-E_3^{\text{cm}})\, \frac{A(s,t)}{(t-M^2)^2+\Sigma(E,T)^2} \\ &= \frac{1}{16\,\pi^2} \frac{|\mathbf{p}_3^{\text{cm}}|}{\sqrt{s}} \int d^2\Omega_3'\, \frac{A(s,t)}{(t-M^2)^2+\Sigma(E,T)^2}\ ,\end{aligned} \tag{2.60}$$

where $E_3^{\rm cm}$ and $|\mathbf{p}_3^{\rm cm}|$ are the CM values of the energy and momentum, determined by kinematics:

$$E_3^{\rm cm} \equiv \frac{\sqrt{s}}{2} + \frac{m_3^2 - m_4^2}{2\sqrt{s}} \,, \quad |\mathbf{p}_3^{\rm cm}| \equiv \frac{\lambda(s, m_3^2, m_4^2)^{1/2}}{2\sqrt{s}} \,. \tag{2.61}$$

For completeness, let us also write down the CM energy and momentum of the incoming particle:

$$E_1^{\rm cm} \equiv \frac{\sqrt{s}}{2} + \frac{m_1^2 - m_2^2}{2\sqrt{s}} \,, \quad |\mathbf{p}_1^{\rm cm}| \equiv \frac{\lambda(s, m_1^2, m_2^2)^{1/2}}{2\sqrt{s}} \,. \tag{2.62}$$

Here, $\lambda$ denotes the Källén triangle function defined by eq. (0.4). Assuming that the integration range includes the point $t = M^2$ (the other case is discussed at the end of this section), and the regulator $\Sigma$ is small (so that the matrix element squared is sharply peaked at that point), we can use the narrow-width approximation:

$$\frac{1}{x^2 + a^2} \simeq \frac{\pi}{a}\, \delta(x) \tag{2.63}$$

to obtain

$$4E_1 E_2\, v_{12}\, \sigma \simeq \frac{A(s, M^2)}{16\,\pi} \frac{|\mathbf{p}_3^{\rm cm}|}{\sqrt{s}} \int \frac{d^2\Omega_3'}{|\Sigma(E,T)|}\, \delta(t - M^2) \,. \tag{2.64}$$

Since the variable $t$ is given in the CM frame by

$$t = m_1^2 + m_3^2 - 2\, E_1^{\rm cm} E_3^{\rm cm} + 2|\mathbf{p}_1^{\rm cm}||\mathbf{p}_3^{\rm cm}| \cos\theta' \,, \tag{2.65}$$

where $\theta'$ denotes the angle between $\mathbf{p}_1^{\rm cm}$ and $\mathbf{p}_3^{\rm cm}$, the delta function can be transformed to provide

$$4E_1 E_2\, v_{12}\, \sigma \simeq \frac{A(s, M^2)}{32\,\pi\,\sqrt{s}\,|\mathbf{p}_1^{\rm cm}|} \int \frac{d^2\Omega_3'}{|\Sigma(E,T)|}\, \delta(\cos\theta' - c\theta_{M^2}) \,. \tag{2.66}$$

Here, $c\theta_M^2$ is the value of $\cos\theta'$ corresponding to $t = M^2$ (by the aforementioned assumption, such a value exists), given by

$$c\theta_{M^2} = \frac{M^2 - m_1^2 - m_3^2 + 2\, E_1^{\rm cm}\, E_3^{\rm cm}}{2|\mathbf{p}_1^{\rm cm}||\mathbf{p}_3^{\rm cm}|} \,. \tag{2.67}$$

Performing the $d\cos\theta'$ integration and recalling the definition of $|\mathbf{p}_1^{\rm cm}|$ given by eq. (2.62), we finally obtain

$$\begin{aligned} 4E_1 E_2\, v_{12}\, \sigma &= \frac{A(s, M^2)}{32\,\pi\,\sqrt{s}\,|\mathbf{p}_1^{\rm cm}|} \int \frac{d\phi'}{|\Sigma(E,T)|} \\ &= \frac{A(s, M^2)}{16\,\pi\,\lambda(s, m_1^2, m_2^2)^{1/2}} \int \frac{d\phi'}{|\Sigma(E,T)|} \,. \end{aligned} \tag{2.68}$$

This formula has been used in numerical calculations to obtain the plots of $\langle\sigma v\rangle$ presented in sections 5.5.3 and 5.5.4. Here, $\int d\phi'$ denotes integration of $\mathbf{p}_3^{\rm cm}$ over a unit circle lying in a plane perpendicular to $\mathbf{p}_1^{\rm cm}$, while the energy $E$ and the invariants $s$, $t$ are given in terms of the CM variables as

$$E(\phi') = E_1 - \frac{E_3^{\rm cm}\, E_{\rm tot} + |\mathbf{p}_{\rm tot}||\mathbf{p}_3^{\rm cm}|\, \cos(\angle(\mathbf{p}_{\rm tot}, \mathbf{p}_3^{\rm cm}))}{\sqrt{s}} \,, \tag{2.69}$$

where

$$\begin{aligned} |\mathbf{p}_{\rm tot}||\mathbf{p}_3^{\rm cm}| \cos(\angle(\mathbf{p}_{\rm tot}, \mathbf{p}_3^{\rm cm})) &= c\theta_{M^2} |\mathbf{p}_{\rm tot}||\mathbf{p}_3^{\rm cm}| \cos\left(\angle(\mathbf{p}_{\rm tot}, \mathbf{p}_1^{\rm cm})\right) \\ &\quad + \sin\phi\, |\mathbf{p}_{\rm tot}||\mathbf{p}_3^{\rm cm}| \sqrt{1 - c\theta_{M^2}^2}\, \sin\left(\angle(\mathbf{p}_{\rm tot}, \mathbf{p}_1^{\rm cm})\right) \\ &= \frac{|\mathbf{p}_3^{\rm cm}|}{|\mathbf{p}_1^{\rm cm}|} \times \Bigg[ c\theta_{M^2}\, \mathbf{p}_{\rm tot} \cdot \mathbf{p}_1^{\rm cm} \\ &\qquad + \sin(\phi) \sqrt{1 - c\theta_{M^2}^2} \sqrt{\mathbf{p}_{\rm tot}^2\, \mathbf{p}_1^{\rm cm\,2} - (\mathbf{p}_{\rm tot} \cdot \mathbf{p}_1^{\rm cm})^2} \Bigg] \,, \end{aligned} \tag{2.70}$$

and

$$s = E_{\rm tot}^2 - \mathbf{p}_{\rm tot}^2 \ , \quad E_{\rm tot} \equiv E_1 + E_2 \ , \quad \mathbf{p}_{\rm tot} \equiv \mathbf{p}_1 + \mathbf{p}_2 \ . \tag{2.71}$$

It may seem peculiar that we are calculating the dot products of vectors from different reference frames, e.g., $\mathbf{p}_{\rm tot}$ and $\mathbf{p}_1^{\rm cm}$. The reason is that the CM variables $E_1^{\rm cm}$, $\mathbf{p}_1^{\rm cm}$ are related to $E_1$, $\mathbf{p}_1$ through the following Lorentz transformation:

$$\begin{aligned} E_1^{\rm cm} &= \frac{E_1 E_{\rm tot} - \mathbf{p}_1 \cdot \mathbf{p}_{\rm tot}}{\sqrt{s}} \ , \\ \mathbf{p}_1^{\rm cm} &= \mathbf{p}_1 + \left[ -E_1 + \frac{\mathbf{p}_1 \cdot \mathbf{p}_{\rm tot}}{E_{\rm tot} + \sqrt{s}} \right] \frac{\mathbf{p}_{\rm tot}}{\sqrt{s}} \end{aligned} \tag{2.72}$$

(the four-momenta of the other particles transform analogously). Thus, the dot product of $\mathbf{p}_{\rm tot}$ and $\mathbf{p}_1^{\rm cm}$ can be expressed as

$$\begin{aligned} \mathbf{p}_{\rm tot} \cdot \mathbf{p}_1^{\rm cm} &= \mathbf{p}_{\rm tot} \cdot \mathbf{p}_1 + \left[ -E_1 + \frac{\mathbf{p}_1 \cdot \mathbf{p}_{\rm tot}}{E_{\rm tot} + \sqrt{s}} \right] \frac{\mathbf{p}_{\rm tot}^2}{\sqrt{s}} \\ &= \frac{(E_1 \, E_2 - \mathbf{p}_1 \cdot \mathbf{p}_2)(E_1 - E_2) - m_1^2 \, E_2 + m_2^2 \, E_1}{\sqrt{s}} \ , \end{aligned} \tag{2.73}$$

using only quantities from the same reference frame.

If we are not in the singular range of $s$ (i.e., $t \neq M^2$ in the whole integration range), $\Sigma$ becomes irrelevant and the result for $4E_1 E_2 \, v_{12} \, \sigma$ is simply

$$\begin{aligned} 4E_1 E_2 \, v_{12} \, \sigma &= \frac{1}{16 \, \pi^2} \frac{|\mathbf{p}_3^{\rm cm}|}{\sqrt{s}} \int d^2\Omega_3' \, \frac{A(s,t)}{(t - M^2)^2} \\ &= \frac{1}{8 \, \pi} \frac{|\mathbf{p}_3^{\rm cm}|}{\sqrt{s}} \int_{-1}^{1} d\cos\theta' \, \frac{A(s, t(\cos\theta'))}{(t(\cos\theta') - M^2)^2} \ , \end{aligned} \tag{2.74}$$

where

$$t(\cos\theta') \equiv m_1^2 + m_3^2 - 2 \, E_1^{\rm cm} E_3^{\rm cm} + 2 \, |\mathbf{p}_1^{\rm cm}||\mathbf{p}_3^{\rm cm}| \cos\theta' \ . \tag{2.75}$$

### 2.3.3 Convenient variables

In this section, we will express the Boltzmann equation (2.48) using variables $x$, $y$, defined as

$$x \equiv \frac{m}{T} \ , \quad y \equiv \frac{n_x}{s} \ , \tag{2.76}$$

where $m$ is a reference mass, $T$ is temperature of the thermal bath and $s$ is the entropy density of the Universe. Note that the variable $x$ should not be confused with the index $x$ denoting the considered species of particles. The total entropy of the Universe is assumed to be conserved [9], so

$$\begin{aligned} 0 &= R^{-3} \frac{d}{dt}(R^3 s) \\ &= 3 \, H \, s + \dot{s} \ . \end{aligned} \tag{2.77}$$

Let prime denote differentiation with respect to $x$. The derivative of $y$ is

$$\begin{aligned} y' &= \frac{\dot{y}}{\dot{x}} \\ &= \frac{\dot{n} - n \, \frac{\dot{s}}{s}}{-\frac{s \, m}{T^2} \dot{T}} \\ &= \frac{\dot{n} + 3 \, H \, n}{-\frac{s \, m}{T^2} \dot{T}} \ , \end{aligned} \tag{2.78}$$

which is proportional to the left-hand side of the Boltzmann equation. After a replacement of $n$ by $y\,s$ on the right-hand side, eq. (2.48) becomes

$$\begin{aligned} y'_x = \frac{s\,m}{x^2\,\dot{T}} \sum_{2\to F} & \frac{\delta_{x,i_1}+\delta_{x,i_2}-\delta_{x,f_1}-\delta_{x,f_2}-\ldots-\delta_{x,f_F}}{c_I} \\ & \times \left[y_{i_1}y_{i_2} - \bar{y}_{i_1}\bar{y}_{i_2}\ldots\bar{y}_{i_I}\,\frac{y_{f_1}y_{f_2}\ldots y_{f_F}}{\bar{y}_{f_1}\bar{y}_{f_2}\ldots\bar{y}_{f_F}}\right] \\ & \times \langle\sigma v\rangle_{i_1,i_2\to f_1,f_2,\ldots,f_F}\ , \\ +\frac{m}{x^2\,\dot{T}} \sum_{1\to F} & (\delta_{x,i_1}-\delta_{x,f_1}-\delta_{x,f_2}-\ldots-\delta_{x,f_F})\left[y_{i_1} - \bar{y}_{i_1}\,\frac{y_{f_1}y_{f_2}\ldots y_{f_F}}{\bar{y}_{f_1}\bar{y}_{f_2}\ldots\bar{y}_{f_F}}\right] \\ & \times \langle\Gamma\rangle_{i_1\to f_1,f_2,\ldots,f_F}\ . \end{aligned} \tag{2.79}$$

The value of $\bar{y}\equiv\bar{n}/s$ is given by

$$\bar{y}(x) = \frac{45}{4\pi^{7/2}\sqrt{2}}\,\frac{g}{g_{*s}}\,x^{3/2}\,e^{-x}\ . \tag{2.80}$$

We have used the fact that in the radiation-dominated era, the entropy density is given by eq. (2.23):

$$s \simeq \frac{2\pi^2}{45}\,g_{*s}\,T^3\ . \tag{2.81}$$

Moreover, it can be shown [9] that in that period, the time derivative of temperature is

$$\dot{T} = -\sqrt{\frac{4\,\pi^3\,g_*}{45}}\,\frac{T^3}{m_{\rm Pl}}\ , \tag{2.82}$$

where $m_{\rm Pl}\simeq 1.22\times 10^{19}$ GeV. The effective numbers of relativistic degrees of freedom, $g_*$ and $g_{*s}$, have been defined in eq. (2.24). Finally, the Boltzmann equation becomes

$$\begin{aligned} y'_x = -a_2\,x^{-2} \sum_{2\to F} & \frac{\delta_{x,i_1}+\delta_{x,i_2}-\delta_{x,f_1}-\delta_{x,f_2}-\ldots-\delta_{x,f_F}}{c_I} \\ & \times \left[y_{i_1}y_{i_2} - \bar{y}_{i_1}\bar{y}_{i_2}\ldots\bar{y}_{i_I}\,\frac{y_{f_1}y_{f_2}\ldots y_{f_F}}{\bar{y}_{f_1}\bar{y}_{f_2}\ldots\bar{y}_{f_F}}\right] \\ & \times \langle\sigma v\rangle_{i_1,i_2\to f_1,f_2,\ldots,f_F}\ , \\ -a_1\,x \sum_{1\to F} & (\delta_{x,i_1}-\delta_{x,f_1}-\delta_{x,f_2}-\ldots-\delta_{x,f_F}) \\ & \times \left[y_{i_1} - \bar{y}_{i_1}\,\frac{y_{f_1}y_{f_2}\ldots y_{f_F}}{\bar{y}_{f_1}\bar{y}_{f_2}\ldots\bar{y}_{f_F}}\right] \\ & \times \langle\Gamma\rangle_{i_1\to f_1,f_2,\ldots,f_F}\ , \end{aligned} \tag{2.83}$$

where

$$\begin{aligned} a_2 &\equiv -\frac{s\,m}{\dot{T}} = \sqrt{\frac{\pi}{45}}\,m\,m_{\rm Pl}\,\frac{g_{*s}}{\sqrt{g_*}}\ , \\ a_1 &\equiv -\frac{m}{x^3\,\dot{T}} = \sqrt{\frac{45}{4\,\pi^3}}\,\frac{m_{\rm Pl}}{m^2}\,\frac{1}{\sqrt{g_*}}\ . \end{aligned} \tag{2.84}$$

### 2.3.4 Boltzmann equation for one-component DM. Freeze-out mechanism

In this section, based on chapter 5.2 of [9], we discuss a Boltzmann equation for a simple case of one-component DM and derive the relic density, which will be used in the next section. The assumption is that the dark particles were initially in thermal and chemical equilibrium with the thermal bath of photons. This equilibrium was maintained by annihilation (chemical equilibrium) and scattering (thermal equilibrium) processes between DM and the SM. It will appear that at some moment, when the density of dark particles reaches a small value due to the Hubble expansion, the annihilation processes become too inefficient to keep DM in chemical equilibrium with photons. Then, the DM density ceases to follow the equilibrium density and approaches an approximately constant value, called relic density. The moment

of chemical decoupling is called the freeze-out. Figure 2.1 shows a qualitative picture of the DM density governed by the freeze-out mechanism.

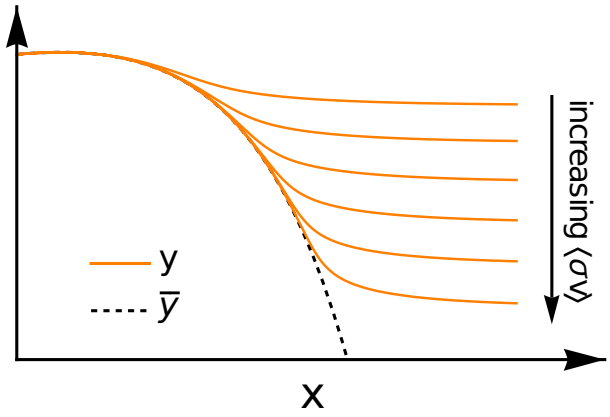


**Figure 2.1:** A qualitative picture of the freeze-out mechanism. The solid orange line is the DM abundance, $y \equiv n/s$, while the dashed black line represents the equilibrium abundance $\bar{y}$. The stronger the annihilation cross section $\langle \sigma v \rangle$ is, the longer dark matter is kept in chemical equilibrium with the thermal bath, which results in lower relic density.

Note that the density of the dark particles, $n_{\rm DM}$, decreases faster than the density of still relativistic light SM particles, $n_{\rm SM}$ (see section 2.2). As the DM annihilation rate should be proportional to $n_{\rm DM}^2$, while the scattering rate depends on $n_{\rm DM} n_{\rm SM}$, the scattering processes are assumed to be still efficient long after the freeze-out, so the thermal equilibrium is assumed to be maintained [9]. This assumption may be invalid in the case of early kinetic decoupling discussed in [17].

We assume that the only processes affecting density of the dark particles are a $2 \to 2$ annihilation process and the corresponding inverse process. The thermally averaged cross section for the annihilation process will be approximated as

$$\langle \sigma v \rangle = \sigma_0 \, x^{-k} \,, \tag{2.85}$$

with $\sigma_0$ being a constant and $k = 0, 1, 2, \ldots$ depending on dynamics of the process. In this simple case, with the reference mass (used to define the variable $x$) equal to the mass of the dark particle, the Boltzmann equation (2.83) takes the following form:

$$\begin{aligned} \frac{dy}{dx} &= -a(x)\, m\, x^{-2} \, \langle \sigma v \rangle \, (y^2 - \bar{y}^2) \\ &= -a(x)\, m\, \sigma_0 \, x^{-(k+2)} \, (y^2 - \bar{y}^2) \,. \end{aligned} \tag{2.86}$$

where

$$a(x) \equiv \sqrt{\frac{\pi}{45}}\, m_{\rm Pl}\, \frac{g_* s(x)}{\sqrt{g_*(x)}} \tag{2.87}$$

can be approximated by a constant value

$$a(x) \simeq a \equiv \sqrt{\frac{\pi}{45}}\, m_{\rm Pl}\, g_*(x_f)^{1/2} = \text{const} \,. \tag{2.88}$$

This approximation is justified by the fact that the effective numbers of relativistic degrees of freedom are close to each other and slowly-changing during most of the history of the Universe. The quantity $x_f$ used here is defined as the value of $x$ for which the interaction ceases to be effective enough to maintain the chemical equilibrium between the dark species and the thermal bath, so that the dark particles decouple and their density is no longer the equilibrium one. This moment is called the freeze-out. More precisely, at $x = x_f$ we require

$$y - \bar{y} = c\, \bar{y} \,, \tag{2.89}$$

where $c$ is a number of the order of unity that will be determined later.

First, let us relate the relic value of $y$ to $x_f$. Shortly after the freeze-out, the equilibrium value $\bar{y}$ can be neglected comparison to $y$, so the Boltzmann equation (2.86) becomes

$$\frac{dy}{dx} = -a\, m\, \sigma_0\, x^{-(k+2)}\, y^2 \,. \tag{2.90}$$

Dividing both sides by $y^2$ and integrating over $dx$ from $x_f$ to $\infty$, we obtain

$$-y_\infty^{-1} + y_f^{-1} = -\frac{a\, m\, \sigma_0}{k+1}\, x_f^{-(k+1)} \,. \tag{2.91}$$

The freeze-out value $y_f$ is assumed to be much larger than the relic value $y_\infty$, so its inverse can be neglected. Consequently, we obtain

$$y_\infty = \frac{k+1}{a\, m\, \sigma_0}\, x_f^{k+1} \,. \tag{2.92}$$

Combining this equation with the results of

- eq. (2.7), defining the density parameter,
- eq. (2.20), relating the energy density of a non-relativistic species to its number density,
- eq. (2.76), defining variable $y$,

we obtain the following present value of the density parameter of the cold dark matter:

$$\begin{aligned} \Omega_c &= \frac{8\,\pi\, G\, s_0}{3\, H^2}\, \frac{k+1}{a\, \sigma_0}\, x_f^{k+1} \\ &\simeq \frac{8.52 \times 10^{-11}\ \mathrm{GeV}^{-2}}{\sigma_0}\, (k+1)\, \frac{x_f^{k+1}}{g_*(x_f)^{1/2}} \,. \end{aligned} \tag{2.93}$$

Here, $s_0$ denotes the present value of the entropy density, equal to ca. $2.2 \times 10^{-38}\ \mathrm{GeV}^3$ [18].

In order to determine $x_f$, let us recall eq. (2.86):

$$y' = -a\, m\, x^{-2}\, \langle \sigma v \rangle\, (y^2 - \bar{y}^2) \,. \tag{2.94}$$

With $\Delta \equiv y - \bar{y}$, this becomes

$$\Delta' + \bar{y}' = -a\, m\, x^{-2}\, \langle \sigma v \rangle\, \Delta\, (\Delta + 2\, \bar{y}) \,. \tag{2.95}$$

Before the freeze-out, $y$ follows the equilibrium value, so $\Delta' \ll \bar{y}'$. Extending validity of this assumption up to the moment of freeze-out, we obtain

$$\frac{\bar{y}'}{\bar{y}} = -a\, m\, x^{-2}\, \langle \sigma v \rangle\, c\, (c+2)\, \bar{y} \,. \tag{2.96}$$

Substituting the explicit form of $\bar{y}$ given by eq. (2.80) we obtain in the limit of large $x$

$$e^x = w\, a\, m\, x^{-1/2}\, \langle \sigma v \rangle\, c\, (c+2) \,, \tag{2.97}$$

where $w \equiv x^{-3/2}\, e^x\, \bar{y} \simeq \mathrm{const}$, see eq. (2.80). After taking the logarithm and using the fixed-point iteration method (starting from the first approximation $x_f = 1$), we obtain

$$x_f \simeq \ln\left[w\, a\, m\, \sigma_0\, c\, (c+2)\right] \,. \tag{2.98}$$

For $c(c+2) = 1$, $g_* \simeq 60$ and $g = 2$ the result is

$$\begin{aligned} x_f &= \ln\left[\sqrt{\frac{3}{2}}\, \frac{m\, m_{\mathrm{Pl}}\, \sigma_0}{4\,\pi^3}\right] \\ &\simeq 39.3 + \ln\left[\frac{m}{\mathrm{GeV}}\, \frac{\sigma_0}{\mathrm{GeV}^{-2}}\right] \,. \end{aligned} \tag{2.99}$$

Note that dependence of $x_f$ on the parameters is logarithmic, thus, the precise values $c(c+2)$, $g_*$ and $g$ are not very important for determination of $x_f$.

### 2.3.5 Miraculous WIMPs

Let us assume a one-component DM model in which the dark particles are allowed to annihilate into the SM. Moreover, let us assume that the value of the thermally averaged cross section is comparable to the cross sections resulting from the SM weak interactions:

$$\langle \sigma v \rangle = \frac{G_F^2 \, m^2}{2\,\pi} \ , \tag{2.100}$$

where $G_F \simeq 1.17 \times 10^{-5}$ GeV$^{-2}$ [19] is the Fermi constant. Then, according to eq. (2.99), the value of $x_f$ is

$$x_f \simeq 14.8 + 3 \, \ln \frac{m}{\text{GeV}} \ . \tag{2.101}$$

Using eq. (2.93), we can estimate the present density parameter of the cold dark matter to be

$$\Omega_c \, h^2 \sim \left( \frac{m}{\text{GeV}} \right)^{-2} (7.4 + 1.5 \, \ln \frac{m}{\text{GeV}}) \ . \tag{2.102}$$

For DM mass of the order of 10 GeV, roughly the same as the order of the masses of the weak gauge bosons, $W^\pm$ and $Z$, the cross section is

$$\begin{aligned} \langle \sigma v \rangle &= 2.2 \times 10^{-9} \ \text{GeV}^{-2} \\ &\simeq 2.5 \times 10^{-26} \ \text{cm}^3/\text{s} \ , \end{aligned} \tag{2.103}$$

and the relic density takes the value

$$\Omega_c \, h^2 \sim 0.1 \ , \tag{2.104}$$

very close to the one observed by Planck [10]:

$$\Omega_c^{\text{obs}} \ h^2 = 0.12 \ . \tag{2.105}$$

Surprisingly, choosing the values of the parameters to be similar to those occurring in the theory of weak interactions or theories of supersymmetry [20], we automatically obtain the correct relic density. This is sometimes referred to as the WIMP miracle.

## 2.4 Boltzmann equations for multicomponent DM

Studying multicomponent DM models, such as the VFDM model [21–23] described in appendix A, one has to face a coupled set of Boltzmann equations describing all the DM components. Those equations must contain not only the terms corresponding to pair annihilation of the dark particles into the SM, but also the contribution of the processes mixing various dark species, which leads to highly non-trivial phenomenology, as discussed in the cited papers. The complexity of equations describing multicomponent dark matter can be illustrated by the set of Boltzmann equations relevant for the VFDM model, governing the abundances of the dark-sector particles $\psi_+$, $\psi_-$, $X$:

$$
\begin{aligned}
\frac{dn_X}{dt} =& -3Hn_X - \langle\sigma_v^{XX\phi\phi'}\rangle\Big(n_X^2 - \bar{n}_X^2\Big) - \langle\sigma_v^{X\psi_+\psi_-h_i}\rangle\Big(n_X n_{\psi_+} - \bar{n}_X\bar{n}_{\psi_+}\frac{n_{\psi_-}}{\bar{n}_{\psi_-}}\Big) \\
&- \langle\sigma_v^{X\psi_-\psi_+h_i}\rangle\Big(n_X n_{\psi_-} - \bar{n}_X\bar{n}_{\psi_-}\frac{n_{\psi_+}}{\bar{n}_{\psi_+}}\Big) - \langle\sigma_v^{Xh_i\psi_+\psi_-}\rangle\bar{n}_{h_i}\Big(n_X - \bar{n}_X\frac{n_{\psi_+}n_{\psi_-}}{\bar{n}_{\psi_+}\bar{n}_{\psi_-}}\Big) \\
&- \langle\sigma_v^{XX\psi_+\psi_+}\rangle\Big(n_X^2 - \bar{n}_X^2\frac{n_{\psi_+}^2}{\bar{n}_{\psi_+}^2}\Big) - \langle\sigma_v^{XX\psi_-\psi_-}\rangle\Big(n_X^2 - \bar{n}_X^2\frac{n_{\psi_-}^2}{\bar{n}_{\psi_-}^2}\Big) \\
&+ \Gamma_{\psi_+\to X\psi_-}\Big(n_{\psi_+} - \bar{n}_{\psi_+}\frac{n_X}{\bar{n}_X}\frac{n_{\psi_-}}{\bar{n}_{\psi_-}}\Big)\,,
\end{aligned}
\tag{2.106a}
$$

$$
\begin{aligned}
\frac{dn_{\psi_-}}{dt} =& -3Hn_{\psi_-} - \langle\sigma_v^{\psi_-\psi_-\phi\phi'}\rangle\Big(n_{\psi_-}^2 - \bar{n}_{\psi_-}^2\Big) - \langle\sigma_v^{\psi_-\psi_+Xh_i}\rangle\Big(n_{\psi_-}n_{\psi_+} - \bar{n}_{\psi_-}\bar{n}_{\psi_+}\frac{n_X}{\bar{n}_X}\Big) \\
&- \langle\sigma_v^{X\psi_-\psi_+h_i}\rangle\Big(n_X n_{\psi_-} - \bar{n}_X\bar{n}_{\psi_-}\frac{n_{\psi_+}}{\bar{n}_{\psi_+}}\Big) - \langle\sigma_v^{\psi_-h_iX\psi_+}\rangle\bar{n}_{h_i}\Big(n_{\psi_-} - \bar{n}_{\psi_-}\frac{n_{\psi_+}}{\bar{n}_{\psi_+}}\frac{n_X}{\bar{n}_X}\Big) \\
&- \langle\sigma_v^{\psi_-\psi_-XX}\rangle\Big(n_{\psi_-}^2 - \bar{n}_{\psi_-}^2\frac{n_X^2}{\bar{n}_X^2}\Big) - \langle\sigma_v^{\psi_-\psi_-\psi_+\psi_+}\rangle\Big(n_{\psi_-}^2 - \bar{n}_{\psi_-}^2\frac{n_{\psi_+}^2}{\bar{n}_{\psi_+}^2}\Big) \\
&+ \Gamma_{\psi_+\to X\psi_-}\Big(n_{\psi_+} - \bar{n}_{\psi_+}\frac{n_{\psi_-}}{\bar{n}_{\psi_-}}\frac{n_X}{\bar{n}_X}\Big)\,,
\end{aligned}
\tag{2.106b}
$$

$$
\begin{aligned}
\frac{dn_{\psi_+}}{dt} =& -3Hn_{\psi_+} - \langle\sigma_v^{\psi_+\psi_+\phi\phi'}\rangle\Big(n_{\psi_+}^2 - \bar{n}_{\psi_+}^2\Big) - \langle\sigma_v^{\psi_+\psi_-Xh_i}\rangle\Big(n_{\psi_+}n_{\psi_-} - \bar{n}_{\psi_+}\bar{n}_{\psi_-}\frac{n_X}{\bar{n}_X}\Big) \\
&- \langle\sigma_v^{X\psi_+\psi_-h_i}\rangle\Big(n_X n_{\psi_+} - \bar{n}_X\bar{n}_{\psi_+}\frac{n_{\psi_-}}{\bar{n}_{\psi_-}}\Big) - \langle\sigma_v^{\psi_+h_iX\psi_-}\rangle\bar{n}_{h_i}\Big(n_{\psi_+} - \bar{n}_{\psi_+}\frac{n_{\psi_-}}{\bar{n}_{\psi_-}}\frac{n_X}{\bar{n}_X}\Big) \\
&- \langle\sigma_v^{\psi_+\psi_+XX}\rangle\Big(n_{\psi_+}^2 - \bar{n}_{\psi_+}^2\frac{n_X^2}{\bar{n}_X^2}\Big) - \langle\sigma_v^{\psi_+\psi_+\psi_-\psi_-}\rangle\Big(n_{\psi_+}^2 - \bar{n}_{\psi_+}^2\frac{n_{\psi_-}^2}{\bar{n}_{\psi_-}^2}\Big) \\
&- \Gamma_{\psi_+\to X\psi_-}\Big(n_{\psi_+} - \bar{n}_{\psi_+}\frac{n_{\psi_-}}{\bar{n}_{\psi_-}}\frac{n_X}{\bar{n}_X}\Big)\,.
\end{aligned}
\tag{2.106c}
$$

Here, $\langle\sigma_v\rangle$ denotes the thermally averaged cross section, $\Gamma$ is the thermally averaged width, and $\phi\phi'$ denote all possible SM particles, including the Higgs-portal mediators $h_1$ and $h_2$. As discussed in chapter 5, some of the processes contributing to those equations are affected by the $t$-channel singularity, which makes the corresponding $\langle\sigma_v\rangle$ infinite, making solving the equations impossible.

# Chapter 3

# Dark matter

## 3.1 Definition and evidence

Dark matter is the component of the Universe that does not interact electromagnetically, but provides the missing mass needed to explain various phenomena observed. This chapter briefly summarizes the required properties of dark matter and presents the most notable evidence of its existence. It is evident that most of DM should exist in a form of cold BSM particles. Moreover, the small-scale problems described in section 3.3 indicate that the dark sector should be self-interacting.

### 3.1.1 Historical perspective

According to [24], the first to use the term "dark matter" (Fr. "matière obscure") was Henri Poincaré in 1906 [25], discussing Lord Kelvin's proposal [26] to apply the kinetic theory of gases to the stars of the Milky Way and deduce their number from the observed dispersion of their velocity. As Poincaré concluded, the numbers theoretically predicted by Kelvin are close to the observed ones, hence, the amount of non-luminous matter should be very small in comparison to the number of stars. Since the models used by Kelvin and Poincarè to derive this conclusion were highly inaccurate comparing to the current state of knowledge, their results are no longer valid. Nevertheless, this was probably the first attempt to estimate the amount of the non-luminous matter in the Universe using a strict methodology.

An argument for existence of DM has been provided by Fritz Zwicky in his famous paper [27]. He applied the virial theorem to the observed velocity dispersion of galaxies forming the Coma cluster. The mean potential energy of the system constituents, $\langle V \rangle$, should be proportional to the mean kinetic energy, $\langle T \rangle$, in the following way:

$$\langle T \rangle = -\frac{1}{2}\langle V \rangle \, . \tag{3.1}$$

The mean potential energy can be expressed in terms of the cluster's mass and size, while the mean kinetic energy should roughly determine velocities achieved by the constituents. The resulting estimation of the cluster's mass has been confronted with the estimation based on the observed number of galaxies forming the cluster (800). Zwicky assumed the total mass of the cluster to be $10^9$ solar masses, and estimated its size as $10^6$ ly. The resulting square root of the average square velocity should is 80 km/s, while the observed velocities were of the order of 1000 km/s. Zwicky concluded that the missing mass, needed to provide additional gravitational potential resulting in higher kinetic energies, exists in the form of dark matter (Ger. "dunkle Materie"). However, as his work based on many rough assumptions, this conclusion was subject to large uncertainties, hence, not imposing a significant impact on the community. Moreover, due to technical limitations, applying a similar procedure to the stars forming a single galaxy was impossible that time. Zwicky himself stated that *it is not possible to derive the masses of [galaxies] from observed rotations, without the use of additional information* [28].

The first convincing proof of existence of DM based on the analysis of the galactic rotation curves. In 1970, Vera Rubin and Kent Ford published the analysis of the optical rotation curve of the Andromeda Galaxy (M31) [29]; simultaneously, Kenneth Freeman compared the rotation curves of M33 and NGC 300, observed in 21 cm radiation, with the predictions deduced from the assumed mass distribution [30]. As the position of the distribution peak appeared further from the galactic centre than expected, Freeman concluded that the dark component should be at least as massive in total as the luminous matter,

and its distribution should be much different than the assumed exponential one. Numerous subsequent observations of the rotation curves of various galaxies brought the authors to the conclusion that non-luminous matter, present in large amounts, is necessary to explain the observation.

### 3.1.2 Evidence

**Rotation curves.** Using the Newtonian laws of motion and theory of gravity, the non-relativistic velocities of gravitationally bounded bodies rotating around the center of the bounding system can be easily related to the distribution of mass in the system: in the reference frame of a given body, the gravitational force should balance the centrifugal force. If the velocity of the body is denoted by $v$ and the distance from the centre is $r$, the resulting relation reads

$$v^2 = \frac{GM(r)}{r} \,, \tag{3.2}$$

where $M(r)$ is the mass contained within a sphere of radius $r$, and $G$ is Newton's constant. Consequently, it is possible to determine the density profile of the system (assuming it is isotropic) from the observed dependence of rotation velocity on the radius,

As mentioned, since early 1970s, this relation applied to the contents of galaxies provides a strong evidence of DM existence. The observed rotation velocity often appears to be larger than the value expected from estimation of mass of the luminous matter in a given galaxy. The missing mass is attributed to a DM halo. For an illustration, fig. 3.1 shows the rotation curve of the M33 galaxy and the fitted profile of DM.

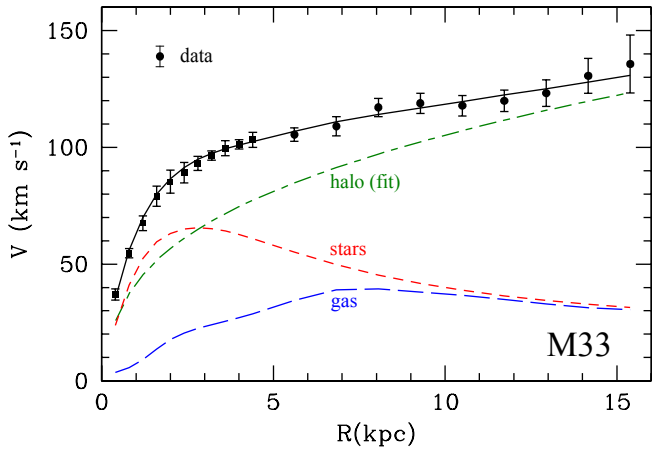


**Figure 3.1:** Rotation curve of the M33 galaxy (solid line) observed in 21 cm radiation. Points denote the data, while the dashed lines represent the rotation curves corresponding to the contributions of the DM halo, the stellar disk, and the gas. The DM halo contribution has been fitted to agree with the data. Plot adapted from [31].

**Anisotropies of CMB.** Among other cosmological parameters, the amount of DM can be deduced from the power spectrum of the cosmic microwave background (CMB). According to [32], in the early Universe, initial fluctuations of DM density grew and formed wells of gravitational potential which attracted baryonic matter. When the density of the baryonic matter grows, its temperature grows as well, finally causing it to radiate. The increasing radiation pressure provides a repulsive force to the system. At some moment, the pressure starts to dominate the gravitational attraction and the baryonic cloud begins to expand, decreasing its density and cooling down. Then, when the density becomes small enough, the attractive force dominates again and the cycle repeats. In this way, the density of baryons and photons oscillates. At the moment of decoupling of the CMB, those photons that were in the expanded phase were slightly cooler than those in the dense phase. This is considered to be the origin of small anisotropies of the CMB temperature, depicted in the left panel of fig. 3.2.

The density parameter of baryons, $\Omega_b$. determines the ratio between the even and odd peaks of the CMB spectrum (see the right panel of fig. 3.2), while the sum $\Omega_b + \Omega_c$, where $\Omega_c$ is the contribution

of cold DM, determines the damping rate of the spectrum. Measurements of the Planck satellite [10] indicate that the Λ-CDM model of the Universe, which assumes cold DM and a non-zero value of the cosmological constant Λ, appears to be in excellent agreement with observations, with the present values of $\Omega_b$, $\Omega_c$ and $\Omega_\Lambda$ (the value corresponding to the cosmological constant) equal to

$$\Omega_b = 0.022\, h^{-2}\ , \quad \Omega_c = 0.120\, h^{-2}\ , \quad \Omega_\Lambda = 0.685\ , \tag{3.3}$$

and a negligible contribution of the relativistic species (photons, neutrinos). This means that 68.5% of the Universe energy density is provided by the dark energy (represented by the cosmological constant), 26.6% comes from cold dark matter and the remaining 4.9% is formed by the baryonic matter.

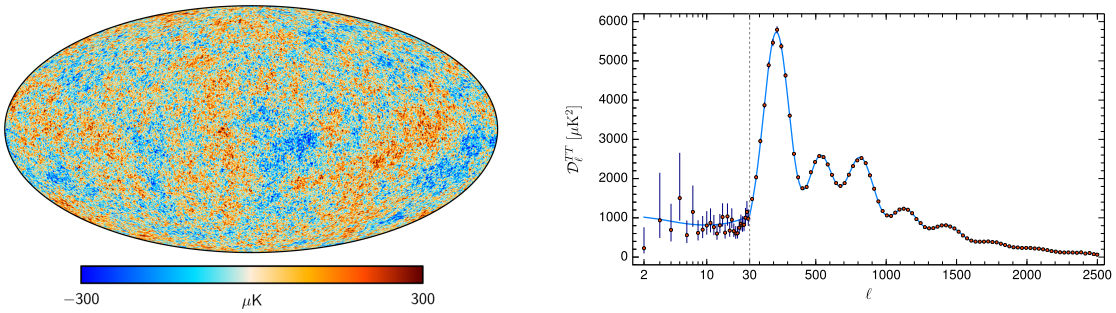


**Figure 3.2: Left:** map of temperature anisotropy of the CMB observed by Planck, with the dipole anisotropy (which corresponds to the Earth's motion relatively to the CMB rest frame) removed. Colouring denotes the difference between the temperature of each point and the mean value of 2.7255 K [33]. **Right:** the power spectrum of the anisotropies shown in the left plot. The shape of the spectrum allows to determine cosmological parameters, including DM density parameter (see text for discussion). In the plot, the points represent the observed values and the line is the Λ-CDM fit. Plots adapted from [10, 34].

**Colliding clusters.** Observations of gravitationally bended light allow to reconstruct the mass distribution that caused the lensing effect. It may happen that the reconstructed mass is distributed differently than the observed luminous matter. The most famous example of such a discrepancy is the 1E0657-558 cluster (known as the Bullet Cluster) [35], formed by two colliding clusters. As can be seen in the plot presented in fig. 3.3, the luminous matter observed in the X-rays is distributed closer to the center than the mass reconstructed from the lensing. The interpretation is that during the collision, the baryonic matter has decelerated due to particle interactions, while the dark halos of both clusters have passed through with only small slowdown. Figure 3.4 presents other examples of observed colliding clusters, with distribution of luminous and DM mass marked by different colours.

Observations of the Bullet Cluster provide an important constraint of the strength of DM self-interaction, as too strong interactions would prevent DM from splitting apart. Moreover, they are the most direct proof of existence of DM and one of the most serious arguments against theories of modified gravity.

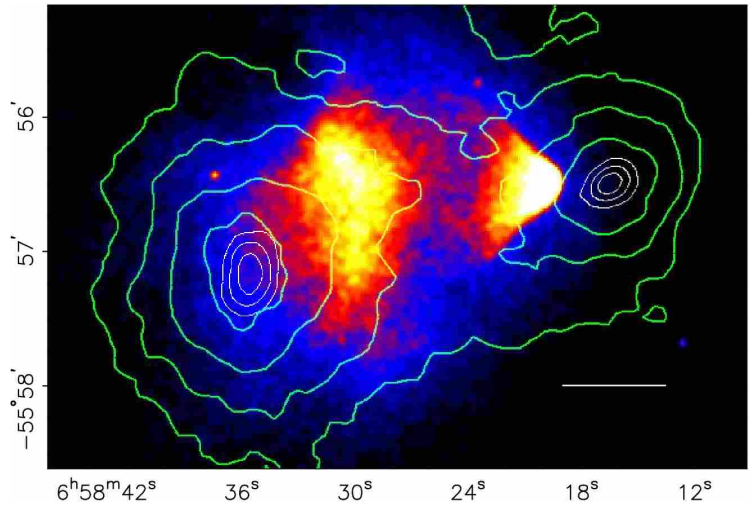


**Figure 3.3:** The Bullet Cluster. The colours represent the X-ray image of the system, while the green contours show the mass distribution deduced from lensing effects. It can be observed that the luminous matter is concentrated near the centre of the image, while the mass distribution forms two distinct regions (interpreted as DM halos of the colliding clusters) far from each other. The length of the white bar, added for scale, is 200 kpc. Image from [35].

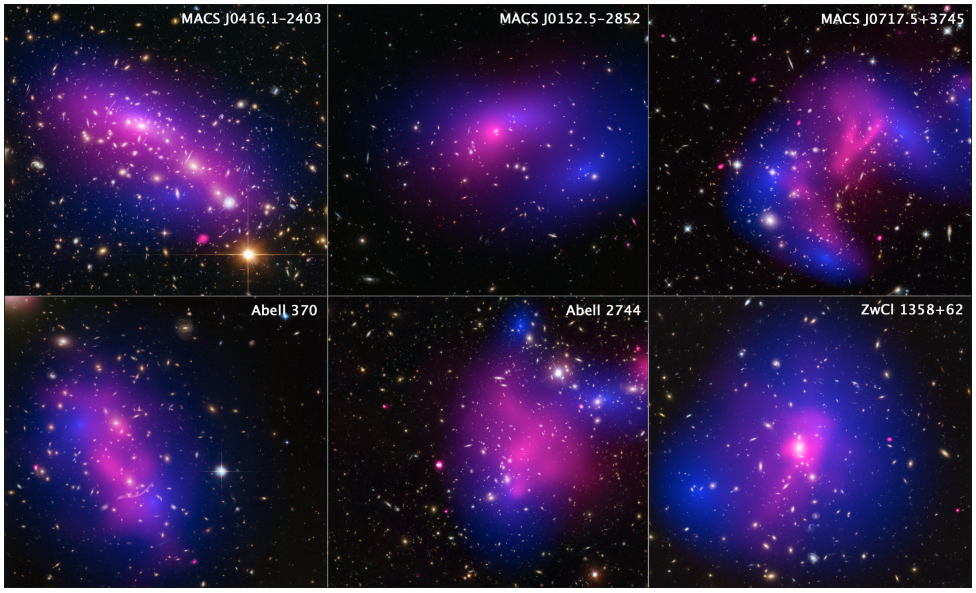


**Figure 3.4:** Images of six colliding clusters (names are annotated in the top-right corner of each image) observed with NASA's Hubble Space Telescope and Chandra X-ray Observatory. The colour shading overlaid on optical images denotes distribution of X-ray sources (pink) and dark matter (blue). Image from [36].

### 3.1.3 Candidates

Here, we discuss proposed constituents of the missing mass and summarize the arguments leading to the conclusion that the most proper candidate for DM is a non-relativistic, non-baryonic, electrically neutral particle, at most weakly coupled to the SM. To maintain the correct relic density, the dark particles should be stable (or, at least, their lifetime should be comparable to the age of the Universe).

**MACHOs and other baryonic candidates.** Initially, DM was supposed to consist of objects of known objects: interstellar gas, dust, and the so-called massive astrophysical compact halo objects (MACHOs): asteroids, planets and dark stellar remnants (neutron stars, dwarfs, black holes). However further evidence shows that if the baryonic matter was the main source of the missing mass, the content of light nuclei would be disturbed. The primordial production of light nuclei is almost fully determined by the value of baryon-to-photon ratio $\eta$ [37]. The observed deuterium-to-hydrogen ratio, equal to $2.6 \times 10^{-5}$, is consistent with $\eta \simeq 6 \times 10^{-10}$ [38]. On the other hand, knowing the energy density of photons from the Planck observations of CMB [10], it is possible to use $\eta$ to calculate the density parameter of baryons, $\Omega_b$, as

$$\begin{aligned} \Omega_b\, h^2 &= 3.66 \times 10^7\, \eta \\ &\simeq 0.022\ . \end{aligned} \tag{3.4}$$

This result perfectly agrees with the value determined from the damping rate of the spectrum of the CMB anisotropies, provided in section 3.1.2. Thus, baryonic matter can form only a small amount of the missing mass.

**Primordial black holes.** A possibility that demands a dedicated discussion is that DM could consist of primordial black holes (PBHs), forming at the early stage of the Universe evolution, when the amount of baryons is still small, so that the abundance of PBHs is not constrained by the Big-Bang nucleosyndissertation [39], which limits the contribution of baryons to DM as discussed above. However, the amount of PBHs is limited by numerous other observations: taking into account only robust constraints allows PBHs to form all DM only if their masses fit in a small window around $10^{-13}$ solar mass, while if the less established constraints are also included, the contribution of PBHs of any masses is limited to at most 10% of DM [40, 41].

**Modified gravity.** So far, all evidence of the existence of DM, described in section 3.1.2, is of gravitational nature. Hence, a question arises: if our understanding of gravity demands improvement, maybe the observed effects could be explained by modifying theory of gravity, without introducing any new particles?

Such an idea has been first suggested in 1983 by Mordehai Milgrom [42–44]. He proposed to modify the Newtonian laws of motion (hence the name of the theory: modified Newtonian dynamics, abbreviated as MoND) to reproduce the rotation curves without introducing additional dark mass. He stated that the second Newton's law could include an additional factor, depending on acceleration of the body with respect to some reference frame. This factor would be close to one for high acceleration, and proportional to the acceleration for small values, e.g.:

$$F = m\, a\, \mu\!\left(\frac{a}{a_0}\right)\ , \quad \mu(x) \equiv \frac{x}{x+1}\ , \tag{3.5}$$

where $a$ is acceleration and $a_0$ is a new constant of dimension of acceleration and a small value (of the order of $10^{-10}$ m/s$^2$). Using this assumption, Milgrom has successfully reproduced the observed rotation curves using only stellar and gas contribution to the mass.

Equivalently to adding the extra term to the law of motion, the theory can introduce a corresponding term to the Newtonian law of gravity, without altering the whole dynamics. Thus, MoND is treated as the first example of theories of modified gravity. MoND and its relativistic generalization, the tensor-vector-scalar theory (TeVeS) [45], as well as other theories of modified gravity, are able to reproduce some of phenomena attributed to DM, but still have troubles to explain the shape of the spectrum of the CMB anisotropies [46] and observations of colliding clusters (both those types of evidence are discussed in the next section). Moreover, those theories are severely constrained by all observations fully consistent with Einstein's general relativity, e.g., those involving gravitational waves [47]. Summing up, modifying gravity is currently unable to provide a satisfactory alternative to theories of particle DM.

**Hot and cold non-baryonic particle dark matter.** The discussion of various DM candidates presented in this section brings us to the conclusion that most of DM should exist in a form of non-baryonic particles. Here, we argue that most of those particles should be "cold", i.e., non-relativistic.

There is one component of non-baryonic DM which is already known, namely, the neutrinos. They are electrically neutral, interact very weakly, and are known to have a non-zero mass due to their oscillations [48]. However, their mass is so tiny that they are still relativistic when they decouple from the thermal

bath, thus neutrinos are hot relics contributing to the effective number of relativistic degrees of freedom of the Universe, defined by eq. (2.24).

The effective number of relativistic degrees of freedom, defined by eq. (2.24), affects the expansion rate of the Universe during Big-Bang nucleosyndissertation, and influences the shape of envelope of the CMB spectrum [49–51]. Consequently, the number of BSM relativistic degrees of freedom is strongly constrained. At the 95%C.L., the discrepancy between the value predicted by the SM, 3.04, and the true value must be smaller than 1 [49].

It can be shown [9], that the relic density of hot relics is proportional to their mass, which results [49] in the following relation between the sum of neutrinos masses and their abundance:

$$\Omega_\nu h^2 = \frac{\sum m_\nu}{93.14 \text{ eV}} . \tag{3.6}$$

Combining this relation with the upper limit of $\sum m_\nu < 0.12$ eV [10] gives

$$\Omega_\nu h^2 < 0.0013 , \tag{3.7}$$

which is much smaller than the required value of DM relic density. Therefore, most of DM should exist in a form of cold particles.

## 3.2 Small-scale structure: the galactic halos

This section, basing on [52], describes the usual assumption regarding DM distribution at the galaxy level, known as the Standard Halo Model (SHM).

The model of the halo, currently known as the SHM, has been first proposed by A.K. Drukeir, K. Freese and D.N. Spergel in 1986 [53]. Approximating the rotation curve of the galaxy of the interest by a flat line, and assuming that the distribution of DM is isotropic, they deduced from eq. (3.2) that the density should scale with the distance from the galactic centre, denoted by $r$, as $r^{-2}$. The DM halo is assumed to form an isothermal sphere, which leads to the following velocity distribution of the velocities of the dark particles:

$$f(\mathbf{v}) = \mathcal{N} \exp\left(-\frac{\mathbf{v}^2}{2\sigma_v^2}\right) \theta(v_{\text{esc}} - |\mathbf{v}|) , \tag{3.8}$$

where $\sigma_v$ denotes the velocity dispersion and $\mathcal{N}$ is a normalization constant. The step function $\theta$ is introduced to reflect the fact that, assuming DM to be gravitationally bounded, the maximal speed is cut off at the galactic escape velocity. The local value of this cut-off scale in the vicinity of the Sun (treated as a part of the Galaxy) is ca. 533 km/s [54].

The SHM assumes the galactic halos to be stationary (non-rotating). Thus, for the Earth moving through the Milky Way, the total velocity with respect to the DM halo is

$$v = v_s + v_e \cos\gamma \cos\left(2\pi \frac{t - t_0}{1 \text{ yr}}\right) , \tag{3.9}$$

where $v_s \simeq 230$ km/s is the velocity of the Sun, $\gamma \simeq 60^\circ$ is the angle between the plane of the planetary motion in the Solar System and the direction of the solar motion, and $t_0$ denotes the date corresponding to the maximal total velocity, i.e., the 2nd of June [55]. A consequence of the periodical modulation of this velocity is expected modulation of the signal in DD experiments discussed in section 4.1.

It is worth to bear in mind that the SHM is a *convenient assumption*. In fact, observations indicate that it is not applicable to dwarf galaxies, whose DM density profile, as deduced from the rotation curves, appears to not satisfy the inverse square profile, see section 3.3 for more details. Moreover, the assumption of isotropy is a subject of discussion at small scales, and could be tested to some extent if the proposed experiments involving paleo-detectors (section 4.1.8) are performed.

Simulations (see, e.g., [56–58] ) predict that a DM halo of a size corresponding to the Milky Way should be accompanied by hundreds of smaller subhalos. The largest of them should be capable to form satellite galaxies in a number exceeding those observed. This leads to the missing-satellite problem discussed in the next section.

## 3.3 Self-interacting dark matter

### 3.3.1 Cusp-core problem

The simple assumption that DM consists of identical massive, collisionless particles is sufficient to explain the large-scale effects, but has some troubles when it comes to analysis at the galactic scale [59]. Namely, simulations indicate that the density profile generated by such a collisionless DM in dwarf galaxies should have a profile which is peaked at the galaxy centre. However, from observations, it appears that many rotation curves provide a flat region (core) at small values of $r$. This discrepancy is often called the cusp-core problem. For an illustration, an exemplary comparison between the profile of collisionless DM and the actual one is presented in fig. 3.5.

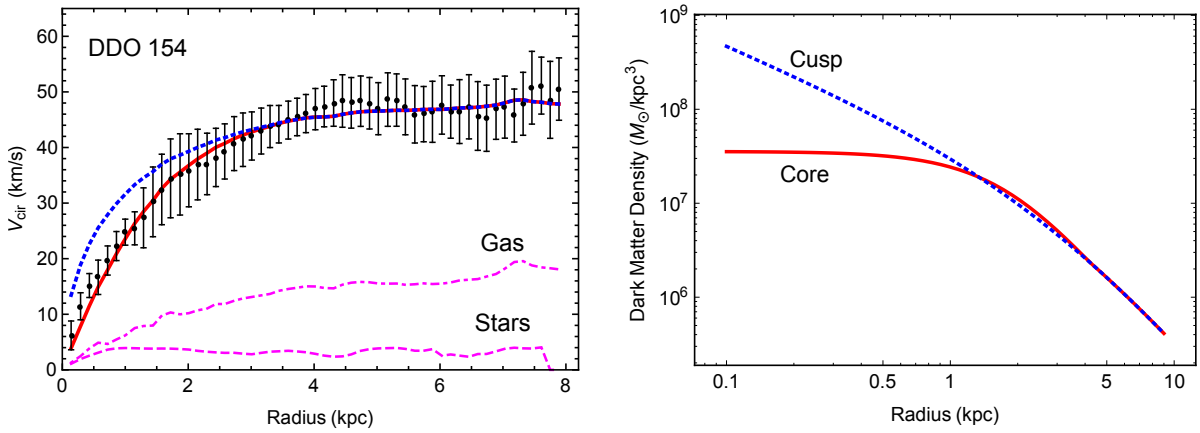


**Figure 3.5: Left:** rotation curve of the DDO 154 dwarf galaxy. Black points indicate the observed values, while the blue dashed line represents the profile predicted for collisionless DM. The red line is the actual fit. Contribution of the stars and gas are presented as the pink lines. **Right:** DM density profiles deduced from the rotation curves from the left plot. The correct rotation curve provides the profile with a central core, while the cuspy profile leads to incorrect results. Plots from [59].

### 3.3.2 Missing-satellites problem

Another small-scale issue is the so-called missing-satellites problem. The simulations predict the Milky Way halo to have hundreds of subhalos, in principle large enough to contain a dwarf galaxy [56–58]. On the other hand, only several tens of dwarf satellites of the Milky Way are known (for instance, [60] claims 39 confirmed and 22 candidate objects). Although some of the recent works (e.g., [61]) argue that the problem disappears if one modifies the method of estimation of the number of dwarf satellites, other (e.g., [62]) confirm the discrepancy. Figure 3.6 shows results of an exemplary simulation of the Milky Way satellites confronted with the actually observed distribution.

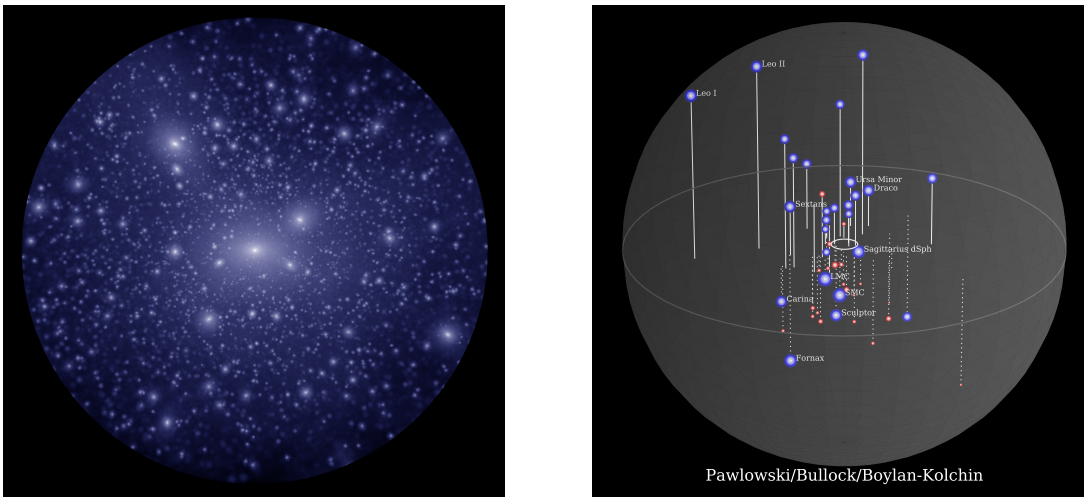


**Figure 3.6: Left:** simulation of a structure of collisionless DM within a 250 kpc sphere centred at the centre of the Milky Way. **Right:** the satellites of the Milky Way (represented by the central disk) known in 2017, drawn inside the same sphere. The red ones are those discovered after 2015. The size of a given circle is proportional to the logarithm of the stellar mass, and the brightest satellites are labelled by names. A clear discrepancy between the simulation and the observations is visible. Plots from [62].

### 3.3.3 Too-big-to-fail problem

Probably the most natural approach to the missing-satellites problem is to assign the most massive of the predicted subhalos to the observed satellite galaxies of the Milky Way, and state that due to unknown, non-trivial effects affecting galaxy formation, the rest of subhalos fail to form galaxies bright enough to be noticed [62]. This, however, requires the dark halos of the observed satellite galaxies to match the largest masses predicted in simulations. The comparison shows that the densities of the halos of the known satellites of the Milky Way are too small to fit the predictions [63, 64]: more than ten subhalos with the maximal circular velocity $v_{\max}$ greater than 25 km/s are predicted, while none of the dwarf spheroidal satellites of the Milky Way exceeds this threshold. Surprisingly, it seems that the largest of the predicted halos fail to form observable galaxies, while those smaller are able to gather enough baryonic matter. This apparent contradiction is referred to as the too-big-too-fail problem. Figure 3.7 shows the comparison between observed satellites and the results of the simulations.

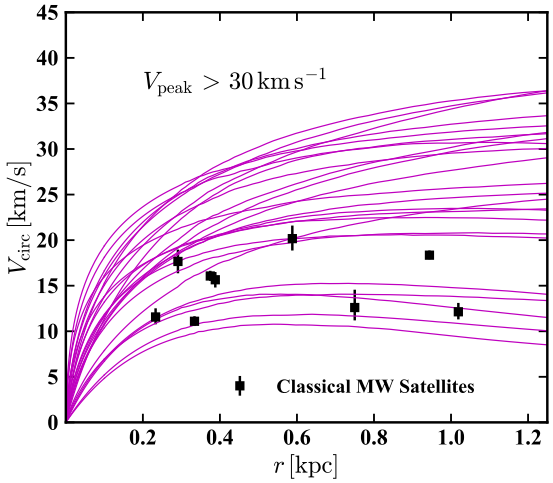


**Figure 3.7:** The lines represent rotation curves of the largest from the simulated DM subhalos of the Milky Way, while the points denote the rotation velocity of the largest satellite galaxies measured at the half-light radius. The densest of the predicted subhalos, represented by the upper lines, surprisingly fail to form galaxies. Plot from [62].

### 3.3.4 Solution: interactions within the dark sector

All the small-scale problems described above arise from the assumption that DM exists in a form of cold, collisionless particles. As coldness of the dark particles is well-motivated (see section 3.1.3) the solution is to allow for self-interactions of DM. Indeed, if the dark particles interact with each other, their energy is redistributed in regions of high DM concentration, which leads to flat inner region of the density profiles, resolving the core-cusp problem. The simple physical picture is that the self-interactions produce pressure when the DM density reaches large values, preventing DM from forming a density peak. Moreover, reduced central density makes the simulations consistent with number and densities of the observed halos. Assuming the self-interactions are present, simulations predict galaxies to be more spheroidal, which agrees with observations of the satellite galaxies, while there are no differences at the large scales [65, 66].

According to [65], the cross section of DM self-interactions required to resolve the problems is around

$$\sigma_{\mathrm{DM}}/m_{\mathrm{DM}} \simeq 0.1 \text{ cm}^2/\text{g} \,. \tag{3.10}$$

Higher values seem to be excluded by observations of the Bullet cluster, as they would lead to deceleration of DM, similarly to the way it happens to the baryonic matter [67, 68], while lower values are not sufficient to achieve the required drop of central density [65, 66].

The presence of the self-interactions may indicate that the dark sector consists of more than one type of particles; for example, containing a proper cold dark particle, constituting the correct relic abundance, and a lighter mediator responsible for interactions. A long list of references to papers describing various multi-component DM models can be found in the introductory section of [22]. The self-interactions naturally appear in the Higgs-portal theories, like those employed in this dissertation (see appendices A and B).

# Chapter 4

# Experimental search for particle DM: a short overview

As stated in chapter 3, most of dark matter should exist in a form of BSM particles. If any non-gravitational interactions between them and the SM particles exist, as it it the case for the Higgs-portal models (see chapter 1), the dark particles could be detectable. It is, thus, natural to search for them in experiments. Currently, the search for DM employs numerous experimental approaches, which can be grouped into the following three main branches [69]:

- direct detection (DD) searches, aiming to detect effects of interactions between the dark particles and the baryonic matter of which the detectors are built;
- indirect detection (ID) experiments, searching the observed Universe for a flux of SM products of DM annihilation or decay;
- searches for dark particles produced at colliders.

The following sections discuss those three approaches: section 4.1 describes the DD experiments, the ID approach is discussed in section 4.2, and the collider searches are the topic of section 4.3.

Despite constant efforts, no proper candidate for the dark particle has been discovered so far. Instead, the null-results of the experiments provide stringent limits on the DM-SM interaction strength. Even though several excesses over the predicted background have been noticed by ID experiments analysing cosmic rays, announcing them to be of DM origin seem to contradict the relic-density constraints; moreover, alternative explanations exist (see section 4.2.2 for details).

## 4.1 Earth-based direct detection experiments

As a part of the Milky Way, the Solar System (and, in particular, the Earth) is immersed in the Galactic DM halo. Hence, if DM exists in the form of particles, they should be present everywhere around us. The so-called direct detection (DD) experiments aim to observe the possible effects of interactions between those particles and the matter of the detectors, such as ionization, phonon excitation or defects of the crystal lattice.

As already mentioned, no convincing signal[1] of DM direct detection has been observed so far. Figure 4.1 presents the current limits on the cross section for spin-independent (see section 4.1.5) scattering of dark particles on nucleons, deduced from the null-results of the DD experiments.

[1] Unconvincing signals include the results of the DAMA/LIBRA experiment, see section 4.1.6.

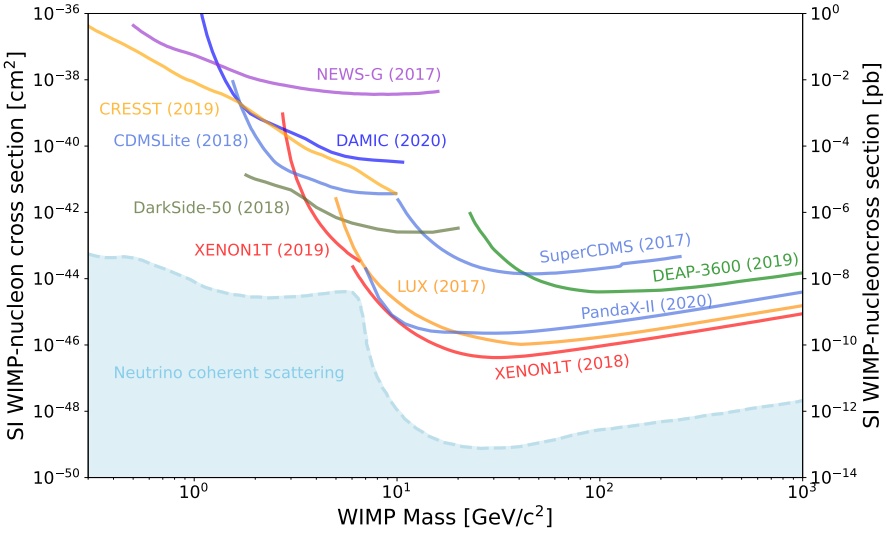


**Figure 4.1:** Upper limits on the SI DM-nucleon cross section as a function of DM mass [69]. The most stringent limits have been obtained in experiments employing liquid-xenon detectors: XENON1T, LUX, PandaX-II. The so-called neutrino floor, i.e., the background coming from coherent neutrino-nucleus scattering (see section 4.1.2 for details), is denoted by the blue shading.

The remaining part of this section discusses the ID approach in some detail. Section 4.1.1 describes the unique features expected from the DM signal. Section 4.1.2 is devoted to the possible sources of experimental background and ways to reduce it. Section 4.1.3 explains the difference between nuclear-recoil and electronic-recoil events, and section 4.1.4 shortly describes the Migdal effect, facilitating detection of nuclear-recoil events. In section 4.1.5 the difference between spin-dependent and spin-independent interactions is briefly discussed. Finally, a list of DD methods, along with examples of experiments utilizing them, is provided in sections 4.1.6 to 4.1.8. Although the list covers the most widespread approaches to DD, it is by no means exhaustive, as new techniques are constantly being invented and proposed.

### 4.1.1 Expected signatures

The yet-unobserved flux of dark particles is believed to be caused by the motion of the Earth relatively to the dark Galactic halo. Thus, the DD signal is expected to possess some unique features that may allow to distinguish it from possible background. Those features are:

- directional dependence,
- daily modulation,
- annual modulation,
- (possibly) long-period (ca. 250 Myr) modulation.

Regarding the directional dependence, the velocity of the Sun in its motion around the Galactic centre, equal to ca. 230 km/s, is currently directed towards the Cygnus constellation. Consequently, most of the DM flux should be directed oppositely to that direction [70].

The reason for the daily modulation is a combination of the directional dependence of the flux with the rotational motion of the Earth. When the Earth faces the Sun with the side the experiment of interest is performed on, the DM flow should be enhanced comparing to the opposite situation, assuming that dark particles interact with particles that conform the Earth [71].

The annual modulation (discussed in detail in [55]) is a consequence of the Earth's motion around the Sun (with velocity of ca. 30 km/s) with the Sun's motion with respect to the DM halo. When both velocities are pointing similar direction (around the 2nd of June), they add up, so that the flux should be larger, while when they are opposite (around the 2nd of December), the flux should be reduced. Let us estimate the difference. As described in section 3.2, the Standard Halo Model assumes that the total

velocity of the Earth with respect to the stationary DM halo is

$$v = v_s + v_e \cos\gamma \cos\left(2\pi \frac{t - t_0}{1 \text{ yr}}\right) , \tag{4.1}$$

with $v_s \simeq 230$ km/s denoting the Sun's velocity, $\gamma \simeq 60°$ being the angle between the plane containing Earth's orbit and the direction of the solar motion, and $t_0$ denoting the 2nd of June. It is clear that the relative change of the flux should be equal to $(v_e/v_s) \cos\gamma \simeq 7\%$. A similar mechanism, taking into account the rotational velocity of the Earth, can influence the daily modulation as well, however only by a small relative factor of ca. 0.1%, as the rotational velocity of the Earth's surface is around 0.5 km/s.

Finally, if the angular distribution of the DM halo is not homogeneous (in contrast to the SHM, see section 3.2), motion of the Sun around the Galactic centre may provide an additional modulation of a period of ca. 250 Myr and an unknown shape, induced by fluctuations of the local DM density. This kind of modulation could be observed using the so-called mineral paleo-detectors, briefly described in section 4.1.8.

### 4.1.2 Experimental background

Because DM is expected to interact with the baryonic matter very weakly, the main challenge of the DD experiments is to reduce the experimental background inevitably appearing when sensitivity of the detectors is increased. Most of the experimental background is caused by

- neutrinos (solar and atmospheric),
- cosmic-ray induced muonic showers,
- neutrons (from radioactive decays of surrounding matter),
- $\beta$ and $\gamma$ radioactivity,

see sec. 4 of [72].

To ensure that a sufficient amount of observed signal is of DM origin, the detectors are set in underground facilities and use additional shielding against the possible background. Usually, lead is utilized to protect the detector from $\gamma$ radiation, while polyethylene absorbs environmental neutrons. Moreover, the detectors and their shielding must be built of radiopure materials; for example, the lead used for shielding is obtained from centuries-old archaeological finds [73, 74].

Further reduction of the background is achieved by vetoing so-called multiple events, i.e., those inducing detector reaction at more than one place, which suggests multiple scattering of the incoming particle. Due to low expected cross section, such events would by highly unlikely caused by dark particles; on the other hand, such a scenario is probable for neutrons.[2] Also the events occurring in the external parts of the detector (outside the so-called fiducial mass) are often rejected, as possibly caused by external radiation [75].

A type of background which is irreducible unless the aforementioned modulation effects are taken into account is the so-called neutrino floor, shown in fig. 4.1 as the blue shading. A neutrino (solar or atmospheric) can mimic dark particles in the processes known as elastic neutrino-electron scattering and coherent neutrino-nucleus scattering (predicted by D. Z. Freedman in 1973 [76] and observed in 2017 by the COHERENT collaboration [77]). Although reaching the neutrino floor will substantially decrease sensitivity, it should not be treated as a hard limit [78]. The processes responsible for this kind of background are depicted in fig. 4.2. A detailed discussion, containing numerical results, can be found in [79].

[2] However, part of them still scatter only once, constituting background that is irreducible unless the modulation effects (see section 4.1.1) are taken into account [72].

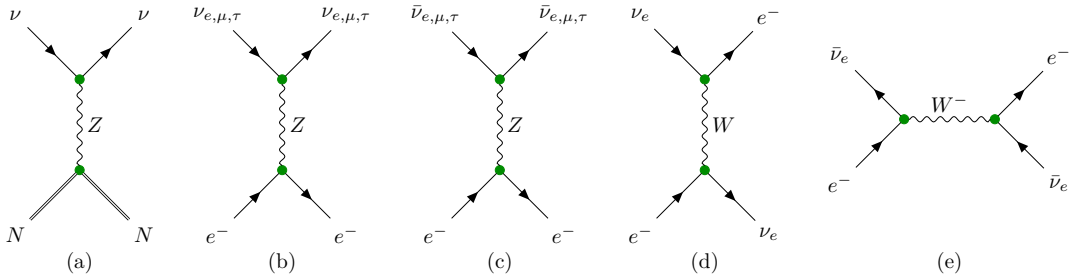


**Figure 4.2:** Diagrams representing the coherent neutrino-nucleus scattering (a) and neutrino-electron scattering (b-e) processes, constituting the neutrino floor for the DD experiments. In the diagram (a), the nucleus, denoted by $N$, is additionally distinguished by a double line.

For further details of implementation of background-reduction methods, the reader is encouraged to follow the references given in sections 4.1.6 to 4.1.8 which describe actual experiments.

### 4.1.3 Nuclear vs. electronic recoil

The DD experiments search for a signal induced by scattering of dark particles. Depending on what target the dark particle interacts with, the scattering may induce a nuclear (NR) or an electronic (ER) recoil in the detector [69]. Assuming that before and after the interaction all particles involved in the process are non-relativistic (which should be the case for cold dark matter) and the scattering is elastic, simple kinematics allows to establish a relation between the recoil energy $E_R$, the mass of the dark particle $m_{\rm DM}$, and the relative velocity $v$:

$$E_R = \frac{\mu^2\, v^2}{m_{N,e}} \left(1 - \cos\theta_{\rm cm}\right) \tag{4.2}$$

Here, $m_{N,e}$ is the mass of the target particle (either a nucleus or an electron), $\mu$ is the reduced mass of the dark particle–target system, given by

$$\mu \equiv \frac{m_{N,e} m_{\rm DM}}{m_{N,e} + m_{\rm DM}} \,, \tag{4.3}$$

and $\theta_{\rm cm}$ is the scattering angle in the CM frame, related to the angle in the laboratory frame, $\theta$, in the following way:

$$\cos\theta = \frac{m_{\rm DM} + m_{N,e}\, \cos\theta_{\rm cm}}{\sqrt{m_{\rm DM}^2 + m_{N,e}^2 + 2\, m_{\rm DM}\, m_{N,e}\, \cos\theta_{\rm cm}}} \tag{4.4}$$

The maximal recoil energy induced by an elastic NR event, obtained for a collinear scattering ($\theta_{\rm cm} = \pi$), is

$$E_{\rm NR}^{\rm max} = 2\, \frac{\mu^2\, v^2}{m_N} \,, \tag{4.5}$$

which, for a light dark particle, reduces to

$$E_{\rm NR}^{\rm max} = 2\, \frac{m_{\rm DM}^2}{m_N}\, v^2 \,. \tag{4.6}$$

The range of DM masses that can be tested via NR events is limited from below by sensitivity of the detector of interest to the nuclear recoil. As DM is expected to move relatively to the Earth with the velocity of ca. 230 km/s (see section 3.2), the minimal DM mass that can be probed through the elastic NR event involving a heavy nucleus is roughly

$$m_{\rm DM}^{\rm min} \simeq 920 \sqrt{m_N E_{\rm NR}^0} \,, \tag{4.7}$$

where $E_{\rm NR}^0$ denotes the NR sensitivity threshold.

For an electron being the target, the maximal recoil energy is independent of DM mass (assuming it is much larger than $m_e$) and equal to

$$E_{\mathrm{ER}}^{\mathrm{max}} = 2\, m_e\, v^2 \ . \tag{4.8}$$

Comparing this result with eq. (4.6) we conclude that for dark particles lighter than roughly $\sqrt{m_N m_e} \sim 0.1$ GeV the electronic recoil energy is larger than the nuclear recoil energy, making electrons a preferable target for light dark particles.

### 4.1.4 Migdal effect

Even if a given NR event is of low energy, it may induce ionization in the detector through the so-called Migdal effect [80]: the nuclear recoil is followed by a subsequent perturbation of the atomic electron cloud, possibly inducing electronic excitation (followed by deexcitation with photon emission) or ionization. This effect, which may affect electrons from inner orbitals, should not be confused with scintillation effects that appear due to interactions between atoms of the detector and affect electrons from outer orbitals only. Some of the experiments taking into account the Migdal effect in their searches are XENON [81], EDELWEISS [74] and CDEX [82].

### 4.1.5 Spin-dependent and spin-independent interactions

Interactions between the dark particles and the SM nuclei can be either nuclear-spin-independent (SI) or nuclear-spin-dependent (SD) (see sec. 3.4 of [72]). The former arise from scalar, vector and tensor couplings, while the latter from pseudo-scalar and axial-vector terms.

For the SI interaction, the cross section should be proportional to

$$\sigma_{\mathrm{SI}} \propto \left[\, Z\, f_p + (A - Z)\, f_n \,\right]^2 \ , \tag{4.9}$$

where $Z$ and $A - Z$ are the numbers of, respectively, protons and neutrons in the nucleus, while $f_{p,n}$ represents the strength of the DM-proton and DM-neutron coupling. If the momentum transfer is small, so that the internal structure of the nucleus is not accessed by the interaction, it is usually assumed that $f_p \simeq f_n$. Then, the cross section scales as $A^2$, the squared size of the nucleus. Hence, the highest chance of detection is provided by detectors employing heavy elements as the target material.

For the SD interactions, the cross section of the following form is usually assumed:

$$\sigma_{\mathrm{SD}} \propto \frac{J+1}{J} \left[\, a_p \left\langle S_p \right\rangle + a_n \left\langle S_n \right\rangle \,\right]^2 \ , \tag{4.10}$$

where $J$ is the nuclear angular momentum, $\langle S_{p,n} \rangle$ denotes the expectation value of the proton (neutron) spin and $a_{p,n}$ parametrizes the DM-nucleon coupling strength. Of course, for the SD coupling $J$ must be non-zero (otherwise, the expectation values vanish; in particular, cancelling the denominator $J$).

The nucleons are fermions of spin one half. Due to the Pauli exclusion principle, if the nucleus contains an even number of protons, their total angular momentum is zero since their spins must alternate. The same applies to an even number of neutrons. Hence, the even-even nuclei do not interact in the SD way. Consequently, only utilizing the nucleons with an odd number of protons or neutrons allows to investigate the SD interactions. This can affect the choice of detector material; e.g., this is one of the reasons using xenon is often preferred over using argon in the detectors employing liquid nobles (see the next section for details).

### 4.1.6 Ionization and scintillation detectors

Most of the DD experiments employ ionization or scintillation detectors. This section contains a short description of the most important methods utilized by those detectors, illustrated by examples.

**Liquid and gaseous detectors.** Currently, the DD experiments providing the most stringent limits on DM interactions of masses higher than a few GeV (see fig. 4.1) are those employing dual-phase noble-liquid time-projection chambers. Examples include XENON [75], LUX [83], PandaX [84], utilizing xenon as the target material, and DarkSide-50 [85], using argon. A detector of this kind consists of a tank filled to a certain level with a large amount (of the order of 100–1000 kg) of a noble liquid, while the remaining space above contains the gaseous phase. The upper and lower surfaces of the detector are covered with

photomultiplier tubes (PMTs). After a recoil event, resulting in local ionization of the liquid, part of electrons recombine, emitting a scintillation flash (denoted S1), while the remaining part, accelerated by the external electric field, enters the gaseous phase and emits the second flash (S2). The time separation between the two signals allows to determine the vertical coordinate of the event, while the horizontal coordinates are read by the PMTs. Knowing the position of the event allows to reject signals originating outside the detector's fiducial volume, possibly induced by the external radiation. The ratio between the strength of S1 and S2 enables to distinguish NR events (possibly induced by the dark particles) from ER (likely caused by $\beta$ or $\gamma$ radiation, and so constituting the background).

Utilizing xenon, the heaviest stable[3] noble gas, as a target material [86] is a popular choice due to its high mass number (increasing probability of SI interactions as described in section 4.1.5), high boiling temperature (reducing efforts required to maintain the liquid phase), and lack of radioactivity which would increase the experimental background. Moreover, as a noble gas, xenon is relatively easy to purify, so that the possible radioactive contaminants can be removed. Another advantage is transparency of the liquid xenon to the scintillation light induced by the incident particles, which facilitates spatial reconstruction of the event. Finally, using the $^{131}_{54}$Xe isotope, with an odd value of the nuclear spin, makes the xenon-based experiments sensitive to SD interactions (see section 4.1.5). On the other hand, utilizing argon instead allows for easier separation of the NR events from the ER background through the so-called pulse shape discrimination procedure [85]. A disadvantage of both methods is that they are mostly sensitive to NR events, while the ER events are likely to be induced by the background processes, so a lower limit for the mass of detectable dark particles appears as shown in section 4.1.3. Taking into account the Migdal effect, described in section 4.1.4, may allow to decrease this minimal value from several GeV to tens of MeV [81].

Another technology that utilizes liquids to seek dark particles employs bubble chambers filled with several tens to several hundreds kilograms of a superheated freon liquid. Examples are PICO [88] and MOSCAB [89], both using octafluoropropane ($C_3F_8$) as the target liquid. The sensitivity range of these experiments is similar as for those utilizing noble liquids. An advantage of this kind of experiments is the possibility of adjusting the experimental conditions (temperature, pressure and type of the liquid) in such a way that most of the background events, induced by muon scattering, $\beta$ and $\gamma$ radiation, X-rays etc., do not exceed the bubble nucleation threshold (a minimal value of energy loss per unit track length that leads to a bubble production in the superheated liquid) [90]. Another source of the background, neutron scattering events, is mostly discriminated by discarding multi-bubble events (likely for neutron and very unlikely for DM scattering) from the data.

The NEWS-G experiment [91] employs a spherical proportional counter, consisting of a copper sphere of diameter of the order of 1 m, filled with gas (whose type can be changed; among others, methane and neon have been used). The copper surface serves as a cathode, while the anode is placed on a supporting rod in the centre of the sphere. Any ionization signal is amplified by the electric field, whose strength is adjusted in such a way that detector response is proportional to the number of ionized electrons. The range of DM mass to which the experiment is sensitive is 0.1–10 GeV.

The NEWAGE detector [92] is an example of a direction-sensitive detector. It consists of time-projection chamber containing ca. 40 dm$^3$ of low-pressure (0.1 atm.) $CF_4$ gas. Low gas density makes the track of a recoiled nucleus long enough to enable determination of the recoil direction. The ionized electrons, released from the molecules as the recoiled nucleus passes through the gas, are attracted by the electric field to the readout plane where their XY position is detected. The difference in detection time between the electrons ionized at different points of the track allow to deduce the value of the third coordinate. As the recoiled fluorine nucleus is predicted to ionize the gas more efficiently right after the recoil event (when its kinetic energy is maximal), the signal-strength gradient can be used to distinguish between the start and the end of the track, finally determining the recoil direction, which can be compared with the predicted anisotropy of the signal described in section 4.1.1. Since this experiment is sensitive to NR events, it covers the DM masses above a few GeV.

**Solid detectors.** Detectors used in room-temperature scintillation experiments, like DAMA/LIBRA [93], ANAIS [94], COSINE-100 [95], consist of multiple cylindrical crystals of thallium-activated sodium iodide, NaI(Tl), acting as scintillators, with PMTs attached to both sides. The total mass of such a detector is of the order of several hundreds of kilograms. To reduce the background, events inducing a scintillation flash in more than one crystal (multiple-hit events) are rejected, as dark particles are

[3] Two naturally occurring long-lived radioactive isotopes of Xe are $^{136}$Xe and $^{124}$Xe, with half-life time of $2.17 \times 10^{21}$ y and $1.8 \times 10^{22}$ y, respectively [86,87]. The two-neutrino double electron capture of $^{124}$Xe is the rarest process ever observed.

unlikely to cause them, in contrast to the neutron, $\beta$ and $\gamma$ background. These experiments should enable detection of dark particles of masses higher than 1 GeV.

In 2013, the DAMA/LIBRA experiment gained attention by announcing [96] annual modulation of observed rate of single-hit events (i.e., with a flash in only one crystal), which should be a clear evidence of DM interactions, as explained in section 4.1.1. That result, however, could not have been undoubtedly reproduced by other experiments and seems to be a residue of the chosen method of statistical analysis [97].

Another type of solid detectors are CCD ionization detectors, employed in, e.g., DAMIC [73], SENSEI [98] and DMSQUARE [71] experiments. Due to their extreme sensitivity, those detectors aim to detect low-mass DM particles. The utilized silicon charge-coupled devices (CCDs) are sensitive to ionization signals even at the single-electron level, which makes the experiments able to seek dark particles as light as 1 MeV. The CCD patterns are divided into pixels, which enables background reduction: as scattering of a dark particle should induce well-localized ionization (the track length of the recoiled particle should be much shorter than the pixel size), with energy deposition less than 10 keV of electron equivalent, multi-pixel-cluster events of higher energies are discarded. DMSQUARED focuses on searching for a daily-modulated signal, see section 4.1.1 for a brief discussion.

Some experiments, like CoGeNT [99] or CDEX [82, 100], utilize the so-called p-type point-contact germanium detectors of active mass of the order of 100 g, sensitive to sub-keV recoil energies. Such detectors are based on germanium diodes. A recoil event is expected to generate an electron-hole pair, which is then detected by external electrodes. These detectors can probe dark particles heavier than a few GeV.

### 4.1.7 Cryogenic calorimeter search

The cryogenic calorimeter method, employed in, e.g., SuperCDMS [101], CRESST [102] and EDELWEISS [74] experiments, utilizes solid cryogenic detectors consisting of one or more crystals (germanium for EDELWEISS and SuperCDMS; silicon, $CaWO_4$, $Al_2O_3$ or $LiAlO_2$ for CRESST). Attached to each crystal is a transition edge sensor, a high-precision thermometer maintained nearby the critical temperature (for example, the critical temperature of $\alpha$-tungsten used in sensors of the CRESST detector is 15 mK). In such conditions, any temperature bump induced by energy deposition in the detector causes a proportional increase of continuously measured sensor resistance. Detectors of this kind are sensitive to energy deposition even at the level of 10 eV (in the case of CRESST using a 0.35 g Si crystal as a target), which means they should be able to detect dark particles as light as 0.1 GeV. To facilitate distinguishing between ER and NR events, an additional light detector can be used to detect photons produced in ER events. The SuperCDMS and EDELWEISS experiments combine calorimetric search with ionization measurements performed similarly to the way it is done in the aforementioned CoGeNT and CDEX experiments.

### 4.1.8 Some novel methods

**Directional solid detectors.** The proposed NEWSdm [70] experiment, sensitive mainly to 10–100 GeV WIMPS, is going to utilize thin layers of a gelatin nuclear emulsion containing tiny silver bromide (AgBr) crystals. A recoiled nucleus passing through the emulsion changes the structure of the crystals in a direction-dependent way. After exposition, the layers have to be developed and checked for a signal. What complicates the experiment is the fact that after the emulsion is produced, it accumulates signals *constantly* until it is developed. Hence, to reduce the time of unshielded measurement, the machines used to produce and develop the emulsion layers must be placed as close to the experimental site as possible. Indeed, during the demonstration run in 2022, they have been installed in hall F of Gran Sasso complex, while the experiment has been performed in hall C.

The PTOLEMY experiment [103], aiming to detect dark particles of masses in the MeV–GeV range, is proposed to employ stacked graphene monolayers as the target, each of them forming a field-effect transistor with the substrate underneath. As a result of an ER event, an electron should be ejected from the layer, and then caught by another layer or a calorimeter placed at the boundary of the detector. Removal or addition of an electron from the graphene layer would affect conductivity of the transistor, constantly measured. The sheets would be divided into pixels, enabling 3D determination of ejection and acceptance events, thus providing a method to determine recoil direction, making the detector sensitive to the signal anisotropy. Measuring time between both impulses allows to deduce the electron velocity, while the calorimetric readout is an additional test of kinematics.

**Paleo-detectors.** The idea of mineral paleo-detectors [104] bases on the fact that the detector exposure, which should be as large as possible to collect efficient amount of DM-induced signal, can be increased in two ways: by expanding the detector size or by extending the exposure time. As construction and maintenance of a detector heavier than several tonnes may be troublesome due to large costs and difficult signal analysis, the latter possibility should be considered.

The naturally occurring minerals can be treated as detectors with the exposure time reaching the Gyr scale, making a 1 kg specimen equivalent to a thousand-tonne detector operating for a millennium. However, the main disadvantages of natural crystals (in contrast to those produced in laboratory) are: chemical impurity, presence of natural radioactive isotopes, and heterogeneous crystal structure. Those properties increase the amount of the background processes and impede analysis of the specimens. To reduce the impact of those obstacles on the potential experiments, the detector material has to be carefully selected. One of the proposed target minerals is muscovite mica due to its perfect basal cleavage and transparency, facilitating readout of the samples. Some other candidates include nchwaningite, halite, epsomite, nickelbischofite and olivine; all of them occurring in marine evaporite deposits and ultra-basic rocks, characterized by low concentration of radioactive isotopes and shielded by the surrounding rock against external radiation.

An attractive feature of such experiments is that examining specimens of various ages may provide an access to the possible signal modulation corresponding to the motion of the Sun around the Galactic centre, see section 4.1.1.

## 4.2 Astrophysical search

As it is clear from the previous section, direct detection of dark particles poses serious difficulties. Moreover, if the local DM density is for some reason much lower than usually assumed, DD experiments may not provide positive conclusions at all.

Another direction of DM searches are astrophysical observations. If the dark particles are able to produce SM content in their interactions, the products could be detectable. A signal is expected from regions where gravitational attraction induces high concentration of DM. Those include centres of dwarf galaxies, centre of the Milky Way, accretion disks, or celestial bodies (stars and planets).

The search focusing on the first three possibilities is called indirect detection (ID). The first possibility is especially promising due to high signal-to-background ratio. Contrary, the signal from the Galactic centre would be highly noised by millisecond pulsars.

Regarding the last possibility, due to large nucleon density, stars and planets may serve as giant DM detectors, capturing the dark particles like the Earth-based detectors do. Hence, although belonging to astrophysical search, experiments investigating this kind of signals contribute to DD limits.

### 4.2.1 Gamma-ray search: Fermi-LAT and Cherenkov detectors

The most popular type of ID experiments seeks gamma rays produced in DM-annihilation processes like those depicted in fig. 4.3. The advantages of such experiments include low background at the super-GeV range, good development of methods of photon detection, and directionality of the experiments which enables to focus on regions of expected high concentration of DM.

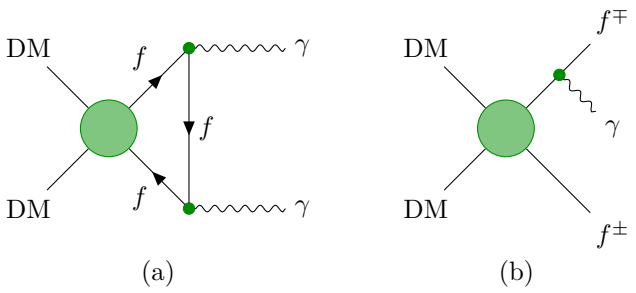


**Figure 4.3:** Exemplary DM-annihilation processes with photon production; $f$ denotes an SM fermion.

Among the potential astrophysical sources of the DM signal, the most important are the dwarf spheroidal satellite galaxies of the Milky Way and the Galactic centre [69, 105]. The dwarf spheroidal

galaxies are believed to be dominated by the DM contents, with only a small amount of the baryonic matter, which reduces the amount of poorly-known background caused by production of the gamma rays in the SM processes. The small distance between the satellite galaxies and the Milky Way makes the expected gamma flux still large at the detectors. On the other hand, the Galactic centre, being close to the Earth and probably characterized by a large concentration of DM, should provide the most powerful ID signals available [106]. Unfortunately, its baryonic content also strongly radiates (in the range between long radio wavelengths to hard X-rays except the 1 $\mu$m–1 nm band due to so-called extinction caused by the dust in the Galactic plane [107,108]), so the signal-to-background ratio is probably worse than in the previous case.

Since the gamma rays are blocked to a large extent by the Earth's atmosphere, ground-based telescopes cannot observe then directly. Instead, the gamma radiation can be detected by space telescopes (for example, Fermi-LAT described below) operating outside the atmosphere. Unfortunately, installing a detector on the orbit is a complicated and expensive task, with costs increasing proportionally to the detector's mass. For this reason, the data-collecting surface of the currently operating space gamma telescopes is limited to the values of the order of $m^2$. Another method employs arrays of ground-based detectors of Cherenkov radiation induced by relativistic charged particles that are produced when highly energetic photons reach the atmosphere. Examples include H.E.S.S., MAGIC and VERITAS, see below.

When combined, searches performed by multiple detectors operating at similar energy scales are more sensitive than each of the experiments separately. Nevertheless, no convincing gamma-ray signal attributed to DM annihilation has been observed so far [109]. Figure 4.4 presents the current limits on the rate of DM annihilation into $b\bar{b}$ and $\tau^+\tau^-$ pairs (those two channels are treated as representative in ID studies, as they exemplify signals of quark and lepton nature). The following part of this section describes the aforementioned experiments that provided the data used to create the plots in fig. 4.4.

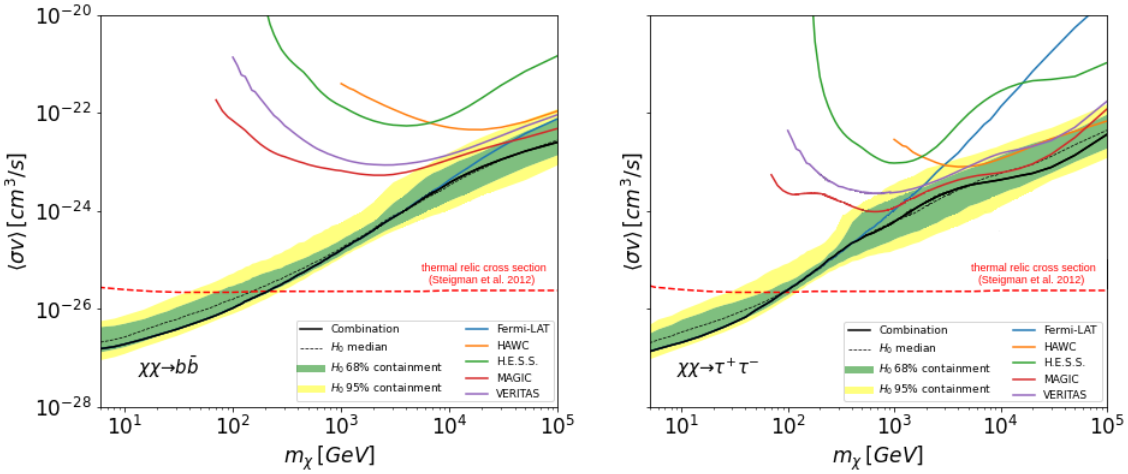


**Figure 4.4:** Upper limits on thermally averaged cross section for annihilation of dark particles (denoted by $\chi$) into $b\bar{b}$ (left) and $\tau^+\tau^-$ (right) pairs, as a function of the mass of the dark particle. The limits have been obtained by the Fermi-LAT (blue), HAWC (orange), H.E.S.S. (green), MAGIC (red) and VERITAS (violet) experiments. The black line represents combined limits, while the red dashed line corresponds to the value of cross section that leads to the correct value of the DM relic density, as calculated in [110]. For dark particles lighter than $10^3$ GeV, the most stringent constraints are imposed by the results of Fermi-LAT. Plots from [109].

**Fermi-LAT.** So far, the most stringent limits on DM annihilation into SM fermion pairs have been imposed by Fermi-LAT [111] observations of the gamma rays from nearby dwarf spheroidal galaxies. This experiment employs a pair-conversion gamma-ray telescope of almost 1 $m^2$ of effective area, divided into a 4×4 array of 16 modules. Each module consists of two layers: a precision converter-tracker above and a calorimeter beneath. The tracker (see fig. 4.5) is a stack of 19 trays, each containing two layers of silicon strip detectors, performing the readout in perpendicular directions. Each of the top 16 trays is preceded by a tungsten plane, whose purpose is to convert the incident gamma rays into $e^+e^-$ pairs. The tracker module, measuring position and time of subsequent readouts of the induced $e^+e^-$ pair, determines the momentum of the incident photon, while the calorimeter placed below the tracker measures the total energy of the secondary particle shower. To reduce the background caused by charged particles hitting

the device, a surrounding anticoincidence detector is used, which consists of plastic scintillator tiles and PMTs collecting the flashes. The telescope is sensitive to gamma rays of energies of ca. 20 MeV–300 GeV.

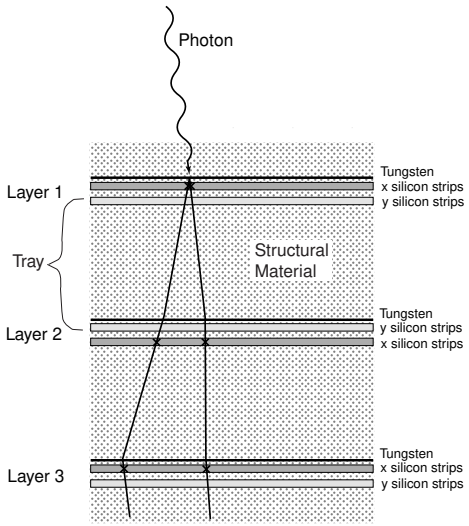


**Figure 4.5:** The structure of the tracker modules of Fermi-LAT, based on [112]. On one of the tungsten conversion planes, the incident photon is converted into an $e^+e^-$ pair. Directions of the particles are determined by the silicon strips and the total energy is measured by the underneath calorimeter, so that the photon's momentum can be reconstructed.

In 2009, an excess of the gamma radiation from the Galactic centre, with energy peak around 1–5 GeV, has been observed [106]. Annihilation of DM of mass around 30–50 GeV has been proposed as an explanation, but an alternative proposal suggests nearby pulsar as the source. Currently, both interpretations are still under discussion [113]. Figure 4.6 presents the excess and a possible fit of DM-induced signal.

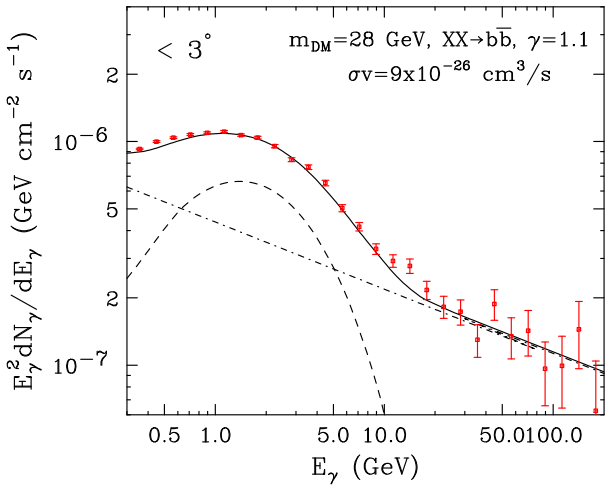


**Figure 4.6:** The excess of gamma rays produced in the region within $3^o$ from the Galactic centre [106]. The red points are the measured values of energy, while the dashed line corresponds to a theoretical signal of dark matter annihilation (mass and cross section are provided in the plot). The dash-dotted line represents the contribution of the astrophysical sources known at the time of publication (2009), and the solid line is the combination.

**Cherenkov telescopes.** The ground-based atmospheric Cherenkov detectors consist of arrays of telescopes observing atmospheric Cherenkov light, emitted by the atmospheric showers of charged particle

induced by incident gamma photons. Utilizing multiple telescopes allows for stereoscopic reconstruction of the gamma-induced showers. The examples described here are the H.E.S.S., MAGIC and VERITAS detectors. The H.E.S.S. detector [105] consists of five Cherenkov telescopes, four of them, having diameter of 12 m, placed at the corners of a 120 m × 120 m square, and the fifth one, of diameter 28 m, at the centre. The detector is sensitive to DM masses of ca 100 GeV–20 TeV. The MAGIC [114] instrument involves two telescopes of 17 m diameter, sensitive to energies between tens of GeV and tens of TeV. The VERITAS [115] experiment employs four telescopes, each of ca. 100 $m^2$ data-collecting area, observing gamma rays of energies of 100 GeV–100 TeV.

Another method is utilized by the HAWC experiment [116], being an array of 300 water Cherenkov detectors. Each of them, having diameter 7.3 m and depth 4.5 m, is filled with almost $2 \times 10^5$ l of purified water. Like H.E.S.S., MAGIC and VERITAS, the detectors register gamma-induced showers of relativistic charged particles. The gamma rays detected by HAWC are of 1–100 TeV of energy.

### 4.2.2 Antiparticle-oriented search

Apart of photons, the DM searches can focus on positrons and other antiparticles possibly produced in DM-annihilation processes, which results in excess of cosmic rays in the form of antimatter. Indeed, such an excess (see fig. 4.7), peaked around 300 GeV of positron energy, has been observed in several experiments [117], including Fermi-LAT (which has appeared to be sensitive not only to gamma radiation, but to this type of signature as well [118]) and cosmic-ray telescopes: satellite-borne AMS [119] and PAMELA [120], and balloon-borne CAPRICE [121], MASS [122] and HEAT [123]. The excess could be explained by annihilation of dark particles of mass around 500 GeV, with the annihilation rate $\langle \sigma v \rangle = 4 \times 10^{-24}$ cm$^3$/s [124]. This value, much greater than $(2\text{–}3) \times 10^{-26}$ cm$^3$/s corresponding to the correct relic density of a classical WIMP DM [110], may suggest self-interacting DM as a source. However, an alternative explanation interprets the excess as produced by the nearby young pulsars [125] (similarly as in the case of the Galactic-centre gamma excess mentioned in section 4.2.1).

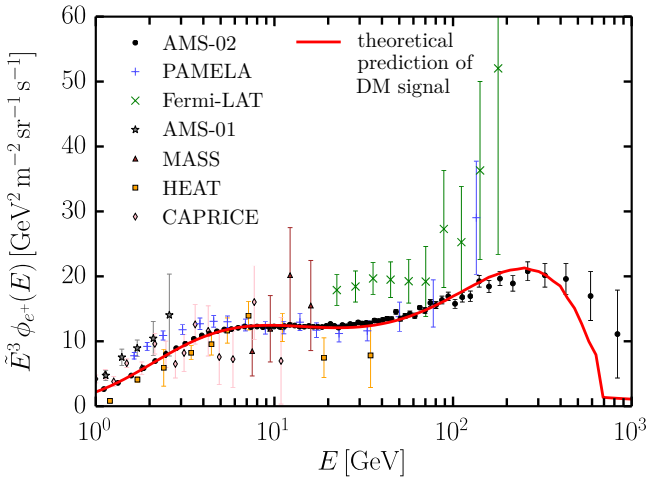


**Figure 4.7:** The positron flux measured by AMS-02 (black dots) and other experiments [117]. The red line correspond to a theoretically predicted flux caused by dark matter of annihilation rate $\langle \sigma v \rangle = 4.63 \times 10^{24}$ cm$^3$/s and mass $m_{\mathrm{DM}} = 780$ GeV.

The detectors employed in the aforementioned experiments (see fig. 4.8 for a scheme of the AMS-02 detector) consist of several types of modules (not every detector contains all of them):

- A **transition radiation detector** measures the energy of the radiation emitted by the incident charged particle passing between layers of different media. Knowing the energy-loss profile of the particle, it is possible to distinguish electrons and positrons from hadrons.
- A **tracking system**, consisting of layers of silicon strip detectors, placed inside a magnetic coil. The momentum-to-charge ratio (also called rigidity) of the particle is deduced from the way its trajectory bends in the magnetic field.
- A **calorimeter** measures the energy.

- A **time-of-flight hodoscope**, consisting of scintillator layers separated by a certain distance, determines velocity (value and direction).
- A **Cherenkov detector** performs charge- and velocity-dependent measurements.

Combined, the measurements of all the modules allow to determine the mass, charge, energy, and velocity vector of the detected particle.

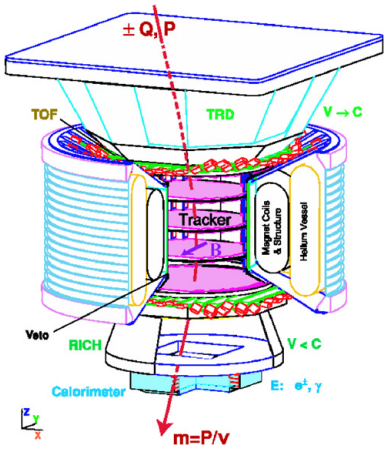


**Figure 4.8:** Scheme of the AMS-02 detector [119]. TRD is the transition radiation detector, TOF denotes the time-of-flight plate, RICH is the ring imaging Cherenkov counter (see the text for description). The red line represents the track of the detected particle.

Searching for antinuclei originating from DM annihilation has also been proposed. For example, the GAPS experiment [126] is going to search for antideuterons.

### 4.2.3 Neutrino astronomy

Neutrino telescopes can participate in DM searches by looking for neutrinos produced in DM-annihilation processes, e.g., the one depicted in fig. 4.3 (b), with $f^-$ being a virtual SM lepton subsequently decaying into a $W^-\nu$ pair. As it is with the gamma-ray and cosmic-ray searches, the highest signal is expected to be emitted from the objects locally increasing the concentration of DM, e.g., the Galactic centre, stars (including the Sun) or planets (including the Earth).

Neutrino detectors observe Cherenkov light emitted by relativistic charged particles, whose motion has been induced by neutrinos passing through the used medium. As all the neutrino detectors listed below are Earth-based (i.e., not satellite-borne), the atmospheric muons produced by cosmic rays reaching the atmosphere form most of the experimental background. The background reduction can be achieved by rejecting signals induced by particles going downwards (i.e., from the sky), keeping those directed upwards, which have passed through the Earth. Unfortunately, that method cannot significantly reduce another type of background, caused by the atmospheric neutrinos. Their flux is, however, well-studied, which allows to subtract them from the observed signal [127].

Some of the neutrino experiments that are partially focused on DM searches are IceCube [128], ANTARES [129] and KM3NeT (under construction) [127], each of them employing an array of PMTs attached to 100-1000 m strings suspended in the sea (ANTARES, KM3NET) or within the Antarctic ice (IceCube). The size of the arrays is of the order of $(100–1000\ \mathrm{m})^3$, which allows to reconstruct the direction of the signal. Another type of neutrino detectors able to search for the dark particles include Super-Kamiokande [130] and its successor, Hyper-Kamiokande (under construction) [131,132], consisting of a cylindrical tank filled with water (50 kt for Super-Kamiokande, 258 kt for Hyper-Kamiokande), whose internal surface is covered with PMTs. The IceCube, ANTARES and KM3NeT experiments are mostly oriented towards detection of Galactic neutrinos, while Super- and Hyper-Kamiokande focus on analysis of the solar neutrinos, however all of them are able to perform both types of measurements. The most stringent limits on DM annihilation rate imposed by the neutrino telescopes are presented in fig. 4.9.

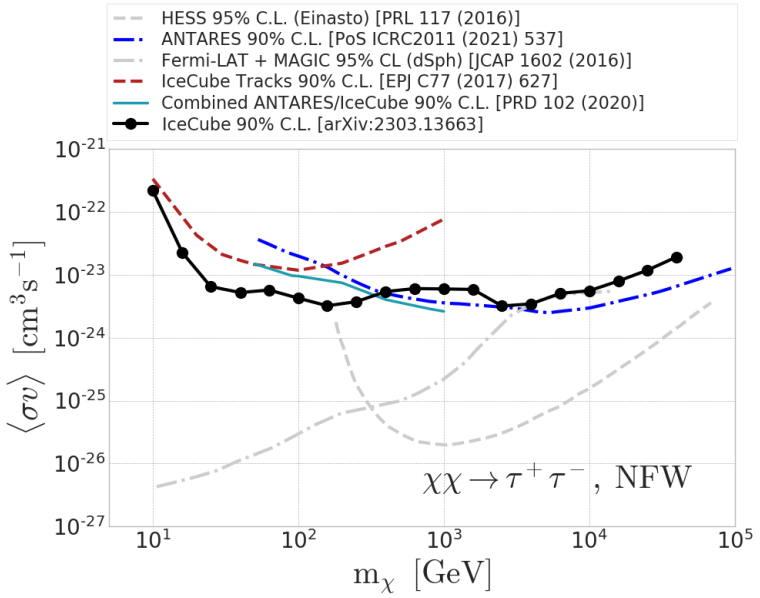


**Figure 4.9:** Upper limits on thermally averaged cross section for annihilation of dark particles (denoted by $\chi$) into a $\tau^+\tau^-$ pair, as a function of the mass of the dark particle, imposed by the null-results of the following experiments: neutrino-oriented IceCube (dashed red, solid teal, solid-with-points black) and ANTARES (dot-dashed blue, solid teal); and gamma-ray-oriented H.E.S.S. (dashed gray), MAGIC and Fermi (dot-dashed gray). Plot from [128].

While the DM-capture rate of the supermassive black hole in the Galactic centre should be governed mostly by the gravitational interaction, the capture rate of stars and planets is affected by the DM-nuclei interactions. Thus, in particular, the experiments measuring the flux of solar neutrinos are an additional source of DD limits. Basing on [133], let us show how the DM annihilation rate in the Sun, $\Gamma_A$, limited by measurements of the neutrino flux, can be related to the capture rate, $C_C$. The number of dark particles within the Sun, $N$, evolves with time according to

$$\dot{N} = C_C - C_A\, N^2 - C_E\, N\ , \tag{4.11}$$

where $C_C$, $C_E$ and $C_A \equiv 2\,\Gamma_A/N^2$ are assumed to be $N$-independent. For the Sun, the term containing $C_E$, describing evaporation of the dark particles, can be neglected. Then, the solution of this equation is

$$N(t) = \sqrt{C_C/C_A}\,\tanh \omega\, t\ , \tag{4.12}$$

where $\omega \equiv \sqrt{C_C C_A}$, and the current value of $t$ is the age of the Sun. As $t$ grows, the hyperbolic tangent tends to one. In the limit, equilibrium is reached and $N$ becomes constant. Then, from eq. (4.11) it follows that

$$\Gamma_A = \frac{1}{2}\, C_C\ , \tag{4.13}$$

so the neutrino production rate, determined by $\Gamma_A$, is related to the capture rate that depends on the cross section for the DM-nucleon scattering. After further calculations, it eventually appears that the cross section is proportional to the neutrino flux, with the proportionality constant dependent on DM mass. Currently, the limits on the DM-nucleon interactions obtained in this way [130] are still weaker than those presented in section 4.1, but this may change after the Hyper-Kamiokande is built.

### 4.2.4 Heating effect of DM interactions inside celestial bodies

Dark matter captured by celestial bodies, such as stars and planets, may interact with the matter forming them or annihilate into SM particles, thus transferring its energy to those bodies. Using the relation eq. (4.13), one can estimate the energy transfer through the annihilation process to be $E = C_C\, m_{\rm DM}$, where $C_C$ is the capture rate and $m_{\rm DM}$ denotes the mass of the dark particle [134]. This may significantly

heat up the body of interest. Predictions concerning that heating have to be confronted with the known planetary heat flow data.

That mechanism has been discussed in the context of the Earth [134], as well as Uranus, Neptune and hot Jupiter exoplanets [135], and could explain the unusually small heat production of Uranus in comparison to the other gas giants: the collision with a supermassive impactor, believed to have tilted the rotational axis of Uranus 98 degrees with respect to the planetary plane, could have knocked Uranus out of its local DM cloud, depriving the planet of the DM-induced heat production.

The constraints on the DM-nucleon interaction cross section, deduced from the heat balance of the Earth, are presented in fig. 4.10.

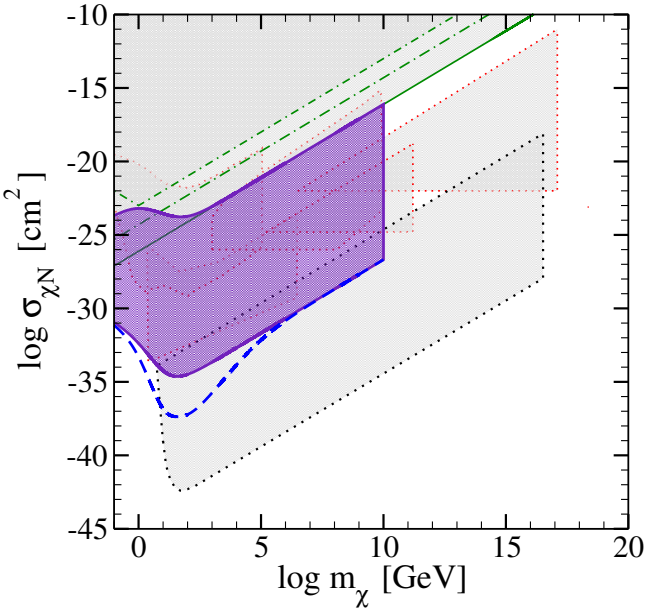


**Figure 4.10:** The purple shading indicates the region in which the predicted heat production caused by DM interactions would contradict the observed heat balance of the Earth. Plot from [134].

## 4.3 Collider searches for DM

If there exists a mechanism of particle interaction between DM and the baryonic matter, the dark particles could be not only detected in the DD and ID experiments, but also produced at colliders. Below, the expected signatures of DM production at colliders are described (section 4.3.1) and the current constraints imposed by the LHC measurements are presented (section 4.3.2). Section 4.3.3 discusses strengths and weaknesses of different types of colliders in the context of DM searches, with a particular emphasis on the future $e^+e^-$ colliders.

### 4.3.1 Expected signatures

Searching for DM at colliders is based on the two main approaches described below: the missing-energy analysis and looking for extra resonant peaks [136].

If the total energy of the observed collision products is distinctly lower than the total collision energy, the missing part could have been taken away by invisible states, including dark particles (see fig. 4.11). Unfortunately, production of the SM neutrinos provides exactly the same experimental signature, constituting the background. The analysed signatures of this type include missing energy produced in association with the so-called mono-states: a jet, a photon, a $Z$ boson, a top quark, a Higgs boson, or a $t\bar{t}$ pair. As the energy of the collision products emitted along the beam axis cannot be measured, the actual observed signature is the momentum imbalance along the transverse directions, called missing transverse energy or missing transverse momentum.

As an example, chapter 6 discusses the mono-$Z$ signature of DM production at the future $e^+e^-$ colliders in some detail, focusing on differences between signatures of DM of different spins.

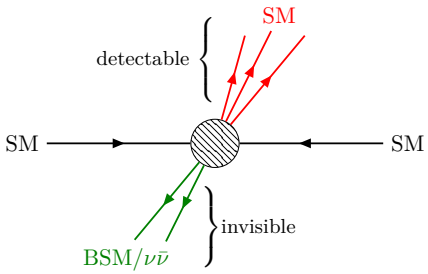


**Figure 4.11:** Collision of the SM particles may result in associate production of invisible states, including neutrinos and dark particles. This event would be observed in the detector as a missing-energy event, in which the total energy of detected collision products is smaller then the collision energy.

In the second method, the signature of BSM physics would be an unexpected enhancement of the measured cross section for a given SM→SM collision process. If the process can be mediated by a BSM particle, the energy of the observed enhancement could correspond to the mass of the mediator allowed to be on its mass shell, as shown in fig. 4.12. The standard way to seek this signature is to reconstruct the invariant mass of jets produced in the so-called dijet events.

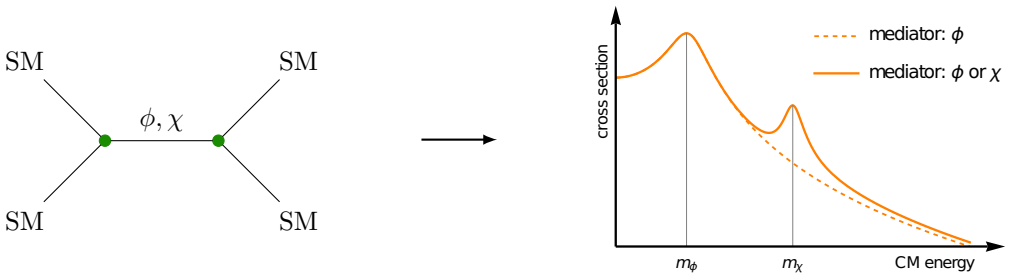


**Figure 4.12:** An exemplary SM→SM process mediated by an SM particle $\phi$ or a beyond-SM particle $\chi$. **Left:** Feynman diagram, **right:** cross section as a function of the CM energy. In the plot, the dashed line is the SM prediction while the values represented by the solid line include contribution of the $\chi$-mediated diagram. A BSM mediator can induce an unexpected resonant enhancement of the cross section at collision energy equal to $m_\chi$.

### 4.3.2 Current constraints from the LHC

So far, there are no signals of DM production at existing colliders. Consistency of the missing-energy measurements with the SM predictions is interpreted dependently on the assumed model of invisible particle production. In the case of the Higgs-portal DM models, the most important results are the limits on the invisible Higgs branching ratio and on the scalar-sector mixing angle. Currently, the most stringent 95% C.L. limit on the invisible branching ratio is $\mathrm{BR}(H \to \mathrm{inv}) < 0.107$, provided by the ATLAS collaboration [137]. To obtain numerical results presented in chapter 6, a value of $\mathrm{BR}(H \to \mathrm{inv}) < 0.19$, obtained by the CMS experiment [138], has been used. Figure 4.13 presents examples of ATLAS and CMS missing energy analysis. Due to its relevance for chapter 6, the mono-$Z$ case has been chosen as an illustration.

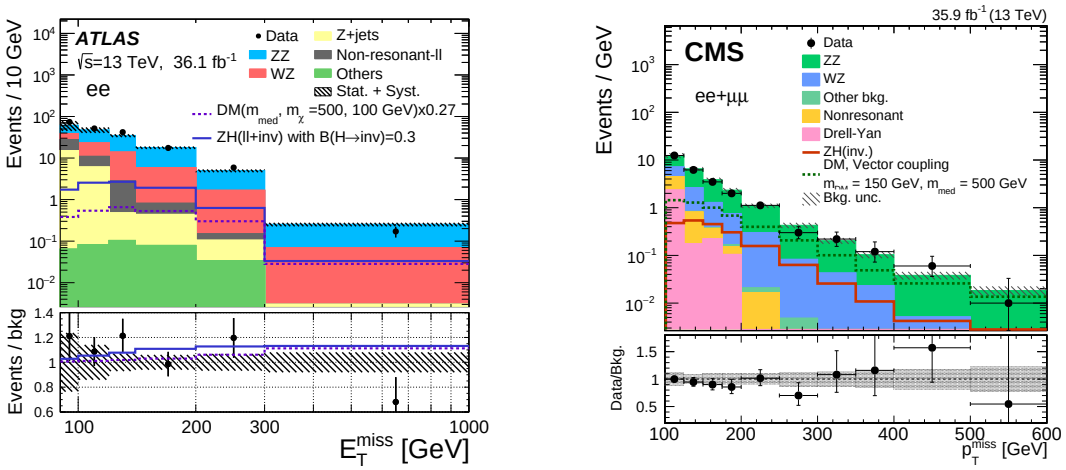


**Figure 4.13:** Atlas [139] and CMS [140] results for $pp \to ll+$inv. events, a signature for $pp \to Z+$DM process. Bands of different colors denote different kinds of background caused by production of the SM bosons decaying to neutrinos. The solid line represents a simulated signal of $pp \to Z + H(\text{DM})$ process, with $\text{BR}(H \to \text{inv}) = 0.3$. No excess over the SM background has been observed.

Lack of extra resonant enhancement of the $pp \to$ dijet processes provides limits on the coupling strength between the mediator and the SM quarks, see fig. 4.14.

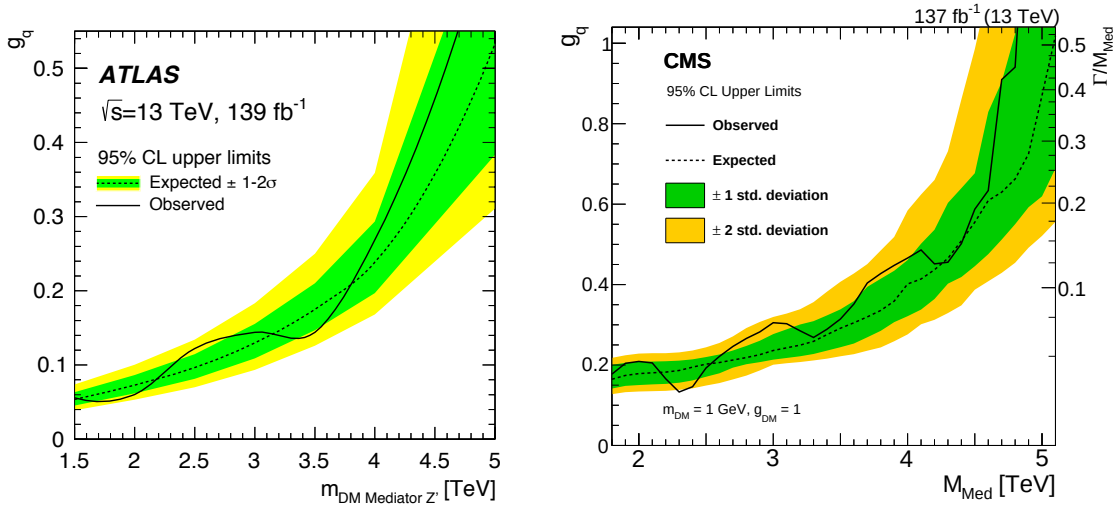


**Figure 4.14:** ATLAS [141] and CMS [142] limits on coupling strength between a dark mediator and quarks in the so-called leptophobic $Z'$ model [143].

### 4.3.3 Strengths and weaknesses of different types of colliders

In order to enable a collider discovery of DM, a perfect device should be characterized by a high luminosity, low background, and the collision energy high enough to produce potentially heavy dark particles. Unfortunately, the better the detector of interest satisfies one of those requirements, the worse its performance is regarding at least one of the other two properties. Hence, the best strategy would be to utilize multiple colliders performing complementary measurements.

**Hadron vs. lepton colliders.** The hadron colliders generally operate at higher energies, making the production of DM easier, especially if the dark particles are heavy. However, since hadrons participate in the strong interactions and have a complex structure, colliding them provides huge amounts of background. Moreover, as the momentum of a given hadron is distributed among the constituting partons, the precise values of the components of the collision momentum vector are to a large extent unknown, which

makes the missing-energy analysis a challenging task. On the other hand, colliding leptons do not interact strongly, which significantly diminishes the number of possible outcomes, reducing the background. At the same time, energies of colliding leptons are much better defined than in the case of hadronic collisions. Thus, lepton colliders seem to be the right tool for DM searches.

**Circular vs. linear colliders.** Another possibly important factor, discussed in, e.g., [144], is the shape of the collider. In general, the luminosity of linear colliders increases with beam energy, which facilitates obtaining larger number of interesting events if the particles of interest will appear to be heavy. Moreover, linear machines are easy to upgrade to higher energies, since it basically requires simple elongation. Circular colliders seem to be a better choice at smaller energies, as their luminosity at this range is larger than at linear colliders, while dropping above ca. 350–400 GeV due to synchrotron radiation.

Another feature of the linear colliders is that they can be easily adapted to produce longitudinally polarized beams, consisting predominantly of particles of given chirality.[4] Among other advantages, discussed in sec. 5.3 of [147], this allows to reduce the experimental background, suppressing processes in which the electron and the positron scatter exchanging a $W^{\pm}$ boson (see fig. 4.15). Obtaining longitudinally polarized beams at circular colliders requires much more effort, as due to the so-called Sokolov-Ternov effect, emission of the synchrotron radiation is likely to reorient the electron spin parallel to the external magnetic field, causing the beam to be mostly (the asymptotic value is 92.3%) transversally-polarized [148].

Figure 4.16 presents the relation between the collision energy and the luminosity for the planned future $e^+e^-$ colliders. It can be observed that the luminosity of circular colliders decreases with energy, while for linear collider the opposite is true.

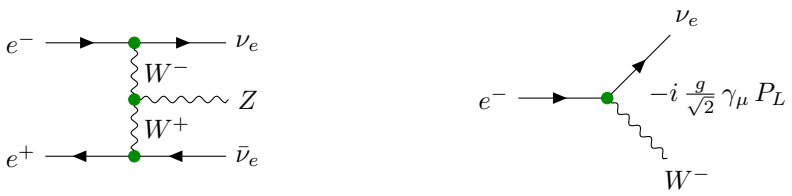


**Figure 4.15: Left:** an exemplary process of electron-positron scattering (with production of $Z$ boson) that can be suppressed if polarized beams are used. **Right:** the relevant Feynman vertex. If the electron is right-handed, the projection operator $P_L$ acting on the corresponding field gives 0. Physically, this corresponds to the fact that the SM neutrinos are left-handed only.

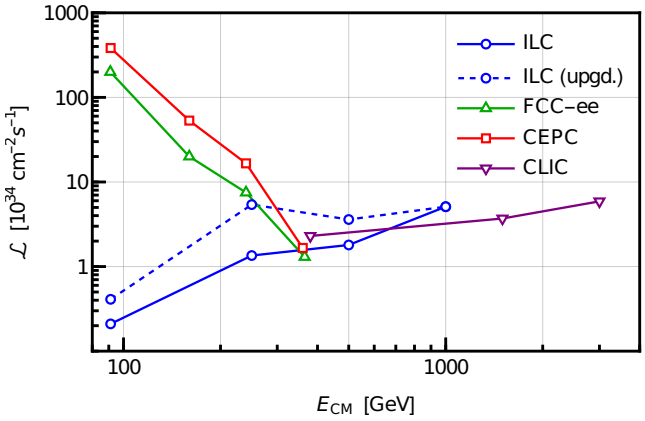


**Figure 4.16:** Luminosity of the proposed future $e^+e^-$ colliders: ILC, FCC-ee, CEPC, CLIC, as a function of collision energy. Luminosity of the circular colliders, FCC-ee and CEPC, drops with energy, while for the linear colliders, ILC and CLIC, the opposite holds. Data from [147, 149–151].

[4] Strictly speaking, the method that will be used to produce a polarized beam (that is, illuminating a photocathode with a circularly polarized laser light, see [145]) enhances production of electrons of given *helicity*, not chirality. However, at energies achieved at the collider, electrons are ultra-relativistic and chirality is almost fully determined by helicity [146].

**Future lepton colliders.** The most established proposals of future lepton colliders are: linear ILC [147] and CLIC [149], and circular FCC-ee [150] and CEPC [151]. Other concepts, focusing on novel techniques that could improve performance and lower power consumption, include $C^3$ [152], CERC [153] and ReLiC [154]. Table 4.1 collects the most relevant characteristics of the described colliders, while fig. 4.16 shows their luminosity as a function of the collision energy.

The colliders are going to operate at various CM collision energies. The most popular physically-motivated values (a brief discussion can be found, e.g., in sec. 5.1 of [147]) are (approximately):

- 91.2 GeV, the $Z$ pole, corresponding to $s$-channel processes mediated by the on-shell $Z$ boson;
- 160 GeV, the $W^+W^-$ production threshold;
- 240 GeV, the $HZ$ production peak;
- 350 GeV, the $t\bar{t}$ production threshold;
- 400+ GeV, where $W^+W^-$ fusion process ($e^+e^- \to H\nu_e\bar{\nu}_e$) dominates the $HZ$ production;

Indeed, all the future $e^+e^-$ colliders present in table 4.1 cover one or more of these values.

| collider | type | length[a] [km] | beam pol.[b] [% $e^-$/% $e^+$] | $E_{\mathrm{CM}}$ [GeV] | $\mathcal{L}$[c] [$10^{34}$ cm$^{-2}$s$^{-1}$] | $\int \mathcal{L}\,dt$ [ab$^{-1}$] | run time [yr] | source |
|---|---|---|---|---|---|---|---|---|
| ILC | linear | 20.5–40 | 80/30 | 91.2 | 0.21/0.41 | 0.1 | 1.5 | [147] |
| | | | | 250 | 1.35/5.4 | 2.0 | 11 | |
| | | | | 500 | 1.8/3.6 | 4.0 | 9 | |
| | | | | 1000 | 5.1 | 8.0 | 10 | |
| CLIC | linear | 11.4–50.1 | 80/0 | 380 | 2.3 | 1.5 | 8 | [149] |
| | | | | 1500 | 3.7 | 2.5 | 7 | |
| | | | | 3000 | 5.9 | 5.0 | 8 | |
| FCC-ee | circular | 91.2 | – | 91 | 400 | 192 | 4 | [150] |
| | | | | 160 | 40 | 6–12 | 1–2 | |
| | | | | 240 | 15 | 5.1 | 3 | |
| | | | | 365 | 2.6 | 1.7 | 5 | |
| CEPC | circular | 100 | – | 91.2 | 191.7 | 100 | 2 | [151] |
| | | | | 160 | 26.6 | 6 | 1 | |
| | | | | 240 | 8.3 | 20 | 10 | |
| | | | | 360 | 0.83 | 1 | 5 | |
| $C^3$ | linear | 8 | 80/0 | 250 | 1.3 | 1.0 | 10 | [152] |
| | | | | 550 | 2.4 | 4.0 | 10 | |
| CERC[d] | circular | 100 | – | 240 | 78 | ? | ? | [153] |
| ReLiC[d] | linear | 20 | ? | 240 | 343 | ? | ? | [154] |
| LEP[e] | circular | 26.7 | – | 202 | 0.01 | $2.5 \times 10^{-4}$ | 1 | [155] |

[a] For circular colliders: circumference. Wherever a range is provided, the lower value denotes the initial length, possibly extensible up to the higher value.
[b] Longitudinal polarization, defined as in [156], provided for linear colliders only.
[c] Per interaction point, if there are more than one. If two values are provided, smaller of them is the initial one, while the larger value is planned to be achieved after an upgrade.
[d] The 240 GeV mode.
[e] The 1999 run.

**Table 4.1:** The most relevant parameters of the proposed future $e^+e^-$ colliders. For comparison, the value corresponding to the 1999 run of LEP, the most powerful $e^+e^-$ collider already built, have been provided.

Besides the $e^+e^-$ devices, muon colliders have also been proposed [157]. Circular colliders employing muons, which are leptons ca. 200 times heavier than electrons, may combine a clean collision environment with high achievable energies (as the synchrotron radiation would be much lower for muons than for electrons). However, as muons are unstable, a serious challenge would be to accelerate and collide them within their short lifetime.

Production of dark particles at the future $e^+e^-$ colliders is investigated in some detail in chapter 6, which discusses the influence of DM spin on detection probability.

# Chapter 5

# $t$-channel singularity

This chapter, based on [1, 2], describes the $t$-channel singularity which arises in some processes with a massive, stable $t$-channel mediator. After a discussion of importance of the singularity, conditions for its occurrence are provided. After that, a regularization mechanism, basing on interactions between the mediator and the surrounding medium, is proposed.

Let us consider a $2 \to 2$ process (with possible decays of the final-state particles) mediated by a $t$-channel mediator. If the mediator is on its mass shell, the matrix element describing this process contains zero in the denominator and is, thus, ill-defined. This leads to a singular cross section.

For a massless mediator, the singularity can be ruled out using known IR regularization schemes that move the singular point out of the integration range [158].

This cannot be used if the mediator has a non-zero mass. In such a case, the usual way to regularize the singularity is to replace the bare propagator of the mediator by a resummed propagator, which appears as a sum of a series of self-energy corrections. From the optical theorem it follows that on the mass shell, the imaginary part of the self-energy is proportional to the width of the mediator. If the mediator is unstable (so its decay width is non-zero), the denominator of the propagator is non-zero even on-shell and the matrix element is always finite. For this reason, the problem does not exist for $s$-channel processes: an $s$-channel mediator that is on-shell can always decay into the initial state of the process and, thus, has a non-zero width.

In the case of a massive, stable mediator no standard way to deal with the singularity exists, so it becomes a real issue that deserves a careful investigation. We call this case a (genuine) $t$-channel singularity.

## 5.1 Awareness of the issue among the community and proposed regularization methods

The problem has been noticed, probably for the first time, by Peierls [159], who observed that the scattering amplitudes of the pion-isobar scattering $\pi N^* \to N^* \pi$ mediated by a $t$-channel nucleon $N$ may become divergent when the mediator is on its mass shell. The author argues that this process can be treated as a decay of $N^*$ into a pair $\pi$, $N$, followed by an absorption of the nucleon by another pion. Similarly, any scattering of an unstable particle with one of its decay products should exhibit the same singular behaviour. Those so-called Peierls singularities have been discussed in, e.g., [160–163], as a potential source of energy peaks observed in scattering experiments.

The issue of the $t$-channel singularity has been also investigated by the authors of [164–169] in the context of the muonic scattering process $\mu^+\mu^- \to W^+W^{-*} \to W^+e^-\bar{\nu}_e$ (see fig. 5.1), in connection to planned experiments involving lepton colliders. In most[1] of those papers, a regularization mechanism that uses the finite beam width as a regulator has been proposed and developed. A similar method has been proposed in [170, 171] to deal with singular processes encountered during studies of neutrino oscillations. Their proposal is to take into account the non-local effects taking place within the source and the detector. Although both those methods can cure the issue when the colliding particles originate from

[1] In [164], the author proposes modifying the wave function of the colliding particles using their finite lifetime, which results in a simple multiplication of the initial-state momentum by a complex term $(1 + i\Gamma/m)$, where $\Gamma$ and $m$ are the decay width and the mass of the unstable initial-state particle. Then, the momentum of the mediator contains a non-zero imaginary part that regularizes the scattering amplitude. This simple and elegant proposition, however, seems to not be internally consistent, as applying it to the final-state particles gives different results.

a source of a finite size, they are not applicable to the processes taking place in the early Universe due to lack of any characteristic size that could influence the mathematical description of colliding particles.

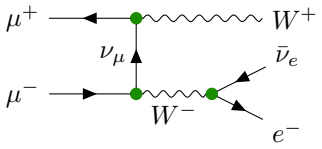


**Figure 5.1:** A muon-muon scattering that can be affected by the $t$-channel singularity. As the neutrinos are stable particles known to have a non-zero mass due to the fact they oscillate [48], they can serve as singular mediators.

The issue has been addressed directly in the context of particles interacting in thermal gas in Giudice et al. [172]. In sec. 3.2.3, the authors propose a regularization way that is also used here, namely, including the imaginary part of the self-energy of the mediator to the propagator. They refer to a paper of Weldon [173], who has calculated the imaginary part of the self energy that is a result of interactions between the mediator and the surrounding gas. In that paper, the imaginary-time (Matsubara) formalism has been used, in contrast to this dissertation, where we use the real-time (Keldysh-Schwinger) formalism. Weldon's results are in agreement with those presented in section 5.5 up to an additional numerical constant, namely, $1/2$ for a fermion particle and $1/3$ for a vector particle.

In contrast to Giudice et al., we provide analytical results that are fully integrated and ready to use.

## 5.2 Relevance of the singularity

The discussed singularity can affect processes in the very Standard Model of particle physics. Apart of the reactions already mentioned, the weak Compton-like scattering $Ze^- \to e^- Z$ with an electron in the $t$-channel should be mentioned as a simple example. Note that in order to keep that process truly $t$-channel singular, it is crucial to not neglect the electron mass, otherwise the divergence becomes infrared and can be regularized using the known procedures.

The singularity can play a great role in dark matter studies, because models of dark matter inherently assume existence of stable, massive particles that can serve as the mediator of a given singular process. This chapter is devoted to find a way to regularize the divergence in the case of particles interacting in early Universe.

It should be emphasized that, due to massiveness of the mediator, the $t$-channel singularity discussed here is different from infrared singularities widely discussed in literature. Its appearance influences the scattering amplitude dramatically. The amplitude becomes divergent, which means that the interaction rates cannot be calculated (or even estimated). Hence, finding a practical solution to that issue can be potentially very useful.

## 5.3 Conditions for occurrence

The purpose of this section is to provide a strict condition for a given $2 \to 2$ process to be affected by the $t$-channel singularity.

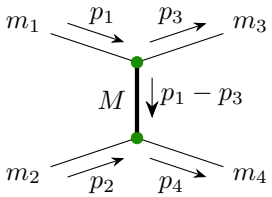


**Figure 5.2:** Diagram of a general $2 \to 2$ $t$-channel process. The four-momentum $p_i \equiv (E_i, \mathbf{p}_i)$ $(i = 1, 2, 3, 4)$ are assumed to be on-shell: $E_i^2 = \mathbf{p}_i^2 + m_i^2$. The mediator has been distinguished by a thick line.

Let us consider the process depicted in fig. 5.2. Particles of masses $m_1$ and $m_2$ collide and exchange a $t$-channel mediator of mass $M$, producing particles of masses $m_3$ and $m_4$ in the final state.

By definition, the condition for the mediator to be on-shell reads

$$t \equiv (p_1 - p_3)^2 = M^2 \,, \tag{5.1}$$

which can be reformulated as

$$2\,|\mathbf{p}_1||\mathbf{p}_3|\cos\theta_{13} = M^2 - m_1^2 - m_3^2 + 2\,E_1 E_3 \,. \tag{5.2}$$

Here, $\theta_{13}$ denotes the angle between $\mathbf{p}_1$ and $\mathbf{p}_3$. In the CM frame, the energies and momenta can be expressed as

$$E_1 = \frac{\sqrt{s}}{2} + \frac{m_1^2 - m_2^2}{2\sqrt{s}} \,, \qquad E_2 = \frac{\sqrt{s}}{2} - \frac{m_1^2 - m_2^2}{2\sqrt{s}} \,, \qquad |\mathbf{p}_1| = |\mathbf{p}_2| = \frac{\lambda(s, m_1^2, m_2^2)^{1/2}}{2\sqrt{s}} \,, \tag{5.3a}$$

$$E_3 = \frac{\sqrt{s}}{2} + \frac{m_3^2 - m_4^2}{2\sqrt{s}} \,, \qquad E_4 = \frac{\sqrt{s}}{2} - \frac{m_3^2 - m_4^2}{2\sqrt{s}} \,, \qquad |\mathbf{p}_3| = |\mathbf{p}_4| = \frac{\lambda(s, m_3^2, m_4^2)^{1/2}}{2\sqrt{s}} \,, \tag{5.3b}$$

where $s$ is the centre-of-mass energy of the process, defined as

$$s \equiv (p_1 + p_2)^2 = (p_3 + p_4)^2 \,, \tag{5.4}$$

and $\lambda$ denotes the Källén triangle function defined by eq. (0.4). Using eq. (5.3), we rewrite the condition (5.2) as

$$\begin{aligned} \lambda(s, m_1^2, m_2^2)^{1/2}\lambda(s, m_3^2, m_4^2)^{1/2}\,\cos\theta_{13} = s^2 - s\,(m_1^2 + m_2^2 + m_3^2 + m_4^2 - 2M^2) \\ + (m_1^2 - m_2^2)(m_3^2 - m_4^2) \,. \end{aligned} \tag{5.5}$$

If eq. (5.5) holds for at least one value of $s$ that is kinematically allowed for the process under consideration, the mediator is on-shell and the process is affected by the $t$-channel singularity. Calculating the cross section, one integrates over the final-state momenta, which includes a $\cos\theta_{13}$-integration over the $(-1, 1)$ interval. The process is singular when the value of $\cos\theta_{13}$ calculated from eq. (5.5) lies within this range. It happens when

$$\cos^2\theta_{13} < 1 \,, \tag{5.6}$$

so the singularity condition (5.5) becomes

$$\lambda(s, m_1^2, m_2^2)\lambda(s, m_3^2, m_4^2) > \left[s^2 - s\,(m_1^2 + m_2^2 + m_3^2 + m_4^2 - 2M^2) + (m_1^2 - m_2^2)(m_3^2 - m_4^2)\right]^2 \,, \tag{5.7}$$

which is equivalent to

$$A\,s^2 + B\,s + C < 0 \tag{5.8}$$

with $A$, $B$ and $C$ defined as

$$\begin{aligned} A &\equiv M^2 \,, \\ B &\equiv M^4 - M^2(m_1^2 + m_2^2 + m_3^2 + m_4^2) + (m_1^2 - m_3^2)(m_2^2 - m_4^2) \,, \\ C &\equiv M^2(m_1^2 - m_2^2)(m_3^2 - m_4^2) + (m_1^2 m_4^2 - m_2^2 m_3^2)(m_1^2 - m_2^2 - m_3^2 + m_4^2) \,. \end{aligned} \tag{5.9}$$

Inequality (5.8) is satisfied when

$$s \in \left(\frac{-B - \sqrt{\Delta}}{2M^2} \,,\; \frac{-B + \sqrt{\Delta}}{2M^2}\right) \,, \tag{5.10}$$

where

$$\begin{aligned} \Delta &\equiv B^2 - 4\,A\,C \\ &= \lambda(m_1^2, m_3^2, M^2)\,\lambda(m_2^2, m_4^2, M^2) \\ &= \left[M^2 - (m_1 + m_3)^2\right]\left[M^2 - (m_2 + m_4)^2\right]\left[M^2 - (m_1 - m_3)^2\right]\left[M^2 - (m_2 - m_4)^2\right] \,. \end{aligned} \tag{5.11}$$

If the value of $s$ lies within this range (in particular, $\Delta$ must be positive for the solution to exist), the cross section for the process depicted in fig. 5.2 is $t$-channel singular.

Let us now check when the thermally averaged cross section for that process is singular. That quantity can be calculated by integrating the cross section over statistical distribution of momenta of the initial-state particles. The result will be singular if condition (5.10) is satisfied for any value of $s$ that is allowed for the process. Since the integration is performed over the whole range of momenta that are kinematically allowed, the range of $s$ is

$$s \in [s_{\min}, \infty) \,, \qquad s_{\min} \equiv \max\{(m_1+m_2)^2, (m_3+m_4)^2\} \,. \tag{5.12}$$

The thermally averaged cross section is singular when the above integration range contains a non-empty subinterval of eq. (5.10), which means that $\Delta$ must be positive and

$$s_{\min} < \frac{-\beta + \sqrt{\Delta}}{2M^2} \,, \tag{5.13}$$

i.e.

$$\sqrt{\Delta} > 2M^2 s_{\min} + \beta \,. \tag{5.14}$$

If the RHS of the above inequality is positive, this inequality is equivalent to

$$\begin{aligned} 0 &> (2M^2 s_{\min} + \beta)^2 - \Delta \\ &= \begin{cases} 4M^2 \left[(m_1 m_2 + M^2)(m_1+m_2) - m_2 m_3^2 - m_1 m_4^2\right]^2 & \text{if} \quad m_1+m_2 > m_3+m_4 \\ 4M^2 \left[(m_3 m_4 + M^2)(m_3+m_4) - m_2^2 m_3 - m_1^2 m_4\right]^2 & \text{if} \quad m_1+m_2 < m_3+m_4 \end{cases} , \end{aligned} \tag{5.15}$$

which forms an obvious contradiction. On the other hand, if the RHS of (5.14) is negative, the inequality is obviously satisfied for any positive $\Delta$. Hence, the singularity conditions can be rewritten as

$$\Delta > 0 \,, \tag{5.16a}$$

$$2M^2 s_{\min} + \beta < 0 \,. \tag{5.16b}$$

It can be explicitly checked that

$$\begin{aligned} 2M^2 s_{\min} + \beta = M^2 \left|(m_1+m_2)^2 - (m_3+m_4)^2\right| \\ + \left[M^2 + (m_1-m_3)(m_2-m_4)\right]\left[M^2 + (m_1+m_3)(m_2+m_4)\right] \end{aligned} \tag{5.17}$$

(note the absolute value in the first term). Consequently, if

$$M^2 + (m_1-m_3)(m_2-m_4) > 0 \,, \tag{5.18}$$

eq. (5.16b) cannot be satisfied and the process cannot be singular. To make use of that observation, let us notice that as $\Delta$ is given by

$$\Delta = \left[M^2 - (m_1+m_3)^2\right]\left[M^2 - (m_2+m_4)^2\right]\left[M^2 - (m_1-m_3)^2\right]\left[M^2 - (m_2-m_4)^2\right] \,, \tag{5.19}$$

it is positive if and only if one of the following two conditions holds:

$$M > |m_1 - m_3| \quad \text{and} \quad M > |m_2 - m_4| \,, \tag{5.20a}$$

$$M < |m_1 - m_3| \quad \text{and} \quad M < |m_2 - m_4| \,, \tag{5.20b}$$

because negativeness of the first two brackets of eq. (5.19) (so, positiveness of their product) is a consequence of stability of the mediator. If the condition (5.20a) is true, the inequality (5.18) is obviously satisfied and the process cannot be singular. If eq. (5.20b) holds, in the following two cases the inequality (5.18) is obviously satisfied as well:

$$m_1 > m_3 \quad \text{and} \quad m_2 > m_4 \,, \tag{5.21a}$$

$$m_1 < m_3 \quad \text{and} \quad m_2 < m_4 \,. \tag{5.21b}$$

Therefore, for the singularity to occur it is necessary that either

$$m_1 > m_3 \quad \text{and} \quad m_2 < m_4 \tag{5.22a}$$

or

$$m_1 < m_3 \quad \text{and} \quad m_2 > m_4 \,. \tag{5.22b}$$

Combining this result with eq. (5.20b), we conclude that either

$$m_1 > m_3 + M \quad \text{and} \quad m_4 > m_2 + M \tag{5.23a}$$

or

$$m_3 > m_1 + M \quad \text{and} \quad m_2 > m_4 + M \tag{5.23b}$$

must hold for the thermally averaged cross section to be affected by the $t$-channel singularity.

Note that any of the conditions expressed by eqs. (5.23a) and (5.23b) ensures that eqs. (5.16a) and (5.16b) are satisfied. Indeed, let us assume that eq. (5.23a) holds. Then, condition (5.20b) is satisfied, which means that $\Delta$ is positive. Moreover,

$$2M^2 s_{\min} + \beta = \begin{cases} -A_{12}B_{12} - 2\,m_1\,M\,B_{12} - 2\,m_2\,M\,A_{12} & \text{if} \quad m_1 + m_2 > m_3 + m_4 \\ -A_{34}B_{34} - 2\,m_3\,M\,B_{34} - 2\,m_4\,M\,A_{34} & \text{if} \quad m_1 + m_2 < m_3 + m_4 \end{cases} , \tag{5.24}$$

where

$$\begin{aligned} A_{12} &\equiv (m_1 - M)^2 - m_3^2 \,, \quad B_{12} \equiv m_4^2 - (m_2 + M)^2 \,, \\ A_{34} &\equiv m_1^2 - (m_3 + M)^2 \,, \quad B_{34} \equiv (m_4 - M)^2 - m_2^2 \,. \end{aligned} \tag{5.25}$$

Since for $m_1 > m_3 + M$ and $m_4 > m_2 + M$ all of the above four quantities are positive, $2M^2 s_{\min} + \beta$ must be negative, which means that the condition (5.16b) is fulfilled. In the case (5.23b), the proof goes analogously.

Summing up, we conclude that the process depicted in fig. 5.2 has a singular thermally averaged cross section if and only if one of the conditions (5.23a), (5.23b) holds. It means that the process can be treated as a sequence of two subprocesses with all particles on-shell: a decay of particle "1" into "3" and the mediator, and an inverse decay of the mediator and particle "2" producing "4". Those possibilities are illustrated in fig. 5.3 This appears to be a special case of the so-called Coleman-Norton theorem which states that *a Feynman amplitude has singularities on the physical boundary if and only if the relevant Feynman diagram can be interpreted as a picture of an energy- and momentum-conserving process occurring in space-time, with all internal particles real, on the mass shell, and moving forward in time* [174].

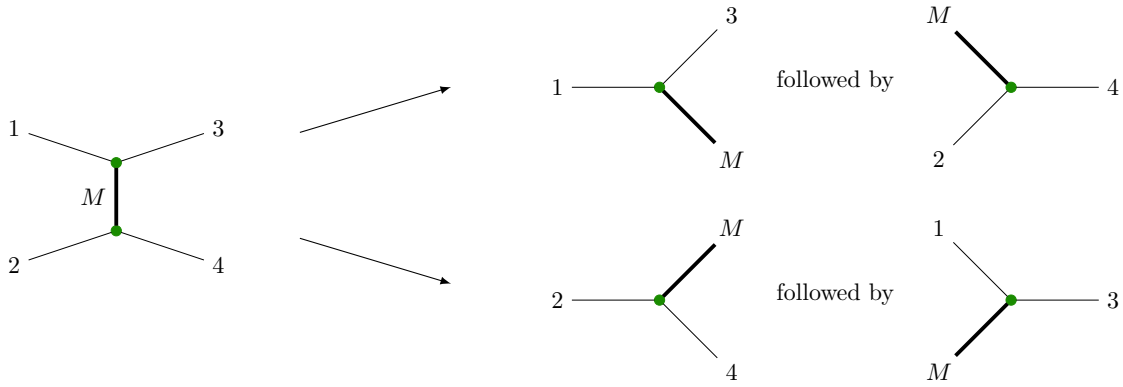


**Figure 5.3:** The possible decompositions of the considered $t$-channel process corresponding to the conditions (5.23a) and (5.23b). For clarity, the mediator has been distinguished by thick lines.

## 5.4 Resummed propagators and the effective width

In this section, the resummed propagator, being a sum of a series of self-energy corrections (see fig. 5.4), is determined for a scalar, a fermion and a vector field. For simplicity, the calculation is restricted to one-loop self-energy. Basing on the result, a formula for the effective width is obtained.

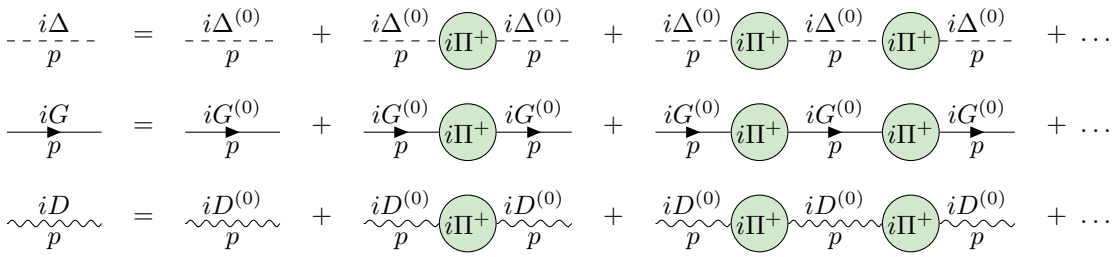


**Figure 5.4:** Resummed propagator as a sum of a series of one-loop self-energy corrections for a scalar (top), a fermion (centre) and a vector (bottom) field. $\Delta$, $G$ and $D$ denote resummed propagators of the fields, while $\Delta^{(0)}$, $G^{(0)}$ and $D^{(0)}$ are the bare propagators. $\Pi^+$ is the retarded self-energy, calculated within the Keldysh-Schwinger formalism.

For a scalar field, the resummed propagator is

$$\begin{aligned} i\Delta(p,T) &\equiv i\Delta^{(0)}(p)\sum_{n=0}^{\infty}\left[i\Pi^+(p,T)i\Delta^{(0)}(p)\right]^n \\ &= i\Delta^{(0)}(p)\left[1-i\Pi^+(p,T)i\Delta^{(0)}(p)\right]^{-1}\,, \end{aligned} \tag{5.26}$$

while for a fermion

$$\begin{aligned} iG(p,T) &\equiv iG^{(0)}(p)\sum_{n=0}^{\infty}\left[i\Pi^+(p,T)iG^{(0)}(p)\right]^n \\ &= iG^{(0)}(p)\left[1-i\Pi^+(p,T)iG^{(0)}(p)\right]^{-1}\,, \end{aligned} \tag{5.27}$$

and for a vector

$$\begin{aligned} iD_{\mu\nu}(p,T) &\equiv iD^{(0)}_{\mu\alpha}(p)\left(\sum_{n=0}^{\infty}\left[i\Pi^+(p,T)iD^{(0)}(p)\right]^n\right)^{\alpha}_{\nu} \\ &= iD^{(0)}_{\mu\alpha}(p)\left(\left[1-i\Pi^+(p,T)iD^{(0)}(p)\right]^{-1}\right)^{\alpha}_{\nu}\,. \end{aligned} \tag{5.28}$$

In the above equations, $\Delta$, $G$ and $D$ denote resummed propagators of a scalar, a fermion and a vector field, while $\Delta^{(0)}$, $G^{(0)}$ and $D^{(0)}$ are bare propagators. In section 5.5, $\Pi^+$ denotes the retarded self-energy, calculated within the Keldysh-Schwinger formalism. Here, however, the precise definition of $\Pi^+$ is irrelevant; the index plus is kept only for consistency.

The following sections 5.4.1 to 5.4.3 provide the sums for the above series. In section 5.4.4, the effective width is introduced.

### 5.4.1 Scalar case

For a scalar field, $\Pi^+$ is a scalar quantity as well as $\Delta^{(0)}$ given by.

$$\Delta^{(0)}(p) = \frac{1}{p^2 - M^2}\,. \tag{5.29}$$

From eq. (5.26) it is straightforward to obtain:

$$\Delta(p,T) = \frac{1}{p^2 - M^2 + \Pi^+(p,T)}\,. \tag{5.30}$$

### 5.4.2 Fermion case

For a fermion field, both $G^{(0)}$ and $\Pi^+$ are expressed through the gamma matrices (see appendix D) as follows:[2]

$$\begin{aligned} G^{(0)}(p) &= \frac{1}{\not{p} - M} \ , \\ \Pi^+(p,T) &= \left[A_v(p,T) + A_a(p,T)\gamma_5\right] \not{p} + \left[B_v(p,T) + B_a(p,T)\gamma_5\right] M \ . \end{aligned} \tag{5.31}$$

Here, $A_{v,a}$ and $B_{v,a}$ are dimensionless Lorentz scalars and we use the Feynman slash notation: $\not{p} \equiv p^\mu \gamma_\mu$. Using the trace operator, we can conveniently extract coefficients $A_v$ and $B_v$ from the self-energy:

$$A_v(p,T) = \frac{1}{4p^2}\mathrm{Tr}[\not{p}\Pi^+(p,T)] \ , \quad B_v(p,T) = \frac{1}{4M}\mathrm{Tr}[\Pi^+(p,T)] \ , \tag{5.32}$$

The resummed propagator from eq. (5.27) can be calculated as follows:

$$\begin{aligned} iG &= iG^{(0)}\left[1 - i\Pi^+ iG^{(0)}\right]^{-1} \\ &= i\frac{1}{\not{p} - M}\left[\frac{(1 + A_v + A_a\gamma_5)\not{p} + (-1 + B_v + B_a\gamma_5)M}{\not{p} - M}\right]^{-1} \\ &= i\frac{(1 + A_v + A_a\gamma_5)\not{p} + (1 - B_v + B_a\gamma_5)M}{[(1+A_v)^2 - A_a^2]p^2 - [(1-B_v)^2 - B_a^2]M^2} \ . \end{aligned} \tag{5.33}$$

Therefore,

$$G(p,T) = \frac{[1 + A_v(p,T) + A_a(p,T)\gamma_5]\not{p} + [1 - B_v(p,T) + B_a(p,T)\gamma_5]M}{\Big([1 + A_v(p,T)]^2 - A_a(p,T)^2\Big)p^2 - \Big([1 - B_v(p,T)]^2 - B_a(p,T)^2\Big)M^2} \ . \tag{5.34}$$

The following assumptions are made to simplify the above result:

- the self-energy is much smaller than mass: $|A_{v,a}| \ll 1$, $|B_{v,a}| \ll 1$,
- the axial components of the self-energy do not dominate the vector components: $|A_a|, |B_a| \lesssim |A_v|, |B_v|$,
- the propagating field is approximately on-shell:[3] $|p^2 - M^2| \ll M^2$.

The simplified formula reads

$$G(p,T) \simeq \frac{\not{p} + M}{p^2 - M^2 + 2\left[A_v(p,T) + B_v(p,T)\right]M^2} \ , \tag{5.35}$$

which is in agreement with eq. (11) from [176] (coefficients $A$ and $B$ defined there are equivalent to, respectively, $-B_v M$ and $-A_v$ used here). Using eq. (5.32) we obtain

$$G(p,T) \simeq \frac{\not{p} + M}{p^2 - M^2 + 2\mathrm{Tr}\left[\frac{\not{p}+M}{4}\Pi^+(p,T)\right]} \ . \tag{5.36}$$

### 5.4.3 Vector case

For a vector field, $\Delta^{(0)}$ and $\Pi^+$ are tensors that can be split into a transverse and a longitudinal part with respect to the momentum of the field:

$$\begin{aligned} D^{(0)}_{\mu\nu}(p) &= -\left(\frac{T_{\mu\alpha}}{p^2 - M^2} - \frac{L_{\mu\alpha}}{M^2}\right) \ , \\ \Pi^+_{\mu\nu}(p) &= \Pi_\mathrm{T}(p,T)\,T_{\mu\nu} + \Pi_\mathrm{L}(p,T)\,L_{\mu\nu} \ . \end{aligned} \tag{5.37}$$

[2] For a brief discussion, see section A of chapter III in [175].

[3] Mathematically, the on-shell contribution dominates the integration over four momentum.

Here, the scalar quantities $\Pi_{\mathrm{T}}$ and $\Pi_{\mathrm{L}}$ of dimension [mass]$^2$ denote, respectively, the longitudinal and the transverse part of the self-energy. Operators $T_{\mu\nu}$ (transverse projector) and $L_{\mu\nu}$ (longitudinal projector) are given by

$$T_{\mu\nu} \equiv g_{\mu\nu} - \frac{p_\mu p_\nu}{p^2} \ , \qquad\qquad L_{\mu\nu} \equiv \frac{p_\mu p_\nu}{p^2} \ . \tag{5.38}$$

Note that $\Pi_T$ can be obtained from $\Pi^+$ ad

$$\Pi_T(p,T) = \frac{1}{3}\left(g^{\mu\nu} - \frac{p^\mu p^\nu}{p^2}\right)\Pi^+_{\mu\nu}(p,T) \ . \tag{5.39}$$

From eq. (5.28) we obtain

$$\begin{aligned}
iD_{\mu\nu} &= iD^{(0)}_{\mu\alpha}\left(\left[1 - i\Pi^+(p,T)iD^{(0)}(p)\right]^{-1}\right)^\alpha_{\ \nu} \\
&= -i\left(\frac{T_{\mu\alpha}}{p^2-M^2} - \frac{L_{\mu\alpha}}{M^2}\right)\left(\left[\frac{p^2-M^2-\Pi_T}{p^2-M^2}T + \frac{M^2+\Pi_L}{M^2}L\right]^{-1}\right)^\alpha_{\ \nu} \\
&= -i\left(\frac{T_{\mu\alpha}}{p^2-M^2} - \frac{L_{\mu\alpha}}{M^2}\right)\left[\frac{p^2-M^2}{p^2-M^2-\Pi_T}T^\alpha_\nu + \frac{M^2}{M^2+\Pi_L}L^\alpha_\nu\right] \\
&= -i\,\frac{T_{\mu\nu}}{p^2-M^2-\Pi_T} + i\frac{L_{\mu\nu}}{M^2+\Pi_L} \\
&= i\,\frac{-g_{\mu\nu} + \frac{p_\mu p_\nu}{M^2+\Pi_L}\frac{p^2-\Pi_T+\Pi_L}{p^2}}{p^2-M^2-\Pi_T} \ .
\end{aligned} \tag{5.40}$$

As a consequence,

$$D_{\mu\nu}(p,T) = \frac{-g_{\mu\nu} + \frac{p_\mu p_\nu}{M^2+\Pi_L(p,T)}\frac{p^2-\Pi_T(p,T)+\Pi_L(p,T)}{p^2}}{p^2-M^2-\Pi_T(p,T)} \ . \tag{5.41}$$

This formula, up to a sign of their $\Pi_T$, is in agreement with eq. (20) of [177]. The conventions of that paper are slightly different than those here: $\Pi_T(q^2)$ from that paper is equivalent to our $\Pi_T(q^2)$, and their $\Pi_L(q^2)$ would be expressed by our $[\Pi_L(q^2) - \Pi_T(q^2)]/q^2$.

Similarly to the previous case, we assume that the self-energy is negigible in comparison to mass squared, $|\Pi_L|, |\Pi_T| \ll M^2$. Moreover, the propagator is assumed to be on-shell (so $|p^2 - M^2| \ll M^2$). Then, the following simplified result can be obtained:

$$D_{\mu\nu}(p,T) \simeq \frac{-g_{\mu\nu} + \frac{p_\mu p_\nu}{M^2}}{p^2-M^2-\Pi_T(p,T)} \ , \tag{5.42}$$

which, after applying eq. (5.39), becomes

$$D_{\mu\nu}(p,T) \simeq \frac{-g_{\mu\nu} + \frac{p_\mu p_\nu}{M^2}}{p^2 - M^2 + \frac{1}{3}\left(-g^{\mu\nu} + \frac{p^\mu p^\nu}{p^2}\right)\Pi^+_{\mu\nu}(p,T)} \ . \tag{5.43}$$

### 5.4.4 Effective width

We will call the difference between the imaginary parts of the denominators of the resummed and free propagator "regulator" and denote it by $\Sigma(p,T)$. According to sections 5.4.1 to 5.4.3, it is given by

$$\Sigma(p,T) \equiv \begin{cases} \Im\Pi^+(p,T) & \text{scalar case} \\ \Im\left(\mathrm{Tr}\left[\frac{\not{p}+M}{2}\Pi^+(p,T)\right]\right) & \text{fermion case} \\ \Im\left[\frac{1}{3}\left(-g^{\mu\nu} + \frac{p^\mu p^\nu}{p^2}\right)\Pi^+_{\mu\nu}(p,T)\right] & \text{vector case} \end{cases} \ . \tag{5.44}$$

As the resummed propagators resemble the Breit-Wigner propagator of unstable particle, we introduce an effective decay width $\Gamma_{\mathrm{eff}}(p,T)$ defined in the following way:

$$\Gamma_{\mathrm{eff}}(p,T) \equiv \frac{|\Sigma(p,T)|}{M} \ . \tag{5.45}$$

This effective width regularizes the propagator in the same manner as the standard decay width regularizes the Breit-Wigner propagator.

## 5.5 Regularization by the thermal medium

In this section, the regularization method is derived and illustrated by examples within a toy model described in appendix C and the VFDM model described in appendix A. The regularization is performed using the one-loop self-energy of the mediator propagating through a thermal medium, corresponding to a diagram of the type shown in fig. 5.5. The assumption that the medium has defined temperature is convenient, as it simplifies the calculations,, but not necessary: it is enough to know the distribution function of the medium to apply the method proposed here.

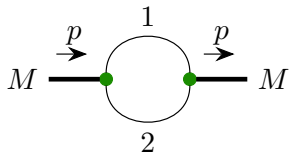


**Figure 5.5:** Diagram of mediator's one-loop self-energy.

Throughout the whole derivation, $\beta$ denotes inverse temperature, $E_p$ is the on-shell energy of the mediator with momentum $\mathbf{p}$, and $E_1$, $E_2$ denotes the on-shell energies of particles "1" and "2", respectively, moving with momentum $\mathbf{k}$.

$$\beta \equiv \frac{1}{T}\,, \quad E_p \equiv \sqrt{\mathbf{p}^2 + M^2}\,, \quad E_{1,2} \equiv \sqrt{\mathbf{k}^2 + m_{1,2}^2}\,, \tag{5.46}$$

Since the singularity leads to a strong enhancement of on-shell contribution to the propagator of the mediator, the mediator is assumed to be well-approximated by an on-shell particle, so it is assumed that

$$p_0 = E_p\,, \qquad p^2 = M^2\,. \tag{5.47}$$

As stated at the beginning of this chapter, for a true singularity to occur the mediator must be stable in vacuum. Therefore, it is assumed that

$$M < m_1 + m_2\,. \tag{5.48}$$

In the Keldysh-Schwinger formalism, the retarded one-loop self-energy for all particles scalar is given by

$$\Pi^+(p,T) = \frac{i}{2}\int \frac{d^4k}{(2\pi)^4}\left[\mu\,\Delta_1^+(k+p)\,\mu\,\Delta_2^{\mathrm{sym}}(k,T) + \mu\,\Delta_1^{\mathrm{sym}}(k,T)\,\mu\,\Delta_2^-(k-p)\right]\,, \tag{5.49}$$

In general, if the spins are non-zero, the scalar propagators $\Delta^{\pm}$, $\Delta^{\mathrm{sym}}$ must be replaced by their fermion ($G^{\pm}$, $G^{\mathrm{sym}}$) or vector ($D^{\pm}_{\mu\nu}$, $D^{\mathrm{sym}}_{\mu\nu}$) counterparts. All the propagators are defined in appendix F.

Let us recall that if the mediator is a scalar particle, the imaginary part of the self-energy is the regulator defined in section 5.4.4:

$$\Sigma(p,T) = \Im\Pi^+(p,T)\,. \tag{5.50}$$

To obtain the regulator for a fermionic mediator, one should calculate the following trace:

$$\Sigma(p,T) = \Im\mathrm{Tr}\left[\frac{\not{p} + M}{2}\Pi^+(p,T)\right]\,, \tag{5.51}$$

and for a vector mediator, the regulator is obtained as

$$\Sigma(p,T) = \Im\left[\frac{1}{3}\left(-g^{\mu\nu} + \frac{p^\mu p^\nu}{p^2}\right)\Pi^+_{\mu\nu}(p,T)\right]\,. \tag{5.52}$$

Regardless which case is the actual one, eq. (5.49) takes the following form:

$$\begin{aligned}\Sigma(p,T) = \Im\Bigg[\frac{1}{2}\int\frac{d^4k}{(2\pi)^4}\Bigg\{ & \frac{X_{(p^2,\,k^2,\,(k+p)^2)}}{(k+p)^2 - m_1^2 + i\,\mathrm{sgn}(k_0+p_0)\,0^+} \\ & \times\frac{\pi}{E_2}\Big(\delta(E_2-k_0)+\delta(E_2+k_0)\Big)\,f_2(\beta k_0) \\ & + \frac{X_{(p^2,\,(k-p)^2,\,p^2)}}{(k-p)^2 - m_2^2 - i\,\mathrm{sgn}(k_0-p_0)\,0^+} \\ & \times\frac{\pi}{E_1}\Big(\delta(E_1-k_0)+\delta(E_1+k_0)\Big)\,f_1(\beta k_0)\Bigg\}\Bigg]\,,\end{aligned} \tag{5.53}$$

with function $f_i$ $(i=1,2)$ defined as

$$f_i(x) \equiv \begin{cases} \frac{e^x-1}{e^x+1} & \text{for fermionic particle } i \\ \frac{e^x+1}{e^x-1} & \text{for bosonic particle } i \end{cases} \tag{5.54}$$

(see appendix F). A Lorentz-invariant factor $X_{(p^2,k^2,(k+p)^2)}$ is the effect of applying the appropriate operation from eqs. (5.50) to (5.52) to the product of the couplings and the numerators of the propagators. Its value has to be determined for each model separately.

As the $d^4k$ integration makes direction of $\mathbf{p}$ irrelevant, the imaginary part of the self-energy depends on energy only (instead of the full four-momentum):

$$\Sigma(p,T) = \Sigma(E_p,T)\,. \tag{5.55}$$

Integration over $k_0$ leads to the following result:

$$\begin{aligned}\Sigma(E_p,T) = \Im\Bigg[\frac{1}{4}\int\frac{d^3k}{(2\pi)^3}\Bigg\{ & \frac{X_{(p^2,\,k^2,\,(k+p)^2)}}{E_2}\,f_2 \\ & \times\Bigg[\frac{1}{M^2+m_2^2-m_1^2+2pk+i\,\mathrm{sgn}(E_2+E_p)\,0^+} \\ & \quad + \frac{1}{M^2+m_2^2-m_1^2+2pk+i\,\mathrm{sgn}(-E_2+E_p)\,0^+}\Bigg] \\ & + \frac{X_{(p^2,\,(k-p)^2,\,k^2)}}{E_1}\,f_1 \\ & \times\Bigg[\frac{1}{M^2-m_2^2+m_1^2-2pk-i\,\mathrm{sgn}(E_1-E_p)\,0^+} \\ & \quad + \frac{1}{M^2-m_2^2+m_1^2-2pk-i\,\mathrm{sgn}(-E_1-E_p)\,0^+}\Bigg]\Bigg\}\Bigg]\,.\end{aligned} \tag{5.56}$$

Using Sochocki's formula:

$$\lim_{\varepsilon\to 0^+}\frac{1}{x\pm i\varepsilon} = \mathcal{P}\frac{1}{x} \pm i\pi\delta(x) \tag{5.57}$$

with $\mathcal{P}$ denoting the principal value and $\delta$ being the Dirac delta, we obtain

$$\begin{aligned}\Sigma(E_p,T) = \frac{\pi}{4}\int\frac{d^3k}{(2\pi)^3}\Bigg\{ & -X_0\,f_2\left[\frac{\mathrm{sgn}(E_2+E_p)}{E_2}+\frac{\mathrm{sgn}(-E_2+E_p)}{E_2}\right] \\ & \times\delta(M^2+m_2^2-m_1^2+2pk) \\ & X_0\,f_1\left[\frac{\mathrm{sgn}(E_1-E_p)}{E_1}+\frac{\mathrm{sgn}(-E_1-E_p)}{E_1}\right] \\ & \times\delta(M^2-m_2^2+m_1^2-2pk)\Bigg\}\,.\end{aligned} \tag{5.58}$$

Here, $X_0$ denotes the value of $X$ calculated on-shell:

$$X_0 \equiv X_{(p^2=M^2,\,k^2=m_2^2,\,(k+p)^2=m_1^2)}\,. \tag{5.59}$$

In order to perform the spatial integration, we can choose the spherical coordinate system in which

$$\begin{aligned} p^\mu &= (E_p = \sqrt{\mathbf{p}^2 + M^2},\, 0,\, 0,\, |\mathbf{p}|)\ , \\ k^\mu &= (k_0,\, |\mathbf{k}|\sin\theta\cos\phi,\, |\mathbf{k}|\sin\theta\sin\phi,\, |\mathbf{k}|\cos\theta)\ . \end{aligned} \tag{5.60}$$

In this system, the products of four-momenta take the form

$$p^\mu p_\mu = M^2\ , \quad k^\mu k_\mu = k_0^2 - \mathbf{k}^2\ , \quad p^\mu k_\mu = E_p k_0 - |\mathbf{k}||\mathbf{p}|\cos\theta\ . \tag{5.61}$$

It can be shown that taking $\mathbf{p} = 0$ at this point gives the same result as the corresponding limit of the result obtained for a non-zero momentum (this limit is discussed in section 5.5.1). Hence, from now on we assume that $\mathbf{p} \neq 0$. After performing the trivial integration over $d\phi$, we obtain

$$\begin{aligned} \Sigma(E_p, T) = \frac{X_0}{32\pi}\int_0^\infty \mathbf{k}^2 d|\mathbf{k}| \int_{-1}^{1} d\,\cos\theta \\ \times\Bigg\{ -f_2\Bigg[ \frac{\mathrm{sgn}\big(E_2+E_p\big)}{E_2}\,\frac{\delta(\cos\theta-\cos\alpha_2)}{|\mathbf{k}||\mathbf{p}|} \\ + \frac{\mathrm{sgn}\big(-E_2+E_p\big)}{E_2}\,\frac{\delta(\cos\theta-\cos\beta_2)}{|\mathbf{k}||\mathbf{p}|}\Bigg] \\ +f_1\Bigg[ \frac{\mathrm{sgn}\big(E_1-E_p\big)}{E_1}\,\frac{\delta(\cos\theta-\cos\alpha_1)}{|\mathbf{k}||\mathbf{p}|} \\ + \frac{\mathrm{sgn}\big(-E_1-E_p\big)}{E_1}\,\frac{\delta(\cos\theta-\cos\beta_1)}{|\mathbf{k}||\mathbf{p}|}\Bigg]\Bigg\} \\ = \frac{X_0}{32\pi|\mathbf{p}|}\Bigg\{ -\int_0^\infty dE_2 \int_{-1}^{1} d\,\cos\theta\, f_2 \\ \times\big[\ \mathrm{sgn}\,(E_2+E_p)\,\delta(\cos\theta-\cos\alpha_2) \\ +\mathrm{sgn}\,(-E_2+E_p)\,\delta(\cos\theta-\cos\beta_2)\big] \\ +\int_0^\infty dE_1 \int_{-1}^{1} d\,\cos\theta\, f_1 \\ \times\big[\ \mathrm{sgn}\,(E_1-E_p)\,\delta(\cos\theta-\cos\alpha_1) \\ +\mathrm{sgn}\,(-E_1-E_p)\,\delta(\cos\theta-\cos\beta_1)\big]\Bigg\} \end{aligned} \tag{5.62}$$

with $\cos\alpha_1$, $\cos\alpha_2$, $\cos\beta_1$ and $\cos\beta_2$ defined via the following relations

$$\begin{aligned} \cos\alpha_1 &\equiv \frac{-m_1^2+m_2^2-M^2+2E_1E_p}{2\,|\mathbf{k}||\mathbf{p}|}\ , \quad \cos\beta_1 \equiv -\frac{m_1^2-m_2^2+M^2+2E_1E_p}{2\,|\mathbf{k}||\mathbf{p}|}\ , \\ \cos\alpha_2 &\equiv \frac{-m_1^2+m_2^2+M^2+2E_2E_p}{2\,|\mathbf{k}||\mathbf{p}|}\ , \quad \cos\beta_2 \equiv -\frac{m_1^2-m_2^2-M^2+2E_2E_p}{2\,|\mathbf{k}||\mathbf{p}|}\ . \end{aligned} \tag{5.63}$$

Let us observe that

- if $m_2 > |m_1 - M|$, then $\cos\alpha_1 > 1$:

$$\cos\alpha_1 = \frac{-m_1^2+m_2^2-M^2+2E_1E_p}{2\,|\mathbf{k}||\mathbf{p}|} > \frac{-2m_1M+2E_1E_p}{2\,|\mathbf{k}||\mathbf{p}|} > 1\ , \tag{5.64}$$

- if $m_2 < m_1 + M$, then $\cos\beta_1 < -1$:

$$\cos\beta_1 = -\frac{m_1^2-m_2^2+M^2+2E_1E_p}{2\,|\mathbf{k}||\mathbf{p}|} < -\frac{-2m_1M+2E_1E_p}{2\,|\mathbf{k}||\mathbf{p}|} < -1\ , \tag{5.65}$$

- if $m_1 < m_2 + M$, then $\cos\alpha_2 > 1$:

$$\cos\alpha_2 = \frac{-m_1^2+m_2^2+M^2+2E_2E_p}{2\,|\mathbf{k}||\mathbf{p}|} > \frac{-2m_2M+2E_2E_p}{2\,|\mathbf{k}||\mathbf{p}|} > 1\ , \tag{5.66}$$

- if $m_1 > |m_2 - M|$, then $\cos\beta_2 < -1$:

$$\cos\beta_2 = -\frac{m_1^2 - m_2^2 - M^2 + 2E_2E_p}{2\,|\mathbf{k}||\mathbf{p}|} < -\frac{-2m_2M + 2E_2E_p}{2\,|\mathbf{k}||\mathbf{p}|} < -1\ . \tag{5.67}$$

From the above eqs. (5.64) to (5.67) it follows that the regulator vanishes if $m_1$, $m_2$ and $M$ satisfy the triangle inequality. Hence, in order to regularize the singularity, one of "1", "2" must be alllowed to decay into the other one and the mediator. Fortunately, there always exists a loop with an unstable particle as to have a singularity $M$ must be a decay product. Without loss of generality let us assume that "1" is unstable, so that

$$m_1 > m_2 + M\ . \tag{5.68}$$

From this assumption it follows that $\cos\beta_{1,2} < -1$ so the delta functions containing $(\cos\theta - \cos\beta_{1,2})$ must vanish.

It can be observed that

$$4\,k^2p^2(\cos^2\alpha_1 - 1) = 4\,M^2\,E_1^2 - 4\,(m_1^2 - m_2^2 + M^2)\,E_p\,E_1 + 4\,m_1^2\,E_p^2 + \lambda(m_1^2, m_2^2, M^2)\ , \tag{5.69}$$

where $\lambda$ denotes the Källén function, defined by eq. (0.4). This formula, treated as a function of $E_1$, is negative for

$$b - a < E_1 < b + a\ , \tag{5.70}$$

with $a$ and $b$ given by

$$a \equiv \frac{\lambda(m_1^2, m_2^2, M^2)^{1/2}}{2M^2}\,|\mathbf{p}|\ , \qquad b \equiv \frac{m_1^2 - m_2^2 + M^2}{2M^2}\,E_p\ . \tag{5.71}$$

This means that the absolute value of $\cos\alpha_1$ is smaller than 1 for $E_1$ satisfying eq. (5.70), so the delta function limits the range of integration over $dE_1$ to the one provided in eq. (5.70).

Analogously,

$$4\,k^2p^2(\cos^2\alpha_2 - 1) = 4\,M^2\,E_2^2 - 4\,(m_1^2 - m_2^2 - M^2)\,E_p\,E_2 + 4\,m_2^2\,E_p^2 + \lambda(m_1^2, m_2^2, M^2) \tag{5.72}$$

is negative when

$$b - a - E_p < E_2 < b + a - E_p\ , \tag{5.73}$$

which is, thus, the range of the integration over $dE_2$ imposed by the delta function.

Then, the regulator becomes

$$\Sigma(E_p, T) = \frac{X_0}{32\pi}\frac{1}{|\mathbf{p}|}\left[\ -\int_{b-a-E_p}^{b+a-E_p} dE_2\,f_2\,\mathrm{sgn}\,(E_2 + E_p) + \int_{b-a}^{b+a} dE_1\,f_1\,\mathrm{sgn}\,(E_1 - E_p)\ \right]\ , \tag{5.74}$$

where $a$ and $b$ are given by

$$\begin{aligned} a &\equiv \frac{\lambda(m_1^2, m_2^2, M^2)^{1/2}}{2M^2}\,|\mathbf{p}|\ , \qquad b \equiv \frac{m_1^2 - m_2^2 + M^2}{2M^2}\,E_p\ , \\ \lambda(m_1^2, m_2^2, M^2) &\equiv \left[m_1^2 - (m_2 - M)^2\right]\left[m_1^2 - (m_2 + M)^2\right]\ . \end{aligned} \tag{5.75}$$

In eq. (5.74), the first sign function gives obviously $+1$ as both $E_2$ and $E_p$ are positive. The value of the second sign function is $+1$ as well: at the lower integration limit the argument is

$$E_1 - E_p = b - a - E_p = \frac{(m_1^2 - m_2^2 - M^2)E_p - \lambda(m_1^2, m_2^2, M^2)^{1/2}|\mathbf{p}|}{2M^2}\ , \tag{5.76}$$

which is positive as $E_p > |\mathbf{p}|$ and $m_1^2 - m_2^2 - M^2 > \lambda(m_1^2, m_2^2, M^2)^{1/2}$. Therefore,

$$\begin{aligned} \Sigma(E_p, T) &= \frac{X_0}{32\pi}\frac{1}{|\mathbf{p}|}\left[\ -\int_{b-a-E_p}^{b+a-E_p} dE_2\,f_2(\beta E_2) + \int_{b-a}^{b+a} dE_1\,f_1(\beta E_1)\ \right] \\ &= \frac{X_0}{32\pi}\frac{1}{\beta|\mathbf{p}|}\left[\ \int_{\beta(b-a)}^{\beta(b+a)} f_1(x)\,dx - \int_{\beta(b-a-E_p)}^{\beta(b+a-E_p)} f_2(x)\,dx\ \right]\ , \end{aligned} \tag{5.77}$$

Finally, after the integration the result becomes

$$\boxed{\begin{aligned}\Gamma_{\text{eff}}(E_p,T) &\equiv \frac{1}{M}|\Sigma(E_p,T)|\,,\\ \Sigma(E_p,T) &= \frac{1}{16\pi}\,\frac{X_0}{\beta|\mathbf{p}|}\left[\ln\frac{e^{\beta(b+a)}+\eta_1}{e^{\beta(b-a)}+\eta_1}-\ln\frac{e^{\beta(b+a)}e^{-\beta E_p}+\eta_2}{e^{\beta(b-a)}e^{-\beta E_p}+\eta_2}\right]\\ &= \frac{1}{16\pi}\,\frac{X_0}{\beta|\mathbf{p}|}\,\ln\left[1+\frac{e^{-\beta(b-a)}e^{\beta E_p}\left(1-e^{-2\beta a}\right)\left(\eta_2-\eta_1\,e^{-\beta E_p}\right)}{\left(1+\eta_1\,e^{-\beta(b-a)}\right)\left(1+\eta_2\,e^{-\beta(b+a)}e^{\beta E_p}\right)}\right],\end{aligned}} \tag{5.78}$$

where $\eta_i$ $(i=1,2)$ is $+1$ for fermions, $-1$ for bosons, and quantities $a$ and $b$ are

$$\begin{aligned} a &\equiv \frac{\lambda(m_1^2,m_2^2,M^2)^{1/2}}{2M^2}\,|\mathbf{p}|\,, \qquad b \equiv \frac{m_1^2-m_2^2+M^2}{2M^2}\,E_p\,,\\ \lambda(m_1^2,m_2^2,M^2) &\equiv \left[m_1^2-(m_2-M)^2\right]\left[m_1^2-(m_2+M)^2\right]\,. \end{aligned} \tag{5.79}$$

To obtain the values of thermally averaged cross section, presented in sections 5.5.3 and 5.5.4 we use the results obtained in section 2.3.2.

### 5.5.1 Discussion of the result

The result presented by the eq. (5.78) is consistent with the one obtained in [173] up to a numerical factor of $1/2$ (for a fermion mediator) or $1/3$ (for a vector mediator).

As can be inferred from the last line of eq. (5.78), the sign of the logarithmic part is the same as the sign of

$$\eta_2 - \eta_1\,e^{-\beta E_p}\,. \tag{5.80}$$

As the exponential function of a negative argument is always smaller than one, the overall sign of the logarithmic part is the same as the sign of $\eta_2$. Hence, the logarithmic part is positive if particle 2 is a fermion and negative otherwise. This corresponds to the sign of $X_0$, as can be seen in tables 5.1 to 5.3. Consequently, the imaginary part of the self-energy given by eq. (5.78) is always positive and, in particular, never equal to zero. Thus, a $t$-channel would-be-singular process occurring in a medium can always be regularized using the method proposed here.

In the limit of $m_1 = m_2 + M$, quantity $a$ defined in eq. (5.79) becomes zero and so does the effective width. This is expected, as the derivation has been performed under an assumption that $m_1$ is grater than $m_2 + M$, see eq. (5.68).

It should be noticed that interchanging spins of the loop states 1 and 2 (mathematically, switching $\eta_1$ and $\eta_2$ in eq. (5.78)) changes the result, as the statistical factors corresponding to the decaying and the produced particle are taken into account differently.

In the zero-temperature limit ($\beta \to \infty$) the regulator given by eq. (5.78) vanishes (argument of the logarithmic function in the second line becomes 1). It comes from the fact that the regulator is a result of interactions between the mediator and the thermal medium, while the zero-temperature limit corresponds to a lack of a medium.

In the limit of infinite momentum of the mediator ($|\mathbf{p}| \to \infty$), variable $b$ defined in eq. (5.79) is proportional to the momentum. Consequently, in eq. (5.78), for large momentum, the inverse temperature $\beta$ is always multiplied by the momentum and the regulator depends on the product $\beta|\mathbf{p}|$. Therefore, the limit of the regulator for $|\mathbf{p}| \to \infty$ is the same as in the case of $\beta \to \infty$, i.e., the regulator vanishes. The physical picture can be described as follows: the would-be singular propagator is regularized by interactions of the mediator with the thermal medium. The process responsible for limiting the medium's lifetime is production of particle "1" in an inverse decay process, $M, 2 \to 1$, where the source of particle "2" is the medium. This process is followed by a decay of particle "1" into "2" and the mediator particle of the same momentum as before the inverse decay. The minimal energy $E_2$ required for an on-shell production of particle "1", defined by eq. (5.73), increases with the value of $|\mathbf{p}|$. For $|\mathbf{p}|$ much larger than the temperature, the amount of particles "2" of sufficient energy in the thermal medium is statistically suppressed and decreases exponentially, making it hard to find a particle capable to merge with the mediator and produce an on-shell particle "1".

For negligible momentum of the mediator ($\mathbf{p} \to 0$), the limit becomes finite and takes the following form:

$$\Gamma_{\text{eff}}(\mathbf{p}=0,T) = \frac{X_0}{16\pi\, M}\, \frac{\lambda(m_1^2, m_2^2, M^2)^{1/2}}{M^2}\, \frac{e^{-\beta(b_0-M)}\, \left(\eta_2 - \eta_1\, e^{-\beta M}\right)}{\left(1+\eta_1\, e^{-\beta b_0}\right)\left(1+\eta_2\, e^{-\beta(b_0-M)}\right)}\,, \tag{5.81}$$

with $b_0 \equiv (m_1^2 - m_2^2 + M^2)/(2M) > M$.

A useful approximation of eq. (5.78) can be provided if

$$\beta(b-a-E_p) \gtrsim 3\,, \tag{5.82}$$

so that

$$e^{\beta(b-a-E_p)} \gg 1\,. \tag{5.83}$$

The first non-vanishing term of expansion around $e^{-\beta(b-a-E_p)} = 0$ is

$$\Gamma_{\text{eff}}(E_p,T) \simeq \frac{1}{16\pi\, M}\, \frac{X_0}{\beta|\mathbf{p}|}\, e^{-\beta(b-a-E_p)}\, \left(1-e^{-2\,\beta a}\right)\left(\eta_2 - \eta_1\, e^{-\beta E_p}\right)\,. \tag{5.84}$$

This form is convenient to use in numerical calculations.

### 5.5.2 $X_0$ in general

Here, we provide the value of the factor $X_0$ calculated for any combination of the spins of the mediator and particles 1, 2. Tables 5.1 to 5.3 show the values for a scalar, fermion or vector mediator, respectively. Each of the tables consists of two panes. The upper one assigns a three-letter code to each possible type of a loop and the corresponding interaction vertex. The first, the second and the third letter of the code denote the spin of the mediator and particles 1 and 2, respectively, with "S" standing for a scalar (spin-0), "F" for a fermion (spin-1/2) and "V" for a vector (spin-1). The lower panel provides the value of the "spin & vertex factor" (i.e., the matrix element that corresponds to the loop, with denominators omitted), the value of the factor $X_0$ and the ratio between $X_0$ and the matrix-element-squared corresponding to the decay of particle 1 into 2 and the mediator.

| loop code | loop | relevant vertex |
|---|---|---|
| SSS | 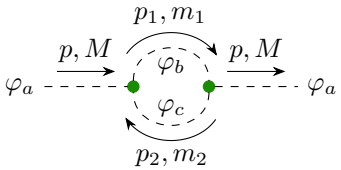 | 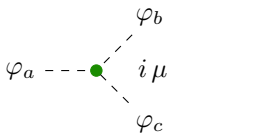 |
| SSV | 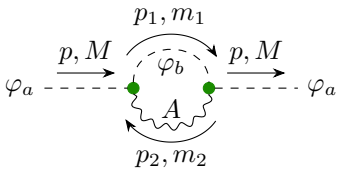 | 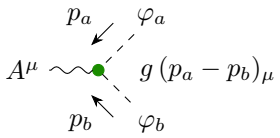 |
| SVS | 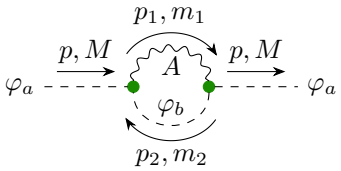 | 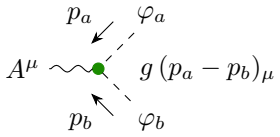 |
| SVV | 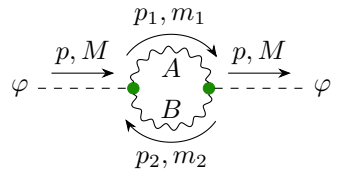 | 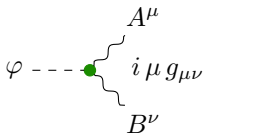 |
| SFF | 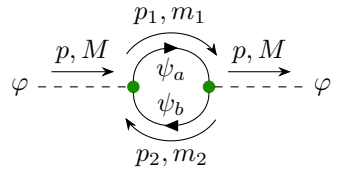 | 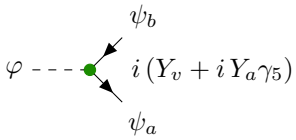 |

| loop code | spin & vertex factor | $X_0 \equiv$ [spin & vertex factor]$_{\text{on-shell}}$ | $\dfrac{X_0}{\lvert\mathcal{M}\rvert^2_{\text{dec}}}$ |
|---|---|---|---|
| SSS | $-\mu^2$ | $-\mu^2$ | $-1$ |
| SSV | $-g^2(p_1+p)^\alpha(p_1+p)^\beta\left(-g_{\alpha\beta}+\frac{p_{2\alpha}p_{2\beta}}{m_2^2}\right)$ | $-g^2\frac{\lambda(m_1^2,m_2^2,M^2)}{m_2^2}$ | $-1$ |
| SVS | $-g^2(p_2-p)^\alpha(p_2-p)^\beta\left(-g_{\alpha\beta}+\frac{p_{1\alpha}p_{1\beta}}{m_1^2}\right)$ | $-g^2\frac{\lambda(m_1^2,m_2^2,M^2)}{m_1^2}$ | $-1$ |
| SVV | $-\mu^2\left(-g_{\alpha\beta}+\frac{p_{1\alpha}p_{1\beta}}{m_1^2}\right)\left(-g^{\alpha\beta}+\frac{p_2^\alpha p_2^\beta}{m_2^2}\right)$ | $-\mu^2\left[\frac{\lambda(m_1^2,m_2^2,M^2)}{4m_1^2m_2^2}+3\right]$ | $-1$ |
| SFF | $-(-1)\mathrm{Tr}\left[(Y_v^*+i\,Y_a^*\gamma_5)(\not{p}_1+m_1)\right.$<br>$\left.\times(Y_v+i\,Y_a\gamma_5)(\not{p}_2+m_2)\right]$ | $2\,\lvert Y_v\rvert^2\left[(m_1+m_2)^2-M^2\right]$<br>$+2\,\lvert Y_a\rvert^2\left[(m_1-m_2)^2-M^2\right]$ | 1 |

**Table 5.1:** Values of the factor $X_0$ corresponding to two-particle loops of a scalar mediator.

| loop code | loop | relevant vertex |
|---|---|---|
| FSF | 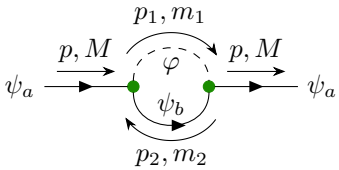 | 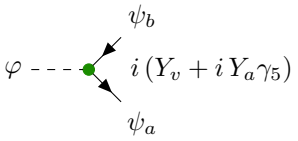 |
| FFS | 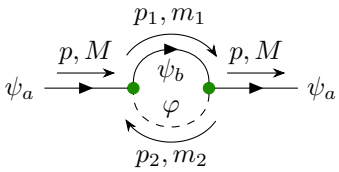 | 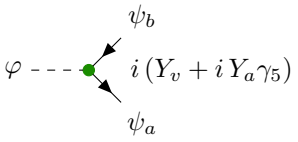 |
| FVF | 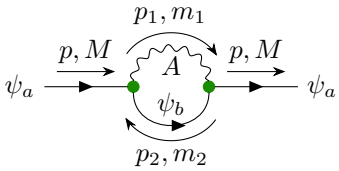 | 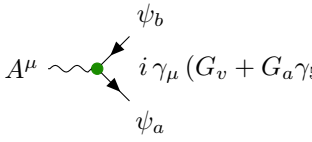 |
| FFV | 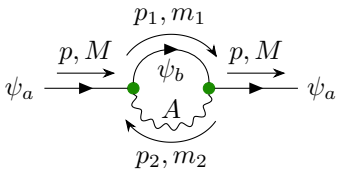 | 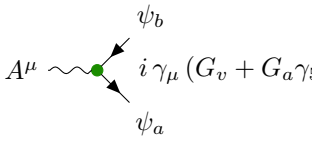 |

| loop code | spin & vertex factor | $X_0 \equiv \mathrm{Tr}\left[\frac{\not{p}+M}{2}\,[\text{spin \& vertex f.}]\right]_{\text{on-shell}}$ | $\frac{X_0}{\lvert\mathcal{M}\rvert^2_{\text{dec}}}$ |
|---|---|---|---|
| FSF | $-(Y_v^* + i\,Y_a^*\gamma_5)(-\not{p}_2 + m_2)(Y_v + i\,Y_a\gamma_5)$ | $\lvert Y_v\rvert^2\left[m_1^2 - (m_2+M)^2\right]$<br>$+\lvert Y_a\rvert^2\left[m_1^2 - (m_2-M)^2\right]$ | $\frac{1}{2}$ |
| FFS | $-(Y_v^* + i\,Y_a^*\gamma_5)(\not{p}_1 + m_1)(Y_v + i\,Y_a\gamma_5)$ | $-\lvert Y_v\rvert^2\left[(m_1+M)^2 - m_2^2\right]$<br>$-\lvert Y_a\rvert^2\left[(m_1-M)^2 - m_2^2\right]$ | $-\frac{1}{2}$ |
| FVF | $-\gamma^\beta(G_v^* + G_a^*\gamma_5)(-\not{p}_2 + m_2)$<br>$\gamma^\alpha(G_v + G_a\gamma_5)\left(-g_{\alpha\beta} + \frac{p_{1\alpha}p_{1\beta}}{m_1^2}\right)$ | $\lvert G_v\rvert^2\,\frac{[2\,m_1^2+(m_2+M)^2]\,[m_1^2-(m_2-M)^2]}{m_1^2}$<br>$+\lvert G_a\rvert^2\,\frac{[2\,m_1^2+(m_2-M)^2]\,[m_1^2-(m_2+M)^2]}{m_1^2}$ | $\frac{1}{2}$ |
| FFV | $-\gamma^\beta(G_v^* + G_a^*\gamma_5)(\not{p}_1 + m_1)$<br>$\gamma^\alpha(G_v + G_a\gamma_5)\left(-g_{\alpha\beta} + \frac{p_{2\alpha}p_{2\beta}}{m_2^2}\right)$ | $-\lvert G_v\rvert^2\,\frac{[(m_1+M)^2+2\,m_2^2]\,[(m_1-M)^2-m_2^2]}{m_2^2}$<br>$-\lvert G_a\rvert^2\,\frac{[(m_1-M)^2+2\,m_2^2]\,[(m_1+M)^2-m_2^2]}{m_2^2}$ | $-\frac{1}{2}$ |

**Table 5.2:** Values of the factor $X_0$ corresponding to two-particle loops of a fermion mediator.

| loop code | loop | relevant vertex |
|---|---|---|
| VSS | 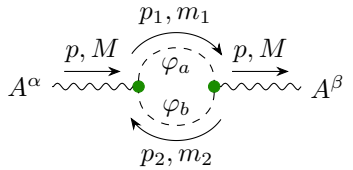 | 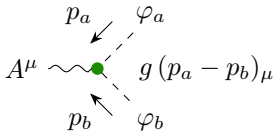 |
| VSV | 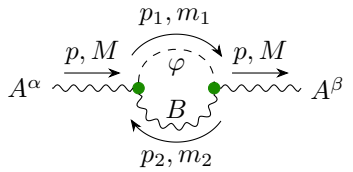 | 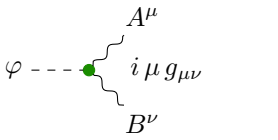 |
| VVS | 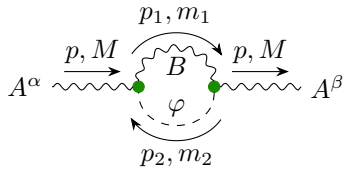 | 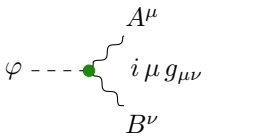 |
| VVV | 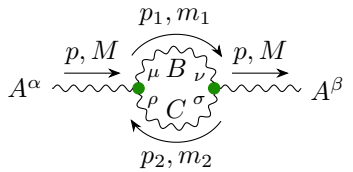 | 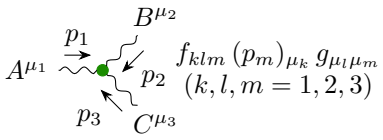 |
| VFF | 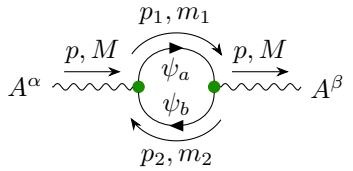 | 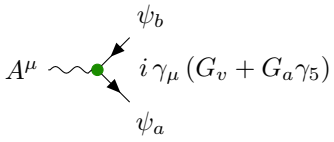 |

| loop code | spin & vertex factor | $X_0 \equiv \frac{1}{3}\Big[\big(-g_{\alpha\beta} + \frac{p_\alpha p_\beta}{M^2}\big) \times [\text{spin \& vertex f.}]^{\alpha\beta}\Big]_{\text{on-shell}}$ | $\frac{X_0}{\lvert\mathcal{M}\rvert^2_{\text{dec}}}$ |
|---|---|---|---|
| VSS | $-g^2(p_1+p_2)^\alpha(p_1+p_2)^\beta$ | $-\frac{g^2}{3}\frac{\lambda(m_1^2,m_2^2,M^2)}{M^2}$ | $-\frac{1}{3}$ |
| VSV | $-\mu^2\left(-g^{\alpha\beta} + \frac{p_2^\alpha p_2^\beta}{m_2^2}\right)$ | $-\frac{\mu^2}{3}\left[\frac{\lambda(m_1^2,m_2^2,M^2)}{4m_2^2M^2} + 3\right]$ | $-\frac{1}{3}$ |
| VVS | $-\mu^2\left(-g^{\alpha\beta} + \frac{p_1^\alpha p_1^\beta}{m_1^2}\right)$ | $-\frac{\mu^2}{3}\left[\frac{\lambda(m_1^2,m_2^2,M^2)}{4m_1^2M^2} + 3\right]$ | $-\frac{1}{3}$ |
| VVV | $-f_{123}^2\left(-g_{\mu\nu} + \frac{p_{1\mu}p_{1\nu}}{m_1^2}\right)\left(-g_{\rho\sigma} + \frac{p_{2\rho}p_{2\sigma}}{m_2^2}\right)$ $\times\left[g^{\nu\sigma}(p_1+p_2)^\beta + g^{\sigma\beta}(p-p_2)^\nu - g^{\beta\nu}(p+p_1)^\sigma\right]$ $\times\left[g^{\mu\rho}(p_1+p_2)^\alpha + g^{\rho\alpha}(p-p_2)^\mu - g^{\alpha\mu}(p+p_1)^\rho\right]$ | $-\frac{f_{ABC}^2}{3}\lambda(m_1^2,m_2^2,M^2)$ $\times\frac{\lambda(m_1^2,m_2^2,M^2)+12(m_1^2M^2+m_2^2M^2+m_1^2m_2^2)}{4m_1^2m_2^2M^2}$ | $-\frac{1}{3}$ |
| VFF | $-(-1)\text{Tr}\left[\gamma^\beta(G_v^* + G_a^*\gamma_5)(\not{p}_1 + m_1)\right.$ $\left.\times\gamma^\alpha(G_v + G_a\gamma_5)(\not{p}_2 + m_2)\right]$ | $\frac{2}{3}\lvert G_v\rvert^2\frac{[(m_1-m_2)^2-M^2][(m_1+m_2)^2+2M^2]}{M^2}$ $+\frac{2}{3}\lvert G_a\rvert^2\frac{[(m_1+m_2)^2-M^2][(m_1-m_2)^2+2M^2]}{M^2}$ | $\frac{1}{3}$ |

**Table 5.3:** Values of the factor $X_0$ corresponding to two-particle loops of a vector mediator.

### 5.5.3 $X_0$ in the toy model

This section provides the results of application of the developed regularization method to the 3-scalar toy model described in appendix C. The process that suffers from the $t$-channel singularity is the $\phi_1\phi_2 \to \phi_2\phi_1$ scattering mediated by $\Phi$, depicted in fig. 5.6 along with the relevant loop diagram.

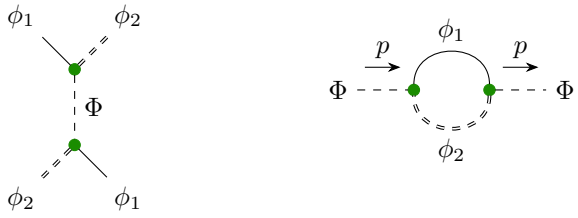


**Figure 5.6: Left:** the $t$-channel singular process of the 3-scalar toy model. **Right:** the loop diagram relevant for the regularization of the singularity.

For this process, the factor $X_0$ is equal to $-\mu^2$ and all particles are bosons, so the regulator given by eq. (5.78) becomes

$$\Sigma(E_p, T) = \frac{1}{16\pi}\,\frac{-\mu^2}{\beta|\mathbf{p}|}\left[\ln\frac{e^{\beta(b+a)}-1}{e^{\beta(b-a)}-1} - \ln\frac{e^{\beta(b+a)}e^{-\beta E_p}-1}{e^{\beta(b-a)}e^{-\beta E_p}-1}\right]. \tag{5.85}$$

with

$$\begin{aligned} a &= \frac{\lambda(m_1^2, m_2^2, M^2)^{1/2}}{2M^2}\,|\mathbf{p}|\,, \qquad b = \frac{m_1^2 - m_2^2 + M^2}{2M^2}\,E_p\,, \\ \lambda(m_1^2, m_2^2, M^2) &= \left[m_1^2 - (m_2 - M)^2\right]\left[m_1^2 - (m_2 + M)^2\right]\,. \end{aligned} \tag{5.86}$$

The thermally averaged cross section calculated using this regulator is plotted in fig. 5.7. As can be observed, the cross section decreases with temperature. It happens because the larger temperature is, the larger is the regulator which enters the matrix element in the denominator. For diminishing temperature, the cross section rises, reproducing the infinite result without the regularization in the limit of zero temperature. That agrees with the asymptotic behaviour described in section 5.5.1.

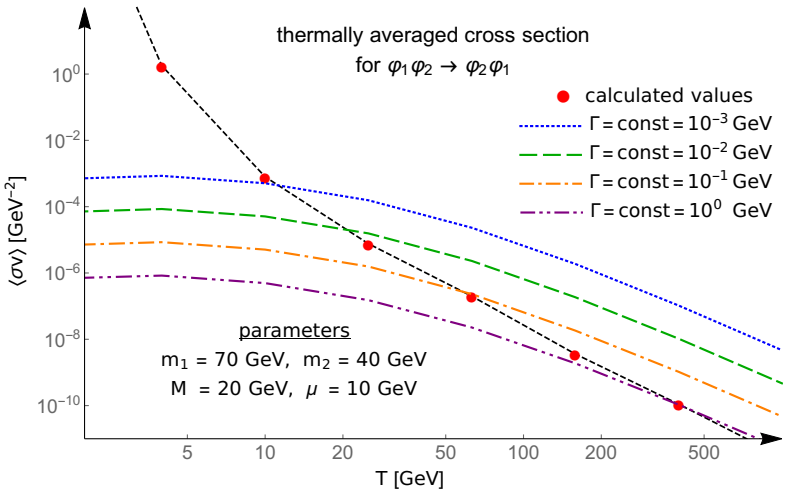


**Figure 5.7:** Thermally averaged cross section calculated for $\varphi_1\,\varphi_2 \to \varphi_2\,\varphi_1$ scattering using the proposed regularization method. The red dots denote the values calculated with the thermal width, with a black dashed line added to guide reader's eyes. The dotted blue, dashed green, dash-dotted orange and dash-double-dotted purple lines provide the cross section calculated under an assumption that the mediator has a non-zero, constant decay width equal to 1 MeV, 10 MeV, 100 MeV or 1 GeV, respectively. Values of parameters of the model are shown in the plot.

### 5.5.4 $X_0$ in VFDM

Here, we present the value of factor $X_0$ calculated for singular processes occurring in the VFDM model, see appendix A.

In fig. 5.8, the relevant vertices of the VFDM model are presented, while fig. 5.9 shows the spin factors, i.e., propagators with the part $i\,(p^2 - m^2 + i\Pi)^{-1}$ omitted, corresponding to particles of the model.

Tables 5.4 to 5.6 show the value of $X_0$, calculated for particle $X$, $\psi_+$ or $\psi_-$, respectively, being the mediator. Also the corresponding loop diagram and a condition for a given loop to provide a non-zero contribution to the regulator is included. In each case, a diagram of the $t$-channel singular process is depicted as well.

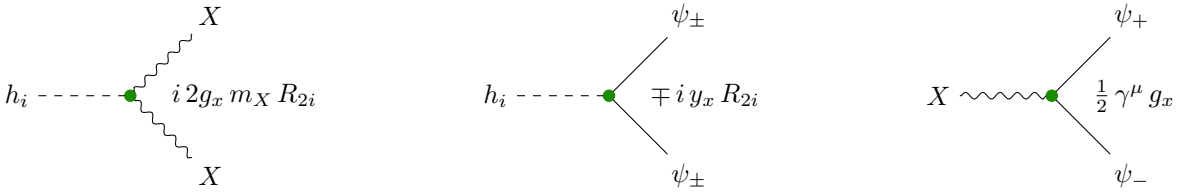


**Figure 5.8:** Vertices of the VFDM model relevant for calculation of the effective thermal width. For a detailed description of the variables, see appendix A.

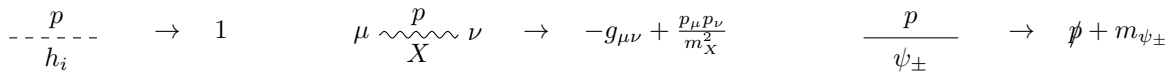


**Figure 5.9:** Spin factors, i.e., propagators with the part $i\,(p^2 - m^2 + i\Pi)^{-1}$ omitted, corresponding to particles of the VFDM model: $h_i$ $(i = 1, 2)$ (left), $X$ (centre), $\psi_\pm$ (right).

| mediator: $X$ | | | |
|---|---|---|---|
| loop | $X_0$ | condition | singular process |
| 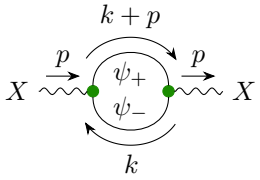  | $\frac{1}{6}\,\frac{g_x^2}{m_X^2}\,\left[(m_{\psi_+} - m_{\psi_-})^2 - m_X^2\right] \times \left[(m_{\psi_+} + m_{\psi_-})^2 + 2\,m_X\right]$ | $m_{\psi_+} > m_X + m_{\psi_-}$ | 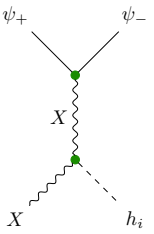  |
| 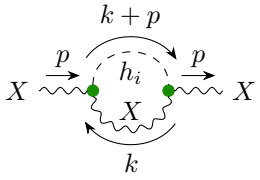  | $-\frac{1}{3}\,g_x^2\,R_{2i}^2\,\frac{m_{h_i}^4 - 4\,m_{h_i}^2\,m_X^2 + 12\,m_X^2}{m_X^2}$ | $m_{h_i} > 2\,m_X$ | |

**Table 5.4:** Factor $X_0$ (second column) corresponding to the one-loop self-energy (depicted in the first column) of the vector mediator $X$. In the third column, a condition for the masses for a given loop to provide a non-zero contribution to the effective width is provided. In the rightmost column, a diagram of the singular process mediated by the $t$-channel $X$ is shown.

| mediator: $\psi_+$ | | | |
|---|---|---|---|
| loop | $X_0$ | condition | singular process |
| 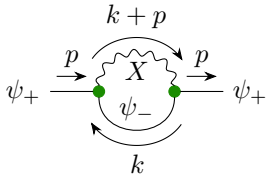 | $\frac{1}{4}\frac{g_x^2}{m_X^2}\left[m_X^2-(m_{\psi_+}-m_{\psi_-})^2\right]$ $\times\left[2\,m_X^2+(m_{\psi_+}+m_{\psi_-})^2\right]$ | $m_X > m_{\psi_+}+m_{\psi_-}$ | 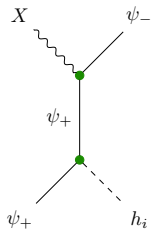 |
| 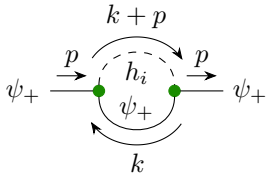 | $y_X^2\,R_{2i}^2\left(m_{h_i}^2-4\,m_{\psi_+}^2\right)$ | $m_{h_i} > 2\,m_{\psi_+}$ | |

**Table 5.5:** Like table 5.4, but with the fermion $\psi_+$ as a mediator.

| mediator: $\psi_-$ | | | |
|---|---|---|---|
| loop | $X_0$ | condition | singular process |
| 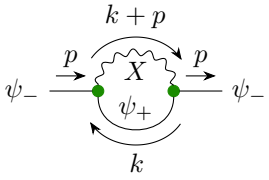 | $\frac{1}{4}\frac{g_x^2}{m_X^2}\left[m_X^2-(m_{\psi_+}-m_{\psi_-})^2\right]$ $\times\left[2\,m_X^2+(m_{\psi_+}+m_{\psi_-})^2\right]$ | $m_X > m_{\psi_+}+m_{\psi_-}$ | 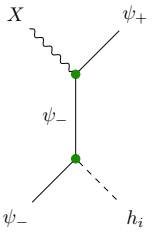 or 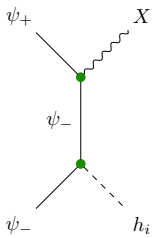 |
| 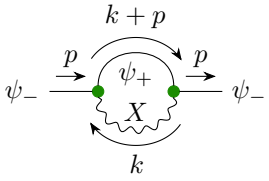 | $-\frac{1}{4}\frac{g_x^2}{m_X^2}\left[(m_{\psi_+}-m_{\psi_-})^2-m_X^2\right]$ $\times\left[(m_{\psi_+}+m_{\psi_-})^2+2\,m_X^2\right]$ | $m_{\psi_+} > m_X+m_{\psi_-}$ | |
| 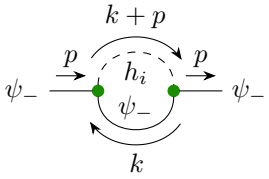 | $y_x^2\,R_{2i}^2\left(m_{h_i}^2-4\,m_{\psi_-}^2\right)$ | $m_{h_i} > 2\,m_{\psi_-}$ | |

**Table 5.6:** Like table 5.4, but with the fermion $\psi_-$ as a mediator.

The following fig. 5.10 present the effective width of particle $X$ as a function of momentum of the mediator and its mass. Figure 5.11 contains plots of cross section and thermally averaged cross section for the singular process $\psi_+ X \to \psi_- h_2$ mediated by a $t$-channel $X$.

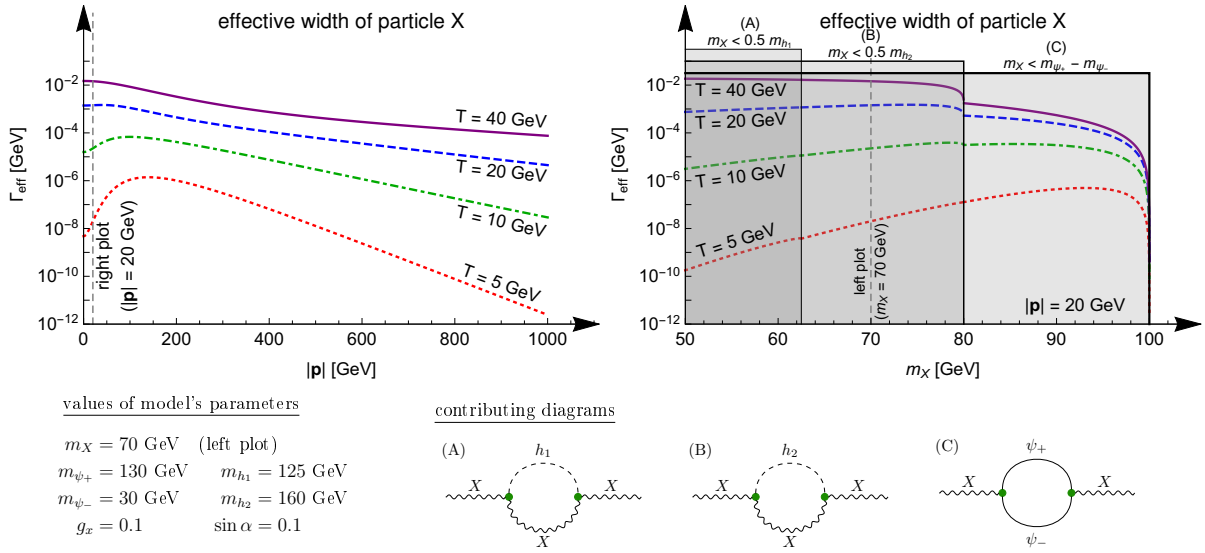


**Figure 5.10:** Effective width of particle $X$ as a function of momentum (left) and mass (right) of the particle. The solid purple, dashed blue, dot-dashed green and dotted red line correspond to different values of temperature: 40 GeV, 20 GeV, 10 GeV and 5 GeV, respectively. Parameters of the model and diagrams of the first-order loop corrections contributing to the effective width are provided below the plots. In the right plot, the regions that allow the given loop (denoted by $(A)$, $(B)$ or $(C)$) to contribute are marked with shading.

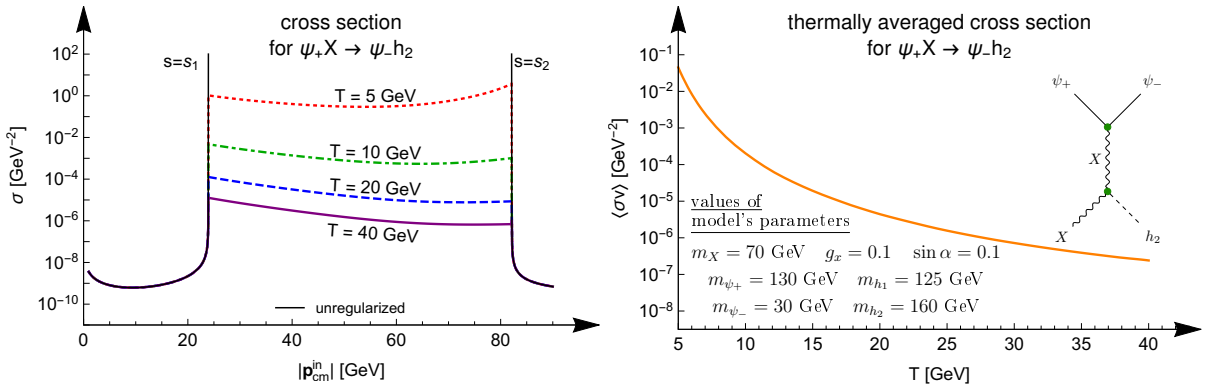


**Figure 5.11:** Cross section as a function of CM momentum (left) and thermally averaged cross section as a function of temperature (right) of the $t$-channel singular $\psi_+ X \to \psi_- h_2$ process mediated by the $t$-channel mediator $X$. In the left plot, the solid purple, dashed blue, dot-dashed green and dotted red line correspond to different values of temperature: 40 GeV, 20 GeV, 10 GeV and 5 GeV, respectively. The black solid line corresponds to the result before the regularization, which is infinite for $s_1 < s < s_2$. The parameters are provided in the right plot.

Analogously, the following fig. 5.12 present the effective width of particle $\psi_+$ as a function of momentum of the mediator and its mass. Figure 5.13 contains plots of cross section and thermally averaged cross section for the singular process $X\psi_+ \to \psi_- h_2$ mediated by a $t$-channel $\psi_+$. This set resembles the previous one but the masses of $X$ and $\psi_+$ have been switched to perform the comparison between cases of various spins: vector vs fermion mediator. Note that in notation used here, $\psi_+ X \to \psi_- h_2$ and $X\psi_+ \to \psi_- h_2$ denote two different diagrams.

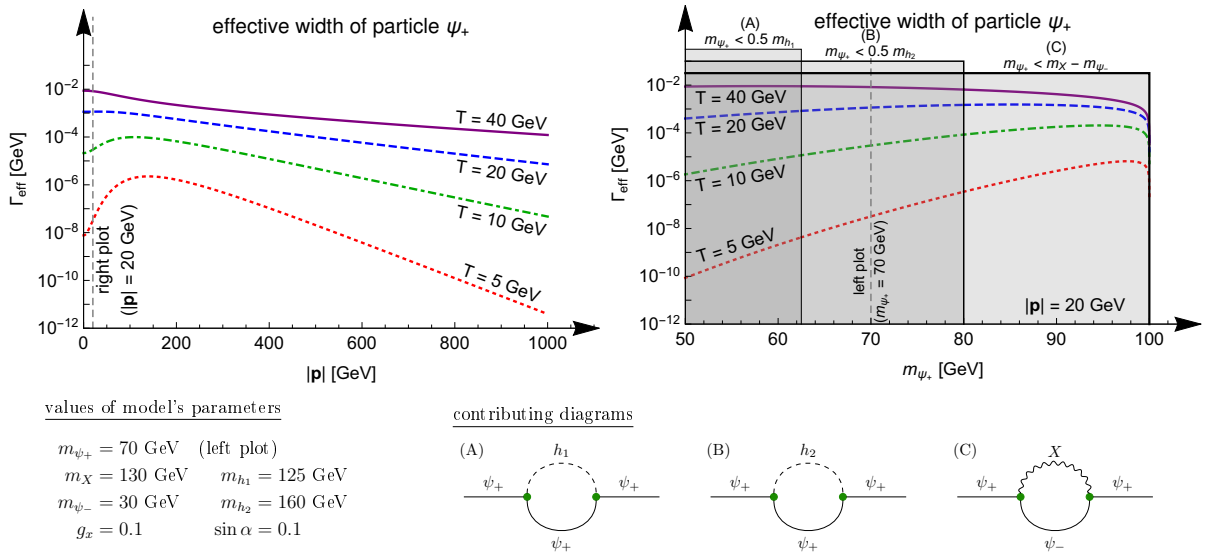


**Figure 5.12:** Like fig. 5.10, but for $\psi_+$ being the mediator.

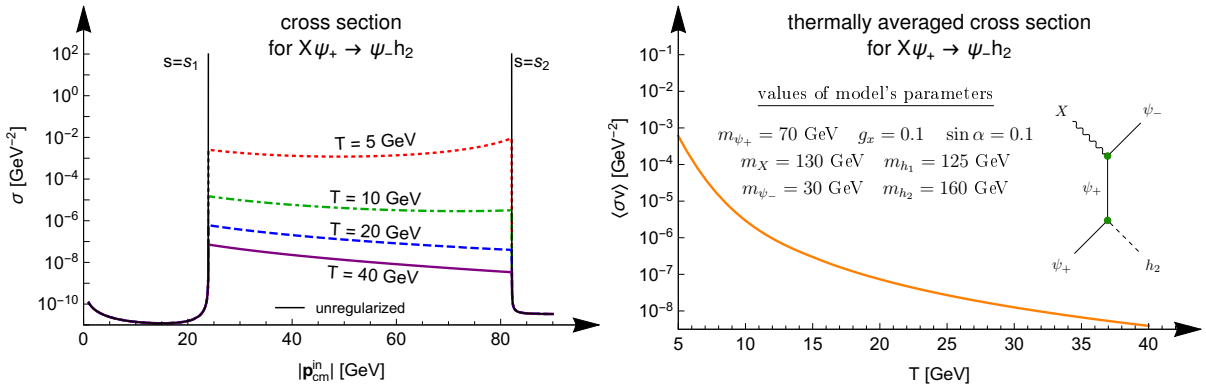


**Figure 5.13:** Like fig. 5.11, but for $X\psi_+ \to \psi_- h_2$ process mediated by $\psi_+$.

# Chapter 6

# Collider production and detection of Higgs-portal dark matter at the future $e^+e^-$ colliders

As mentioned in chapter 4, the planned lepton colliders may be particularly suitable for the purpose of searching for dark matter particles. Here, basing on based on publications [3, 4] and conference proceedings [5–7], we provide a detailed discussion of possible production of Higgs-portal dark matter at the future $e^+e^-$ colliders. Although we focus on the case of the ILC working at $\sqrt{s} = 250$ GeV, the methodology and results described here can be applied to the studies of other $e^+e^-$ colliders operating at similar energies, such as FCC-ee or CEPC (see section 4.3.3).

The goal of the work summarized in this chapter was to estimate the chance for dark particles to be produced at the future colliders efficiently enough to be noticed at detectors. Another question was whether it is possible to determine properties of the produced particles, such as their mass and spin. Taking into account limits and constraints imposed on considered models by the experimental results (like measured values of the DM relic density) and theoretical requirements (such as perturbativity of the theory), we have determined the area of the parameter space where efficient production of Higgs-portal dark particles at the ILC may be possible. We have estimated the maximal possible cross section for the considered DM production process and compared the cases of various spins.

The analysis has been carried out basing on three simple models of one-component DM, described in appendix B:

- pseudo-Goldstone DM model (shortened as pGDM and described in appendix B.1),
- fermion DM model (FDM, appendix B.2),
- vector DM model (VDM, appendix B.3).

They extend the SM to provide a dark particle interacting with the baryonic matter through the Higgs portal consisting of two Higgs-like scalar states: $h_1$, identified with the discovered Higgs particle, and $h_2$. All the models share exactly the same parameter space:

- $\sin\alpha$, sine of the scalar-sector mixing angle;
- $v_S$, the vacuum expectation value of the additional scalar $S$;
- $m_{\mathrm{DM}}$, mass of the dark particle;
- $m_{h_2}$, mass of the second Higgs state that couples mostly to the dark sector;

but differ in the spin of the proposed dark particle, which is 0, 1/2 and 1 for the pGDM, FDM and VDM models, respectively. This made it possible to investigate the influence of DM spin on detection probability, while keeping other relevant quantities, such as masses and couplings, the same for each model.

Note that even though dark matter may actually consist of more than one component (as discussed in section 3.3), so that none of the three models discussed here is fully appropriate, it is not unlikely that

one of them or a combination can serve as an approximation of a more complete theory, especially if one of the DM components has significantly smaller mass or stronger coupling to the SM than the others.

This chapter is organized as follows. In section 6.1, we discuss the limitations and constraints on the parameter space imposed by the experimental results and theoretical requirements (such as perturbativity of the theory). Then, for each model, we calculate the cross section for the analysed DM production process, the so-called Higgs-strahlung described in section 6.2. To estimate a chance for detection of the dark particles, the predicted numbers of DM production events have to be compared with the detection thresholds provided in section 6.3. Section 6.4 collects the results.

It appeared that most of the points of the parameter space are already excluded by the existing limits or lead to the DM production rate that is too small to enable detection. In spite of that, in the vicinity of $m_{h_1} \simeq 2\,m_{\mathrm{DM}}$ or $m_{h_2} \simeq 2\,m_{\mathrm{DM}}$, the amount of the produced dark particles may be not only sufficient, but even allow to distinguish between the cases of different spins.

## 6.1 Experimental and theoretical constraints

In this section, we discuss the main sources of constraints and limits on DM models, of both experimental and theoretical nature. Among them are:

- measurements of DM relic abundance (section 6.1.1),
- null-results of indirect-detection (section 6.1.2) and direct-detection (section 6.1.3) experiments,
- Higgs-measurements at the LHC, limiting invisible branching ratio of the Higgs particle (section 6.1.4),
- requirements of theoretical nature (section 6.1.5).

Here, we interpret those limits and constraints in the context of the pGDM, FDM and VDM models.

### 6.1.1 Relic abundance

The main process that governs evolution of dark matter abundance in the early Universe is the DM pair annihilation into the SM fermions, $\sigma(\mathrm{DM\ DM} \to \bar{f}f)$, which is depicted in fig. 6.1. Due to large masses of other SM particles coupled to Higgs, the other annihilation channels are strongly kinematically suppressed for DM masses considered here.

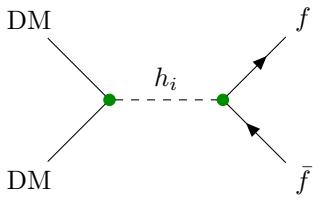


**Figure 6.1:** Annihilation of two dark paticles into a pair of SM fermion-antifermion through the Higgs portal. This is the main process responsible for dark matter abundance for the range of masses under consideration.

The thermally averaged cross section for this process can be calculated as

$$\langle\sigma v\rangle = \frac{n_c}{3}\frac{m_{\mathrm{DM}}m_f^2}{\pi}\cdot\mathcal{X}\cdot\frac{\left(m_{\mathrm{DM}}^2-m_f^2\right)^{3/2}}{\left[(4m_{\mathrm{DM}}^2-m_{h_1}^2)^2+m_{h_1}^2\Gamma_1^2\right]\left[(4m_{\mathrm{DM}}^2-m_{h_2}^2)^2+m_{h_2}^2\Gamma_2^2\right]}\cdot \times\begin{cases}12+\mathcal{O}\left[\left(\frac{m_{\mathrm{DM}}}{T}\right)^{-1}\right] & (\mathrm{pGDM})\\ 1+\mathcal{O}\left[\left(\frac{m_{\mathrm{DM}}}{T}\right)^{-1}\right] & (\mathrm{VDM})\\ \frac{9}{4}\left(\frac{m_{\mathrm{DM}}}{T}\right)^{-1}+\mathcal{O}\left[\left(\frac{m_{\mathrm{DM}}}{T}\right)^{-2}\right] & (\mathrm{FDM})\end{cases}, \tag{6.1}$$

where $n_c = 1(3)$ denotes the number of colour degrees of freedom for $f$ being a lepton (quark), while quantity $\mathcal{X}$ is defined by the following formula:

$$\mathcal{X} \equiv (\sin\alpha\cos\alpha)^2 \frac{\left[(m_{h_1}^2 - m_{h_2}^2)^2 + (m_{h_1}\Gamma_1 - m_{h_2}\Gamma_2)^2\right]}{v^2 v_S^2} \,. \tag{6.2}$$

At the tree level, this formula reduces to a square of the coupling constant $\kappa$ given by eq. (B.29a).

The 2018 Planck results [10], discussed in section 3.1.2, provide a value of the relic abundance

$$\left(\Omega h^2\right)_{\rm DM}^{\rm obs} = 0.1200 \pm 0.0012 \,. \tag{6.3}$$

According to eq. (2.93), if

$$\langle\sigma v\rangle_{{\rm DM}\to b\bar{b}} = \sigma_0 (m_{\rm DM}/T)^{-n} \,, \tag{6.4}$$

the relic density should be approximately equal to

$$\Omega h^2 \simeq \frac{8.52\times10^{-11}\ {\rm GeV}^{-2}}{\sigma_0}\,(n+1)\,\frac{(m_{\rm DM}/T_f)^{n+1}}{g_*(T_f)^{1/2}} \,. \tag{6.5}$$

where $T_f \sim m_{\rm DM}/25$ is the DM temperature at the freeze-out. Combining eqs. (6.3) and (6.5), we obtain

$$\sigma_0 = 7.10\times10^{-10}\ {\rm GeV}^{-2}\,(n+1)\,\frac{(m_{\rm DM}/T_f)^{n+1}}{g_*(T_f)^{1/2}} \,, \tag{6.6}$$

which means that

$$\begin{aligned}\langle\sigma v\rangle\Big|_{\rm now} &= 7.10\times10^{-10}\ {\rm GeV}^{-2}\,(n+1)\,\frac{(m_{\rm DM}/T_f)^{n+1}}{g_*(T_f)^{1/2}}\,(T_0/m_{\rm DM})^n \\ &\simeq 1.92\times10^{-9}\ {\rm GeV}^{-2}\,(n+1)\,(T_0/T_f)^n \,,\end{aligned} \tag{6.7}$$

assuming $m_{\rm DM}/T_f \simeq 25$ and $g_*(T_f) \simeq 85$. Note that the value of $g_*$ is slightly different from the one assumed in section 2.3.4, but, as stated there, the precise value is of small importance for cold dark matter since $x_f$ depends on $g_*$ only logarithmically. Parameter $n$ is defined as 0 for bosonic dark matter (which is the case of the pGDM and VDM models) and 1 for fermion dark matter (FDM).

The leading contribution to eq. (6.1) comes from annihilation into $b\bar{b}$ due to high coupling to Higgs while still light enough to not be kinematically suppressed. Thus, we can apply eq. (6.7) to eq. (6.1) to obtain

$$\begin{aligned}\mathcal{X} \simeq X(\Omega_0^{\rm DM}) \equiv\ & \frac{\left[(m_{h_1}^2 - 4m_{\rm DM}^2)^2 + m_{h_1}^2\Gamma_1^2\right]\,\left[(m_{h_2}^2 - 4m_{\rm DM}^2)^2 + m_{h_2}^2\Gamma_2^2\right]}{m_{\rm DM}(m_{\rm DM}^2 - m_b^2)^{3/2}} \\ & \times 3.5\cdot10^{-10}\ {\rm GeV}^{-4} \times \begin{cases} 0.83 & ({\rm pGDM}) \\ 1 & ({\rm VDM}) \\ 22.2 & ({\rm FDM}) \end{cases} \,.\end{aligned} \tag{6.8}$$

### 6.1.2 Indirect detection

As discussed in the previous section, assuming the freeze-out temperature to be of the order of $m_{\rm DM}/25$, the present value of the cross section for DM annihilation is fixed by eq. (6.7) to depend on $m_{\rm DM}$ only. Thus, the null-results of the ID experiments (see section 4.2), which limit the annihilation cross section, can be translated into limits on DM mass. Taking into account the $b\bar{b}$ data of the Fermi-LAT experiment [178] that are provided in fig. 6.2, we obtain the following lower limit for the mass of bosonic DM particles in the pGDM and VDM models:

$$m_{\rm DM} \gtrsim 20\ {\rm GeV} \,. \tag{6.9}$$

From now on, only the values that exceed this limit are considered.

The factor of $T_0/T_f$ present in the cross section calculated within the FDM model (eq. (6.7) with $n = 1$) suppresses the obtained value by orders of magnitude ($T_f$ should be of the order of $1 - 10$ GeV while the present temperature of the Universe, $T_0$, is of the order of $10^{-13}$ GeV), so that it is consistent

with the null-results of the ID experiments for any mass. Hence, the mass of fermionic DM is not limited by the ID experiments. Nevertheless, for consistency, we consider the same range of masses for both fermionic and bosonic models.

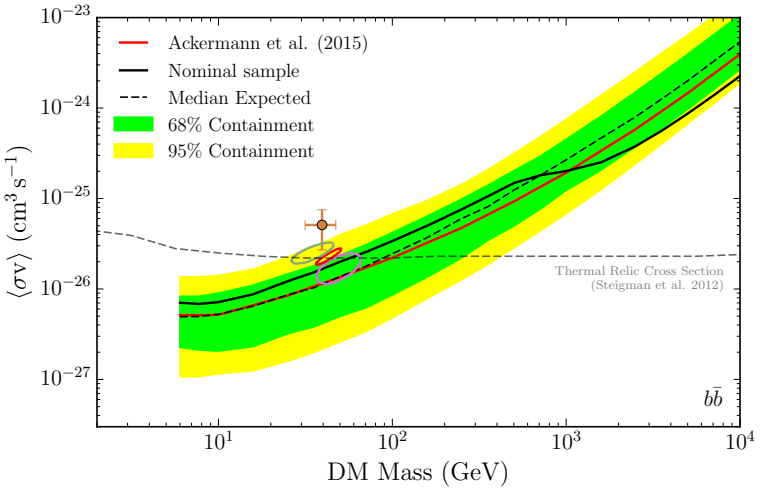


**Figure 6.2:** The upper limit on the DM annihilation cross section, coming from null-results of the Fermi-LAT experiment [178], used in this analysis. The dashed gray line denotes the value leading to the correct relic density of bosonic DM, as calculated in [110]. Comparison between the limit and the expected value provides a lower limit for bosonic DM mass. For fermionic dark matter, the value of cross section that provides the correct relic density is orders of magnitude smaller than in the bosonic case (see eq. (6.7)).

### 6.1.3 Direct detection

The current null-results of the DD search for dark matter (see section 4.1) lead to limits on DM parameters range.

For the one-component DM models discussed in this chapter (described in appendices B.1 to B.3), the spin-independent cross-section for the DM-nucleon scattering is equal to

$$\sigma_{\rm SI} \simeq \frac{\mu^2 f_N^2}{\pi} \cdot \mathcal{X} \cdot \frac{m_{\rm DM}^2 m_N^2}{m_{h_1}^4 m_{h_2}^4} \begin{cases} \left[\frac{\mathcal{A}}{64\pi^2 v v_S^2}\right]^2 & \text{(pGDM)} \\ 1 & \text{(VDM), (FDM)}\,, \end{cases} \tag{6.10}$$

with $m_N$ denoting the nucleon mass, $\mu$ standing for the reduced mass defined for the DM-nucleon system, and the form factor $f_N$ approximated by $f_N \simeq 0.3$ GeV. The momentum transfer and decay widths in the denominator are omitted as negligible in comparison to masses.

In the limit of zero momentum transfer, the cross section for the pGDM model vanishes [179, 180]. Hence, 1-loop results are used to calculate the factor $\mathcal{A}$, defined as in [179][1] in the following way:

$$\mathcal{A} = a_1 \cdot \mathcal{C}_{12} + a_2 \cdot \mathcal{D}_{112} + a_3 \cdot \mathcal{D}_{122}\,, \tag{6.11}$$

where the mass-dependent functions $\mathcal{C}$ and $\mathcal{D}$ are defined in appendix G and the coefficients $a_1$, $a_2$, $a_3$ are given by

$$a_1 = \; 4\,(m_{h_1}^2 \sin^2\alpha + m_{h_2}^2 \cos^2\alpha)\left[2v(m_{h_1}^2 \sin^2\alpha + m_{h_2}^2 \cos^2\alpha) - (m_{h_1}^2 - m_{h_2}^2) v_S \sin 2\alpha\right]\,, \tag{6.12a}$$

$$a_2 = -2\,m_{h_1}^4 \sin\alpha\left[(m_{h_1}^2 + 5m_{h_2}^2) v_S \cos\alpha - (m_{h_1}^2 - m_{h_2}^2)(v_S \cos 3\alpha + 4v \sin^3\alpha)\right]\,, \tag{6.12b}$$

$$a_3 = \; 2\,m_{h_2}^4 \cos\alpha\left[(5m_{h_1}^2 + m_{h_2}^2) v_S \sin\alpha - (m_{h_1}^2 - m_{h_2}^2)(v_S \sin 3\alpha + 4v \cos^3\alpha)\right]\,. \tag{6.12c}$$

Note that the sign of $\sin\alpha$ is relevant here. However, the above formulae are used only to show (see the right panel of fig. 6.3) that for the pGDM model the value of $\mathcal{X}$ saturating the DD limit on $\sigma_{\rm SI}$ is much greater than the one corresponding to the correct relic density. This conclusion remains valid regardless of the sign of $\sin\alpha$.

[1] The loop integrals in Appendix B of [179] are defined with the wrong factor $1/(2\pi)^4$ instead of the correct $1/(i\pi^2)$. Nevertheless, the results in the main text of that paper are correct.

The XENON1T limit [75] on the spin-independent cross section for DM-nucleon interaction, $\sigma_{\rm SI}$, is plotted in the left panel of fig. 6.3. For $m_{\rm DM} \gtrsim 40$ GeV, the limit can be approximately parametrized in the following way:

$$\frac{\sigma_{\rm SI}^{\rm max}}{1\ {\rm cm}^2} \simeq 8.5 \times 10^{-49} \frac{m_{\rm DM}}{1\ {\rm GeV}} \ . \tag{6.13}$$

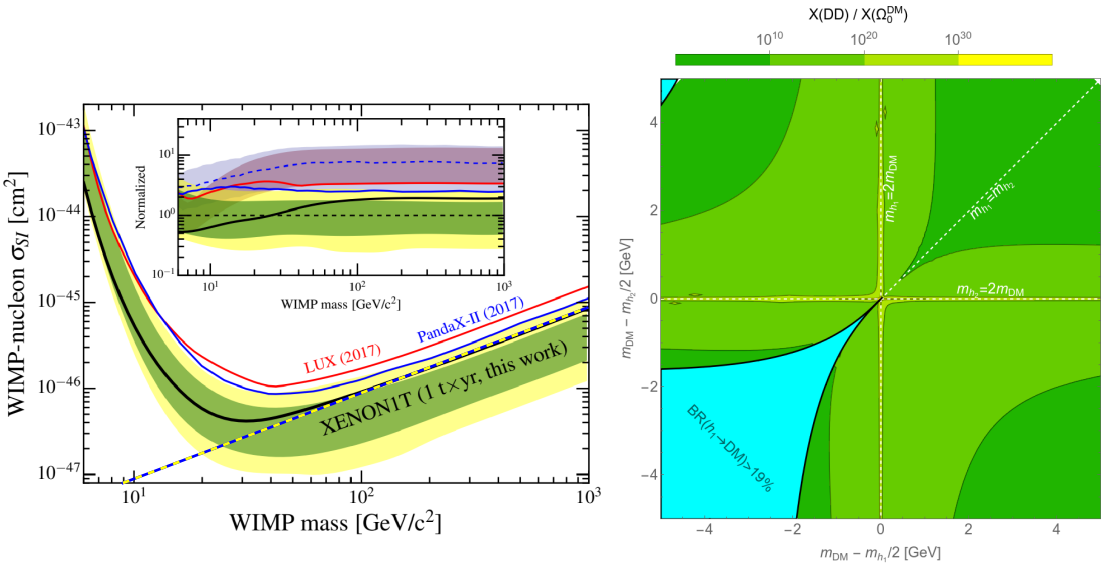


**Figure 6.3: Left:** the DD limits from the XENON experiment [75]. The yellow-blue line corresponds to the used approximation: $\sigma_{\rm SI} \simeq \frac{m_{\rm DM}}{1\ {\rm GeV}}\, 10^{-48.05}\ {\rm cm}^2$. **Right:** Comparison between $\mathcal{X}({\rm DD})$ (defined in eq. (6.14)), which is the value of the variable $\mathcal{X}$ that saturates the DD limit, and $\mathcal{X}(\Omega_0^{\rm DM})$ (see eq. (6.8)), the one leading to the correct relic density, in the pGDM model. As $\mathcal{X}({\rm DD})$ is always much greater than $\mathcal{X}(\Omega_0)$, DD does not restrict the parameter space of that model.

This leads to the following limit on $\mathcal{X}$:

$$\begin{aligned} \mathcal{X} \lesssim \mathcal{X}({\rm DD}) &\equiv \frac{m_{h_1}^4\, m_{h_2}^4}{m_{\rm DM}\, m_N^2\, f_N^2}\, \frac{\pi}{\mu^2} \times 8.5 \times 10^{-49}\, \frac{{\rm cm}^2}{\rm GeV} \times \begin{cases} \left[\frac{\mathcal{A}}{64\pi^2 v v_S^2}\right]^{-2} & ({\rm pGDM}) \\ 1 & ({\rm VDM}), ({\rm FDM}) \end{cases}, \\ &\simeq \frac{m_{h_2}^4}{m_{\rm DM}} \cdot 2.4 \cdot 10^{-11}\ {\rm GeV}^{-3} \times \begin{cases} \left[\frac{\mathcal{A}}{64\pi^2 v v_S^2}\right]^{-2} & ({\rm pGDM}) \\ 1 & ({\rm VDM}), ({\rm FDM}) \end{cases}. \end{aligned} \tag{6.14}$$

As already mentioned, in the case of the pGDM model, this value is always much larger than $X(\Omega_0^{\rm DM})$ provided in eq. (6.8), which has been proved numerically, see the right panel of fig. 6.3. Hence, in that case, the DD limit does not restrict the parameter range. For the FDM or VDM model, the DD limit has to be taken into account, which is done numerically by calculating $\sigma_{\rm SI}$ (as given by eq. (6.10)) and comparing with the limiting value (6.13) at each considered point of the parameter space.

### 6.1.4 LHC measurements

Here, we discuss the implications of the LHC measurements of the Higgs boson decay and production rates, which are consistent with the SM predictions within the achieved accuracy (see section 4.3.2).

In the case of multi-Higgs models (in particular, our Higgs-portal DM models), that consistency implies the following condition on the scalar-sector mixing angle $\alpha$ [181, 182]:

$$\cos^2\alpha = 1.09 \pm 0.11 \,. \tag{6.15}$$

In the SM, the value would be just 1. At the $2\sigma$ C.L., this result is equivalent to

$$\cos^2\alpha > 0.87 \tag{6.16}$$

This means that the sine of the mixing angle should satisfy

$$\sin^2\alpha < 0.13 \,. \tag{6.17}$$

In this dissertation, a slightly stricter limit of is used:

$$\sin\alpha < 0.3 \,. \tag{6.18}$$

If the SM-like Higgs boson $h_1$ is allowed to decay into two dark particles (i.e., $m_{h_1} > 2\,m_{\mathrm{DM}}$), the decay widths calculated within the models:

$$\Gamma_{h_i\to\mathrm{DM}} = \frac{R_{2i}^2}{v_S^2}\frac{m_{h_i}^3}{32\pi}\sqrt{1-\frac{4m_{\mathrm{DM}}^2}{m_{h_i}^2}} \times \begin{cases} 1 & \text{(pGDM)} \\ 1 - 4\frac{m_{\mathrm{DM}}^2}{m_{h_i}^2} + 12\left(\frac{m_{\mathrm{DM}}^2}{m_{h_i}^2}\right)^2 & \text{(VDM)} \\ 2\frac{m_{\mathrm{DM}}^2}{m_{h_i}^2}\left(1 - 4\frac{m_{\mathrm{DM}}^2}{m_{h_i}^2}\right) & \text{(FDM)} \end{cases} \tag{6.19}$$

should be compared with the 95% C.L. LHC limit on invisible Higgs decays [138]:

$$\mathrm{BR}(h_1 \to \mathrm{inv}) < 19\% \,. \tag{6.20}$$

To obtain the results presented in this chapter, that comparison has been performed numerically.

### 6.1.5 Theoretical constraints

All the decay widths and cross sections used in this chapter are calculated in the lowest order of the perturbation theory. For these results to be meaningful, the models has to satisfy perturbativity conditions. First, let us consider the coupling between the Higgs states and the dark particles. For the FDM and VDM models, the coupling constants $y_x$ and $g_x$, respectively, must satisfy:

$$y_x < 4\pi \,, \qquad g_x < 4\pi. \tag{6.21}$$

In both models it implies that

$$v_S > \frac{m_{\mathrm{DM}}}{4\pi} \,. \tag{6.22}$$

In the pGDM model, the relevant coupling constant is equal to $m_{h_i}^2/v_S$ multiplied by the appropriate function of the scalar-sector mixing angle (cf. fig. B.1). In that case, we demand that

$$m_{h_i}/v_S < 4\pi \qquad (i = 1, 2) \,. \tag{6.23}$$

The perturbativity also requires that the scalar-potential quartic couplings $\lambda_S$, $\kappa$ are equal to at most $4\pi$. Hence, the set of the perturbativity conditions is:

$$\underbrace{\frac{m_{\mathrm{DM}}}{v_S} < 4\pi}_{\text{for VDM and FDM}} \,, \qquad \underbrace{\frac{m_{h_i}}{v_S} < 4\pi}_{\text{for pGDM}} \,, \qquad \lambda_S < 4\pi \,, \qquad |\kappa| < 4\pi \,. \tag{6.24}$$

Also the vacuum-stability conditions, discussed in appendices B.1 to B.3, should be taken into account. Equations (B.7) and (B.25) (for the pGDM model), (B.37), (B.45) and (B.47) (for the FDM model), (A.12), (A.20) and (A.21) (for the VDM model) provide:

- for all models:

$$\lambda_H > 0\,, \qquad \lambda_S > 0\,, \qquad \kappa > -2\sqrt{\lambda_H \lambda_S}\,, \qquad 4\,\lambda_H\,\lambda_S - \kappa^2 > 0\,, \tag{6.25}$$

- for the pGDM model:

$$2\lambda_S \mu_H^2 - \kappa(\mu_S^2 - 2\mu^2) > 0\,, \qquad 2\lambda_H(\mu_S^2 - 2\mu^2) - \kappa\mu_H^2 > 0\,, \tag{6.26}$$

- for the FDM and VDM models:

$$2\lambda_S \mu_H^2 - \kappa\mu_S^2 > 0\,, \qquad 2\lambda_H \mu_S^2 - \kappa\mu_H^2 > 0\,. \tag{6.27}$$

Those conditions, expressed in terms of the input parameters $m_{h_1}$, $m_{h_2}$, $v$, $v_S$, $m_{\mathrm{DM}}$ and $\sin\alpha$, are automatically satisfied:

$$0 < \lambda_H \qquad \Leftrightarrow \qquad 0 < \frac{m_{h_1}^2 \cos^2\alpha + m_{h_2}^2 \sin^2\alpha}{2v^2}\,, \tag{6.28a}$$

$$0 < \lambda_S \qquad \Leftrightarrow \qquad 0 < \frac{m_{h_1}^2 \sin^2\alpha + m_{h_2}^2 \cos^2\alpha}{2v_S^2}\,, \tag{6.28b}$$

$$0 < 4\lambda_H\lambda_S - \kappa^2 \qquad \Leftrightarrow \qquad 0 < \frac{m_{h_1}^2 m_{h_2}^2}{v^2 v_S^2}\,, \tag{6.28c}$$

$$0 < \begin{cases} 2\lambda_S\mu_H^2 - \kappa(\mu_S^2 - 2\mu^2) & \text{(pGDM)} \\ 2\lambda_S\mu_H^2 - \kappa\mu_S^2 & \text{(VDM, FDM)} \end{cases} \qquad \Leftrightarrow \qquad 0 < \frac{m_{h_1}^2 m_{h_2}^2}{2v_S^2}\,, \tag{6.28d}$$

$$0 < \begin{cases} 2\lambda_H(\mu_S^2 - 2\mu^2) - \kappa\mu_H^2 & \text{(pGDM)} \\ 2\lambda_H\mu_S^2 - \kappa\mu_H^2 & \text{(VDM, FDM)} \end{cases} \qquad \Leftrightarrow \qquad 0 < \frac{m_{h_1}^2 m_{h_2}^2}{2v^2}\,. \tag{6.28e}$$

This happens because choosing the input parameters we implicitly assumed that $v^2$, $v_S^2$, $m_{h_1}^2$, and $m_{h_2}^2$ are all positive, which is equivalent to stability of the vacuum state.

In the pGDM model, two more conditions must be satisfied to ensure that the chosen minimum is the global one:

$$2\lambda_H\mu_S^2 - \kappa\mu_H^2 > 0\,. \tag{6.29}$$

$$\mu_S^2 > 0\,. \tag{6.30}$$

In terms of the input parameters it means that:

$$0 < 2\lambda_H\mu_S^2 - \kappa\mu_H^2 \quad \Leftrightarrow \quad 0 < \frac{2m_{h_1}^2 m_{h_2}^2 - (m_{h_1}^2 + m_{h_2}^2)m_{\mathrm{DM}}^2 + (-m_{h_1}^2 + m_{h_2}^2)m_A^2\cos(2\alpha)}{4v^2}\,, \tag{6.31}$$

$$0 < \mu_S^2 \quad \Leftrightarrow \quad 0 < \frac{1}{2}m_{h_1}^2\sin^2\alpha + \frac{1}{2}m_{h_2}^2\cos^2\alpha + \frac{1}{4}\frac{v}{v_S}(m_{h_1}^2 - m_{h_2}^2)\sin 2\alpha - \frac{1}{2}m_{\mathrm{DM}}^2\,. \tag{6.32}$$

Figure 6.4 presents results of numerical tests showing that these inequalities are satisfied for within the parameter range under consideration.

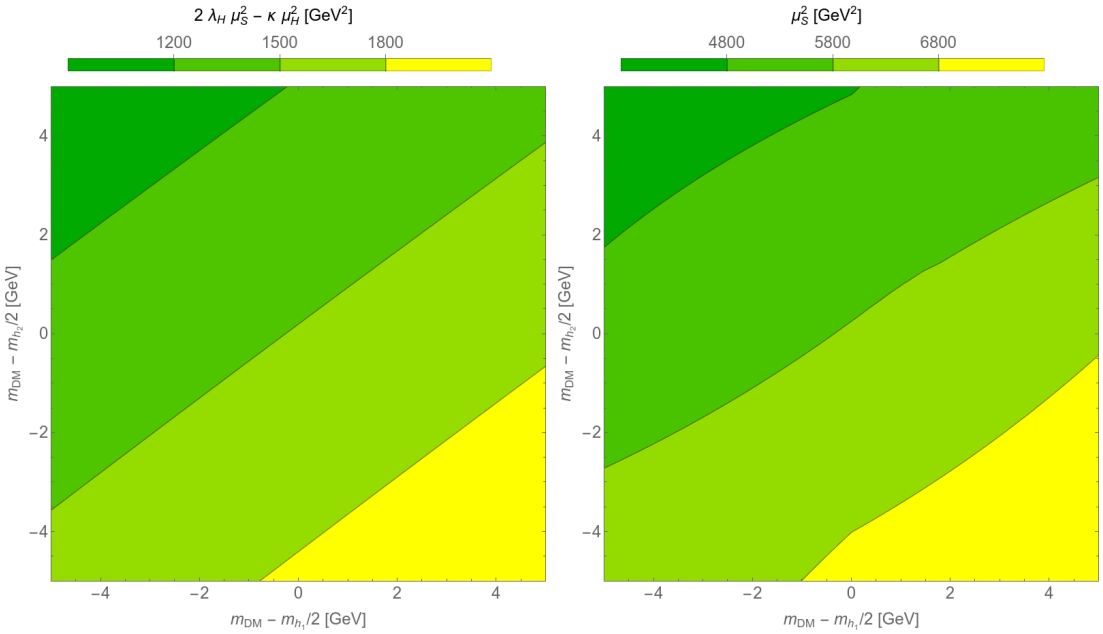


**Figure 6.4:** These plot show that the conditions (6.31) (left pannel) and (6.32) (right pannel) are always true for the considered parameters range (this is equivalent to positiveness of the plotted quantities). We assume $\sin\alpha = 0.3$ and calculate $v_S$ from eq. (6.8).

## 6.2 Production process

This analysis is focused on the so-called Higgs-strahlung process (or: mono-$Z$ emission), in which dark particles could be produced along with a $Z$ boson [183–189]. The process is depicted in fig. 6.5.

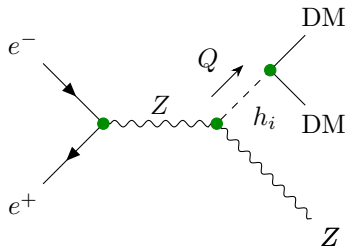


**Figure 6.5:** The Higgs-strahlung process, a DM production channel discussed in this chapter. The dark particle denoted by DM can be $A$, $X$ or $\psi$, depending on the model, and $h_i$ $(i = 1, 2)$ denotes one of the scalar states, carrying four-momentum $Q$.

Although the $Z$ boson is not directly registered, as it is an unstable particle that decays before reaching the detector, we assume that it is possible to reconstruct energy of the boson from the collected data. Consequently, the recoil mass, i.e., invariant mass of the pair of dark particles equal to $\sqrt{Q^2}$, is a known quantity.

The largest number of production events is expected at the peak of the Higgs-strahlung process. The cross section is given by

$$\begin{aligned}\sigma_{\mathrm{SM}}(s, Q^2) \equiv\ & \frac{g_V^2 + g_A^2}{24\pi}\left(\frac{g^2}{\cos\theta_W^2}\right)^2 \\ & \times \frac{\lambda^{1/2}(s, Q^2, m_Z^2)}{8s^2}\,\frac{12\,s\,m_Z^2 + \lambda(s, Q^2, m_Z^2)}{(s - m_Z^2)^2}\,,\end{aligned} \tag{6.33}$$

where $\lambda$ is the Källén triangle function defined by eq. (0.4). and $g_V$, $g_A$ denote, respectively, the vector and axial coupling of electron to the Z boson.

For $Q^2 = m_{h_1}^2$, the value of $\sigma_{\rm SM}$ is maximal around $240 - 250$ GeV. Hence, we focus on the case of colliders operating with the CM energy close to that value, specializing to the case of the ILC operating at $\sqrt{s} = 250$ GeV.

The differential cross section for that process is given by

$$\frac{d\sigma}{dQ^2} = \frac{\sigma_{\rm SM}(s,Q^2)\,v^2}{32\pi^2} \frac{\mathcal{X}\cdot\left(Q^2\right)^2}{\left[(Q^2-m_{h_1}^2)^2+(m_{h_1}\Gamma_1)^2\right]\left[(Q^2-m_{h_2}^2)^2+(m_{h_2}\Gamma_2)^2\right]} \times \\ \times \sqrt{1-4\frac{m_{\rm DM}^2}{Q^2}} \cdot \begin{cases} 1 & \text{(pGDM)} \\ 1-4\frac{m_{\rm DM}^2}{Q^2}+12\left(\frac{m_{\rm DM}^2}{Q^2}\right)^2 & \text{(VDM)} \\ 2\frac{m_{\rm DM}^2}{Q^2}\left(1-4\frac{m_{\rm DM}^2}{Q^2}\right) & \text{(FDM)} \end{cases} . \tag{6.34}$$

The quantity $\mathcal{X}$ is given by eq. (6.2). The cross section for the SM process of Higgs boson production, $e^+e^- \to Zh_{\rm SM}$, is denoted by $\sigma_{\rm SM}(s,Q^2)$. Here, $s$ denotes the CM energy of the process and the Higgs mass is assumed to be equal to $m_{h_{\rm SM}} = \sqrt{Q^2}$. This cross section is given by eq. (6.33).

$$\sigma_{\rm SM}(s,Q^2) \equiv \frac{g_V^2+g_A^2}{24\pi}\left(\frac{g^2}{\cos\theta_W^2}\frac{1}{s-m_Z^2}\right)^2 \times \\ \times \frac{\lambda^{1/2}(s,Q^2,m_Z^2)\left[12\,s\,m_Z^2+\lambda(s,Q^2,m_Z^2)\right]}{8s^2} , \tag{6.35}$$

### 6.2.1 Polarized beams

At linear lepton colliders, polarized beams are proposed to be used to improve the signal-to-background ratio [147, 149]. In such a case, the cross section for the DM production process should be multiplied by the factor

$$\frac{(1+P_+)(1-P_-)(g_V+g_A)^2+(1-P_+)(1+P_-)(g_V-g_A)^2}{2\,(g_V^2+g_A^2)} , \tag{6.36}$$

where $P_-$ and $P_+$ denote polarizations of the electron and the positron beam, respectively, defined as in [156], and are in the range $[-1,1]$. For the ILC, the predicted polarizations are $P_+ = -30\%$ and $P_- = 80\%$, so that the factor (6.36) is approximately 1.5. Although, because of reduced luminosity, the resulting number of production events will be smaller, some of the background processes (e.g., the one depicted in the right panel of fig. 6.6) are suppressed; see a short discussion in section 4.3.3.

The results presented in section 6.4 are expressed in terms of the ratio $\sigma/\sigma_{\rm SM}$. Therefore, it does not matter whether the polarization factor (6.36) is used to perform the calculations, because it appears both in $\sigma$ and $\sigma_{\rm SM}$.

### 6.2.2 Resonant propagator

We observe that the cross section eq. (6.34) is enhanced if $m_{h_2}$ is close to $m_{h_2}$ and $h_i$ is on-shell, so that $Q^2 \simeq m_{h_{1,2}}^2$. On the other hand, according to eqs. (B.29a) and (B.50), $m_{h_1} = m_{h_2}$ means that the portal coupling $\kappa$ should vanish, making DM completely decoupled from the SM and, thus, making the cross section zero. Those two statements seem to contradict, which deserves a deeper investigation.

To resolve the contradiction, let us examine the propagator of the mediating scalar state $h_i$ in the limit of $m_{h_2} \to m_{h_1}$. It appears that in that limit, when calculating the resummed propagator of $h_i$, we should take into account not only the diagonal ($i = j$), but the off-diagonal terms as well. In the case of our process, the matrix element reads

$$\mathcal{M} = \mathcal{M}_{e^+e^-\to Zh_i}(Q^2)\cdot\Delta_{ij}(Q^2)\cdot\mathcal{M}_{h_j\to XX}(Q^2) = \\ = \mathcal{M}_{e^+e^-\to Zh}(Q^2)\cdot\underbrace{R_{1i}\cdot\Delta_{ij}(Q^2)\cdot R_{2j}}_{\widehat{\Delta}(Q^2)}\cdot\mathcal{M}_{h\to XX}(Q^2) , \tag{6.37}$$

where $\Delta_{ij}$ is the propagator and $\widehat{\Delta}$ denotes the propagator contracted with the scalar-sector mixing

matrix $R$. This contracted propagator has the following form, derived in [190, 191]:

$$\begin{aligned}\widehat{\Delta}(Q^2) &= R_{1i}R_{2j}\cdot\frac{1}{\det D}\overbrace{\begin{bmatrix} Q^2-m_{h_2}^2+\Pi_{22}(Q^2) & -\Pi_{12}(Q^2) \\ -\Pi_{21}(Q^2) & s-m_{h_1}^2+\Pi_{11}(Q^2)\end{bmatrix}}^{D}_{ij} = \\ &= \sin\alpha\cos\alpha\cdot\frac{(m_{h_1}^2-m_{h_2}^2)-\left[\Pi_{11}(Q^2)-\Pi_{22}(Q^2)\right]+\left[\tan\alpha\cdot\Pi_{12}(Q^2)-\cot\alpha\cdot\Pi_{21}(Q^2)\right]}{\left[Q^2-m_{h_1}^2+\Pi_{11}(Q^2)\right]\left[Q^2-m_{h_2}^2+\Pi_{22}(Q^2)\right]-\Pi_{12}(Q^2)\Pi_{21}(Q^2)}\,.\end{aligned} \tag{6.38}$$

Here, $\Pi_{ij}$ stands for the self-energy imaginary part of the $h_ih_j$ (times $i$). They are provided in appendix H. Important is that all of them are roughly the same order of magnitude as $m_{h_i}\Gamma_i$.

From the optical theorem it follows that $\Pi_{ii}(Q^2=m_{h_i}^2)=im_{h_i}\Gamma_i$.

It can be easily observed that if $|m_{h_1}-m_{h_2}|\gg\Gamma_1,\Gamma_2$, the numerator is dominated by the $m_{h_1}^2-m_{h_2}^2$ term, while in the denominator the $\Pi_{12}\Pi_{21}$ term can be neglected, which leads to the formula

$$\widehat{\Delta}(Q^2)\simeq\sin\alpha\cos\alpha\cdot\frac{m_{h_1}^2-m_{h_2}^2}{(Q^2-m_{h_1}^2+\Pi_{11})(Q^2-m_{h_2}^2+\Pi_{22})}\,, \tag{6.39}$$

which can be rewritten in the following way

$$\widehat{\Delta}(Q^2)\simeq\widehat{\Delta}^{(BW)}(Q^2)\equiv\sin\alpha\cos\alpha\cdot\left[\frac{1}{Q^2-m_{h_1}^2+im_{h_1}\Gamma_1}-\frac{1}{Q^2-m_{h_2}^2+im_{h_2}\Gamma_2}\right]\,, \tag{6.40}$$

given that the terms proportional to the widths are dropped in the numerator.

However, in the $m_{h_2}\to m_{h_1}$ limit the full formula eq. (6.38) should be used. Then, the propagator becomes

$$\widehat{\Delta}(Q^2)\xrightarrow{m_{h_2}\to m_{h_1}}\sin\alpha\cos\alpha\cdot\frac{-\left[\Pi_{11}(Q^2)-\Pi_{22}(Q^2)\right]+\left[\tan\alpha\cdot\Pi_{12}(Q^2)-\cot\alpha\cdot\Pi_{21}(Q^2)\right]}{\left[Q^2-m_{1,2}^2+\Pi_{11}(Q^2)\right]\left[Q^2-m_{1,2}^2+\Pi_{22}(Q^2)\right]-\Pi_{12}(Q^2)\Pi_{21}(Q^2)}\,. \tag{6.41}$$

In appendix H it is shown that this limiting value vanishes:

$$(\Pi_{11}-\Pi_{22})-(\tan\alpha\cdot\Pi_{12}-\cot\alpha\cdot\Pi_{21})\xrightarrow{m_{h_1}\to m_{h_2}}0\,. \tag{6.42}$$

It means that the whole propagator vanishes as well, consistently with vanishing of $\kappa$.

Although it is not strictly justified, we nevertheless use the Breit-Wigner propagator (6.40) because the region of inapplicability of this approximation is so narrow that it would not be visible in the plots. It is just important to bear in mind that the quantity $\mathcal{X}$ given by eq. (6.2) in fact vanishes at $m_{h_1}=m_{h_2}$.

## 6.3 Standard Model background and detection sensitivity

In collider experiments, the $Z$ boson produced in the discussed process depicted in fig. 6.5 is not observed directly. What is detected are products of its decay. Hence, the experimental signature of the DM production process would be a leptonic/hadronic shower along with missing energy. The energy of $Z$ is reconstructed from measured energies of the decay products. Then, the recoil mass, i.e., the invariant mass of the invisible states, is calculated as

$$\begin{aligned}m_{\text{rec}}^2 &\equiv Q^2 \\ &= (\sqrt{s}-E_Z)^2-\mathbf{p}_Z^2 \\ &= s-2\,E_Z\sqrt{s}+m_Z^2\,.\end{aligned} \tag{6.43}$$

Obviously, for this calculation $\sqrt{s}$ should be precisely known. However, mainly due to the initial-state radiation effects, energy of the incident particles is not absolutely known. In fact, the energies can be less than assumed, leading to overestimation of the recoil mass.

Another source of measurement uncertainty are the SM background processes, mostly the two shown in fig. 6.6, namely, the $ZZ$ production (with one of the $Z$ bosons decaying into neutrinos) and production of neutrinos along with the $Z$ boson through the $WW$ fusion. In both processes, the observed final state

(products of $Z$-boson decay plus missing energy) is identical to the one expected from the DM production process. Therefore, to claim that dark matter is produced, the number of DM production events must not only be non-zero, but exceed the background.


**Figure 6.6:** The main processes constituting the SM background of the discussed DM production process. **Left:** $ZZ$ production with one of the bosons decaying into neutrinos. **Right:** production of neutrinos and $Z$ boson through the $WW$ fusion.

For $m_{h_2} \lesssim 125$ GeV, the best estimation of $Z$ invariant mass is obtained if the muonic decay of $Z$ is chosen, as the invariant mass of the $\mu^+\mu^-$ system can be reconstructed very precisely. Moreover, the SM background is much less than in the case of the hadronic decay. The hadronic background increases for low recoil masses. For hadronic, also detector resolution effects (due to jet energy resolution) play an important role.

Figure 6.7 shows the expected 95% C.L limits for detection of BSM invisible Higgs decays at the ILC operating at $\sqrt{s} = 250$ GeV. The limit is expressed as the ratio between the cross section that provides an exceed above the background with the 95% C.L. to the cross section with the SM Higgs boson of a given mass, assuming selection of $\mu^+\mu^-$ channel, while making no assumption on the decay modes or branching ratios of the Higgs [192–194].

The predicted loss of sensitivity around $m_{h_2} = m_Z \simeq 91$ GeV comes from the $ZZ$ production, with one of the bosons decaying invisibly into neutrinos and the other into muons. The upper limit is $\sqrt{s} - m_Z \simeq 155$ GeV.

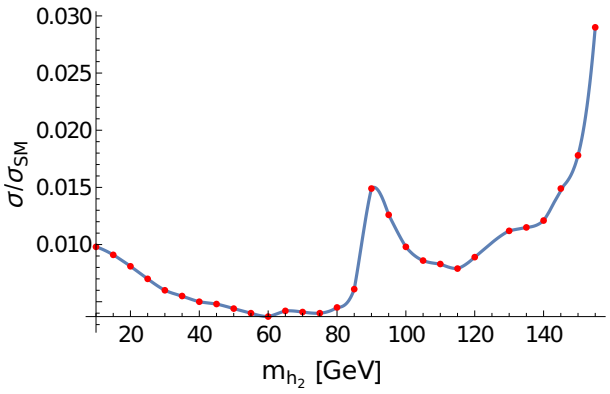


**Figure 6.7:** The predicted 95% C.L. detection limit [192–194] on the cross section for $\sigma(e^+e^- \to Z + \text{inv})$ at the ILC at $\sqrt{s} = 250$ GeV, as a function of the mass of the additional Higgs boson $h_2$, calculated using the CL(s) approach [195]. The cross section is normalized to $\sigma_{\text{SM}}$ with mass of the SM Higgs boson equal to $m_{h_2}$.

This threshold has been obtained assuming only one scalar mediator, while our processes are superpositions of diagrams mediated by $h_1$ and $h_2$. Nevertheless, as the considered masses of $h_1$ and $h_2$ are close to each other, the threshold can be employed to estimate detection chance corresponding to the results presented in the next section.

## 6.4 Numerical results

In this section, the numerical predictions for DM production at the future lepton colliders are presented. As a benchmark, we use the ILC working at $\sqrt{s} = 250$ GeV [192, 194].

All three models: pGDM, FDM and VDM, are parametrized by the following variables:

- $m_{h_2}$, mass of the additional Higgs-like particle $h_2$;
- $m_{\mathrm{DM}}$, mass of the dark particle (scalar $A$, fermion $\psi$ or vector $X$, depending on the model);
- $v_S$, VEV of the additional scalar field $S$;
- $\sin\alpha$, sine of the scalar-sector mixing angle.

The value of $v_S$ is fixed by the relic-density constraint eq. (6.8) for the value of parameter $X$, as given by (6.2). The value of $\sin\alpha$ is chosen from the allowed range of $(0, 0.3)$ in a way that maximizes the cross section (usually the maximizing value is just the maximal one, i.e., $\sin\alpha \simeq 0.3$). Then, two independent parameters are left: $m_{h_2}$ and $m_{\mathrm{DM}}$. For convenience, we reparametrize the parameter space using $m_{\mathrm{DM}} - m_{h_1}/2$ and $m_{\mathrm{DM}} - m_{h_2}$ as variables. Now, degeneracy in the scalar sector, $m_{h_1} = m_{h_2}$, is represented by the diagonal line, $m_{\mathrm{DM}} - m_{h_1}/2 = m_d m - m_{h_2}$, while the vertical and horizontal line correspond to $m_{\mathrm{DM}} = m_{h_1}/2$, $m_{\mathrm{DM}} = m_{h_2}/2$, respectively.

The cross section is strongly enhanced when the mediator can be on-shell, i.e., when $h_i$ $(i = 1, 2)$ is allowed to decay into a pair of dark particles. This happens for $m_{\mathrm{DM}} < m_{h_i}/2$. From eq. (6.34) it follows that the cross section is largest when $m_{h_1} \simeq m_{h_2}$, so that both $Q^2 - m_{h_1}^2$ and $Q^2 - m_{h_2}^2$ can be simultaneously small. Consequently, the maximum appears in the lower-left quarter of the plots, corresponding to $m_{h_2} \simeq m_{h_1} > 2\, m_{\mathrm{DM}}$.

Note that although the exact formula for the propagator, given by eq. (6.38), should be used instead of the Breit-Wigner approximation (6.39) if the scalar masses $m_{h_1}$, $m_{h_2}$ are very close to each other, the region affected by the difference is to narrow to be noticeable in the plots.

The FDM and VDM models are strongly constrained by the direct detection limits (see section 6.1.3). The DM-SM coupling, as proportional to $\mathcal{X}$ (see eq. (6.10)) is suppressed (according to eq. (6.14)). In order to provide the annihilation cross section at the sufficient level, while keeping the DD cross section small enough, the parameters must be close to the resonant values: $\Rightarrow 2m_{\mathrm{DM}} - m_{h_1} \simeq 0$ or $2m_{\mathrm{DM}} - m_{h_2} \simeq 0$.

On the contrary, in the pGDM the tree-level DD cross section vanishes for zero momentum transfer, see section 6.1.3, so that the DD does not limit the parameters severely and resonant annihilation is not necessary to keep the relic density correct. Nevertheless, for comparison with the FDM and VDM models, we focus on the same range:

$$\left| m_{\mathrm{DM}} - \frac{m_{h_{1,2}}}{2} \right| < 5 \text{ GeV} , \tag{6.44}$$

which means that $m_{\mathrm{DM}}$ is between 57.5 GeV and 67.5 GeV, while $m_{h_2}$ is between 105 GeV and 145 GeV (keep in mind that the analysed region is not rectangular in variables $(m_{\mathrm{DM}}, m_{h_2})$ eq. (6.44)).

Figures 6.8 and 6.9 show the value of the cross section calculated for the process depicted in fig. 6.5, normalized to $\sigma_{\mathrm{SM}}$ with the mass of the Higgs boson equal to $m_{h_1} = 125$ GeV. The values are compared with the threshold shown in fig. 6.7; also the regions contradicting the constraints discussed in section 6.1 are marked.

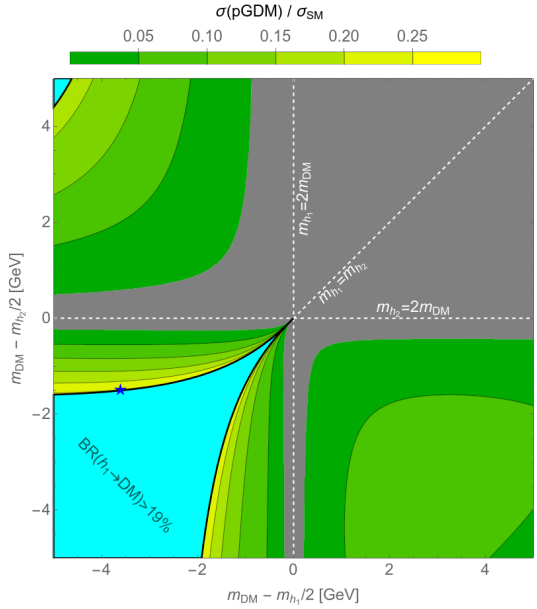


benchmark point for pGDM

$m_{h_2} = 120.8$ GeV , $m_{\mathrm{DM}} = 58.9$ GeV ,
$\sin\alpha = 0.30$ , $v_S = 646$ GeV ,
$\Gamma_1 = 7.4 \cdot 10^{-3}$ GeV , $\Gamma_2 = 9.8 \cdot 10^{-3}$ GeV ,
$\mathrm{BR}(h_1 \to \mathrm{DM}) = 19\%$ , $\mathrm{BR}(h_2 \to \mathrm{DM}) = 95\%$ ,
$\sigma = 62$ fb

**Figure 6.8:** The cross section for the DM production process $e^+e^- \to Zh_i \to ZAA$, calculated within the pGDM model and normalized to the cross section $\sigma_{\mathrm{SM}}$ for the SM process $e^+e^- \to Zh$. Cyan denotes the region where the limits for invisible Higgs branching ratio are exceeded, while gray corresponds to cross section too small to be distinguishable from the SM background. In the remaining area, yellow corresponds to high cross section while green denotes small values. The benchmark point, whose parameters are listed next to the plot, is denoted by the star.

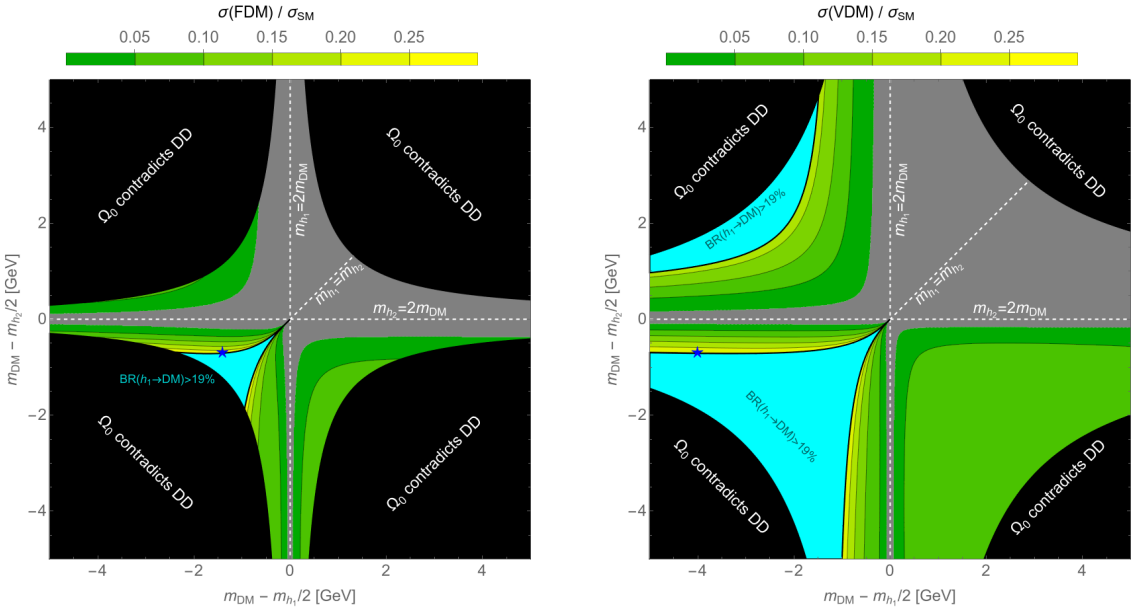


benchmark point for FDM

$m_{h_2} = 123.6$ GeV , $m_{\mathrm{DM}} = 61.1$ GeV ,
$\sin\alpha = 0.30$ , $v_S = 76$ GeV ,
$\Gamma_1 = 7.4 \cdot 10^{-3}$ GeV , $\Gamma_2 = 5.9 \cdot 10^{-3}$ GeV ,
$\mathrm{BR}(h_1 \to \mathrm{DM}) = 18\%$ , $\mathrm{BR}(h_2 \to \mathrm{DM}) = 91\%$ ,
$\sigma = 59$ fb

benchmark point for VDM

$m_{h_2} = 118.4$ GeV , $m_{\mathrm{DM}} = 58.5$ GeV ,
$\sin\alpha = 0.30$ , $v_S = 561$ GeV ,
$\Gamma_1 = 7.4 \cdot 10^{-3}$ GeV , $\Gamma_2 = 6.4 \cdot 10^{-3}$ GeV ,
$\mathrm{BR}(h_1 \to \mathrm{DM}) = 18\%$ , $\mathrm{BR}(h_2 \to \mathrm{DM}) = 92\%$ ,
$\sigma = 61$ fb

**Figure 6.9:** Like fig. 6.8, but for the FDM model (left) and the VDM model (right). Black denotes the area where the direct-detection limits contradict the relic-density constraint.

Assuming the mass of dark particle and the mass of the additional Higgs particle can be measured, they can be used as a probe to disentangle the models. The measured results should be compared with the values allowed by the experimental constraints, presented in fig. 6.10. As seen from the figure, there are regions forbidden for a given value of DM spin and allowed for another, e.g., point $(m_{\mathrm{DM}}, m_{h_2}) = (64.5\ \mathrm{GeV}, 133\ \mathrm{GeV})$ (so that $m_{\mathrm{DM}} - m_{h_1}/2 = 2\ \mathrm{GeV}$ and $m_{\mathrm{DM}} - m_{h_2}/2 = -2\ \mathrm{GeV}$) is forbidden for the FDM model, while allowed for the pGDM and VDM model.

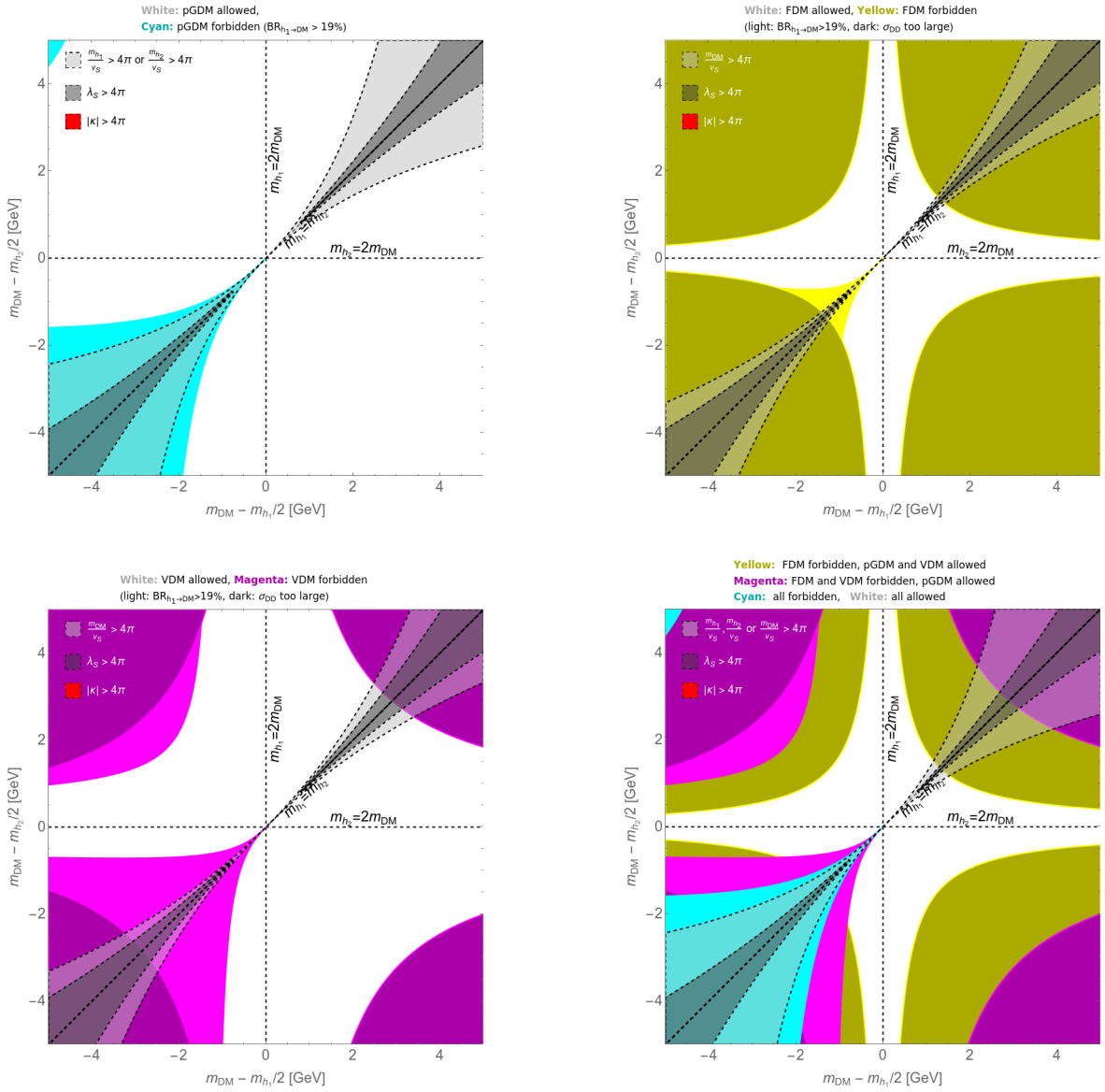


**Figure 6.10:** Comparison of parameter space allowed for the DM models under discussion. Top-left: pGDM model, top-right: FDM model, bottom-left: VDM model, bottom-right: the previous three plots combined. The coloured regions are forbidden by the limits for the invisible Higgs branching ratio and the direct-detection limits. The light- and dark-gray areas correspond to violation of perturbativity constraints (see eq. (6.24)). The perturbativity condition $|\kappa| < 4\pi$, whose violation would be marked in red, is fulfilled in the whole considered part of the parameter space.

Another possibility to disentangle the models would be to compare the values of cross sections to the theoretical predictions. In the following plots figs. 6.11 and 6.12, we compare the maximal possible difference obtained for the most optimistic value of $\sin\alpha$ with the predicted sensitivity of the detectors fig. 6.7. Whenever the difference is smaller, the models are undistinguishable by this method. There are, however, regions (especially when comparing pGDM to the VDM) where the difference should be large enough to make the models distinguishable.

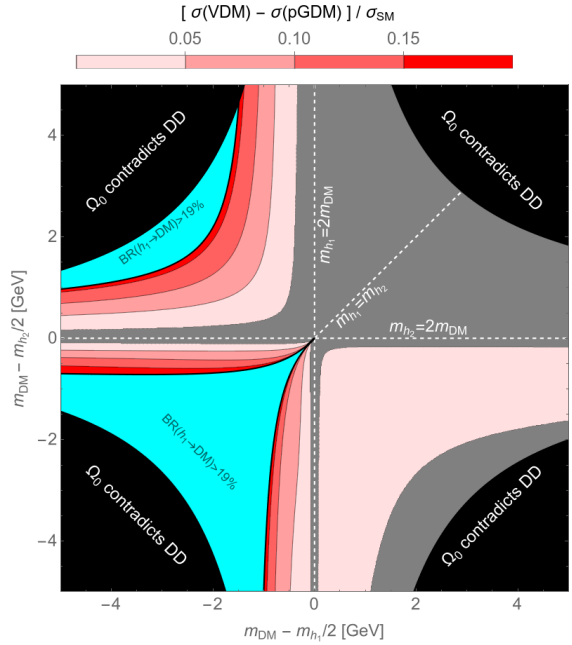


**Figure 6.11:** The difference between the results obtained for the pGDM and VDM models. Cyan and black denote the region where at least one of the models is inconsistent with the experimental limits, while the region where the difference is too small to be noticeable (cf. fig. 6.7) is marked with gray.

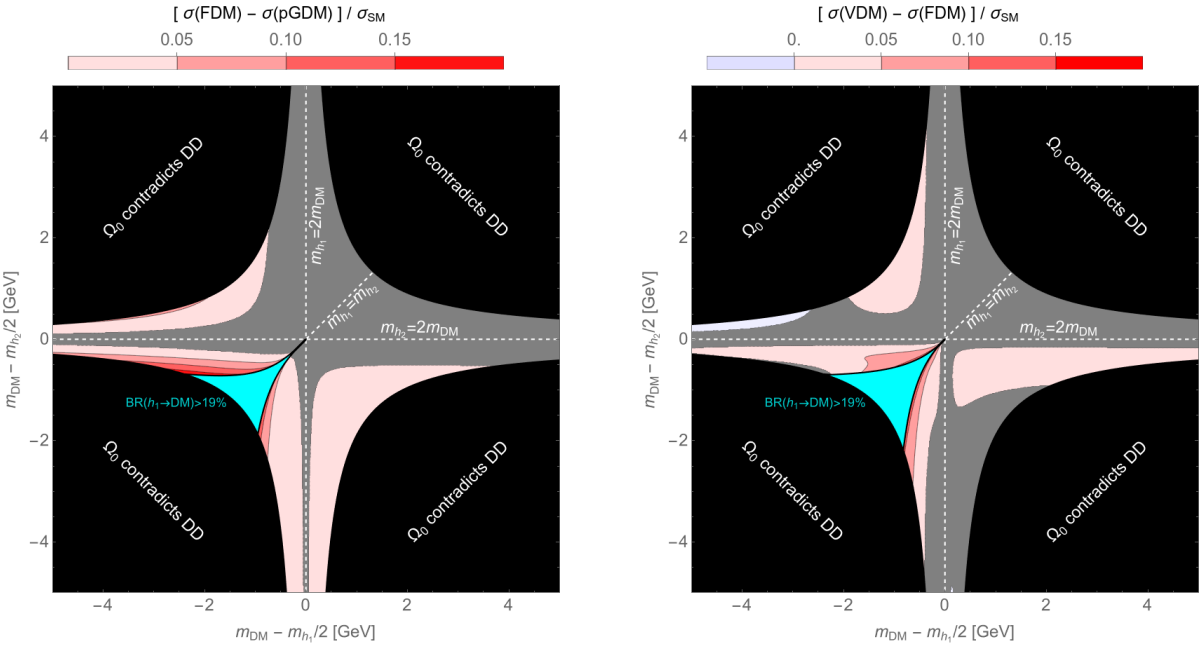


**Figure 6.12:** Like fig. 6.11, but for the pGDM and FDM models (left panel), and for the FDM and VDM models (right panel).

As can be observed in the plots, most of the parameter space is either forbidden by the current experimental constraints or would correspond to a signal too low to be detected. Nevertheless, there still exist combination of parameters leading to effective DM production at the future DM colliders. Moreover, it appears that disentangling dark particles of different spins could be, in principle, possible comparing their measure parameters with the allowed range shown in fig. 6.10. The precise values of cross section differing by the spin of the dark particle are different as well.

# Chapter 7

# Summary

Higgs-portal models satisfy all requirements expected from theories of dark matter. They provide: massive, stable candidates; a mechanism of establishing the relic density; and a possibility of self-interactions within the dark sector. What is worth to stress is that those models are renormalizable gauge-symmetry theories, fully consistent from the theoretical point of view.

In this dissertation, we have focused on interactions of dark matter in the early Universe and at the future $e^+e^-$ colliders. In chapter 5, we have discussed the so-called $t$-channel singularity, affecting processes involving massive stable particles, which are crucial for DM studies, as they influence the relic abundances through the Boltzmann equation (see section 2.4). We have provided a strict condition for a given process to be affected by the singularity, and proposed a regularization method, employing interactions between the on-shell $t$-channel mediator and the surrounding gas to obtain an effective, temperature-dependent decay width of the mediator. As demonstrated, this solution can be applied always if the medium is present. Although the calculations assume that the medium is thermal, this assumption is not necessary, as any form of the phase-space distribution function of the medium components can be used to obtain numerical results. The method has been applied to a simple model consisting of three scalar fields, and to the multi-component vector-fermion DM model, in each case successfully regularizing the would-be singular cross sections.

In chapter 6, we have studied production of dark particles at the future $e^+e^-$ colliders. We have taken into account all types of observational constraints that limit the parameter space of DM models. It has appeared that although the parameters are tightly constrained, there are still regions allowed by the present combined limits. Moreover, in some of those regions, DM production could be efficient enough to enable detection. Thus, building new lepton colliders seems to be a promising perspective from the point of view of DM studies. In our analysis, we have employed models very similar to each other in construction and phenomenology, but differing by the spin of the proposed dark particle. This enabled to investigate the influence of DM spin on production probability. In all three analysed models: the one proposing a scalar dark particle, the one providing a dark fermion, and the one with a dark vector, the obtained results are similar: the maximal possible production cross section of the Higgs-strahlung processes, with a subsequent decay of the Higgs state into dark particles, is around 60 fb. However, the shape of the allowed parameter space is slightly different for each model, which in principle could enable disentangling the cases of different spins.

The results of this dissertation are applicable to a wide range of particle models: the $t$-channel singularity can affect any model with a decay into massive, stable products, while the simple one-component DM models employed in chapter 6 can serve, either treated separately or together, as the first approximation of more involved models of Higgs-portal DM. However, the most important aspect of those studies are not the numerical results, but the developed general methodology that could be adapted to reader's own research.

# Appendix A

# Multicomponent vector-fermion dark matter model

The vector-fermion dark matter (VFDM) model [21–23] is an extension of the Standard Model of particle physics, which provides two or three dark matter candidates (depending on stability of the dark-sector particles). The dark particles are interacting with the SM through the Higgs portal.

## A.1 Introduction

In the VFDM model, the gauge group of the Standard Model is extended by an additional Abelian group, $U(1)_x$, which acts trivially on the SM fields. In the scalar sector, apart from the SM Higgs doublet $H$, an additional complex singlet $S$ is introduced. The real-part fluctuations of $S$ and of the neutral component of $H$ mix to provide two scalar mass-eigenstates: $h_1$, which is identified with the known Higgs particle of the mass $m_{h_1} = 125$ GeV, and $h_2$, which can be, in principle, of any mass. The gauge vector of $U(1)_x$, called $X$, becomes massive through the Higgs mechanism, absorbing the imaginary-part fluctuation of $S$.

Moreover, a Dirac fermion $\chi$ is introduced. The newly introduced fields have the following charges with respect to the $U(1)_x$:

$$S:\ q_x = 1\ , \quad \chi:\ q_x = 1/2\ , \tag{A.1}$$

and are even under the action of the SM gauge group. An additional dark-charge-conjugation symmetry $\mathcal{C}$:

$$\mathcal{C}: \quad X \to -X\ , \quad S \to S^*\ , \quad \chi \to \chi^c \equiv -i\gamma_2\chi^*\ . \tag{A.2}$$

is imposed to forbid the kinetic mixing between $X$ and the SM vector bosons. This symmetry does not affect the SM fields. Here, $\gamma_2$ denotes one of the Dirac matrices (for a brief summary of their properties, see appendix D) and $(\ldots)^*$ is the complex conjugation.

The Lagrangian of the model consists of three parts:

$$\mathcal{L} = \mathcal{L}_{\mathrm{SM}} + \mathcal{L}_{\mathrm{DS}} + \mathcal{L}_{\mathrm{portal}}\ . \tag{A.3}$$

$\mathcal{L}_{\mathrm{SM}}$ is the SM Lagrangian (including the potential of the SM Higgs field), and $\mathcal{L}_{\mathrm{DS}}$ denotes the dark-sector Lagrangian:

$$\begin{aligned}\mathcal{L}_{\mathrm{DS}} \equiv &-\frac{1}{4}X^{\mu\nu}X_{\mu\nu} + (D^\mu S)^* D_\mu S + \bar{\chi}(i\not{D} - m_D)\chi \\ &+ \mu_S^2|S|^2 - \lambda_S|S|^4 - \frac{1}{\sqrt{2}}(y_x S^*\chi^{\intercal}\mathcal{C}\chi + \mathrm{h.c.})\ ,\end{aligned} \tag{A.4}$$

where

$$X_{\mu\nu} \equiv \partial_\mu X_\nu - \partial_\nu X_\mu\ , \quad D_\mu \equiv \partial_\mu + ig_x q_x X_\mu\ , \tag{A.5}$$

$g_x$ is a real dimensionless coupling constant, $q_x$ is the charge defined in eq. (A.1), and $\mathcal{C} \equiv i\gamma_0\gamma_2$ denotes the charge-conjugation operator (see appendix D.3 for a list of its main properties). Moreover, $m_D$

denotes the Dirac mass of $\chi$, $\mu_S^2$ is a coupling constant of dimension of [mass]$^2$, and $\lambda_S$ and $y_x$ are dimensionless. The Higgs-portal Lagrangian, $\mathcal{L}_{\text{portal}}$, is given by

$$\mathcal{L}_{\text{portal}} = -\kappa|S|^2|H|^2 \tag{A.6}$$

with a dimensionless coupling $\kappa$. Since the Lagrangian must be Hermitian, the couplings: $\mu_S^2$, $\lambda_S$, $\kappa$ must be real. The Dirac mass $m_D$ is assumed to be real (due to hermiticity) and positive. Moreover, as the Lagrangian is invariant under complex rotations of $S$, the complex phase of the Yukawa coupling constant $y_x$ can be absorbed by $S$, so it can be assumed that $y_x > 0$.

## A.2 Scalar sector

The scalar-sector potential $V$ consists of the SM Higgs potential and the scalar-potential part of $\mathcal{L}_{\text{DS}}$ (taken with the minus sign):

$$V(H,S) \equiv -\mu_H^2|H|^2 + \lambda_H|H|^4 - \mu_S^2|S|^2 + \lambda_S|S|^4 + \kappa|S|^2|H|^2 \,. \tag{A.7}$$

### A.2.1 Stability conditions

In order for the theory to be stable, the potential must be bounded from below. To provide a strict condition for this requirement to be fulfilled, we assume

$$|S| = r\sin\alpha \,, \quad |H| = r\cos\varphi \,, \tag{A.8}$$

with $r > 0$ and $\varphi \in [0, \frac{\pi}{2}]$, and observe that

$$r^{-4}\, V(H,S) \xrightarrow{r\to\infty} \lambda_H \cos^4\varphi + \lambda_S \sin^4\varphi + \kappa\, \cos^2\varphi\, \sin^2\varphi \,. \tag{A.9}$$

If this limit is positive for any $\varphi \in [0, \frac{\pi}{2}]$, the stability is ensured. For $\varphi = 0$, the limit is $\lambda_H$, while for $\varphi = \frac{\pi}{2}$ it is equal to $\lambda_S$, so both $\lambda_H$ and $\lambda_S$ are required to be positive. In the case of $0 < \varphi < \frac{\pi}{2}$, positivity of the limit means that

$$0 < \lambda_H \cos^4\varphi + \lambda_S \sin^4\varphi + \kappa\, \cos^2\varphi\, \sin^2\varphi \tag{A.10}$$

$$\Leftrightarrow \quad \kappa > -(\lambda_H \cot^2\varphi + \lambda_S \tan^2\varphi) \,. \tag{A.11}$$

Given that $\lambda_H, \lambda_S > 0$, the maximal value (with respect to $\varphi$) of the function on the right-hand side of the last inequality is $-2\sqrt{\lambda_H\lambda_S}$. Hence, to ensure that the potential is stable it is demanded that

$$\lambda_H > 0 \,, \quad \lambda_S > 0 \,, \quad \kappa > -2\sqrt{\lambda_H\lambda_S} \,. \tag{A.12}$$

### A.2.2 Spontaneous symmetry breaking and mass-eigenstates

Since the potential, as a function of $|H|$ and $|S|$, is continuous, bounded from below and tends to positive infinity when its arguments tend to infinity (positive or negative), it has a minimum whose position defines the vacuum expectation values (VEVs) of $H$ and $S$. Due to symmetry of the Lagrangian, the vacuum expectations values can be assumed to be real and non-negative:

$$\langle H\rangle = \begin{pmatrix} 0 \\ \frac{v}{\sqrt{2}} \end{pmatrix} \,, \quad \langle S\rangle = \frac{v_S}{\sqrt{2}} \,, \quad v, v_S \geqslant 0 \,. \tag{A.13}$$

The VEVs must satisfy

$$0 = \frac{\partial V}{\partial|H|}\Big|_{\substack{H=\langle H\rangle \\ S=\langle S\rangle}} = \frac{v}{\sqrt{2}}\,(2\,v^2\,\lambda_H - 2\,\mu_H^2 + \kappa\, v_S^2) \,, \tag{A.14a}$$

$$0 = \frac{\partial V}{\partial|S|}\Big|_{\substack{H=\langle H\rangle \\ S=\langle S\rangle}} = \frac{v_S}{\sqrt{2}}\,(2\,v_S^2\,\lambda_S - 2\,\mu_S^2 + \kappa\, v^2) \,, \tag{A.14b}$$

which gives the following four solutions:

$$v^2 = \frac{4\lambda_S\mu_H^2 - 2\kappa\mu_S^2}{4\lambda_H\lambda_S - \kappa^2}\,, \quad v_S^2 = \frac{4\lambda_H\mu_S^2 - 2\kappa\mu_H^2}{4\lambda_H\lambda_S - \kappa^2} \quad \Rightarrow \quad V = V_1 \equiv -\frac{\lambda_S\,\mu_H^4 - \kappa\,\mu_H^2\,\mu_S^2 + \lambda_H\,\mu_S^4}{4\,\lambda_H\,\lambda_S - \kappa^2}\,, \tag{A.15}$$

$$v^2 = \frac{\mu_H^2}{\lambda_H}\,, \quad v_S^2 = 0 \quad \Rightarrow \quad V = V_2 \equiv -\frac{\mu_H^4}{4\,\lambda_H}\,, \tag{A.16}$$

$$v^2 = 0\,, \quad v_S^2 = \frac{\mu_S^2}{\lambda_S} \quad \Rightarrow \quad V = V_3 \equiv -\frac{\mu_S^4}{4\,\lambda_S}\,, \tag{A.17}$$

$$v^2 = 0\,, \quad v_S^2 = 0 \quad \Rightarrow \quad V = V_4 \equiv 0\,. \tag{A.18}$$

As both VEVs should be non-zero to provide masses to the gauge bosons of the theory (the SM gauge bosons and the one corresponding to $U(1)_x$), the first solution is preferred. It is the global minimum if $V_1$ is smaller than $V_2$, $V_3$ and $V_4$. The difference between $V_2$ and $V_1$ is

$$\begin{aligned} V_2 - V_1 &= -\frac{\mu_H^4}{4\,\lambda_H} + \frac{\lambda_S\,\mu_H^4 - \kappa\,\mu_H^2\,\mu_S^2 + \lambda_H\,\mu_S^4}{4\,\lambda_H\,\lambda_S - \kappa^2} \\ &= \frac{(2\,\lambda_H\,\mu_S^2 - \kappa\,\mu_H^2)^2}{4\lambda_H(4\,\lambda_H\,\lambda_S - \kappa^2)}\,, \end{aligned} \tag{A.19}$$

which is positive if

$$4\,\lambda_H\,\lambda_S > \kappa^2\,. \tag{A.20}$$

Similarly, it can be shown that the same condition leads to $V_1 < V_3$. As $V_2$ and $V_3$ are obviously smaller than $V_4$ (note that (A.12) is assumed), this condition is sufficient to ensure that (A.15) is the global minimum.

For consistency with positivity of $v^2$ and $v_S^2$ specified by eq. (A.15), also the following inequalities must hold:

$$2\,\lambda_S\,\mu_H^2 > \kappa\,\mu_S^2\,, \quad 2\,\lambda_H\,\mu_S^2 > \kappa\,\mu_H^2\,. \tag{A.21}$$

Note that $\mu_H^2$ and $\mu_S^2$ are not necessarily positive. In fact, if $\kappa < 0$, one of them can be negative without spoiling stability of the potential and moving the global minimum out of (A.15).

The scalar fields can be expanded around their VEVs as follows:

$$H = \begin{pmatrix} \pi^+ \\ \frac{v+h+i\pi^0}{\sqrt{2}} \end{pmatrix}\,, \quad S = \frac{v_S + \phi + i\sigma}{\sqrt{2}}\,. \tag{A.22}$$

As the Lagrangian is gauge invariant, we are allowed to work in the unitary gauge, in which the would-be Goldstone bosons $\pi^+$, $\pi^0$ and $\sigma$ vanish, as they are absorbed by the gauge vectors. Using this expansion and eq. (A.15), after the spontaneous symmetry breaking (SSB) we obtain the following scalar-sector mass-squared matrix:

$$M_{h,\phi}^2 \equiv \begin{bmatrix} \frac{\partial^2 V}{\partial h^2} & \frac{\partial^2 V}{\partial\phi\,\partial h} \\ \frac{\partial^2 V}{\partial h\,\partial\phi} & \frac{\partial^2 V}{\partial\phi^2} \end{bmatrix}_{h=\phi=0} = \begin{bmatrix} 2\lambda_H v^2 & \kappa v v_S \\ \kappa v v_S & 2\lambda_S v_S^2 \end{bmatrix}\,. \tag{A.23}$$

Since $v, v_S > 0$, the matrix is positive-definite as long as the condition (A.20) is satisfied. The matrix (A.23) can be diagonalized in the basis of mass eigenstates $h_1$ and $h_2$ obtained by the following rotation of $h$ and $\phi$:

$$\begin{pmatrix} h_1 \\ h_2 \end{pmatrix} \equiv R^{-1} \begin{pmatrix} h \\ \phi \end{pmatrix}\,, \quad R \equiv \begin{bmatrix} \cos\alpha & -\sin\alpha \\ \sin\alpha & \cos\alpha \end{bmatrix}\,, \quad \tan(2\alpha) \equiv \frac{\kappa v v_S}{\lambda_H v^2 - \lambda_S v_S^2}\,. \tag{A.24}$$

After the diagonalization, the mass-squared matrix becomes

$$M_{h_1,h_2}^2 = R^{-1}\,M_{h,\phi}^2\,R = \begin{bmatrix} m_{h_1}^2 & 0 \\ 0 & m_{h_2}^2 \end{bmatrix}\,, \tag{A.25}$$

with

$$m_{h_1}^2 \equiv \lambda_H v^2 + \lambda_S v_S^2 + (\lambda_H v^2 - \lambda_S v_S^2)/\cos(2\alpha)\,, \tag{A.26a}$$

$$m_{h_2}^2 \equiv \lambda_H v^2 + \lambda_S v_S^2 - (\lambda_H v^2 - \lambda_S v_S^2)/\cos(2\alpha)\,. \tag{A.26b}$$

The squared masses $m_{h_1}^2$ and $m_{h_2}^2$ are automatically positive, as the matrix (A.23) is positive-definite. As already mentioned, $h_1$ is identified with the known Higgs state, so $m_{h_1}$ is assumed to be equal to 125 GeV.

## A.3 Dark fermionic sector

The part of the Lagrangian (A.3) that describes dark fermions reads

$$\mathcal{L}_{\mathrm{DF}} \equiv \bar{\chi}(i\not{D} - m_D)\chi - \frac{1}{\sqrt{2}}(y_x S^* \chi^\intercal \mathcal{C}\chi + \mathrm{h.c.}) \,. \tag{A.27}$$

With the charge-conjugated field $\chi^c$, defined as

$$\chi^c \equiv -i\gamma_2 \chi^* = \mathcal{C}\bar{\chi}^\intercal \,, \tag{A.28}$$

and using eq. (E.6), we can rewrite this part of the Lagrangian as

$$\mathcal{L}_{\mathrm{DF}} = \frac{i}{2}(\bar{\chi}\not{\partial}\chi + \bar{\chi^c}\not{\partial}\chi^c) - \frac{g_x}{4}(\bar{\chi}\gamma^\mu\chi - \bar{\chi^c}\gamma^\mu\chi^c)X_\mu - \frac{m_D}{2}(\bar{\chi}\chi + \bar{\chi^c}\chi^c) - \frac{y_x}{\sqrt{2}}(S^*\bar{\chi^c}\chi + S\bar{\chi}\chi^c) \,. \tag{A.29}$$

After the SSB, described by eqs. (A.13) and (A.22), this Lagrangian takes the following form:

$$\begin{aligned} \mathcal{L}_{\mathrm{DF}} = \quad & \frac{i}{2}(\bar{\chi}\not{\partial}\chi + \bar{\chi^c}\not{\partial}\chi^c) - \frac{m_D}{2}(\bar{\chi}\chi + \bar{\chi^c}\chi^c) \\ & - \frac{g_x}{4}(\bar{\chi}\gamma^\mu\chi - \bar{\chi^c}\gamma^\mu\chi^c)X_\mu - \frac{y_x v_S}{2}(\bar{\chi^c}\chi + \bar{\chi}\chi^c) - \frac{y_x}{2}(\bar{\chi^c}\chi + \bar{\chi}\chi^c)\phi \,. \end{aligned} \tag{A.30}$$

Introducing Majorana fermions $\psi_\pm$ with masses $m_{\psi_\pm}$, defined as

$$\psi_+ \equiv \frac{\chi + \chi^c}{\sqrt{2}} = \psi_+^c \,, \qquad \psi_- \equiv \frac{\chi - \chi^c}{i\sqrt{2}} = \psi_-^c \,, \tag{A.31a}$$

$$m_{\psi_\pm} \equiv m_D \pm y_x v_S \,, \tag{A.31b}$$

and using eqs. (E.10) and (E.11), we can rewrite the dark fermionic Lagrangian as

$$\begin{aligned} \mathcal{L}_{\mathrm{DF}} = \quad & \frac{i}{2}(\bar{\psi}_+\not{\partial}\psi_+ + \bar{\psi}_-\not{\partial}\psi_-) - \frac{m_+}{2}\bar{\psi}_+\psi_+ - \frac{m_-}{2}\bar{\psi}_-\psi_- \\ & - \frac{ig_x}{4}(\bar{\psi}_+\gamma^\mu\psi_- - \bar{\psi}_-\gamma^\mu\psi_+)X_\mu - \frac{y_x}{2}(\bar{\psi}_+\psi_+ - \bar{\psi}_-\psi_-)\phi \,. \end{aligned} \tag{A.32}$$

As $y_x$ is assumed to be positive (see appendix A.1), we conclude that

$$m_{\psi_+} > m_{\psi_-} \,. \tag{A.33}$$

## A.4 Dark vector particle

The part of the Lagrangian (A.3) that describes the gauge boson $X$ reads

$$\mathcal{L}_X = -\frac{1}{4}X^{\mu\nu}X_{\mu\nu} + (D^\mu S)^* D_\mu S. \tag{A.34}$$

The terms describing interactions with the dark fermions are not included here as they have already been discussed in the previous section. After the SSB (see (A.13) and (A.22)), this Lagrangian becomes

$$\mathcal{L}_X = -\frac{1}{4}X^{\mu\nu}X_{\mu\nu} + \frac{1}{2}\partial^\mu\phi\,\partial_\mu\phi + \frac{m_X^2}{2}X^\mu X_\mu + g_x m_X X^\mu X_\mu \phi + \frac{g_x^2}{2}X^\mu X_\mu \phi^2 \,, \tag{A.35}$$

with $m_X \equiv |g_x| v_S$ denoting the mass of the gauge boson $X$, gained from the scalar $S$ through the Higgs mechanism. For convenience, we assume that

$$g_X > 0 \,. \tag{A.36}$$

Eventually, the full Lagrangian (A.3) contains three dark-sector particles: Majorana fermions $\psi_+$ and $\psi_-$, and a massive vector boson $X$. Moreover, there are two scalar states: $h_1$ (identified with the known Higgs particle) and $h_2$, that serve as mediators between the SM and the dark sector.

## A.5 Parameters of the model

The free parameters of the theory are:

- the couplings: $g_x$, $y_x$,
- parameters of the scalar potential (A.7): $\mu_H$, $\mu_S$, $\lambda_H$, $\lambda_S$, $\kappa$,
- VEVs of the scalar fields: $v$, $v_S$,
- the Dirac mass: $m_D$.

The number of the parameters necessary to define the theory, eight, can be reduced by two by the assumption that

- $h_1$ is the known Higgs particle,
- the VEV of $H$ is equal to the SM value,

so that

$$m_{h_1} = 125 \text{ GeV} , \quad v = 246 \text{ GeV} . \tag{A.37}$$

As the remaining six parameters the following set is chosen:

- masses of the dark states: $m_{\psi_+}$, $m_{\psi_-}$, $m_X$,
- mass of the second scalar mass-eigenstate: $m_{h_2}$,
- the $U(1)_x$ coupling constant: $g_x$,
- sine of the scalar-sector mixing angle: $\sin\alpha$.

By construction, $m_{\psi_+}$ must always be greater than $m_{\psi_-}$, see relation (A.33). The initial set of free parameters can be expressed in terms of the chosen final set and the known parameters $m_{h_1}$, $v$ as follows:

$$v_S = \frac{m_X}{g_x} , \qquad m_D = \frac{m_{\psi_+} + m_{\psi_-}}{2} , \qquad y_x = \frac{m_{\psi_+} - m_{\psi_-}}{2 v_S} , \qquad \kappa = \sin 2\alpha \, \frac{m_{h_1}^2 - m_{h_2}^2}{2 v v_S} , \tag{A.38a}$$

$$\lambda_H = \frac{\cos^2\alpha \, m_{h_1}^2 + \sin^2\alpha \, m_{h_2}^2}{2 v^2} , \quad \mu_H^2 = \frac{1}{2} m_{h_1}^2 \cos^2\alpha + \frac{1}{2} m_{h_2}^2 \sin^2\alpha + \frac{1}{4} \frac{v_S}{v} \sin 2\alpha \, (m_{h_1}^2 - m_{h_2}^2) , \tag{A.38b}$$

$$\lambda_S = \frac{\sin^2\alpha \, m_{h_1}^2 + \cos^2\alpha \, m_{h_2}^2}{2 v_S^2} , \quad \mu_S^2 = \frac{1}{2} m_{h_1}^2 \sin^2\alpha + \frac{1}{2} m_{h_2}^2 \cos^2\alpha + \frac{1}{4} \frac{v}{v_S} \sin 2\alpha \, (m_{h_1}^2 - m_{h_2}^2) . \tag{A.38c}$$

The conditions expressed by eqs. (A.12), (A.20) and (A.21) are now automatically satisfied, as they have transformed into positivity conditions for $m_{h_1}^2$, $m_{h_2}^2$, $v^2$, $v_S^2$:

$$4 \lambda_H \lambda_S - \kappa^2 = \frac{m_{h_1}^2 m_{h_2}^2}{v^2 v_S^2} > 0 , \tag{A.39a}$$

$$2 \lambda_S \mu_H^2 - \kappa \mu_S^2 = \frac{m_{h_1}^2 m_{h_2}^2}{2 v_S^2} > 0 , \tag{A.39b}$$

$$2 \lambda_H \mu_S^2 - \kappa \mu_H^2 = \frac{m_{h_1}^2 m_{h_2}^2}{2 v^2} > 0 . \tag{A.39c}$$

## A.6 Interaction vertices. Dark matter candidates

Interactions of the dark-sector particles described by the Lagrangians (A.32) and (A.35) are represented by the Feynman vertices provided in fig. A.1. The scalar particles $h_1$, $h_2$ interact with the SM particles like the SM Higgs particle, but multiplied by $R_{11}$ or $R_{12}$, respectively, with the matrix $R$ defined by eq. (A.24).

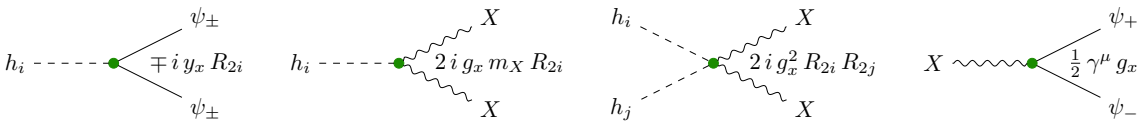


**Figure A.1:** Vertices corresponding to interactions of dark particles (vector $X$ and fermions $\psi_+$, $\psi_-$) in the VFDM model. Matrix $R$ is defined in eq. (A.24) and $i, j = 1, 2$. In [21, 22], a wrong value of the factor corresponding to the $XXh_ih_j$ vertex has been provided (in the numerical calculations therein, however, the correct value has been used).

The leftmost interaction shown in fig. A.1 makes a decay in the dark sector possible. As a consequence, the model provides either two or three massive, stable candidates for dark matter, depending on whether the heaviest from $\psi_+$, $\psi_-$, $X$ is heavy enough to decay into the two others.

# Appendix B

# One-component dark matter models

The pseudo-Goldstone (appendix B.1), fermion (appendix B.2) and vector (appendix B.3) DM models, described here basing on publications [3, 4] and conference proceedings [5–7], are simple, however not necessarily minimal, fully self-consistent, renormalizable models of one-component Higgs-portal dark matter of spin 0, 1/2 and 1, respectively. They have been used to investigate the influence of the spin of dark particles on their interactions with the Standard Model. What makes the models especially useful to perform the comparison, is a common parameter space that consists of:

- $\sin\alpha$, sine of the scalar-sector mixing angle;
- $v_S$, the vacuum expectation value of the additional scalar $S$;
- mass of the dark particle (depending on the model, it is denoted $m_A$, $m_\psi$ or $m_X$);
- $m_{h_2}$, mass of the second Higgs state that couples mostly to the dark sector.

Parameters $m_{h_1}$ and $v$, appearing in the following description of the models, are assumed to correspond to the known values of the mass of the known Higgs boson and the VEV of the SM Higgs field, so

$$m_{h_1} = 125 \text{ GeV} , \quad v = 246 \text{ GeV} . \tag{B.1}$$

All the aforementioned quantities are defined in detail in the following sections.

## B.1 Pseudo-Goldstone (scalar) DM model

In the pseudo-Goldstone dark matter (pGDM) model, the Standard Model is extended by a complex scalar singlet $S$. Analogously to the VFDM model (appendix A), the real-part fluctuation of $S$ mixes with the real-part fluctuation of the neutral component of the SM Higgs field, resulting in two Higgs-like mass eigenstates: $h_1$ (the known Higgs particle) and $h_2$. In contrast to the VFDM model, the imaginary-part fluctuation of $S$, denoted by $A$, obtains a non-zero mass from the symmetry-breaking term $\mu^2(S^2 + S^{*2})$,[1] and become a scalar dark matter particle.

The most general Lagrangian describing $S$ is too complicated to keep the model easily comparable with the other one-component DM models described in this dissertation. Hence, in order to simplify the Lagrangian, a local $U(1)_x$ symmetry which does not affect the SM fields is imposed:

$$U(1)_x : S \to e^{i\varphi} S . \tag{B.2}$$

We allow this symmetry to be softly broken: it cancels all the terms that are power-4[2] in $S$ except $|S|^4$, but the terms of lower power in $S$ are, in principle, allowed. The terms that are of odd powers in $S$ can be cancelled by a discrete $\mathbb{Z}_2$ symmetry:

$$\mathbb{Z}_2 : S \to -S , \tag{B.3}$$

[1] Without this term, $A$ would be a truly massless Goldstone boson

[2] In this paragraph, by "the terms that are power-$n$ in $S$" one should understand the terms proportional to: $S^n$, $S^{n-1}S^*$, $S^{n-2}S^{*2}$, ..., $S^{*n}$.

which, again, does not affect the SM fields. The third symmetry, $\mathcal{C}$, is imposed to make the coefficient of the $U(1)_x$-softly-breaking term $S^2 + S^{*2}$ real, as it will be the source of the mass of the dark particle, as described in the following sections. $\mathcal{C}$ acts on the $S$ field in the following way:

$$\mathcal{C} : S \to S^* \,, \tag{B.4}$$

while all the SM fields remain unchanged. Eventually, the remaining Lagrangian takes the form

$$\mathcal{L} = \mathcal{L}_{\mathrm{SM}} + (D_\mu H)^\dagger (D^\mu H) + (\partial_\mu S)^* (\partial^\mu S) - V(H,S) \,, \tag{B.5}$$

where $\mathcal{L}_{\mathrm{SM}}$ denotes the SM Lagrangian (excluding the Higgs field), $D_\mu$ is the SM covariant derivative and the scalar potential $V$ reads

$$V(H,S) \equiv -\mu_H^2 |H|^2 + \lambda_H |H|^4 - \mu_S^2 |S|^2 + \lambda_S |S|^4 + \kappa |H|^2 |S|^2 + \mu^2 (S^2 + S^{*2}) \,. \tag{B.6}$$

This potential describes the SM Higgs field $H$ and the additional scalar $S$ mixed by the Higgs-portal term $\kappa |H|^2 |S|^2$. Note that all the coefficients of the scalar potential (B.6): $\lambda_H$, $\mu_H^2$, $\lambda_S$, $\mu_S^2$, $\kappa$, $\mu^2$ are real, but not necessarily positive. Conditions that must be satisfied by them are discussed in the following section.

### B.1.1 Stability of the scalar potential and globalness of its minimum

To keep the potential (B.6) asymptotically positive, the following conditions are required:

$$\lambda_H > 0 \,, \quad \lambda_S > 0 \,, \quad \kappa > -2\sqrt{\lambda_H \lambda_S} \,, \tag{B.7}$$

as in the VFDM model (see eq. (A.12)). To find the vacuum expectation values (VEVs) of the scalar fields, let us assume that the potential is minimized by

$$H = \langle H \rangle \equiv \begin{pmatrix} 0 \\ \frac{v}{\sqrt{2}} \end{pmatrix} \,, \quad S = \langle S \rangle \equiv \frac{v_S + i v_A}{\sqrt{2}} \,, \tag{B.8}$$

with real $v$, $v_S$ and $v_A$. The potential is invariant under complex rotations of the neutral component of $H$, so $v$ can be chosen to be real without any loss of generality. On the other hand, as the $U(1)_x$ symmetry is softly broken, the VEV of the $S$ field cannot be a priori assumed to be real. However, due to invariance under the $S \to -S$ symmetry, we can assume that the real part of that VEV is non-negative. Summing up this paragraph, the assumptions are:

$$v \geqslant 0 \,, \quad v_S \geqslant 0 \,, \quad v_A \in \mathbb{R} \,. \tag{B.9}$$

The fields can be expanded around their VEVs as

$$H = \begin{pmatrix} \pi^+ \\ \frac{v + h + i\pi^0}{\sqrt{2}} \end{pmatrix} \,, \quad S = \frac{v_S + \phi + i(v_A + A)}{\sqrt{2}} \,, \tag{B.10}$$

Fields $\pi^+$ and $\pi^0$ are the Goldstone bosons that provide mass to the SM gauge bosons. As already mentioned, $h$ and $\phi$ will mix and provide two Higgs-like particles, while $A$ will serve as the dark particle.

In order for the VEVs to minimize the value of $V$, the following derivatives must vanish

$$0 = \frac{\partial V}{\partial |H|}\Big|_{\substack{H=\langle H\rangle \\ S=\langle S\rangle}} = \frac{v}{\sqrt{2}} \left(-2\mu_H^2 + 2\lambda_H v^2 + \kappa(v_S^2 + v_A^2)\right) \,, \tag{B.11a}$$

$$0 = \frac{\partial V}{\partial \Re S}\Big|_{\substack{H=\langle H\rangle \\ S=\langle S\rangle}} = \frac{v_S}{\sqrt{2}} \left(-2\mu_S^2 + 2\lambda_S(v_S^2 + v_A^2) + \kappa v^2 + 4\mu^2\right) \,, \tag{B.11b}$$

$$0 = \frac{\partial V}{\partial \Im S}\Big|_{\substack{H=\langle H\rangle \\ S=\langle S\rangle}} = \frac{v_A}{\sqrt{2}} \left(-2\mu_S^2 + 2\lambda_S(v_S^2 + v_A^2) + \kappa v^2 - 4\mu^2\right) \,. \tag{B.11c}$$

As it is evident from the second and the third equation, $v_S$ and $v_A$ can be both non-zero only if $\mu^2$ is equal to zero. Since setting $\mu^2$ to zero would make the would-be dark particle $A$ massless, the possibility of $v_S$ and $v_A$ both non-zero is rejected, which means that the following six solutions of eq. (B.11) are possible:

$$v^2 = \frac{4\lambda_S\mu_H^2 - 2\kappa(\mu_S^2 - 2\mu^2)}{4\lambda_H\lambda_S - \kappa^2}\,, \qquad v_S^2 = \frac{4\lambda_H(\mu_S^2 - 2\mu^2) - 2\kappa\mu_H^2}{4\lambda_H\lambda_S - \kappa^2}\,, \qquad v_A^2 = 0$$
$$\Rightarrow \quad V = V_1 \equiv -\frac{\lambda_H(\mu_S^2 - 2\mu^2)^2 - \kappa\mu_H^2(\mu_S^2 - 2\mu^2) + \lambda_S\mu_H^4}{4\lambda_H\lambda_S - \kappa^2}\,, \tag{B.12}$$

$$v^2 = \frac{4\lambda_S\mu_H^2 - 2\kappa(\mu_S^2 + 2\mu^2)}{4\lambda_H\lambda_S - \kappa^2}\,, \qquad v_S^2 = 0\,, \qquad v_A^2 = \frac{4\lambda_H(\mu_S^2 + 2\mu^2) - 2\kappa\mu_H^2}{4\lambda_H\lambda_S - \kappa^2}$$
$$\Rightarrow \quad V = V_2 \equiv -\frac{\lambda_H(\mu_S^2 + 2\mu^2)^2 - \kappa\mu_H^2(\mu_S^2 + 2\mu^2) + \lambda_S\mu_H^4}{4\lambda_H\lambda_S - \kappa^2}\,, \tag{B.13}$$

$$v^2 = \frac{\mu_H^2}{\lambda_H}\,, \qquad v_S^2 = 0\,, \qquad v_A^2 = 0 \qquad \Rightarrow \qquad V = V_3 \equiv -\frac{\mu_H^4}{4\lambda_H}\,, \tag{B.14}$$

$$v^2 = 0\,, \qquad v_S^2 = \frac{\mu_S^2 - 2\mu^2}{\lambda_S}\,, \qquad v_A^2 = 0 \qquad \Rightarrow \qquad V = V_4 \equiv -\frac{(\mu_S^2 - 2\mu^2)^2}{4\lambda_S}\,, \tag{B.15}$$

$$v^2 = 0\,, \qquad v_S^2 = 0\,, \qquad v_A^2 = \frac{\mu_S^2 + 2\mu^2}{\lambda_S} \qquad \Rightarrow \qquad V = V_5 \equiv -\frac{(\mu_S^2 + 2\mu^2)^2}{4\lambda_S}\,, \tag{B.16}$$

$$v^2 = 0\,, \qquad v_S^2 = 0\,, \qquad v_A^2 = 0 \qquad \Rightarrow \qquad V = V_6 \equiv 0\,. \tag{B.17}$$

A non-zero value of $v$ is needed to provide masses to the SM gauge bosons through the Higgs mechanism. Moreover, in order to make the SDM model maximally similar to the FDM (appendix B.2) and VDM (appendix B.3) models, $v_S \neq 0$ is also demanded. Hence, the solution (B.12) is preferable. To ensure that (B.12) defines the global minimum, the mass-squared matrix corresponding to that solution must be positive-definite and the value of $V_1$ must be smaller than $V_2$, $V_3$, $V_4$, $V_5$ and $V_6$.

First, let us observe that the positive-definiteness of the mass-squared matrix, given by:

$$M^2_{h,\phi,A} \equiv \left[\begin{array}{ccc} \frac{\partial^2 V}{\partial h^2} & \frac{\partial^2 V}{\partial\phi\,\partial h} & \frac{\partial^2 V}{\partial A\,\partial h} \\ \frac{\partial^2 V}{\partial h\,\partial\phi} & \frac{\partial^2 V}{\partial\phi^2} & \frac{\partial^2 V}{\partial A\,\partial\phi} \\ \frac{\partial^2 V}{\partial h\,\partial A} & \frac{\partial^2 V}{\partial\phi\,\partial A} & \frac{\partial^2 V}{\partial A^2} \end{array}\right]\Bigg|_{\text{(B.12)}} = \begin{bmatrix} 2\lambda_H v^2 & \kappa v v_S & 0 \\ \kappa v v_S & 2\lambda_S v_S^2 & 0 \\ 0 & 0 & -4\mu^2 \end{bmatrix}\,. \tag{B.18}$$

requires

$$\mu^2 < 0\,, \quad 4\,\lambda_H\,\lambda_S > \kappa^2\,. \tag{B.19}$$

Since $v^2$ and $v_S^2$ are squares of real, non-zero quantities, they should be positive, from eq. (B.12) it follows that

$$2\,\lambda_S\,\mu_H^2 > \kappa\,(\mu_S^2 - 2\mu^2)\,, \quad 2\,\lambda_H\,(\mu_S^2 - 2\mu^2) > \kappa\,\mu_H^2\,. \tag{B.20}$$

Given that eqs. (B.7) and (B.19) are satisfied, $V_1$ is always smaller than $V_3$ and $V_4$ since

$$\begin{aligned} V_3 - V_1 &= -\frac{\mu_H^4}{4\lambda_H} + \frac{\lambda_H(\mu_S^2 - 2\mu^2)^2 - \kappa\mu_H^2(\mu_S^2 - 2\mu^2) + \lambda_S\mu_H^4}{4\lambda_H\lambda_S - \kappa^2} \\ &= \frac{\left(2\lambda_H(\mu_S^2 - 2\mu^2) - \kappa\mu_H^2\right)^2}{4\lambda_H(4\lambda_H\lambda_S - \kappa^2)} > 0\,, \\ V_4 - V_1 &= -\frac{(\mu_S^2 - 2\mu^2)^2}{4\lambda_S} + \frac{\lambda_H(\mu_S^2 - 2\mu^2)^2 - \kappa\mu_H^2(\mu_S^2 - 2\mu^2) + \lambda_S\mu_H^4}{4\lambda_H\lambda_S - \kappa^2} \\ &= \frac{\left(2\lambda_S\mu_H^2 - \kappa(\mu_S^2 - 2\mu^2)\right)^2}{4\lambda_S(4\lambda_H\lambda_S - \kappa^2)} > 0\,. \end{aligned} \tag{B.21}$$

Consequently, $V_1$ is smaller than $V_6$ since $V_6 > V_3$. For $V_1$ to be smaller than $V_5$ we assume that

$$\mu_S^2 > 0\,. \tag{B.22}$$

Then, $V_1 < V_5$ is a consequence of an obvious inequality $V_4 < V_5$. The difference between $V_2$ and $V_1$ is

$$\begin{aligned} V_2 - V_1 &= -\frac{\lambda_H(\mu_S^2 + 2\mu^2)^2 - \kappa\,\mu_H^2(\mu_S^2 + 2\mu^2) + \lambda_S\mu_H^4}{4\lambda_H\lambda_S - \kappa^2} \\ &\quad + \frac{\lambda_H(\mu_S^2 - 2\mu^2)^2 - \kappa\,\mu_H^2(\mu_S^2 - 2\mu^2) + \lambda_S\mu_H^4}{4\lambda_H\lambda_S - \kappa^2} \\ &= -4\,\mu^2\,\frac{2\lambda_H\mu_S^2 - \kappa\,\mu_H^2}{4\lambda_H\lambda_S - \kappa^2}\,. \end{aligned} \tag{B.23}$$

Therefore, since $\mu^2 < 0$ and $4\,\lambda_H\,\lambda_S > \kappa^2$ (see eq. (B.19)), for $V_1$ to be smaller than $V_2$ the following condition must hold:

$$2\,\lambda_H\,\mu_S^2 > \kappa\,\mu_H^2\ . \tag{B.24}$$

To summarize this section, let us collect the conditions for eq. (B.12) to define a global minimum, given by eqs. (B.19), (B.20), (B.22) and (B.24):

$$\mu^2 < 0\ ,\quad \mu_S^2 > 0\ ,\quad 4\,\lambda_H\,\lambda_S > \kappa^2\ , \tag{B.25a}$$

$$2\,\lambda_S\,\mu_H^2 > \kappa\,(\mu_S^2 - 2\mu^2)\ ,\quad 2\,\lambda_H\,\mu_S^2 > \kappa\,\mu_H^2\ . \tag{B.25b}$$

The condition $2\,\lambda_H\,(\mu_S^2 - 2\mu^2) > \kappa\,\mu_H^2$, coming from eq. (B.20), is redundant given that the above conditions hold.

### B.1.2 Mixing of the scalar states. Parametrization of the model

Let us recall the mass-squared matrix provided in eq. (B.18):

$$M^2_{h,\phi,A} = \begin{bmatrix} 2\lambda_H v^2 & \kappa v v_S & 0 \\ \kappa v v_S & 2\lambda_S v_S^2 & 0 \\ 0 & 0 & -4\mu^2 \end{bmatrix} \tag{B.26}$$

with the VEVs defined by eq. (B.12). Similarly to the way it is done in the case of the VFDM model (see eq. (A.24)), this matrix can be diagonalized using the following rotation:

$$\begin{pmatrix} h_1 \\ h_2 \\ A \end{pmatrix} = R^{-1} \begin{pmatrix} h \\ \phi \\ A \end{pmatrix}\ ,\quad R \equiv \begin{bmatrix} \cos\alpha & -\sin\alpha & 0 \\ \sin\alpha & \cos\alpha & 0 \\ 0 & 0 & 1 \end{bmatrix}\ ,\quad \tan 2\alpha \equiv \frac{\kappa v v_S}{\lambda_H v^2 - \lambda_S v_S^2}\ . \tag{B.27}$$

In the rotated basis consisting of $h_1$, $h_2$ and $A$, the mass-squared matrix becomes

$$M^2_{h_1,h_2,A} = R^{-1} M^2_{h,\phi,A} R \ = \begin{bmatrix} m_{h_1}^2 & 0 & 0 \\ 0 & m_{h_2}^2 & 0 \\ 0 & 0 & m_A^2 \end{bmatrix}\ , \tag{B.28}$$

with masses $m_{h_1}$, $m_{h_2}$ and $m_A$ related to the parameters of $V$ in the following way:

$$\kappa = \sin 2\alpha\,\frac{m_{h_1}^2 - m_{h_2}^2}{2 v v_S}\ ,\qquad \mu^2 = -\frac{1}{4} m_A^2\ , \tag{B.29a}$$

$$\lambda_H = \frac{\cos^2\alpha\, m_{h_1}^2 + \sin^2\alpha\, m_{h_2}^2}{2v^2}\ ,\qquad \lambda_S = \frac{\sin^2\alpha\, m_{h_1}^2 + \cos^2\alpha\, m_{h_2}^2}{2 v_S^2}\ , \tag{B.29b}$$

$$\mu_H^2 = \frac{1}{2} m_{h_1}^2\,\cos^2\alpha + \frac{1}{2} m_{h_2}^2\,\sin^2\alpha + \frac{1}{4}\frac{v_S}{v}\sin 2\alpha\,(m_{h_1}^2 - m_{h_2}^2)\ , \tag{B.29c}$$

$$\mu_S^2 = \frac{1}{2} m_{h_1}^2\,\sin^2\alpha + \frac{1}{2} m_{h_2}^2\,\cos^2\alpha + \frac{1}{4}\frac{v}{v_S}\sin 2\alpha\,(m_{h_1}^2 - m_{h_2}^2) - \frac{1}{2}\,m_A^2\ . \tag{B.29d}$$

Note that due to the positive-definiteness of the mass-squared matrix (B.18) before diagonalization, all the masses: $m_{h_1}^2$, $m_{h_2}^2$ and $m_A^2$ are automatically positive.

After the diagonalization, the model can parametrized by the following quantities:

$$v\ ,\quad v_S\ ,\quad m_{h_1}\ ,\quad m_{h_2}\ ,\quad \sin\alpha\ ,\quad m_A \tag{B.30}$$

with an assumption that the values of $v$ and $m_{h_1}$ are SM-like:

$$v = 246\ \text{GeV}\ ,\quad m_{h_1} = 125\ \text{GeV}\ , \tag{B.31}$$

as it was in the case of the VFDM model (see appendix A).

### B.1.3 Interactions of the dark particle

Eventually, after the SSB and dropping the massless Goldstone bosons $\pi^+$, $\pi^0$ absorbed by the SM gauge vectors, the part of the potential (B.6) containing the dark matter particle $A$ becomes:

$$\begin{aligned} V(H,S) \to V(h_1,h_2,A) \supset & \frac{1}{2}\, m_A^2\, A^2 + \frac{1}{2v_S}\left(m_{h_1}^2\, \sin\alpha\, h_1 + m_{h_2}^2\, \cos\alpha\, h_2\right) A^2 \\ & + \frac{1}{4}(2\lambda_S\, \sin^2\alpha + \kappa\, \cos^2\alpha)\, h_1^2\, A^2 + \frac{1}{4}(2\lambda_S\, \cos^2\alpha + \kappa\, \sin^2\alpha)\, h_2^2\, A^2 \\ & + \frac{1}{2}(2\lambda_S - \kappa)\, \cos\alpha\, \sin\alpha\, h_1\, h_2\, A^2 + \frac{\lambda_S}{4}\, A^4\ . \end{aligned} \tag{B.32}$$

Although $\lambda_S$ and $\kappa$ can be expressed in terms of the mixing angle, VEVs and masses of the Higgs-like states (see eq. (B.29a)), they are kept here for compactness. The corresponding interactions of particle $A$ are presented in fig. B.1. Self-interactions have been omitted. The scalar particles $h_1$, $h_2$ interact with the SM particles like the SM Higgs particle, but multiplied by $R_{11}$ or $R_{12}$, respectively, with the matrix $R$ defined by eq. (B.27)

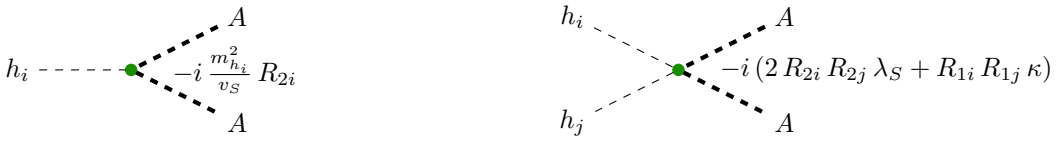


**Figure B.1:** Vertices corresponding to interactions of the dark scalar $A$ in the pGDM model. Self-interactions of $A$ have been omitted. Matrix $R$ is defined in eq. (B.27) and $i,j = 1,2$. In [3,4], a wrong value of the factor corresponding to the $AAh_ih_j$ vertex has been provided (this vertex, however, has not been used to obtain the numerical results therein).

## B.2 Fermion DM model

The fermion dark matter (FDM) model extends the SM by a real scalar singlet $S$ and a left-handed Dirac fermion $\chi$. A Majorana fermion formed as a combination of $\chi$ and its charge conjugation, $\chi^c$, obtains its mass from the Yukawa interaction with $S$ and becomes a fermionic DM particle.

The newly introduced fields are charged under an additional $\mathbb{Z}_4$ group:

$$\mathbb{Z}_4: \quad S \to -S\ , \quad \chi \to i\chi\ . \tag{B.33}$$

This $\mathbb{Z}_4$ does not affect the SM fields. The Lagrangian of the model reads

$$\mathcal{L} = \mathcal{L}_{\rm SM} + i\,\bar{\chi}\,\partial\!\!\!/\chi + \frac{1}{2}\,(D_\mu H)^\dagger\,(D^\mu H) + \frac{1}{2}\,\partial^\mu S\,\partial_\mu S - \frac{y_x}{2}\,(\bar{\chi^c}\chi + \bar{\chi}\chi^c)\,S - V(H,S)\ , \tag{B.34}$$

where $\mathcal{L}_{\rm SM}$ denotes the SM Lagrangian (excluding the Higgs field), $D_\mu$ is the SM covariant derivative, the Yukawa coupling constant $y_x$ is real and dimensionless, and the charge-conjugated field $\chi^c$ is defined as

$$\chi^c \equiv -i\gamma_2\chi^*\ , \tag{B.35}$$

as in the case of the VFDM model (appendix A). The potential $V$ reads

$$V(H,S) = -\mu_H^2|H|^2 + \lambda_H|H|^4 - \frac{\mu_S^2}{2}S^2 + \frac{\lambda_S}{4}S^4 + \frac{\kappa}{2}\,|H|^2S^2\ . \tag{B.36}$$

The stability conditions are

$$\lambda_H > 0\ , \quad \lambda_S > 0\ , \quad \kappa > -2\sqrt{\lambda_H\lambda_S}\ , \tag{B.37}$$

similarly to the case of the VFDM and pGDM models discussed previously (see eqs. (A.12) and (B.7)). The scalar fields $H$ and $S$ are expanded around their VEVs, $v$ and $v_S$, respectively, as

$$H = \begin{pmatrix} \pi^+ \\ \frac{v+h+i\pi^0}{\sqrt{2}} \end{pmatrix}\ , \quad S = v_S + \phi\ . \tag{B.38}$$

Due to symmetry of the potential, it can be assumed without loss of generality that the VEVs are real and non-negative: $v \geqslant 0$, $v_S \geqslant 0$. They must satisfy the following conditions:

$$0 = \frac{\partial V}{\partial H}\Big|_{\substack{H=\langle H\rangle \\ S=\langle S\rangle}} = \frac{v}{\sqrt{2}}\left(-\mu_H^2 + \lambda_H v^2 + \frac{\kappa}{2} v_S^2\right) , \tag{B.39a}$$

$$0 = \frac{\partial V}{\partial S}\Big|_{\substack{H=\langle H\rangle \\ S=\langle S\rangle}} = v_S\left(-\mu_S^2 + \lambda_S v_S^2 + \frac{\kappa}{2} v^2\right) . \tag{B.39b}$$

The above conditions are solved by

$$v^2 = \frac{4\lambda_S\mu_H^2 - 2\kappa\mu_S^2}{4\lambda_H\lambda_S - \kappa^2} , \qquad v_S^2 = \frac{4\lambda_H\mu_S^2 - 2\kappa\mu_H^2}{4\lambda_H\lambda_S - \kappa^2} \qquad \Rightarrow \qquad V_1 = -\frac{\lambda_H\mu_S^4 - \kappa\mu_H^2\mu_S^2 + \lambda_S\mu_H^4}{4\lambda_H\lambda_S - \kappa^2} , \tag{B.40}$$

$$v^2 = 0 , \qquad v_S^2 = \frac{\mu_S^2}{\lambda_S} \qquad \Rightarrow \qquad V_2 = -\frac{\mu_S^4}{4\lambda_S} , \tag{B.41}$$

$$v^2 = \frac{\mu_H^2}{\lambda_H} , \qquad v_S^2 = 0 \qquad \Rightarrow \qquad V_3 = -\frac{\mu_H^4}{4\lambda_H} , \tag{B.42}$$

$$v^2 = 0 , \qquad v_S^2 = 0 \qquad \Rightarrow \qquad V_4 = 0 . \tag{B.43}$$

Non-zero values of $v$ and $v_S$ are necessary to provide masses to the SM gauge bosons and the dark fermionic state, so the solution (B.40) is preferred. It defines the global minimum when $V_1$ is smaller than $V_2$, $V_3$ and $V_4$. To check that, the following difference can be calculated:

$$\begin{aligned} V_2 - V_1 &= \frac{\lambda_H\mu_S^4 - \kappa\mu_H^2\mu_S^2 + \lambda_S\mu_H^4}{4\lambda_H\lambda_S - \kappa^2} - \frac{\mu_S^4}{4\lambda_S} \\ &= \frac{2\lambda_S\mu_H^2 - \kappa\mu_S^2}{4\lambda_S(4\lambda_H\lambda_S - \kappa^2)} , \end{aligned} \tag{B.44}$$

which is positive when

$$4\,\lambda_H\,\lambda_S > \kappa^2 . \tag{B.45}$$

An analogous calculation shows that the same condition ensures that $V_1 < V_3$. Since each of $V_2$, $V_3$ is obviously smaller than $V_4$, the inequality $V_1 < V_4$ holds as well.

As it is clear from eq. (B.40), positivity of $v^2$ and $v_S^2$ means that

$$2\,\lambda_S\,\mu_H^2 > \kappa\,\mu_S^2 , \quad 2\,\lambda_H\,\mu_S^2 > \kappa\,\mu_H^2 . \tag{B.46}$$

The mass-squared matrix for the fields $h$ and $\phi$ reads

$$M_{h,\phi}^2 = \begin{bmatrix} 2\,\lambda_H\,v^2 & \kappa\,v\,v_S \\ \kappa\,v\,v_S & 2\,\lambda_S\,v_S^2 \end{bmatrix} , \tag{B.47}$$

which is positive-definite since eq. (B.45) holds. The same way as it happens in the previously discussed models, the matrix is diagonalized using the following rotation:

$$\begin{pmatrix} h_1 \\ h_2 \end{pmatrix} = R^{-1}\begin{pmatrix} h \\ \phi \end{pmatrix} , \quad R \equiv \begin{bmatrix} \cos\alpha & -\sin\alpha \\ \sin\alpha & \cos\alpha \end{bmatrix} , \quad \tan 2\alpha \equiv \frac{\kappa\,v\,v_S}{\lambda_H v^2 - \lambda_S v_S^2} . \tag{B.48}$$

Then, the mass-squared matrix in the rotated basis consisting of $h_1$ and $h_2$ becomes

$$M_{h_1,h_2}^2 = R^{-1}M_{h,\phi}^2 R \;= \begin{bmatrix} m_{h_1}^2 & 0 \\ 0 & m_{h_2}^2 \end{bmatrix} , \tag{B.49}$$

with the masses related to the parameters of the potential by the following relations:

$$\kappa = \sin 2\alpha\,\frac{m_{h_1}^2 - m_{h_2}^2}{2\,v v_S} , \tag{B.50a}$$

$$\lambda_H = \frac{\cos^2\alpha\,m_{h_1}^2 + \sin^2\alpha\,m_{h_2}^2}{2\,v^2} , \quad \mu_H^2 = \frac{1}{2}m_{h_1}^2\cos^2\alpha + \frac{1}{2}m_{h_2}^2\sin^2\alpha + \frac{1}{4}\frac{v_S}{v}\sin 2\alpha\,(m_{h_1}^2 - m_{h_2}^2) , \tag{B.50b}$$

$$\lambda_S = \frac{\sin^2\alpha\,m_{h_1}^2 + \cos^2\alpha\,m_{h_2}^2}{2\,v_S^2} , \quad \mu_S^2 = \frac{1}{2}m_{h_1}^2\sin^2\alpha + \frac{1}{2}m_{h_2}^2\cos^2\alpha + \frac{1}{4}\frac{v}{v_S}\sin 2\alpha\,(m_{h_1}^2 - m_{h_2}^2) . \tag{B.50c}$$

Note that due to positive-definiteness of the mass-squared matrix (B.47) before diagonalization, both $m_{h_1}^2$ and $m_{h_2}^2$ are automatically positive.

After the SSB, the dark-fermionic Lagrangian becomes

$$\begin{aligned}\mathcal{L}_{\mathrm{DF}} &= i\,\bar{\chi}\,\partial\!\!\!/\chi - \frac{y_x v_S}{2}\left(\bar{\chi^c}\chi + \bar{\chi}\chi^c\right) - \frac{y_x}{2}\left(\bar{\chi^c}\chi + \bar{\chi}\chi^c\right)\phi \\ &= \frac{1}{2}\bar{\psi}(i\partial\!\!\!/ - m_\psi)\psi - \frac{y_x}{2}\,\bar{\psi}\psi\,\phi\end{aligned} \tag{B.51}$$

with Majorana fermion $\psi$ defined as

$$\psi \equiv \chi + \chi^c = \psi^c \tag{B.52}$$

and

$$m_\psi \equiv y_x v_S\ . \tag{B.53}$$

In the second equality of eq. (B.51), eqs. (E.12) and (E.13) have been used.[3] The massive Majorana fermion $\psi$, whose interaction vertex is presented in fig. B.2, serves as the dark particle of the FDM model. The scalar particles $h_1$, $h_2$ interact with the SM particles like the SM Higgs particle, but multiplied by $R_{11}$ or $R_{12}$, respectively, with the matrix $R$ defined by eq. (B.48).

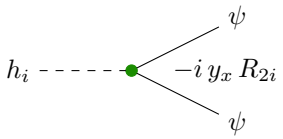


**Figure B.2:** A vertex corresponding to the interaction of the dark fermion $\psi$ in the FDM model. Matrix $R$ is defined in eq. (B.48) and $i = 1, 2$.

The model is parametrized by

$$v\ ,\quad v_S\ ,\quad m_{h_1}\ ,\quad m_{h_2}\ ,\quad \sin\alpha\ ,\quad m_\psi\ . \tag{B.54}$$

with $v$ and $m_{h_1}$ assumed to take their SM values:

$$v = 246\ \mathrm{GeV}\ ,\quad m_{h_1} = 125\ \mathrm{GeV}\ , \tag{B.55}$$

as in the previously discussed VFDM (appendix A) and pGDM (appendix B.1) models.

## B.3 Vector DM model

The vector dark matter (VDM) model introduces a complex scalar singlet $S$ neutral under the action of the SM gauge group and charged under an additional $U(1)_x$ group (which does not affect the SM fields). The gauge vector of the $U(1)_x$ group, $X$, gains its mass, $m_X$, through the Higgs mechanism from interaction with $S$ and becomes a massive dark vector particle.

This model can be treated as a simplified version of the VFDM model, presented in appendix A, with all dark-sector fermionic fields omitted. If we neglect the dark fermions, the description of both models is exactly the same, so the details are not repeated here.

Interactions of the dark particle $X$ are depicted in fig. B.3.


**Figure B.3:** Vertices corresponding to interactions of dark particles in the VDM model. Matrix $R$ is defined in the same way as the one provided by eq. (A.24) and $i, j = 1, 2$.

[3] Note the difference in the coefficient between eq. (B.52) and (E.7a), resulting in a consequent difference between the right-hand sides of eqs. (E.12) and (E.13) and the second line of eq. (B.51).

Parameters of the model are

$$v\ , \quad v_S\ , \quad m_{h_1}\ , \quad m_{h_2}\ , \quad \sin\alpha\ , \quad m_X\ . \tag{B.56}$$

The $g_x$ coupling constant that appears in fig. B.3 is defined in terms of the above parameters as

$$g_x = \frac{m_X}{v_S}\ . \tag{B.57}$$

As in the case of all the models described previously: VFDM (appendix A), pGDM (appendix B.1) and FDM (appendix B.2), values of $v$ and $m_{h_1}$ are assumed to correspond to the SM ones:

$$v = 246\ \text{GeV}\ , \quad m_{h_1} = 125\ \text{GeV}\ . \tag{B.58}$$

# Appendix C

# Three-scalar toy model

This toy model, employed in publication [2] and chapter 5 of this dissertation, consists of three real scalar fields: $\phi_1$, $\phi_2$, $\Phi$, and is equipped with two discrete symmetries, $\mathbb{Z}_2$ and $\mathbb{Z}_2'$, acting on the fields in the following way:

$$\mathbb{Z}_2: \qquad \phi_1 \to -\phi_1\,, \qquad \phi_2 \to \phi_2\,, \qquad \Phi \to -\Phi\,, \tag{C.1a}$$

$$\mathbb{Z}_2': \qquad \phi_1 \to \phi_1\,, \qquad \phi_2 \to -\phi_2\,, \qquad \Phi \to -\Phi\,. \tag{C.1b}$$

These symmetries lead to cancellation of:

- all mixed dimension-2 terms,
- all dimension-3 terms except the one with three different fields,
- most of the dimension-4 terms.

The dimension-4 terms that are products of the mass terms and, therefore, cannot be forbidden if the particles are massive, are dropped for simplicity. Then, the Lagrangian reads

$$\begin{aligned}\mathcal{L} = \quad & \frac{1}{2}\left(\partial^\mu\phi_1\,\partial_\mu\phi_1 - m_1^2\,\phi_1^2\right) + \frac{1}{2}\left(\partial^\mu\phi_2\,\partial_\mu\phi_2 - m_2^2\,\phi_2^2\right) \\ & + \frac{1}{2}\left(\partial^\mu\Phi\,\partial_\mu\Phi - M^2\,\Phi^2\right) + \mu\,\phi_1\phi_2\Phi\,,\end{aligned} \tag{C.2}$$

where $m_1$, $m_2$ and $M$ are masses of the fields $\phi_1$, $\phi_2$ and $\Phi$, respectively. It is assumed that

$$m_1 > m_2 + M\,, \tag{C.3}$$

so that $\phi_2$ and $M$ are stable, while the decay $\phi_1 \to \phi_2 M$ is allowed. The corresponding vertex is shown in fig. C.1.

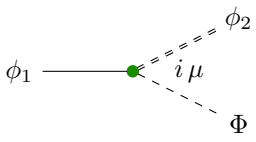


**Figure C.1:** A vertex corresponding to the interaction of the dark particles in the toy model of dark matter. For clarity, different particles are symbolized with different types of line: dashed for $\Phi$, solid for $\phi_1$ and double dashed for $\phi_2$

# Appendix D

# Properties of the Dirac matrices

Here, some properties of the Dirac gamma matrices are collected for reader's convenience. Using them throughout the dissertation is not explicitly stated in text.

In this appendix, $\mathbb{1}$ denotes the identity matrix ($2 \times 2$ or $4 \times 4$, depending on the context).

## D.1 Representation-independent properties

- Defining property:

$$\{\gamma_\mu, \gamma_\nu\} = 2\, g_{\mu\nu}\, \mathbb{1}\,, \tag{D.1}$$

where $\{\bullet, \bullet\}$ denotes the anticommutator. One also defines the fifth matrix, $\gamma_5$:

$$\gamma_5 \equiv i\, \gamma_0\, \gamma_1\, \gamma_2\, \gamma_3\,, \tag{D.2}$$

that anticommutes with the four gamma matrices:

$$\{\gamma_\mu, \gamma_5\} = 0\,. \tag{D.3}$$

- Corollaries:

$$\gamma_0^2 = \mathbb{1}\,, \qquad \gamma_i^2 = -\mathbb{1}\,, \qquad \gamma_5^2 = \mathbb{1}\,, \tag{D.4a}$$

$$\operatorname{Tr}\gamma_\mu = 0\,, \qquad \operatorname{Tr}\gamma_5 = 0\,, \tag{D.4b}$$

where Tr denotes taking trace.

## D.2 Representation-specific properties

Throughout the dissertation, wherever the representation of the gamma matrices matters,they are assumed to be in the Dirac representation, in which

$$\gamma_0 \equiv \begin{bmatrix} \mathbb{1} & 0 \\ 0 & -\mathbb{1} \end{bmatrix}\,, \quad \gamma_i \equiv \begin{bmatrix} 0 & \sigma_i \\ -\sigma_i & 0 \end{bmatrix}\,, \quad \gamma_5 \equiv \begin{bmatrix} 0 & \mathbb{1} \\ \mathbb{1} & 0 \end{bmatrix}\,, \tag{D.5}$$

with $\sigma_i$ denoting Pauli matrices ($i = 1, 2, 3$):

$$\sigma_1 = \begin{bmatrix} 0 & 1 \\ 1 & 0 \end{bmatrix}\,, \quad \sigma_2 = \begin{bmatrix} 0 & -i \\ i & 0 \end{bmatrix}\,, \quad \sigma_3 = \begin{bmatrix} 1 & 0 \\ 0 & -1 \end{bmatrix}\,. \tag{D.6}$$

The gamma matrices expressed in the Dirac representation satisfy the following properties:

- Hermitian conjugation:

$$\gamma_\mu^\dagger = \gamma_0 \gamma_\mu \gamma_0\,, \quad \gamma_5^\dagger = \gamma_5\,, \tag{D.7}$$

- complex conjugation:

$$\gamma_\mu^* = \gamma_2 \gamma_\mu \gamma_2\,, \quad \gamma_5^* = \gamma_5\,, \tag{D.8}$$

- transposition:

$$\gamma_\mu^\intercal = (\gamma_\mu^\dagger)^* = \gamma_2 \gamma_0 \gamma_\mu \gamma_0 \gamma_2\,, \quad \gamma_5^\intercal = \gamma_5\,. \tag{D.9}$$

## D.3 Charge-conjugation and projection operators

The following operators, defined in terms of the gamma matrices, are used in this dissertation:

- charge-conjugation operator $\mathcal{C}$:

$$\mathcal{C} \equiv -i\gamma_2\gamma_0 = i\gamma_0\gamma_2 \,, \tag{D.10}$$

  which satisfies

$$\mathcal{C}^2 = -1 \,, \qquad \mathcal{C}^\dagger = \gamma_0\,\mathcal{C}\,\gamma_0 = -\mathcal{C} \,, \qquad \mathcal{C}\gamma_\mu\mathcal{C} = \gamma_\mu^\intercal \,, \tag{D.11}$$

- projection operators $P_{R,L}$:

$$P_R \equiv \frac{1}{2}(\mathbb{1} + \gamma_5) \,, \quad P_L \equiv \frac{1}{2}(\mathbb{1} - \gamma_5) \,, \tag{D.12}$$

  which satisfy

$$P_R + P_L = \mathbb{1} \,, \tag{D.13a}$$
$$P_R P_L = P_L P_R = 0 \,, \tag{D.13b}$$
$$P_R\gamma_\mu = \gamma_\mu P_L \,, \quad P_L\gamma_\mu = \gamma_\mu P_R \,, \tag{D.13c}$$
$$P_R^2 = P_R^\dagger = P_R^\intercal = P_R \,, \quad P_L^2 = P_L^\dagger = P_L^\intercal = P_L \,. \tag{D.13d}$$

# Appendix E

# Some identities satisfied by fermionic fields

As it was a non-trivial task for the author to correctly take into account all the counter-intuitive minus signs when manipulating fermionic fields, some useful identities are presented here just in case the reader faces similar difficulties. Whenever the identities presented here are used in the dissertation, it is explicitly stated.

First of all, one has to bear in mind that a fermionic field is represented by a four-component vector of anticommuting Grassmann numbers. As a consequence, transposing a product of fermionic fields provides an additional minus sign due to changing the order of the components. For example, if $\psi$ and $\chi$ are fermionic fields, the transposition of their product is:

$$(\psi^\intercal \chi)^\intercal = -\chi^\intercal \psi \,. \tag{E.1}$$

The Hermitian conjugation is defined in such a way that

$$\psi^\dagger = \psi^{\intercal *} = \psi^{* \intercal} \,, \quad (\psi^\dagger \chi)^\dagger = \chi^\dagger \psi \,, \tag{E.2}$$

where $(\ldots)^*$ denotes the complex conjugation, which, therefore, must possess an additional minus:

$$(\psi^\dagger \chi)^* = (\psi^\dagger \chi)^{\dagger \intercal} = (\chi^\dagger \psi)^\intercal = -\psi^\intercal \chi^{\dagger \intercal} = -\psi^{\dagger *} \chi^* \,. \tag{E.3}$$

For a fermionic field $\chi$, one defines the charge-conjugated field $\chi^c$ and the Dirac-conjugated field $\bar{\chi}$ as

$$\chi^c \equiv -i\gamma_2 \chi^* \,, \quad \bar{\chi} \equiv \chi^\dagger \gamma_0 \tag{E.4}$$

(the gamma matrices are described in appendix D).

Using the above identities and the fact that the Lagrangian is defined up to a total derivative, so

$$(\partial_\mu \bar{\chi})\psi = \overbrace{\partial_\mu(\bar{\chi}\psi)}^{\text{irrelevant}} - \bar{\chi}\,\partial_\mu \psi = -\bar{\chi}\,\partial_\mu \psi \,, \tag{E.5}$$

it is straightforward to prove that

$$\chi^c = \mathcal{C}\bar{\chi}^\intercal \,, \qquad \bar{\chi^c} = \chi^\intercal \mathcal{C} \,, \tag{E.6a}$$

$$\chi^\intercal \mathcal{C} \chi = \bar{\chi^c} \chi \,, \qquad (\chi^\intercal \mathcal{C} \chi)^\dagger = \bar{\chi} \chi^c \,, \tag{E.6b}$$

$$\bar{\chi^c} \chi^c = \bar{\chi} \chi \,, \tag{E.6c}$$

$$\bar{\chi^c} \gamma_\mu \chi^c = -\bar{\chi} \gamma_\mu \chi \,, \tag{E.6d}$$

$$\bar{\chi^c} \partial\!\!\!/ \chi^c = \bar{\chi} \partial\!\!\!/ \chi \,, \tag{E.6e}$$

where operator $\mathcal{C}$ is the charge-conjugation operator defined in appendix D.3.

In the DM models containing dark fermions (appendices A and B.2), the Dirac fermion $\chi$ and its charge conjugation are decomposed into a pair of Majorana fermions $\psi_+$, $\psi_-$:

$$\psi_+ \equiv \frac{\chi + \chi^c}{\sqrt{2}} = \psi_+^c \,, \qquad \psi_- \equiv \frac{\chi - \chi^c}{i\sqrt{2}} = \psi_-^c \,, \tag{E.7a}$$

$$\chi = \frac{\psi_+ + i\psi_-}{\sqrt{2}} \,, \qquad \chi^c = \frac{\psi_+ - i\psi_-}{\sqrt{2}} \,. \tag{E.7b}$$

Then,

$$\bar{\chi} = \frac{\bar{\psi}_+ - i\bar{\psi}_-}{\sqrt{2}} \,, \qquad \bar{\chi^c} = \frac{\bar{\psi}_+ + i\bar{\psi}_-}{\sqrt{2}} \,. \tag{E.8}$$

As for Majorana fermions the following identity holds:

$$\bar{\psi}_+\psi_- = \bar{\psi}^c_+\psi^c_- = \psi^\intercal_+ \mathcal{C}\mathcal{C}\bar{\psi}^\intercal_- = -\psi^\intercal_+\bar{\psi}^\intercal_- = (\bar{\psi}_-\psi_+)^\intercal = \bar{\psi}_-\psi_+ \,, \tag{E.9}$$

it can by easily shown that

$$\bar{\chi}\chi = \bar{\chi^c}\chi^c = \frac{1}{2}(\bar{\psi}_+\psi_+ + \bar{\psi}_-\psi_-) \,, \tag{E.10a}$$

$$\bar{\chi^c}\chi = \frac{1}{2}(\bar{\psi}_+\psi_+ - \bar{\psi}_-\psi_-) + i\,\bar{\psi}_+\psi_- \,, \tag{E.10b}$$

$$\bar{\chi}\chi^c = \frac{1}{2}(\bar{\psi}_+\psi_+ - \bar{\psi}_-\psi_-) - i\,\bar{\psi}_+\psi_- \,, \tag{E.10c}$$

Analogously, it can be proved that

$$\bar{\chi}\,\partial\!\!\!/\chi = \bar{\chi^c}\,\partial\!\!\!/\chi^c = \frac{1}{2}(\bar{\psi}_+\,\partial\!\!\!/\psi_+ + \bar{\psi}_-\,\partial\!\!\!/\psi_-) \,. \tag{E.11}$$

Moreover, if $\chi$ is left-handed (i.e., $\chi = P_L\chi$, with the projection operator $P_L$ defined in appendix D.3), it is straightforward to show that

$$\bar{\chi}\chi = \bar{\chi^c}\chi^c = 0 \quad \Rightarrow \quad \bar{\psi}_-\psi_- = -\bar{\psi}_+\psi_+ \quad \Rightarrow \quad \begin{cases} \bar{\chi^c}\chi = \bar{\psi}_+\psi_+ + i\,\bar{\psi}_+\psi_- \\ \bar{\chi}\chi^c = \bar{\psi}_+\psi_+ - i\,\bar{\psi}_+\psi_- \end{cases} . \tag{E.12}$$

Analogously, for a left-handed $\chi$ the following identities hold:

$$\bar{\chi}\,\partial\!\!\!/\chi^c = \bar{\chi^c}\,\partial\!\!\!/\chi = 0 \quad \Rightarrow \quad \begin{cases} \bar{\psi}_+\,\partial\!\!\!/\psi_+ = \bar{\psi}_-\,\partial\!\!\!/\psi_- \\ \bar{\psi}_-\,\partial\!\!\!/\psi_+ = -\bar{\psi}_+\,\partial\!\!\!/\psi_- \end{cases} \quad \Rightarrow \quad \bar{\chi}\,\partial\!\!\!/\chi = \bar{\chi^c}\,\partial\!\!\!/\chi^c = \bar{\psi}_+\,\partial\!\!\!/\psi_+ \,. \tag{E.13}$$

# Appendix F

# Green's functions in the real-time formalism

In section 5.5, we make use of the retarded, advanced and symmetric Green's functions (denoted by the index $+$, $-$ and sym, respectively). We follow the definitions from [196].

The position-space propagators of a scalar particle can be expressed in terms of the real-time Green functions $\Delta^{>}$, $\Delta^{<}$ as follows:

$$\begin{aligned}\Delta^{\mathrm{sym}}(x,y) &= \Delta^{>}(x,y) + \Delta^{<}(x,y)\ ,\\ \Delta^{+}(x,y) &= \Theta(x_0-y_0)\left(\Delta^{>}(x,y) - \Delta^{<}(x,y)\right)\ ,\\ \Delta^{-}(x,y) &= \Theta(y_0-x_0)\left(\Delta^{<}(x,y) - \Delta^{>}(x,y)\right)\ ,\end{aligned} \tag{F.1}$$

with $\Theta(t-t')$ equal to 1 if $t$ succeeds $t'$ along the Keldysh-Schwinger integration contour, $-1$ otherwise. The fermion and vector propagators satisfy analogous relations. For details, see, e.g., section 4.1 of [197].

For convenience, let us define auxiliary functions:

$$\begin{aligned}\Delta^{\pm}_{\mathrm{aux}}(p) &\equiv \frac{1}{p^2 - m^2 \pm i\,\mathrm{sgn}\,p_0\,0^+}\ ,\\ \Delta^{\mathrm{sym}}_{\mathrm{F,B}}(p,T) &\equiv \pm\frac{i\pi}{E_p}\Big(\delta(E_p-p_0)\big[2n_{\mathrm{F,B}}(\mathbf{p},T)\mp 1\big] + \delta(E_p+p_0)\big[2n_{\mathrm{F,B}}(-\mathbf{p},T)\mp 1\big]\Big)\ ,\end{aligned} \tag{F.2}$$

which will serve to define the Green's functions.

Note that, for isotropic distribution functions, the auxiliary function $\Delta^{\mathrm{sym}}$ becomes

$$\begin{aligned}\Delta^{\mathrm{sym}}_{\mathrm{F,B}}(p,T) &\equiv \pm\frac{i\pi}{E_p}\Big(\delta(E_p-p_0)+\delta(E_p+p_0)\Big)\big[2n_{\mathrm{F,B}}(\mathbf{p},T)\mp 1\big]\\ &= -\frac{i\pi}{E_p}\Big(\delta(E_p-p_0)+\delta(E_p+p_0)\Big)\cdot f_{\mathrm{F,B}}(\beta E_p)\end{aligned} \tag{F.3}$$

with

$$f_{F,B}(x) \equiv \pm 2n_{F,B}(\mathbf{p},T) - 1. \tag{F.4}$$

For $n$ describing thermal distribution of Maxwell-Boltzmann or Fermi-Dirac type, given by

$$n_{\mathrm{F,B}}(-\mathbf{p},T) = n_{\mathrm{F,B}}(\mathbf{p},T) = \frac{1}{e^{\beta E_p}\pm 1}\ , \tag{F.5}$$

the function $f$ reads

$$f_{\mathrm{F,B}}(x) = \begin{cases}\frac{e^x-1}{e^x+1} & \text{for fermions}\\ \frac{e^x+1}{e^x-1} & \text{for bosons}\end{cases}\ . \tag{F.6}$$

Then, the scalar Green's functions are given by

$$\begin{aligned}\Delta^{\pm}(p) &= \Delta^{\pm}_{\mathrm{aux}}(p),\\ \Delta^{\mathrm{sym}}(p,T) &= \Delta^{\mathrm{sym}}_{B}(p,T)\ ,\end{aligned} \tag{F.7}$$

while for a fermion particle

$$\begin{aligned} G^{\pm}(p) &= (\not{p} + m)\, \Delta^{\pm}_{\rm aux}(p) \,, \\ G^{\rm sym}(p,T) &= (\not{p} + m)\, \Delta^{\rm sym}_{F}(p,T) \,, \end{aligned} \tag{F.8}$$

and for a vector

$$\begin{aligned} D^{\pm}_{\mu\nu}(p) &= \left[ -g_{\mu\nu} + \frac{p_\mu p_\nu}{m^2} \right] \Delta^{\pm}_{\rm aux}(p) \,, \\ D^{\rm sym}_{\mu\nu}(p,T) &= \left[ -g_{\mu\nu} + \frac{p_\mu p_\nu}{m^2} \right] \Delta^{\rm sym}_{B}(p,T) \,. \end{aligned} \tag{F.9}$$

# Appendix G

# Passarino-Veltman functions

If a given Feynman diagram contains a loop (like the one presented in fig. G.1), its contribution to the scattering amplitude is given as an integral over the loop momentum. The result of the integration can be expressed in terms of so-called Passarino-Veltman functions, introduced in [198, 199]. In this appendix, we follow the notation of chapter 4 of [200].

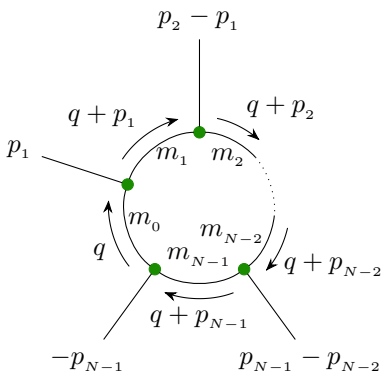


**Figure G.1:** A loop, whose contribution to the amplitude is described by eq. (G.1). All the external momenta are directed towards the loop.

The integral corresponding to the loop presented in fig. G.1 reads

$$T^N_{\mu_1,\ldots,\mu_k}(p_1, p_2, \ldots, p_{N-1}; m_0, m_1, m_2, \ldots, m_{N-1}) \equiv \frac{1}{i\pi^2} \int d^4q \, \frac{q_{\mu_1} \ldots q_{\mu_k}}{D_0 \, D_1 \, \ldots \, D_{N-1}} \, , \tag{G.1}$$

where the factors in the denominator are

$$D_0 \equiv q^2 - m_0^2 + i\varepsilon \, , \quad D_i \equiv (q + p_i)^2 - m_{h_i}^2 + i\varepsilon \quad (i = 1, \ldots, N-1) \, . \tag{G.2}$$

Later, we use $A$ for $T^1$, $B$ for $T^2$ and so on. Functions used in eq. (6.11) are defined in the following way:

$$
\begin{aligned}
\mathcal{D}_{112} &\equiv \frac{p^\mu}{m_{\rm DM}^2} D_\mu(0,0,p;m_{h_1},m_{h_1},m_{h_2},m_{\rm DM})\Big|_{p^2=m_{\rm DM}^2} \\
&= \frac{p^\mu}{m_{\rm DM}^2}\frac{1}{i\pi^2}\int d^4q \frac{q_\mu}{(q^2-m_{h_1}^2)^2(q^2-m_{h_2}^2)\left[(q+p)^2-m_{\rm DM}^2\right]}\Big|_{p^2=m_{\rm DM}^2} \\
&= \frac{1}{m_{h_1}^2-m_{h_2}^2}\left(\mathcal{C}_{11}-\mathcal{C}_{12}\right) \ ,
\end{aligned}
\tag{G.3a}
$$

$$
\begin{aligned}
\mathcal{D}_{122} &\equiv \frac{p^\mu}{m_{\rm DM}^2} D_\mu(0,0,p;m_{h_2},m_{h_1},m_{h_2},m_{\rm DM})\Big|_{p^2=m_{\rm DM}^2} \\
&= \frac{p^\mu}{m_{\rm DM}^2}\frac{1}{i\pi^2}\int d^4q \frac{q_\mu}{(q^2-m_{h_1}^2)(q^2-m_{h_2}^2)^2\left[(q+p)^2-m_{\rm DM}^2\right]}\Big|_{p^2=m_{\rm DM}^2} \\
&= -\frac{1}{m_{h_1}^2-m_{h_2}^2}\left(\mathcal{C}_{22}-\mathcal{C}_{12}\right) \ ,
\end{aligned}
\tag{G.3b}
$$

$$
\begin{aligned}
\mathcal{C}_{12} &\equiv \frac{p^\mu}{m_{\rm DM}^2} C_\mu(0,p;m_{h_1},m_{h_2},m_{\rm DM})\Big|_{p^2=m_{\rm DM}^2} \\
&= \frac{p^\mu}{m_{\rm DM}^2}\frac{1}{i\pi^2}\int d^4q \frac{q_\mu}{(q^2-m_{h_1}^2)(q^2-m_{h_2}^2)\left[(q+p)^2-m_{\rm DM}^2\right]}\Big|_{p^2=m_{\rm DM}^2} \\
&= \frac{1}{m_{h_1}^2-m_{h_2}^2}\left(\mathcal{B}_1-\mathcal{B}_2\right) \ ,
\end{aligned}
\tag{G.3c}
$$

with the following auxiliary functions defined for $i=1,2$:

$$
\begin{aligned}
\mathcal{C}_{ii} &\equiv \frac{p^\mu}{m_{\rm DM}^2} C_\mu(0,p;m_{h_i},m_{h_i},m_{\rm DM})\Big|_{p^2=m_{\rm DM}^2} \\
&= -\frac{1}{m_{\rm DM}^2}\left[1+\frac{x_i^+(x_i^+-1)}{x_i^+-x_i^-}\ln\left(\frac{x_i^+-1}{x_i^+}\right)-\frac{x_i^-(x_i^--1)}{x_i^+-x_i^-}\ln\left(\frac{x_i^--1}{x_i^-}\right)\right] \ ,
\end{aligned}
\tag{G.4a}
$$

$$
\begin{aligned}
\mathcal{B}_i &\equiv \frac{p^\mu}{m_{\rm DM}^2} B_\mu(p;m_{h_i},m_{\rm DM})\Big|_{p^2=m_{\rm DM}^2} \\
&= -\frac{1}{2}\left[\left(\frac{2}{\epsilon}-\gamma+\ln\frac{\mu^2}{m_{\rm DM}^2}\right)+1+\frac{m_{h_i}^2}{m_{\rm DM}^2}+(x_i^+)^2\ln\left(\frac{x_i^+-1}{x_i^+}\right)+(x_i^-)^2\ln\left(\frac{x_i^--1}{x_i^-}\right)\right] \ ,
\end{aligned}
\tag{G.4b}
$$

$$
x_i^\pm \equiv \frac{m_{h_i}^2 \pm \sqrt{m_{h_i}^4-4m_{h_i}^2m_{\rm DM}^2}}{2m_{\rm DM}^2} \ .
\tag{G.4c}
$$

The term $\left(\frac{2}{\epsilon}-\gamma+\ln\frac{\mu^2}{m_{\rm DM}^2}\right)$ appearing in eq. (G.4b) is a remnant of the chosen regularization method and cancels out in eq. (G.3c).

# Appendix H

# Self-energies of the scalar states

In this appendix, we provide the values of the imaginary parts of one-loop two-point Green's functions, $\Pi_{ij}(Q^2)$, calculated for the Higgs-like states. To obtain each value, one has to sum contributions corresponding to all possible intermediate loops:

$$\Pi_{ij} = \Pi_{ij}^{\mathrm{DM}} + \Pi_{ij}^{W^+W^-} + \Pi_{ij}^{ZZ} + \sum_q \Pi_{ij}^{q\bar{q}} + \sum_l \Pi_{ij}^{l^+l^-} + \sum_{k,l} \Pi_{ij}^{h_k h_l} \ . \tag{H.1}$$

The tadpole and seagull diagrams are omitted. Here, DM denotes a pair of dark particles, i.e., $AA$, $\psi\psi$ or $XX$, depending on the model, while $q$ and $l$ denote the SM quarks and leptons, respectively. These one-loop contributions take the following form:

$$\begin{aligned}
\Pi_{ij}^{\mathrm{DM}}(Q^2) &= I(Q^2, m_{\mathrm{DM}}, m_{\mathrm{DM}}) \frac{R_{2i}R_{2j}}{32\pi^2 v_S^2} (m_{h_i} m_j)^2 \times \\
&\quad \times \begin{cases} 1 & \text{(pGDM)} \\ 1 - 2\, m_{\mathrm{DM}}^2 \frac{4Q^2 - m_i^2 - m_j^2}{(m_{h_i} m_{h_j})^2} + 12 \left( \frac{m_{\mathrm{DM}}^2}{(m_{h_i} m_{h_j})^2} \right)^2 & \text{(VDM)} \\ 2 \frac{m_{\mathrm{DM}}^2 Q^2}{(m_{h_i} m_{h_j})^2} \left( 1 - 4 \frac{m_{\mathrm{DM}}^2}{Q^2} \right) & \text{(FDM)} \end{cases} , \\
\Pi_{ij}^{W^+W^-}(Q^2) &= I(Q^2, m_W, m_W) \frac{R_{1i}R_{1j}}{16\pi^2 v^2} (m_{h_i} m_{h_j})^2 \times \\
&\quad \times \left[ 1 - 2 m_W^2 \frac{4Q^2 - m_i^2 - m_j^2}{(m_{h_i} m_{h_j})^2} + 12 \frac{m_W^4}{(m_{h_i} m_{h_j})^2} \right] , \\
\Pi_{ij}^{ZZ}(Q^2) &= I(Q^2, m_Z, m_Z) \frac{R_{1i}R_{1j}}{32\pi^2 v^2} (m_{h_i} m_{h_j})^2 \times \\
&\quad \times \left[ 1 - 2 m_Z^2 \frac{4Q^2 - m_i^2 - m_j^2}{(m_{h_i} m_{h_j})^2} + 12 \frac{m_Z^4}{(m_{h_i} m_{h_j})^2} \right] , \\
\Pi_{ij}^{q\bar{q}}(Q^2) &= I(Q^2, m_q, m_q) \cdot \frac{3 R_{1i}R_{1j}}{8\pi^2 v^2} m_q^2 Q^2 \left( 1 - 4 \frac{m_q^2}{Q^2} \right) , \\
\Pi_{ij}^{l^+l^-}(Q^2) &= I(Q^2, m_l, m_l) \cdot \frac{R_{1i}R_{1j}}{8\pi^2 v^2} m_l^2 Q^2 \left( 1 - 4 \frac{m_l^2}{Q^2} \right) , \\
\Pi_{ij}^{h_k h_l}(Q^2) &= I(Q^2, m_{h_k}, m_{h_l}) \cdot \frac{V_{ikl} V_{jkl}}{32\pi^2} ,
\end{aligned}$$

with $V_{ijk}$ $(i,j,k=1,2)$, given by

$$V_{111} \equiv 3m_1^2\left(\frac{\sin^3\alpha}{v_S}+\frac{\cos^3\alpha}{v}\right)\,, \tag{H.2a}$$

$$V_{112}=V_{121}=V_{211} \equiv (2m_1^2+m_2^2)\sin\alpha\cos\alpha\left(\frac{\sin\alpha}{v_S}-\frac{\cos\alpha}{v}\right)\,, \tag{H.2b}$$

$$V_{221}=V_{212}=V_{122} \equiv (m_1^2+2m_2^2)\sin\alpha\cos\alpha\left(\frac{\cos\alpha}{v_S}+\frac{\sin\alpha}{v}\right)\,, \tag{H.2c}$$

$$V_{222} \equiv 3m_2^2\left(\frac{\cos^3\alpha}{v_S}-\frac{\sin^3\alpha}{v}\right)\,, \tag{H.2d}$$

being the $h_ih_jh_k$ couplings [190] and

$$\begin{aligned} I(Q^2,m_a,m_b) &\equiv i\cdot\Im\left[B_0(Q^2,m_a^2,m_b^2)\right] \\ &= i\cdot\Im\left[\frac{1}{i\pi^2}\int\frac{d^4l}{(l^2-m_a^2)[(l+Q)^2-m_b^2]}\right] \\ &= i\pi\cdot\frac{\lambda^{1/2}(Q^2,m_a^2,m_b^2)}{Q^2}\cdot\mathbb{1}_{Q^2>(m_a+m_b)^2} \end{aligned} \tag{H.3a}$$

$$\rightarrow \quad I(Q^2,m,m) = i\pi\cdot\sqrt{1-\frac{4m^2}{Q^2}}\cdot\mathbb{1}_{Q^2>4m^2} \tag{H.3b}$$

denoting the imaginary parts (times $i$) of appropriate Passarino-Veltman integrals $B_0$ [200]. Here, $\lambda$ is the Källén triangle function defined by eq. (0.4). The overall sign of eq. (H.3a) corresponds to the sign chosen in $\ln(-1)=\pm i\pi$. The positive sign provides values consistent with the optical theorem, $\Pi_{ii}(m_{h_i}^2)=+im_{h_i}\Gamma_i$.

Note that, in [190], the $\Pi_{ij}^{\mathrm{DM}}$ contribution calculated in the VDM model contains an additional minus due to a redundant factor $i$ in their definition of $V_{ijk}$.

We perform a straightforward calculation in the limit of $m_{h_2}=m_{h_1}$ to show that for $ab$ standing for DM, $W^+W^-$, $ZZ$, $q\bar{q}$, $l^+l^-$, or $h_kh_l$, the following equality holds:

$$\left(\Pi_{11}^{ab}-\Pi_{22}^{ab}\right)-\left(\tan\alpha\cdot\Pi_{12}^{ab}-\cot\alpha\cdot\Pi_{21}^{ab}\right)\Big|_{m_1=m_2}=0 \tag{H.4}$$

for (in the last case one has to sum over $k,l=1,2$). Therefore, the sum of all contributions vanishes as well.

From the optical theorem it follows that the partial widths of $h_1$ and $h_2$ are related to the imaginary parts of the appropriate self-energies as

$$\Gamma_{h_i\to ab}=\frac{\Pi_{ii}^{ab}(m_{h_i}^2)}{im_{h_i}}\,, \tag{H.5}$$

so that they take the following form:

$$\Gamma_{h_i\to\mathrm{DM}}=\frac{R_{2i}^2}{v_S^2}\frac{m_{h_i}^3}{32\pi}\sqrt{1-\frac{4m_{\mathrm{DM}}^2}{m_{h_i}^2}}\times\begin{cases}1 & (\mathrm{pGDM})\\ 1-4\frac{m_{\mathrm{DM}}^2}{m_{h_i}^2}+12\left(\frac{m_{\mathrm{DM}}^2}{m_{h_i}^2}\right)^2 & (\mathrm{VDM})\\ 2\frac{m_{\mathrm{DM}}^2}{m_{h_i}^2}\left(1-4\frac{m_{\mathrm{DM}}^2}{m_{h_i}^2}\right) & (\mathrm{FDM})\end{cases}\,, \tag{H.6a}$$

$$\Gamma_{h_i\to\mathrm{SM}}=R_{1i}^2\,\gamma(m_{h_i}) \qquad (\gamma \text{ denotes decay width of the SM Higgs particle of given mass})\,, \tag{H.6b}$$

$$\begin{aligned}\Gamma_{h_1\to h_2h_2} &= \sin^2\alpha\,\cos^2\alpha\,(m_1^2+2m_2^2)^2\left(\frac{\cos\alpha}{v_S}+\frac{\sin\alpha}{v}\right)^2\frac{\sqrt{m_1^2-4m_2^2}}{32\pi m_1^2} \\ &\simeq \frac{\sin^2\alpha\,\cos^4\alpha}{v_S^2}(m_1^2+2m_2^2)^2\frac{\sqrt{m_1^2-4m_2^2}}{32\pi m_1^2}\,,\end{aligned} \tag{H.6c}$$

$$\begin{aligned}\Gamma_{h_2\to h_1h_1} &= \sin^2\alpha\,\cos^2\alpha\,(2m_1^2+m_2^2)^2\left(\frac{\sin\alpha}{v_S}-\frac{\cos\alpha}{v}\right)^2\frac{\sqrt{m_2^2-4m_1^2}}{32\pi m_2^2} \\ &\simeq \frac{\sin^2\alpha\,\cos^4\alpha}{v^2}(2m_1^2+m_2^2)^2\frac{\sqrt{m_2^2-4m_1^2}}{32\pi m_2^2}\,.\end{aligned} \tag{H.6d}$$

# Bibliography


[8] G. Arcadi, A. Djouadi and M. Raidal, *Dark Matter through the Higgs portal*, *Phys. Rept.* **842** (2020) 1 [1903.03616].

[9] E.W. Kolb and M.S. Turner, *The Early Universe*, vol. 69 (1990), 10.1201/9780429492860.

[10] Planck collaboration, *Planck 2018 results. VI. Cosmological parameters*, *Astron. Astrophys.* **641** (2020) A6 [1807.06209].

[11] Planck collaboration, *Planck 2018 results. VII. Isotropy and Statistics of the CMB*, *Astron. Astrophys.* **641** (2020) A7 [1906.02552].

[12] Particle Data Group collaboration, *Review of Particle Physics,* section 25.3.1, *PTEP* **2022** (2022) 083C01.

[13] R. Baierlein, *The elusive chemical potential*, *American Journal of Physics* **69** (2001) 423.

[14] S. Mrowczynski and P. Danielewicz, *Green Function Approach to Transport Theory of Scalar Fields*, *Nucl. Phys. B* **342** (1990) 345.

[15] L.P. Kadanoff and G. Baym, *Quantum Statistical Mechanics*, CRC Press (Mar., 2018), 10.1201/9780429493218.

[16] P. Gondolo and G. Gelmini, *Cosmic abundances of stable particles: Improved analysis*, *Nucl. Phys. B* **360** (1991) 145.

[17] M. Duch and B. Grzadkowski, *Resonance enhancement of dark matter interactions: the case for early kinetic decoupling and velocity dependent resonance width*, *JHEP* **09** (2017) 159 [1705.10777].

[18] Particle Data Group collaboration, *Review of Particle Physics,* chapter 2, *PTEP* **2022** (2022) 083C01.

[19] Particle Data Group collaboration, *Review of Particle Physics,* chapter 1, *PTEP* **2022** (2022) 083C01.

[20] K. Griest and M. Kamionkowski, *Supersymmetric dark matter*, *Phys. Rept.* **333** (2000) 167.

[21] M. Iglicki, *Vector-fermion dark matter*, master's thesis, Warsaw U., 2018, [1804.10289].

[22] A. Ahmed, M. Duch, B. Grzadkowski and M. Iglicki, *Multi-Component Dark Matter: the vector and fermion case*, *Eur. Phys. J. C* **78** (2018) 905 [1710.01853].

[23] A. Ahmed, M. Duch, B. Grzadkowski and M. Iglicki, *Vector-fermion Dark Matter Model*, *Acta Phys. Polon. B* **48** (2017) 2405.

[24] G. Bertone and D. Hooper, *History of dark matter*, *Rev. Mod. Phys.* **90** (2018) 045002 [1605.04909].

[25] H. Poincaré, *La Voie lactée et la théorie des gaz*, *Bulletin de la Société astronomique de France* **20** (1906) 153.

[26] W. Thomson, Baron Kelvin, *Baltimore Lectures on Molecular Dynamics and the Wave Theory of Light*, Cambridge University Press (1904, 2010), 10.1017/cbo9780511694523.

[27] F. Zwicky, *Die Rotverschiebung von extragalaktischen Nebeln*, *Helv. Phys. Acta* **6** (1933) 110.

[28] F. Zwicky, *On the Masses of Nebulae and of Clusters of Nebulae*, *Astrophys. J.* **86** (1937) 217.

[29] V.C. Rubin and W.K. Ford, Jr., *Rotation of the Andromeda Nebula from a Spectroscopic Survey of Emission Regions*, *Astrophys. J.* **159** (1970) 379.

[30] K.C. Freeman, *On the disks of spiral and SO Galaxies*, *Astrophys. J.* **160** (1970) 811.

[31] E. Corbelli and P. Salucci, *The Extended Rotation Curve and the Dark Matter Halo of M33*, *Mon. Not. Roy. Astron. Soc.* **311** (2000) 441 [astro-ph/9909252].

[32] M. Pettini, *Introduction to Cosmology — Lecture 10*, lecture notes, Cambridge U., Institute of Astronomy, 2018, https://people.ast.cam.ac.uk/∼pettini/Intro%20Cosmology/Lecture10.pdf, accessed: 2023-06-03 .

[33] D.J. Fixsen, *The Temperature of the Cosmic Microwave Background*, *Astrophys. J.* **707** (2009) 916 [0911.1955].

[34] ESA and the Planck Collaboration, 2018, https://wiki.cosmos.esa.int/planck-legacy-archive/index.php/CMB_maps, accessed: 2023-06-03 .

[35] D. Clowe, M. Bradac, A.H. Gonzalez, M. Markevitch, S.W. Randall, C. Jones et al., *A direct empirical proof of the existence of dark matter*, *Astrophys. J. Lett.* **648** (2006) L109 [astro-ph/0608407].

[36] NASA and ESA, 2015, https://hubblesite.org/contents/media/images/2015/10/3507-Image.html, accessed: 2023-06-03 .

[37] Particle Data Group collaboration, *Review of Particle Physics,* section 22.3.7, *PTEP* **2022** (2022) 083C01.

[38] B.D. Fields, K.A. Olive, T.-H. Yeh and C. Young, *Big-Bang Nucleosynthesis after Planck*, *JCAP* **03** (2020) 010 [1912.01132].

[39] B.J. Carr, K. Kohri, Y. Sendouda and J. Yokoyama, *New cosmological constraints on primordial black holes*, *Phys. Rev. D* **81** (2010) 104019 [0912.5297].

[40] B. Carr, M. Raidal, T. Tenkanen, V. Vaskonen and H. Veermäe, *Primordial black hole constraints for extended mass functions*, *Phys. Rev. D* **96** (2017) 023514 [1705.05567].

[41] B. Carr, K. Kohri, Y. Sendouda and J. Yokoyama, *Constraints on primordial black holes*, *Rept. Prog. Phys.* **84** (2021) 116902 [2002.12778].

[42] M. Milgrom, *A Modification of the Newtonian dynamics as a possible alternative to the hidden mass hypothesis*, *Astrophys. J.* **270** (1983) 365.

[43] M. Milgrom, *A Modification of the Newtonian dynamics: Implications for galaxies*, *Astrophys. J.* **270** (1983) 371.

[44] M. Milgrom, *A modification of the Newtonian dynamics: implications for galaxy systems*, *Astrophys. J.* **270** (1983) 384.

[45] J.D. Bekenstein, *Relativistic gravitation theory for the MOND paradigm*, *Phys. Rev. D* **70** (2004) 083509 [astro-ph/0403694].

[46] C. Skordis, D.F. Mota, P.G. Ferreira and C. Boehm, *Large Scale Structure in Bekenstein's theory of relativistic Modified Newtonian Dynamics*, *Phys. Rev. Lett.* **96** (2006) 011301 [astro-ph/0505519].

[47] S. Boran, S. Desai, E.O. Kahya and R.P. Woodard, *GW170817 Falsifies Dark Matter Emulators*, *Phys. Rev. D* **97** (2018) 041501 [1710.06168].

[48] SNO collaboration, *Measurement of the rate of $\nu_e + d \to p + p + e^-$ interactions produced by $^8B$ solar neutrinos at the Sudbury Neutrino Observatory*, *Phys. Rev. Lett.* **87** (2001) 071301 [nucl-ex/0106015].

[49] J. Lesgourgues and S. Pastor, *Neutrino cosmology and Planck*, *New J. Phys.* **16** (2014) 065002 [1404.1740].

[50] G. Steigman, *Neutrinos And Big Bang Nucleosynthesis*, *Adv. High Energy Phys.* **2012** (2012) 268321 [1208.0032].

[51] J. Lesgourgues, G. Mangano, G. Miele and S. Pastor, *Neutrino Cosmology*, Cambridge University Press (Feb., 2013), 10.1017/cbo9781139012874.

[52] A.M. Green, *Astrophysical uncertainties on the local dark matter distribution and direct detection experiments*, *J. Phys. G* **44** (2017) 084001 [1703.10102].

[53] A.K. Drukier, K. Freese and D.N. Spergel, *Detecting Cold Dark Matter Candidates*, *Phys. Rev. D* **33** (1986) 3495.

[54] T. Piffl et al., *The RAVE survey: the Galactic escape speed and the mass of the Milky Way*, *Astron. Astrophys.* **562** (2014) A91 [1309.4293].

[55] K. Freese, M. Lisanti and C. Savage, *Colloquium: Annual modulation of dark matter*, *Rev. Mod. Phys.* **85** (2013) 1561 [1209.3339].

[56] A.A. Klypin, A.V. Kravtsov, O. Valenzuela and F. Prada, *Where are the missing Galactic satellites?*, *Astrophys. J.* **522** (1999) 82 [astro-ph/9901240].

[57] B. Moore, S. Ghigna, F. Governato, G. Lake, T.R. Quinn, J. Stadel et al., *Dark matter substructure within galactic halos*, *Astrophys. J. Lett.* **524** (1999) L19 [astro-ph/9907411].

[58] P. Madau, J. Diemand and M. Kuhlen, *Dark matter subhalos and the dwarf satellites of the Milky Way*, *Astrophys. J.* **679** (2008) 1260 [0802.2265].

[59] S. Tulin and H.-B. Yu, *Dark Matter Self-interactions and Small Scale Structure*, *Phys. Rept.* **730** (2018) 1 [1705.02358].

[60] DES collaboration, *Milky Way Satellite Census. I. The Observational Selection Function for Milky Way Satellites in DES Y3 and Pan-STARRS DR1*, *Astrophys. J.* **893** (2020) 1 [1912.03302].

[61] A.M. Brooks, E. Papastergis, C.R. Christensen, F. Governato, A. Stilp, T.R. Quinn et al., *How to Reconcile the Observed Velocity Function of Galaxies with Theory*, *Astrophys. J.* **850** (2017) 97 [1701.07835].

[62] J.S. Bullock and M. Boylan-Kolchin, *Small-Scale Challenges to the ΛCDM Paradigm*, *Ann. Rev. Astron. Astrophys.* **55** (2017) 343 [1707.04256].

[63] M. Boylan-Kolchin, J.S. Bullock and M. Kaplinghat, *Too big to fail? The puzzling darkness of massive Milky Way subhaloes*, *Mon. Not. Roy. Astron. Soc.* **415** (2011) L40 [1103.0007].

[64] M. Boylan-Kolchin, J.S. Bullock and M. Kaplinghat, *The Milky Way's bright satellites as an apparent failure of LCDM*, *Mon. Not. Roy. Astron. Soc.* **422** (2012) 1203 [1111.2048].

[65] N.E. Mavromatos, C.R. Argüelles, R. Ruffini and J.A. Rueda, *Self-interacting dark matter*, *Int. J. Mod. Phys. D* **26** (2016) 1730007.

[66] N.E. Mavromatos, C.R. Argüelles, R. Ruffini and J.A. Rueda, *Self-interacting dark matter*, in *14th Marcel Grossmann Meeting on Recent Developments in Theoretical and Experimental General Relativity, Astrophysics, and Relativistic Field Theories*, vol. 1, pp. 639–666, 2017, DOI.

[67] M. Rocha, A.H.G. Peter, J.S. Bullock, M. Kaplinghat, S. Garrison-Kimmel, J. Onorbe et al., *Cosmological Simulations with Self-Interacting Dark Matter I: Constant Density Cores and Substructure*, *Mon. Not. Roy. Astron. Soc.* **430** (2013) 81 [1208.3025].

[68] C.R. Argüelles, E.A. Becerra-Vergara, J.A. Rueda and R. Ruffini, *Fermionic Dark Matter: Physics, Astrophysics, and Cosmology*, *Universe* **9** (2023) 197 [2304.06329].

[69] Particle Data Group collaboration, *Review of Particle Physics*, chapter 27, *PTEP* **2022** (2022) 083C01.

[70] NEWSDM collaboration, *The NEWSdm experiment for directional dark matter searches*, *PoS* **ICHEP2022** (2022) 253.

[71] N. Ávalos et al., *Skipper CCDs for the search of a daily modulation of Dark Matter signal in the DMSQUARE experiment*, *J. Phys. Conf. Ser.* **2156** (2021) 012074.

[72] J. Cooley, *Dark Matter direct detection of classical WIMPs*, *SciPost Phys. Lect. Notes* **55** (2022) 1 [2110.02359].

[73] DAMIC collaboration, *Search for low-mass WIMPs in a 0.6 kg day exposure of the DAMIC experiment at SNOLAB*, *Phys. Rev. D* **94** (2016) 082006 [1607.07410].

[74] EDELWEISS collaboration, *Search for sub-GeV dark matter via the Migdal effect with an EDELWEISS germanium detector with NbSi transition-edge sensors*, *Phys. Rev. D* **106** (2022) 062004 [2203.03993].

[75] XENON collaboration, *Dark Matter Search Results from a One Ton-Year Exposure of XENON1T*, *Phys. Rev. Lett.* **121** (2018) 111302 [1805.12562].

[76] D.Z. Freedman, *Coherent Neutrino Nucleus Scattering as a Probe of the Weak Neutral Current*, *Phys. Rev. D* **9** (1974) 1389.

[77] COHERENT collaboration, *Observation of Coherent Elastic Neutrino-Nucleus Scattering*, *Science* **357** (2017) 1123 [1708.01294].

[78] C.A.J. O'Hare, *New Definition of the Neutrino Floor for Direct Dark Matter Searches*, *Phys. Rev. Lett.* **127** (2021) 251802 [2109.03116].

[79] J. Billard, L. Strigari and E. Figueroa-Feliciano, *Implication of neutrino backgrounds on the reach of next generation dark matter direct detection experiments*, *Phys. Rev. D* **89** (2014) 023524 [1307.5458].

[80] M. Ibe, W. Nakano, Y. Shoji and K. Suzuki, *Migdal Effect in Dark Matter Direct Detection Experiments*, *JHEP* **03** (2018) 194 [1707.07258].

[81] XENON collaboration, *Search for Light Dark Matter Interactions Enhanced by the Migdal Effect or Bremsstrahlung in XENON1T*, *Phys. Rev. Lett.* **123** (2019) 241803 [1907.12771].

[82] CDEX collaboration, *Results of direct dark matter detection with CDEX experiment at CJPL*, *J. Phys. Conf. Ser.* **1468** (2020) 012070 [1911.05249].

[83] LUX collaboration, *Results from a search for dark matter in the complete LUX exposure*, *Phys. Rev. Lett.* **118** (2017) 021303 [1608.07648].

[84] PANDAX-II collaboration, *Results of dark matter search using the full PandaX-II exposure*, *Chin. Phys. C* **44** (2020) 125001 [2007.15469].

[85] DARKSIDE collaboration, *DarkSide-50 532-day Dark Matter Search with Low-Radioactivity Argon*, *Phys. Rev. D* **98** (2018) 102006 [1802.07198].

[86] F. Agostini, chapter 2 of: *The XENON project: backgrounds and new results*, Ph.D. thesis, GSSI, SISSA, 2017, https://web.bo.infn.it/xenon/sito_web_Bologna/tesi/tesi_agostini_dottorato.pdf.

[87] XENON collaboration, *Observation of two-neutrino double electron capture in $^{124}$Xe with XENON1T*, *Nature* **568** (2019) 532 [1904.11002].

[88] PICO collaboration, *Dark Matter Search Results from the Complete Exposure of the PICO-60 $C_3F_8$ Bubble Chamber*, *Phys. Rev. D* **100** (2019) 022001 [1902.04031].

[89] MOSCAB collaboration, *MOSCAB: direct dark matter search using the geyser technique*, *Nucl. Part. Phys. Proc.* **273-275** (2016) 2354.

[90] COUPP collaboration, *Improved Spin-Dependent WIMP Limits from a Bubble Chamber*, *Science* **319** (2008) 933 [0804.2886].

[91] NEWS-G collaboration, *The NEWS-G detector at SNOLAB*, *JINST* **18** (2023) T02005 [2205.15433].

[92] T. Shimada et al., *Direction-sensitive dark matter search with three-dimensional vector-type tracking in NEWAGE*, 2301.04779.

[93] R. Bernabei et al., *First model independent results from DAMA/LIBRA-phase2*, *Nucl. Phys. Atom. Energy* **19** (2018) 307 [1805.10486].

[94] J. Amare et al., *Annual modulation results from three-year exposure of ANAIS-112*, *Phys. Rev. D* **103** (2021) 102005 [2103.01175].

[95] COSINE-100 collaboration, *Strong constraints from COSINE-100 on the DAMA dark matter results using the same sodium iodide target*, *Sci. Adv.* **7** (2021) abk2699 [2104.03537].

[96] R. Bernabei et al., *Final model independent result of DAMA/LIBRA-phase1*, *Eur. Phys. J. C* **73** (2013) 2648 [1308.5109].

[97] COSINE-100 collaboration, *An induced annual modulation signature in COSINE-100 data by DAMA/LIBRA's analysis method*, *Sci. Rep.* **13** (2023) 4676 [2208.05158].

[98] SENSEI collaboration, *SENSEI: Characterization of Single-Electron Events Using a Skipper Charge-Coupled Device*, *Phys. Rev. Applied* **17** (2022) 014022 [2106.08347].

[99] CoGeNT collaboration, *CoGeNT: A Search for Low-Mass Dark Matter using p-type Point Contact Germanium Detectors*, *Phys. Rev. D* **88** (2013) 012002 [1208.5737].

[100] CDEX collaboration, *CDEX Dark Matter Experiment: Status and Prospects*, *J. Phys. Conf. Ser.* **1342** (2020) 012067 [1712.06046].

[101] SuperCDMS collaboration, *Demonstration of Surface Electron Rejection with Interleaved Germanium Detectors for Dark Matter Searches*, *Appl. Phys. Lett.* **103** (2013) 164105 [1305.2405].

[102] CRESST collaboration, *Results on sub-GeV Dark Matter from a 10 eV Threshold CRESST-III Silicon Detector*, 2212.12513.

[103] Y. Hochberg, Y. Kahn, M. Lisanti, C.G. Tully and K.M. Zurek, *Directional detection of dark matter with two-dimensional targets*, *Phys. Lett. B* **772** (2017) 239 [1606.08849].

[104] S. Baum et al., *Mineral Detection of Neutrinos and Dark Matter. A Whitepaper*, 2301.07118.

[105] HESS collaboration, *Searches for gamma-ray lines and 'pure WIMP' spectra from Dark Matter annihilations in dwarf galaxies with H.E.S.S*, *JCAP* **11** (2018) 037 [1810.00995].

[106] L. Goodenough and D. Hooper, *Possible Evidence For Dark Matter Annihilation In The Inner Milky Way From The Fermi Gamma Ray Space Telescope*, 0910.2998.

[107] Event Horizon Telescope collaboration, *First Sagittarius A* Event Horizon Telescope Results. I. The Shadow of the Supermassive Black Hole in the Center of the Milky Way*, *Astrophys. J. Lett.* **930** (2022) L12.

[108] J. Gao, A. Li and B.W. Jiang, *Modeling the Infrared Extinction toward the Galactic Center*, *Earth Planets Space* **65** (2013) 1127 [1305.7137].

[109] Hess, HAWC, VERITAS, MAGIC, H.E.S.S., Fermi-LAT collaboration, *Combined dark matter searches towards dwarf spheroidal galaxies with Fermi-LAT, HAWC, H.E.S.S., MAGIC, and VERITAS*, *PoS* **ICRC2021** (2021) 528 [2108.13646].

[110] G. Steigman, B. Dasgupta and J.F. Beacom, *Precise Relic WIMP Abundance and its Impact on Searches for Dark Matter Annihilation*, *Phys. Rev. D* **86** (2012) 023506 [1204.3622].

[111] Fermi-LAT collaboration, *The Large Area Telescope on the Fermi Gamma-ray Space Telescope Mission*, *Astrophys. J.* **697** (2009) 1071 [0902.1089].

[112] W.B. Atwood et al., *Design and Initial Tests of the Tracker-Converter of the Gamma-ray Large Area Space Telescope*, *Astropart. Phys.* **28** (2007) 422.

[113] D. Hooper, *The Status of the Galactic Center Gamma-Ray Excess*, in *14th International Workshop on the Identification of Dark Matter 2022*, 9, 2022 [2209.14370].

[114] MAGIC collaboration, *A review of the past and present MAGIC dark matter search program and a glimpse at the future*, in *25th European Cosmic Ray Symposium*, 1, 2017 [1701.05702].

[115] VERITAS collaboration, *VERITAS Highlights 2022*, *J. Phys. Conf. Ser.* **2429** (2023) 012015.

[116] HAWC collaboration, *Searching for TeV Dark Matter in Irregular Dwarf Galaxies with HAWC Observatory*, *Astrophys. J.* **945** (2023) 25 [2302.07929].

[117] A. Das, B. Dasgupta and A. Ray, *Galactic positron excess from selectively enhanced dark matter annihilation*, *Phys. Rev. D* **101** (2020) 063014 [1911.03488].

[118] Fermi-LAT collaboration, *Measurements of the cosmic-ray electron and positron spectrum and anisotropies with the Fermi LAT*, *J. Phys. Conf. Ser.* **934** (2017) 012016.

[119] AMS 02 collaboration, *The antimatter spectrometer (AMS-02): A particle physics detector in space*, *Nucl. Instrum. Meth. A* **588** (2008) 227.

[120] PAMELA collaboration, *Cosmic-Ray Positron Energy Spectrum Measured by PAMELA*, *Phys. Rev. Lett.* **111** (2013) 081102 [1308.0133].

[121] M. Boezio et al., *Measurements of cosmic-ray electrons and positrons by the Wizard/CAPRICE collaboration*, *Adv. Space Res.* **27** (2001) 669.

[122] C. Grimani et al., *Measurements of the absolute energy spectra of cosmic-ray positrons and electrons above 7-GeV*, *Astron. Astrophys.* **392** (2002) 287.

[123] M.A. DuVernois et al., *Cosmic ray electrons and positrons from 1-GeV to 100-GeV: Measurements with HEAT and their interpretation*, *Astrophys. J.* **559** (2001) 296.

[124] H. Zhan, *Constraining the dark matter interpretation of the positron excess with $\gamma$-ray data*, 2305.01992.

[125] R. Liang, *Contribution of Pulsars to the AMS-02 Positron Excess*, *J. Phys. Conf. Ser.* **2346** (2022) 012008.

[126] GAPS collaboration, *Antideuteron Sensitivity for the GAPS Experiment*, *Astropart. Phys.* **74** (2016) 6 [1506.02513].

[127] L.S. Miranda, S. Basegmez du Pree, K.C.Y. Ng, A. Cheek and C. Arina, *Towards detecting super-GeV dark matter via annihilation to neutrinos*, 2211.12235.

[128] IceCube collaboration, *Search for neutrino lines from dark matter annihilation and decay with IceCube*, 2303.13663.

[129] ANTARES collaboration, *Overview of the results from the ANTARES neutrino telescope*, *J. Phys. Conf. Ser.* **2429** (2023) 012027.

[130] Super-Kamiokande collaboration, *Dark Matter Searches at Super-Kamiokande*, *J. Phys. Conf. Ser.* **1342** (2020) 012075.

[131] Hyper-Kamiokande collaboration, *Hyper-Kamiokande Design Report*, 1805.04163.

[132] N.F. Bell, M.J. Dolan and S. Robles, *Searching for dark matter in the Sun using Hyper-Kamiokande*, *JCAP* **11** (2021) 004 [2107.04216].

[133] G. Wikstrom and J. Edsjo, *Limits on the WIMP-nucleon scattering cross-section from neutrino telescopes*, *JCAP* **04** (2009) 009 [0903.2986].

[134] G.D. Mack, J.F. Beacom and G. Bertone, *Towards Closing the Window on Strongly Interacting Dark Matter: Far-Reaching Constraints from Earth's Heat Flow*, *Phys. Rev. D* **76** (2007) 043523 [0705.4298].

[135] S.L. Adler, *Planet-bound dark matter and the internal heat of Uranus, Neptune, and hot-Jupiter exoplanets*, *Phys. Lett. B* **671** (2009) 203 [0808.2823].

[136] ATLAS, CMS collaboration, *Collider Searches for Dark Matter (ATLAS + CMS)*, *Universe* **4** (2018) 131.

[137] ATLAS collaboration, *Combination of searches for invisible decays of the Higgs boson using 139 $fb^{-1}$ of proton-proton collision data at $\sqrt{s} = 13$ TeV collected with the ATLAS experiment*, 2301.10731.

[138] CMS collaboration, *Search for invisible decays of a Higgs boson produced through vector boson fusion in proton-proton collisions at $\sqrt{s} = 13$ TeV*, *Phys. Lett. B* **793** (2019) 520 [1809.05937].

[139] ATLAS collaboration, *Search for an invisibly decaying Higgs boson or dark matter candidates produced in association with a Z boson in pp collisions at $\sqrt{s} = 13$ TeV with the ATLAS detector*, *Phys. Lett. B* **776** (2018) 318 [1708.09624].

[140] CMS collaboration, *Search for new physics in events with a leptonically decaying Z boson and a large transverse momentum imbalance in proton–proton collisions at $\sqrt{s} = 13$ TeV*, *Eur. Phys. J. C* **78** (2018) 291 [1711.00431].

[141] ATLAS collaboration, *Search for new resonances in mass distributions of jet pairs using 139 $fb^{-1}$ of pp collisions at $\sqrt{s} = 13$ TeV with the ATLAS detector*, *JHEP* **03** (2020) 145 [1910.08447].

[142] CMS collaboration, *Search for high mass dijet resonances with a new background prediction method in proton-proton collisions at $\sqrt{s} = 13$ TeV*, *JHEP* **05** (2020) 033 [1911.03947].

[143] D. Abercrombie et al., *Dark Matter benchmark models for early LHC Run-2 Searches: Report of the ATLAS/CMS Dark Matter Forum*, *Phys. Dark Univ.* **27** (2020) 100371 [1507.00966].

[144] A. Blondel and P. Janot, *Circular and Linear $e^+e^-$ Colliders: Another Story of Complementarity*, 1912.11871.

[145] A. Vauth and J. List, *Beam Polarization at the ILC: Physics Case and Realization*, *Int. J. Mod. Phys. Conf. Ser.* **40** (2016) 1660003.

[146] C. Foudas, *Particle Physics Course. Lecture 9: Helicity and Chirality and the Grodzins-Goldhaber-Sunyar Experiment*, lecture notes, Imperial College, London, 2007, https://alpha.physics.uoi.gr/foudas_public/APP/Lecture9-Helicity-and-Chirality.pdf, accessed: 2023-06-03.

[147] ILC International Development Team collaboration, *The International Linear Collider: Report to Snowmass 2021*, 2203.07622.

[148] A.A. Sokolov and I.M. Ternov, *On polarization and spin effects in the theory of synchrotron radiation*, *Dokl. Akad. Nauk SSSR* **153** (1963) 1052.

[149] O. Brunner et al., *The CLIC project*, 2203.09186.

[150] I. Agapov et al., *Future Circular Lepton Collider FCC-ee: Overview and Status*, in *Snowmass 2021*, 3, 2022 [2203.08310].

[151] CEPC Physics Study Group collaboration, *The Physics potential of the CEPC. Prepared for the US Snowmass Community Planning Exercise (Snowmass 2021)*, in *Snowmass 2021*, 5, 2022 [2205.08553].

[152] M. Bai et al., *$C^3$: A "Cool" Route to the Higgs Boson and Beyond*, in *Snowmass 2021*, 10, 2021 [2110.15800].

[153] V.N. Litvinenko, N. Bachhawat, M. Chamizo-Llatas, F. Meot and T. Roser, *CERC - Circular $e^+e^-$ Collider using Energy-Recovery Linac*, in *Snowmass 2021*, 3, 2022 [2203.07358].

[154] V.N. Litvinenko, N. Bachhawat, M. Chamizo-Llatas, Y. Jing, F. Méot, I. Petrushina et al., *The ReLiC: Recycling Linear $e^+e^-$ Collider*, 2203.06476.

[155] R. Assmann, M. Lamont and S. Myers, *A brief history of the LEP collider*, *Nucl. Phys. B Proc. Suppl.* **109** (2002) 17.

[156] K. Fujii et al., *The role of positron polarization for the inital* 250 *GeV stage of the International Linear Collider*, 1801.02840.

[157] J.P. Delahaye, M. Diemoz, K. Long, B. Mansoulié, N. Pastrone, L. Rivkin et al., *Muon Colliders*, 1901.06150.

[158] E. Braaten and R.D. Pisarski, *Soft Amplitudes in Hot Gauge Theories: A General Analysis*, *Nucl. Phys. B* **337** (1990) 569.

[159] R.F. Peierls, *Possible Mechanism for the Pion-Nucleon Second Resonance*, *Phys. Rev. Lett.* **6** (1961) 641.

[160] D.D. Brayshaw, W.A. Simmons and S.F. Tuan, *Some comments on the Brayshaw mechanism for generating peaks in the hadron system*, *Phys. Rev. D* **18** (1978) 1719.

[161] M. Nauenberg and A. Pais, *Remark on energy peaks in meson systems*, *Phys. Rev. Lett.* **8** (1962) 82.

[162] D.D. Brayshaw, *Three-Body Mechanism for Narrow Resonances*, *Phys. Rev. Lett.* **39** (1977) 371.

[163] C. Goebel, *Comments on Higher Resonance Models*, *Phys. Rev. Lett.* **13** (1964) 143.

[164] I.F. Ginzburg, *Initial particle instability in muon collisions*, *Nucl. Phys. B Proc. Suppl.* **51** (1996) 85 [hep-ph/9601272].

[165] K. Melnikov and V.G. Serbo, *New type of beam size effect and the W boson production at mu+ mu- colliders*, *Phys. Rev. Lett.* **76** (1996) 3263 [hep-ph/9601221].

[166] K. Melnikov and V.G. Serbo, *Processes with the T channel singularity in the physical region: Finite beam sizes make cross-sections finite*, *Nucl. Phys. B* **483** (1997) 67 [hep-ph/9601290].

[167] K. Melnikov, G.L. Kotkin and V.G. Serbo, *Physical mechanism of the linear beam size effect at colliders*, *Phys. Rev. D* **54** (1996) 3289 [hep-ph/9603352].

[168] C. Dams and R. Kleiss, *Singular cross-sections in muon colliders*, *Eur. Phys. J. C* **29** (2003) 11 [hep-ph/0212301].

[169] C. Dams and R. Kleiss, *Muon colliders, Monte Carlo and gauge invariance*, *Eur. Phys. J. C* **36** (2004) 177 [hep-ph/0309336].

[170] A. Ioannisian and A. Pilaftsis, *Neutrino oscillations in space within a solvable model*, *Phys. Rev. D* **59** (1999) 053003 [hep-ph/9809503].

[171] D. Karamitros and A. Pilaftsis, *Towards a Non-Local S-Matrix Theory*, 2208.10425.

[172] G.F. Giudice, A. Notari, M. Raidal, A. Riotto and A. Strumia, *Towards a complete theory of thermal leptogenesis in the SM and MSSM*, *Nucl. Phys. B* **685** (2004) 89 [hep-ph/0310123].

[173] H.A. Weldon, *Simple Rules for Discontinuities in Finite Temperature Field Theory*, *Phys. Rev. D* **28** (1983) 2007.

[174] S. Coleman and R.E. Norton, *Singularities in the physical region*, *Nuovo Cim.* **38** (1965) 438.

[175] A. Das, A. Bandyopadhyay, P.K. Roy and M.G. Mustafa, *General structure of fermion two-point function and its spectral representation in a hot magnetized medium*, *Phys. Rev. D* **97** (2018) 034024 [1709.08365].

[176] M.O. Gonchar, A.E. Kaloshin and V.P. Lomov, *Fermion resonance in quantum field theory*, *Mod. Phys. Lett. A* **22** (2007) 2511 [hep-ph/0611314].

[177] M. Nowakowski and A. Pilaftsis, *On gauge invariance of Breit-Wigner propagators*, *Z. Phys. C* **60** (1993) 121 [hep-ph/9305321].

[178] Fermi-LAT, DES collaboration, *Searching for Dark Matter Annihilation in Recently Discovered Milky Way Satellites with Fermi-LAT*, *Astrophys. J.* **834** (2017) 110 [1611.03184].

[179] D. Azevedo, M. Duch, B. Grzadkowski, D. Huang, M. Iglicki and R. Santos, *One-loop contribution to dark-matter-nucleon scattering in the pseudo-scalar dark matter model*, *JHEP* **01** (2019) 138 [1810.06105].

[180] C. Gross, O. Lebedev and T. Toma, *Cancellation Mechanism for Dark-Matter–Nucleon Interaction*, *Phys. Rev. Lett.* **119** (2017) 191801 [1708.02253].

[181] W.-F. Chang, T. Modak and J.N. Ng, *Signal for a light singlet scalar at the LHC*, *Phys. Rev. D* **97** (2018) 055020 [1711.05722].

[182] *Measurements of the Higgs boson production and decay rates and constraints on its couplings from a combined ATLAS and CMS analysis of the LHC pp collision data at $\sqrt{s}$ = 7 and 8 TeV*, ATLAS-CONF-2015-044, http://cds.cern.ch/record/2052552/.

[183] H. Dreiner, M. Huck, M. Krämer, D. Schmeier and J. Tattersall, *Illuminating Dark Matter at the ILC*, *Phys. Rev. D* **87** (2013) 075015 [1211.2254].

[184] Z.-H. Yu, X.-J. Bi, Q.-S. Yan and P.-F. Yin, *Dark matter searches in the mono-Z channel at high energy $e^+e^-$ colliders*, *Phys. Rev. D* **90** (2014) 055010 [1404.6990].

[185] N. Wan, M. Song, G. Li, W.-G. Ma, R.-Y. Zhang and J.-Y. Guo, *Searching for dark matter via mono-Z boson production at the ILC*, *Eur. Phys. J. C* **74** (2014) 3219 [1403.7921].

[186] P. Ko and H. Yokoya, *Search for Higgs portal DM at the ILC*, *JHEP* **08** (2016) 109 [1603.04737].

[187] J. Liu, X.-P. Wang and F. Yu, *A Tale of Two Portals: Testing Light, Hidden New Physics at Future $e^+e^-$ Colliders*, *JHEP* **06** (2017) 077 [1704.00730].

[188] S. Dutta, D. Sachdeva and B. Rawat, *Signals of Leptophilic Dark Matter at the ILC*, *Eur. Phys. J. C* **77** (2017) 639 [1704.03994].

[189] T. Kamon, P. Ko and J. Li, *Characterizing Higgs portal dark matter models at the ILC*, *Eur. Phys. J. C* **77** (2017) 652 [1705.02149].

[190] M. Duch, B. Grzadkowski and A. Pilaftsis, *Gauge-Independent Approach to Resonant Dark Matter Annihilation*, *JHEP* **02** (2019) 141 [1812.11944].

[191] G. Cacciapaglia, A. Deandrea and S. De Curtis, *Nearby resonances beyond the Breit-Wigner approximation*, *Phys. Lett. B* **682** (2009) 43 [0906.3417].

[192] International Large Detector Concept Group collaboration, *Search for Light Scalars Produced in Association with a Z boson at the 250 GeV stage of the ILC*, *PoS* **ICHEP2018** (2019) 630.

[193] International Large Detector concept group collaboration, *Search for Extra Scalars Produced in Association with Muon Pairs at the ILC*, in *International Workshop on Future Linear Colliders*, 2, 2019 [1902.06118].

[194] P. Bambade et al., *The International Linear Collider: A Global Project*, 1903.01629.

[195] A.L. Read, *Presentation of search results: The CL(s) technique*, *J. Phys.* **G28** (2002) 2693.

[196] A. Czajka and S. Mrowczynski, *Collective Excitations of Supersymmetric Plasma*, *Phys. Rev. D* **83** (2011) 045001 [1011.6028].

[197] A. Czajka, *Supersymmetric plasma systems and their nonsupersymmetric counterparts*, Ph.D. thesis, Jan Kochanowski U., 2015. 1601.08215.

[198] G. Passarino and M.J.G. Veltman, *One Loop Corrections for e+ e- Annihilation Into mu+ mu- in the Weinberg Model*, *Nucl. Phys. B* **160** (1979) 151.

[199] G. 't Hooft and M.J.G. Veltman, *Scalar One Loop Integrals*, *Nucl. Phys. B* **153** (1979) 365.

[200] A. Denner, *Techniques for calculation of electroweak radiative corrections at the one loop level and results for W physics at LEP-200*, *Fortsch. Phys.* **41** (1993) 307 [0709.1075].